Behaviour of additively manufactured metallic structures under blast loading

Magda Stańczak

École doctorale C2MP **Technologies de protection, sécurité, perception de la situation**

Behaviour of additively manufactured metallic structures under blast loading

Comportement des structures métalliques fabriquées par le biais un procédé additif contre les menaces de type explosif

THÈSE

présentée et soutenue publiqement le 25 avril 2022

pour l'obtention du

Doctorat de l'Université de Lorraine

(mention Sciences des Matériaux)

par

Magda STAŃCZAK

Directeur de thèse: **Prof. Marion MARTINY**

Co-directeurs de thèse: **Prof. Alexis RUSINEK, Dr. Teresa FRAS**

Composition du jury:

Président du jury		
Rapporteur:	**Jerzy MAŁACHOWSKI**	Military University of Technology in Warsaw
Rapporteur:	**Dirk MOHR**	Swiss Federal Institute of Technology in Zurich
Examinateur:	**Piotr PAWŁOWSKI**	Institute of Fundamental Technological Research (PAS)
Co-directeur de thèse	**Teresa FRAS**	Institut franco-allemand de recherches de Saint-Louis
Directeur de thèse:	**Marion MARTINY**	Université de Lorraine
Directeur de thèse:	**Alexis RUSINEK**	Université de Lorraine
Invité:	**Ludovic BLANC**	Institut franco-allemand de recherches de Saint-Louis

LEM3 (UL) — Laboratoire d'étude de Microstructure et de Mécaniques des Matériaux
PCE (ISL) — Protection contre les explosifs et menaces balistiques

Acknowledgment

Firstly, I would like to thank my supervisor Prof. Alexis Rusinek for his advice during the course of my PhD study. His immense knowledge and vast experience were genuinely influential in shaping my experiment methods and constituted a valuable review of my results. I would also like to thank supervisor Prof. Marion Martiny for her support and guidance that allowed me to complete this thesis.

I am extremely grateful to my supervisor Dr. Teresa Fras for her invaluable supervision, support, and tutelage. Her immense intelligence, vision, sincerity, and dynamism have encouraged me in all the time of my academic research and daily life.

I would like to express gratitude to Dr. Piotr Pawłowski for his mentorship, precious discussions, and attempts to find answers to each of the posed questions. I am grateful for his inquiring insight into the subject, which steered me through this research.

Furthermore, I would like to express my sincere thanks to the reviewers Prof. Jerzy Małachowski and Prof. Dirk Mohr, and all members of the jury for their participation in the doctoral defense process and evaluation of the manuscript.

I sincerely thank Dr. Ludovic Blanc for the time he spent explaining the explosive processes. Many thanks for his kindness and valuable considerations, especially during the tests at the proving ground. I also wish to thank Juliana Abrantes de Sampaio and Thierry Bourre for their technical support during my research.

Special thanks to Dr. Slim Bahi for his help during my stay at the LEM3 laboratory, and for performing additional experimental investigation, which significantly influenced the presented results. I would also like to thank Richard Bernier and Patrick Moll for their support at a wide experimental campaign of material characterization carried out during the pandemic challenging time. Merci beaucoup!

I would like to thank Dr. Jean-Francois Legendre, the head of the PCE group, for all kindness and support during my stay at ISL. My gratitude extends to the directors of the Institute for providing financial support that allowed me to undertake my research.

I want to thank the Institute of Fundamental Technological Research of the Polish Academy of Sciences (IPPT PAN), and Laboratory of Microstructure Studies and Mechanics of Materials (LEM3) for input throughout this PhD program.

I would also like to show gratitude to my monitoring committee, including Dr. Marina Seidl, Prof. Christophe Czarnota, and Dr. Raphaël Pesci. Special thanks to Dr. Marina Seidl for the opportunity to participate in many conferences and workshops, which were influential in shaping my research.

I want to thank my fellow PhD students: Paula Broniszewska, Dr. Laura Delcuse Robert, and Dr. Yann Coget, for our mutual support and absorbing meetings which contributed to extra steps during my research. Many thanks for building our friendliness over the last three years. Last but not least, I would like to thank all my friends and the lab mates from ISL, IPPT PAN, UL, WAT for a chance of exchanging experiences and incredibly inspiring conversations.

Finally, I would like to express my gratitude to my Parents, my Brothers, and our family's friends, without whom this all would not have been possible. Without their tremendous understanding and encouragement in the past few years, it would be impossible to complete my study.

Getting through my dissertation required more than academic support. I have many, many people to thank for listening to and, at times, having to tolerate me over the past three years. I cannot express in right words my gratitude and appreciation for their friendship. I would like to thank all the people whom I have had an opportunity to get to know during my studies, but the list would be too long to mention everyone personally. Exchange of experiences during friendly meetings have made my study and life in France a wonderful time.

Thank you all for your support!
Merci à tous pour votre soutien!
Ich danke euch allen für eure Unterstützung!
Dziękuję Wam wszystkim za wsparcie!

Contents

Abstract

The additive manufacturing technique allows for studies of metallic structures with complex geometry at a laboratory scale. The application of novel structures can be especially beneficial for improving the capacity of energy absorption and blast mitigation. In the presented thesis, the role of the topology of additively manufactured AlSi10Mg aluminum structures of several exemplary cellular structures (i.e., honeycomb, auxetic, lattice, and foam) is studied at static and blast compression. Furthermore, the relationship between the relative density and the deformation responses of the structures, as well as the energy absorption capacities is analyzed. To investigate the influence of the manufacturing process conditions on the mechanical properties, the material behavior of the printed AlSi10Mg aluminum alloy is studied. For completeness, an analysis of the deformed microstructure is also conducted. The obtained results prove the complexity of the material behavior. Therefore, a phenomenological model based on the modified Johnson-Cook approach is proposed. The developed model describes the obtained characteristics of the printed alloy with much better accuracy than the classical constitutive function. The finite element simulations conducted in LS-DYNA software are used to investigate the deformation mechanisms of the structures in detail. The results are consistent with the analytical calculations and the experimental observations. The final responses indicate that by selecting the appropriate topological parameters, it is possible to affect the performance of structures significantly and thus to improve their energy absorption properties. The resulting experiments and their modelling show that the discussed material and the manufacturing technology have a promising potential.

Keywords: Additive Manufacturing, DMSL method, AlSi10Mg, cellular materials, energy absorption, finite element methods

Résumé

La technique de fabrication additive permet d'étudier à l'échelle du laboratoire des structures métalliques à géométrie complexe. L'application de nouvelles structures peut être particuliérement bénéfique pour améliorer la capacité d'absorption d'énergie et d'atténuation des explosions. Dans cette thése, le rêle de la topologie des structures en aluminium AlSi10Mg fabriquées de maniére additive est étudiée. Plusieurs exemplaire de structures cellulaires sont présentées.On analysera la relation entre la densité relative et les réponses de déformation des structures, ainsi que les capacités d'absorption. Le comportement de l'alliage d'aluminium AlSi10Mg imprimé est étudié afin d'étudier l'influence des conditions du processus de fabrication sur les propriétés mécaniques. Pour compléter l'étude, une analyse de la microstructure déformée est également effectuée. Les résultats obtenus prouvent la complexité du comportement du matériau. Par conséquent, un modéle phénoménologique basé sur l'approche modifiée de Johnson-Cook est proposé. Le modèle développé décrit le comportement du matériau avec une bien meilleure précision que la fonction constitutive classique. Les simulations par éléments finis réalisées avec le logiciel LS-DYNA sont utilisées pour étudier en détail les mécanismes de déformation des structures. Les résultats montrent un bon accord avec les calculs analytiques et les observations expérimentales. Les réponses indiquent qu'en sélectionnant les paramètres topologiques appropriés, il est possible d'affecter significativement les performances des structures et ainsi d'améliorer leurs propriétés d'absorption d'énergie.

Mots-clés: Fabrication additive, ALSi10Mg, méthode DMSL,structures celluleires, absorption d'énergie, calculs par éléments finis

Acronyms

Acronyms	Definitions
2D Structure	The unit cell of the structure can be characterized by two-dimensional geometry; here honeycomb and auxetic structures
3D Structure	The unit cell of the structure must be characterized by three-dimensional geometry; here lattice and foam structures
AM	Additive Manufacturing
Aux	Auxetic structure
C-4	Explosive charge
CAD	Computer Aided Design
CFE	Crushing Force Efficiency
CM	Conventionally manufactured samples
DMLS	Direct Metal Laser Sintering
EDST	Explosive Driven Shock Tube
EA	Energy Absorption
EDM	Electrical Discharge Machining
FEM	Finite Element Analysis
HAZ	Heat-Affected Zone
HC	Honeycomb structure
HV	Vickers Pyramid Number
HT	Heat-treatment
JC model	Johnson-Cook model
Lat	Lattice structure
MAPE	Mean Absolute Percentage Error
Pl	Plateau Regime
QS	Quasi-Static conditions
RDX	Nitramide explosive material
SE	Stroke Efficiency
SEA	Specific Energy Absorption
SEM	Scanning Electron Microscope
SHPB	Split Hopkinson Pressure Bar
SR	Stress Ratio
TIR	Third Industrial Revolution
TNT	Trinitrotoluene explosive material
T room	Room temperature (around 20−22 °C)
VEA	Volumetric Energy Absorption
WHT	Without heat-treatment
XY	Sample printed horizontally
XZ	Sample printed vertically

Introduction

A continuous development of new explosive and ballistic threats requires increasing the effectiveness of protection systems [1]. Modern, lightweight cellular materials can be obtained through advanced production methods such as additive manufacturing (AM). Studies on cellular structures under blast loading have proved their better energy absorption capacity compared to monolithic structures of similar dimensions. It is expected that carefully engineered pre-designed structures may improve the protective features [2].

The manufacturing process of new structures should be based on the knowledge of the limitations of the produced AM components and the material properties [3]. This thesis focuses on structures manufactured by melting metal powder obtained by the Direct Metal Laser Sintering (DMLS) method. Understanding the effect of the particle distribution across the microstructure, as well as obtaining the material characteristics, can be crucial to improving the efficiency of AM protective shields. Consequently, the research conducted contributes to increase in survivability of personnel and equipment under the threat of explosions.

The proposed structures should be characterized by a high capacity to mitigate the shock wave with minimal mass and optimal spatial dimensions. The task starts with acquiring deeper knowledge on the protection systems currently used against blast waves. Therefore, the principal knowledge of the deformation mechanism during dynamic compression has been realized based on the literature [4,5], as well as laboratory studies [6,7]. As the conventional, thin-walled aluminum honeycomb structures have proven their potential in various applications such as crashworthiness in automotive or absorption in aircraft, they have been widely used in recent years. They are characterized by uniform damage, in which the cells buckle and fold under applied loading. The collapse process reduces the transmission of force to a protected structure [8]. Based on the experimental quasi-static and dynamic tests of the thin-walled structures, elementary numerical simulations in the LS-DYNA program have been developed.

Based on the research conducted, it is possible to open further studies of the absorption efficiency of the structures manufactured by the DMLS method. Four representative types of the printed structures are tested during quasi-static and blast compression: honeycomb, auxetic, rhomboidal lattice, and regular foam. The comparison of results includes the influence of the sample dimensions, the relative density, as well as the arrangement of the cells on the absorption properties of the structures. The damage process of the structures tested is analyzed, which allows correlating the measured results with the structure response recorded in the tests.

In addition, the mechanical behavior of the AlSi10Mg aluminum alloy used for additively manufactured components is analyzed. The tensile and compressive tests are performed under quasi-static and dynamic conditions. To investigate mechanical properties of the printed alloy, the temperature effect is also considered. Moreover, the experimental investigation has evaluated the influence of the printed direction and the applied heat treatment on the material behavior. Due to the complexity of the obtained experimental characteristics of the printed alloy, developing a phenomenological modified Johnson-Cook model has been necessary to describe the thermo-visco-plastic behavior of the printed AlSi10Mg alloy [9].

The preliminary studies and the obtained material characteristics allow for validation of the simulations in LS-DYNA. As well as, the explicit numerical tasks developed for the AM

structures assess the correctness of the obtained experimental results. The thesis focuses on analyzing the effects observed experimentally, providing a detailed discussion on the material performance. The results can be beneficial for military and industrial applications, and further studies on protective systems.

Background of the project

Understanding the performance of structures and materials under a blast loading is crucial to improve the efficiency of protective components. However, the need to predict the damage caused by the explosion requires wide studies. Analysis of the complex flow field induced by blast and shock waves passing through complex media play a key role in improving the disaster prevention. Depending on the kind of the charge, its mass and shape or its distance from the structure, different impact power in the considered point may be expected [10]. The amount of generated energy, along with the structure's mechanical and geometrical properties, define the damage caused by the explosion. Therefore, the second approach to blast protection is based on designing new security devices.

As the interest in additive manufacturing technologies has increased in recent years, the aim of this thesis is to study and characterize the possibilities of the AM components to absorb energy. The scope of the research includes the investigation of the behavior of the AM structures under static and dynamic conditions, as well as their utility to mitigate the blast effects. In addition, the study has to contribute to increase the survivability of the target (e.g. personnel, equipment) endangered by explosions.

Objectives

To achieve the aim of this thesis, the following objectives are outlined: a) Analysis of the behavior of AM structures used to absorb blast energy. Explanation of operating principles of the experimental technique, i.e., explosive driven shock tube (EDST) based on the conventional structures used to absorb blast energy.

b) Based on the gained knowledge on the behavior of structures affected by a blast wave, selection of the representative geometries of the structures to perform the experimental campaign.

c) Exploration of the additive manufacturing techniques, in particular the DMLS method, which enabled the production of the tested samples. Understanding of the complex operation principles of the EOS EOSINT M 280 system.

d) Design and manufacture of specimens for material characterization, as well as the study on the deformation process of various geometries.

e) Conducting the quasi-static and dynamic material tests over a wide range of the temperature and strain rate on the as-fabricated and heat-treated samples manufactured at different

angles to the build platform. Comparison of the microhardness and microstructure of AlSi10Mg aluminum samples subjected to different compression load conditions to explain the results obtained with the material.

f) Development of phenomenological constitutive material model based on the experimental results, taking into account the physical phenomena observed.

g) Correlation of the deformation modes of the additively manufactured structures with the results measured and development of numerical simulations.

h) Analyze of the investigated processes, summarizing and identifying the perspectives for further development of AM absorbers.

Thesis contents

The completed milestones are described in the following parts of the manuscript:

Chapter I presents a literature review on the experimental setups enabling effective testing of samples subjected to the blast wave, as well as a description of the phenomena occurring during the explosion. The second part deals with the dynamic behavior of cellular structures under quasi-static and dynamic loading by reviewing publications on metamaterials. The aim is also to identify the main comparative parameters that allow the evaluation of the energy absorption properties of the structures.

Chapter II provides insight into the emerging manufacturing technology in application to protection against explosive effects. This chapter describes the manufacturing process, from the preparation of the digital model, configuration of the parameters of the 3D machine, through production, to the final processing of the manufactured parts. The main goal is to point out the challenges and limitations of the powder bed fusion technique focusing particularly on the DMLS method.

Chapter III is focused on the microstructure analysis which is correlated with the obtained mechanical properties. The material characteristics are identified by means of quasi-static and dynamic tests for a wide range of temperature and strain rates. The tests are performed on the "as-fabricated" and heat-treated samples, manufactured at different angles to the build platform. Therefore, the influence of the strain rate, temperature, print angle, and post-processing is presented and discussed. In order to explain the material results obtained in the tests, the comparison of the microhardness and microstructure is presented. The chapter highlights the process of developing a new phenomenological constitutive material model for the printed AlSi10Mg alloy. The method of modifying the Johnson-Cook model in order to fit material curves to complex experimental results is shown in details.

Chapter IV presents the description and final results of the experimental campaign. First, based on the tests performed on the thin-walled metallic honeycomb structure, the EDST test stand is described. The second part is focused on the additively manufactured structures. The

result comparison takes place between structures with different geometries and arrangement of cells, as well as loaded in two directions. Furthermore, the quasi-static tests on the AM structures and image correlation complement the conclusions allowing to carry out a deeper analysis of the absorption properties.

Chapter V highlights one of the ways to develop a numerical task for the AM structures subjected to the blast wave. The software limitations and the issues related to the numerical modelling of advanced materials are pointed out. Finally, the chapter aims to understand the dynamic behavior of AM structures, indicates the most deformed parts, and to explain the physical phenomena that challenge experiments. The simulations obtained provide the complete analysis of the mechanisms experimentally observed, related to energy absorption.

Chapter VI summarizes the main conclusions of the thesis. In addition, some perspectives for future studies and possible application of observations are presented at the end of the manuscript.

Résumé en français

I Contexte et objectifs

Les tests continus (Fig. 1a) et le développement de nouvelles menaces explosives et balistiques (Fig. 1c) nécessitent que l'efficacité des systémes de protection soit optimisée. Des matériaux cellulaires modernes et légers peuvent être obtenus grâce à des méthodes de production avancées, telles que la fabrication additive (AM) (Fig. 1e). Des études menées sur des structures cellulaires impactées par les effets de souffle ont prouvé leur meilleure capacité d'absorption d'énergie par rapport à des structures monolithiques de dimensions similaires (Fig. 1b, Fig. 1d). On s'attend à ce que des structures de géométrie spécifique, soigneusement conçues, pourront améliorer les caractéristiques de protection [11].

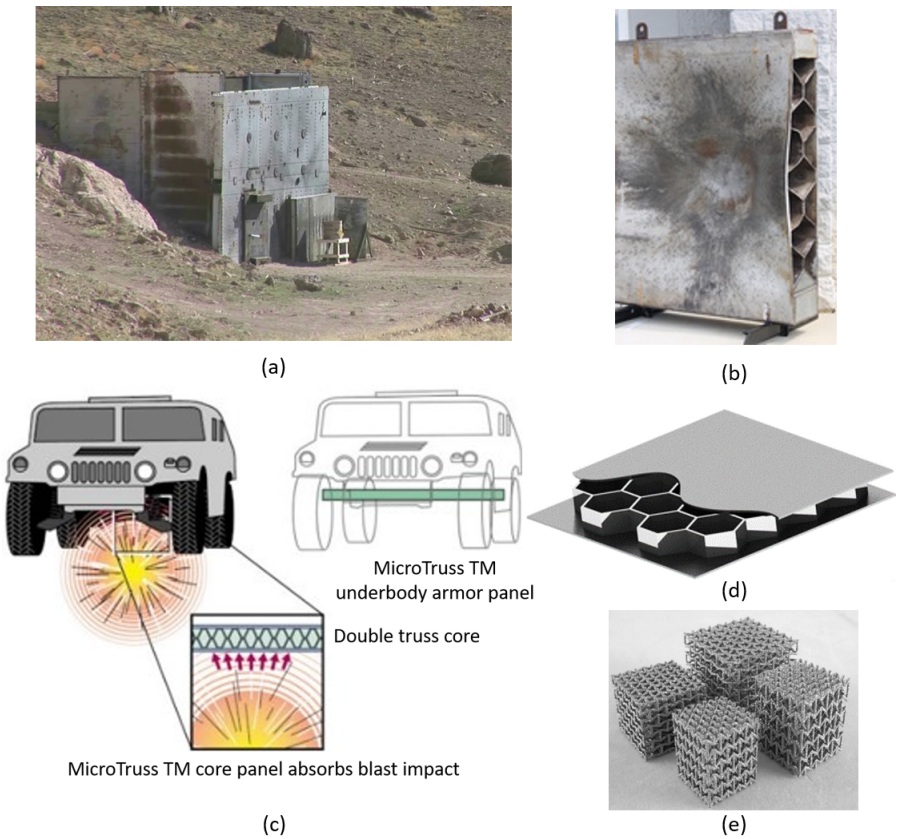

Figure 1: *Systèmes de protection contre les explosions : (a) tests effectués sur un mur résistant aux explosions avec unmontage expérimental simulant une voiture piégée [12], (b) la section centrale* d'un *panneau après test [12], (c) exemple* d'une *protection balistique du plancher du véhicule [12] (d) schéma de sandwich á âme en nid* d'abeille *métallique cellulaire (e) structures cellulaires fabriquées de manière additive testées dans [3].*

II Comportement généralisé des structures métalliques cellulaires sous compression quasi-statique et dynamique

Une représentation schématique et généralisée de la réaction d'une structure cellulaire métallique à la compression est présentée sur la figure 2a, [13]. La courbe peut varier en fonction du type de structure, du taux de déformation et des conditions externes, mais si la structure est entièrement comprimée, les trois parties principales sont généralement reconnaissables. Aprés la plage élastique linéaire de la déformation de la structure, la contrainte maximale enregistrée représente la contrainte d'effondrement plastique, c'est-à-dire la charge maximale que la structure peut supporter. La phase suivante est connue sous le nom de régime plateau et se produit dans la structure jusqu'à sa densification. La valeur du régime plateau peut être déterminée de manière approximative par la contrainte moyenne constante, qui représente la charge généralisée transmise à la structure protégée. Dans le cas des nids d'abeilles métalliques à parois minces (Fig. 2b), en régime de plateau, de nombreux plis plastiques se forment dans la hauteur de la structure, qui est le principale mécanisme de dissipation d'énergie. Les structures absorbent de grandes quantités d'énergie au niveau de contrainte du plateau en raison d'une structure sous-jacente qui n'est pas exposée à une contrainte de compression supplémentaire jusqu'au moment où l'énergie transmise est suffisamment importante pour provoquer la densification de la structure. La longueur du plateau détermine le moment où la structure atteint la phase de densification où de nouvelles déformations plastiques importantes ne sont plus possibles.

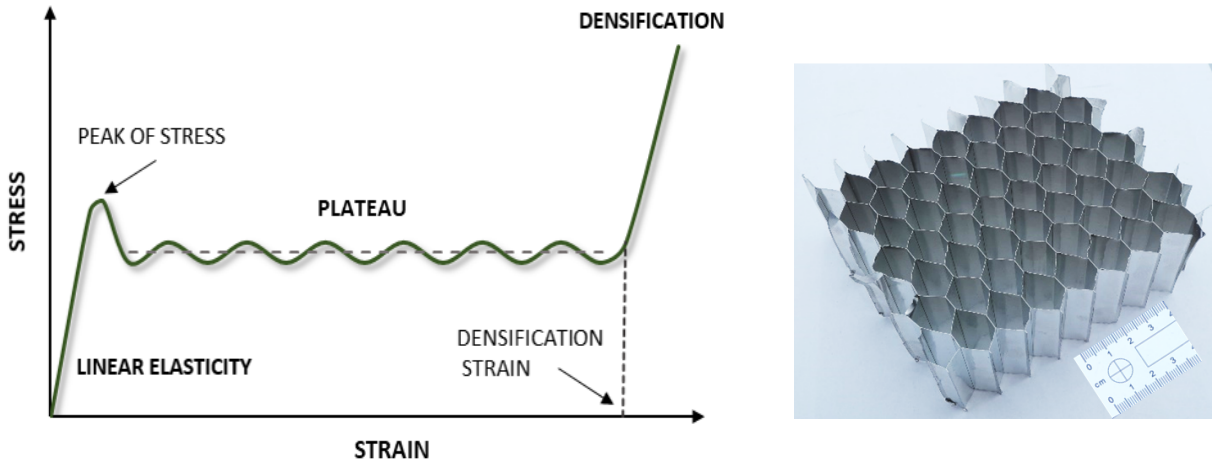

(a) (b)

Figure 2: *(a) Courbe contrainte-déformation généralisée représentant la réponse* d'une *structure cellulaire métallique à une charge de compression, et (b) structure en nid* d'abeilles *en aluminium à paroi mince testée.*

III Etude expérimentale

I Échantillons à tester

Le but de ce paragraphe est d'étudier la réponse mécanique et les modes de défaillance de quatre structures cellulaires : nid d'abeille, auxétique, treillis et mousse. Les éprouvettes cubiques soumises à une compression quasi-statique et dynamique sont présentées dans la Figure 3. Ils sont fabriqués de manière additive grâce au frittage de type Direct Metal Laser Sintering (DMLS).

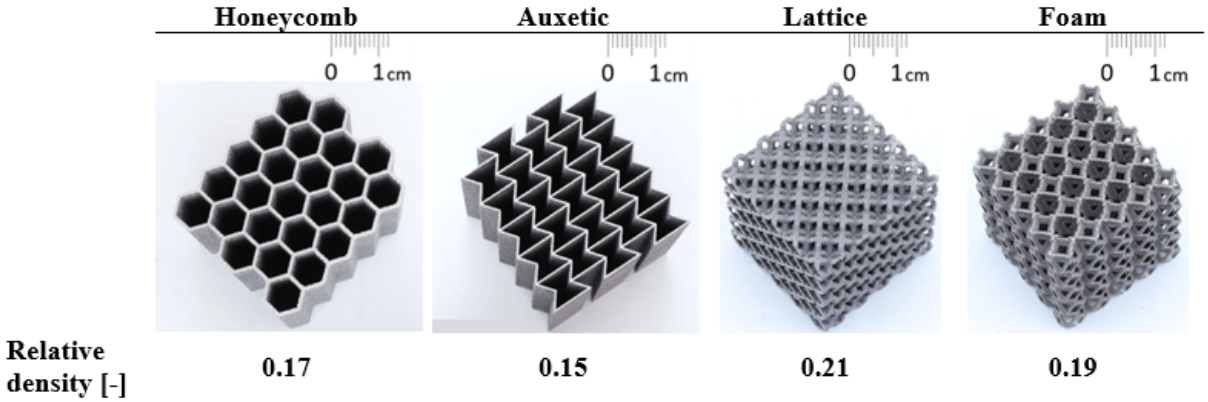

Figure 3: *Photographies des structures fabriquées de manière additive à partir de poudre* d'aluminium *AlSi10Mg utilisées dans les essais quasi-statiques et dynamiques en relation avec la densité relative.*

II Comportement du matériau alliage d'aluminium AlSi10Mg

L'influence du processus d'impression et des conditions externes sur les résultats mécaniques obtenus est étudiée dans la thèse. Les tests de compression dynamique et quasi-statique, ainsi que les tests de traction quasi-statique ont été effectués sur les échantillons fabriqués dans des directions d'impression différentes de la plate-forme de fabrication. Les tests effectués sur une large plage de vitesse de déformation et de changements de température prouvent que l'orientation de l'échantillon influence de manière significative les résultats de résistance. Les résultats de compression contrainte-déformation augmentent lorsque la pente des échantillons imprimés augmente (Fig. 4b). Cependant, le phénomène inverse est observé lors des essais de traction (Fig. 4a). Les échantillons imprimés horizontalement obtiennent des résultats de résistance d'environ 80 MPa supérieurs à ceux imprimés verticalement. Cependant, l'allongement à la rupture est réduit d'environ 7%.

De plus, on observe que l'aluminium imprimé n'est que peu sensible aux variations de la vitesse de déformation (Fig. 5a). Cependant, lorsque la température augmente de l'état ambiant jusqu'à 200 °C, la résistance à la traction ultime peut diminuer deux fois (Fig. 5b).

L'analyse de la microstructure des échantillons tels que fabriqués et traités thermiquement permet d'expliquer certains des phénomènes observés. Une corrélation claire entre l'anisotrophie de la microstructure induite par le procédé AM et les propriétés mécaniques est constatée. La forme des bains de fusion dépend du côté de l'échantillon observé. Le traitement thermique effectué provoque la précipitation des grains de Si de la matrice Al/Si. Les particules de Si

grossissent à travers la structure cellulaire fine, ce qui influence le comportement macroscopique des échantillons fabriqués.

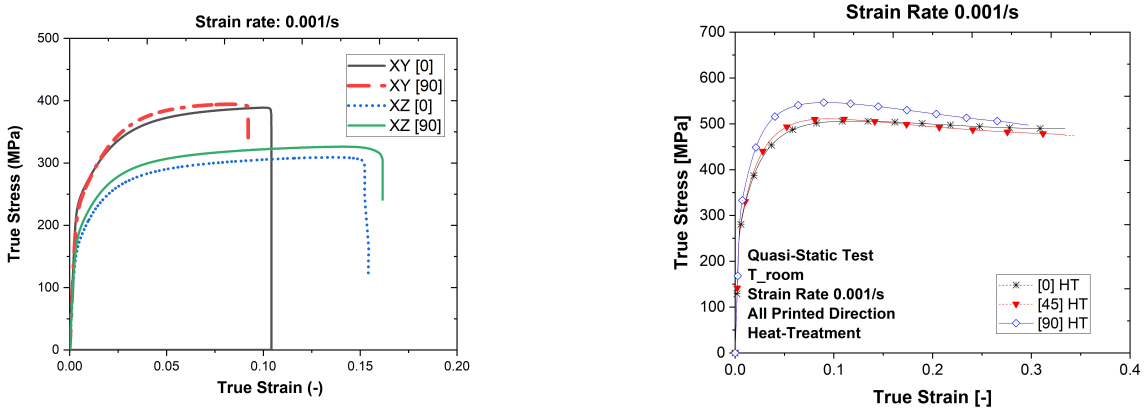

(a) (b)

Figure 4: *Influence de la direction* d'impression *sur la contrainte réelle - résultats de contrainte réelle basés sur les échantillons traités thermiquement. Les essais quasi-statiques de traction (a) et compression (b) sont effectués à une vitesse de déformation égale à 0.001/s.*

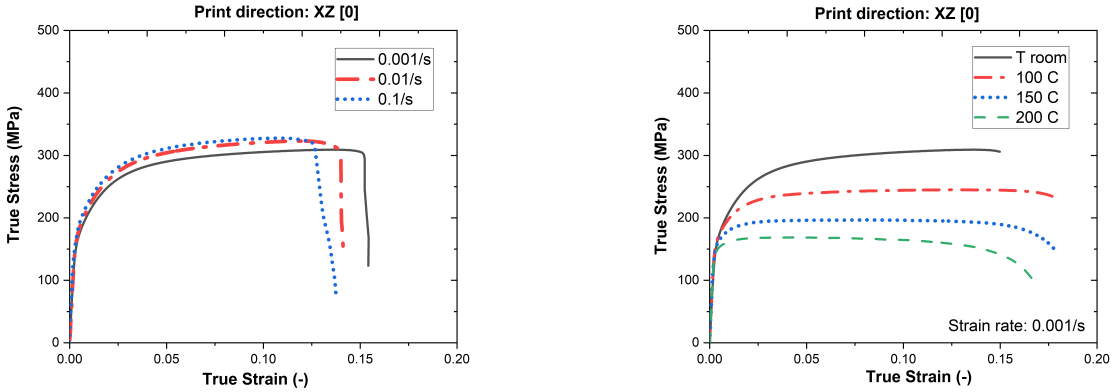

(a) (b)

Figure 5: *Sensibilité à la vitesse de déformation (a) et aux changements de température (b) de* l'alliage d'aluminium *AlSi10Mg sur la base des tests de traction sur les échantillons traités thermiquement imprimés horizontalement.*

Les caractéristiques matérielles obtenues de l'imprimé L'aluminium AlSi10Mg dans un tell domaine de conditions externes permettent de compléter les connaissances dans la recherche sur cet alliage appliquée aux techniques additives. Les résultats obtenus prouvent la complexité du comportement du matériau. Par la suite, il a été constaté que le modèle Johnson-Cook ne peut pas reproduire avec suffisamment de précision les caractéristiques obtenues. Par conséquent, le modèle constitutif phénoménologique JC modifié est proposé sur la base des résultats expérimentaux. Éq. 1 présente le modéle de comportement final de l'alliage d'aluminium AlSi10Mg,

dans lequel la contrainte d'écoulement est la somme des deux plages de contrainte équivalente : σ_I (jusqu'à la déformation de référence sous un adoucissement visible) et σ_{II} (dans lequelle se produit le durcissement dans la région dynamique).

$$\sigma_f = \sigma_I + \sigma_{II}\langle \varepsilon_p - \varepsilon_{ref} \rangle^0 \tag{1}$$

Où ε_p est la déformation plastique équivalente et ε_{ref} est la déformation de référence pour laquelle le ramollissement ne se produit pas dans la région dynamique. La notation de Macaulay est définie en utilisant Eq. 2.

$$\begin{cases} \langle \bullet \rangle^0 = 0, & \bullet < 0 \\ \langle \bullet \rangle^0 = 1, & \bullet \geq 0 \end{cases} \tag{2}$$

Par conséquent, l'erreur moyenne entre les expériences et les résultats analytiques pour toutes les caractéristiques du matériau est minimisée à 3 %.

III Description de l'étude expérimentale

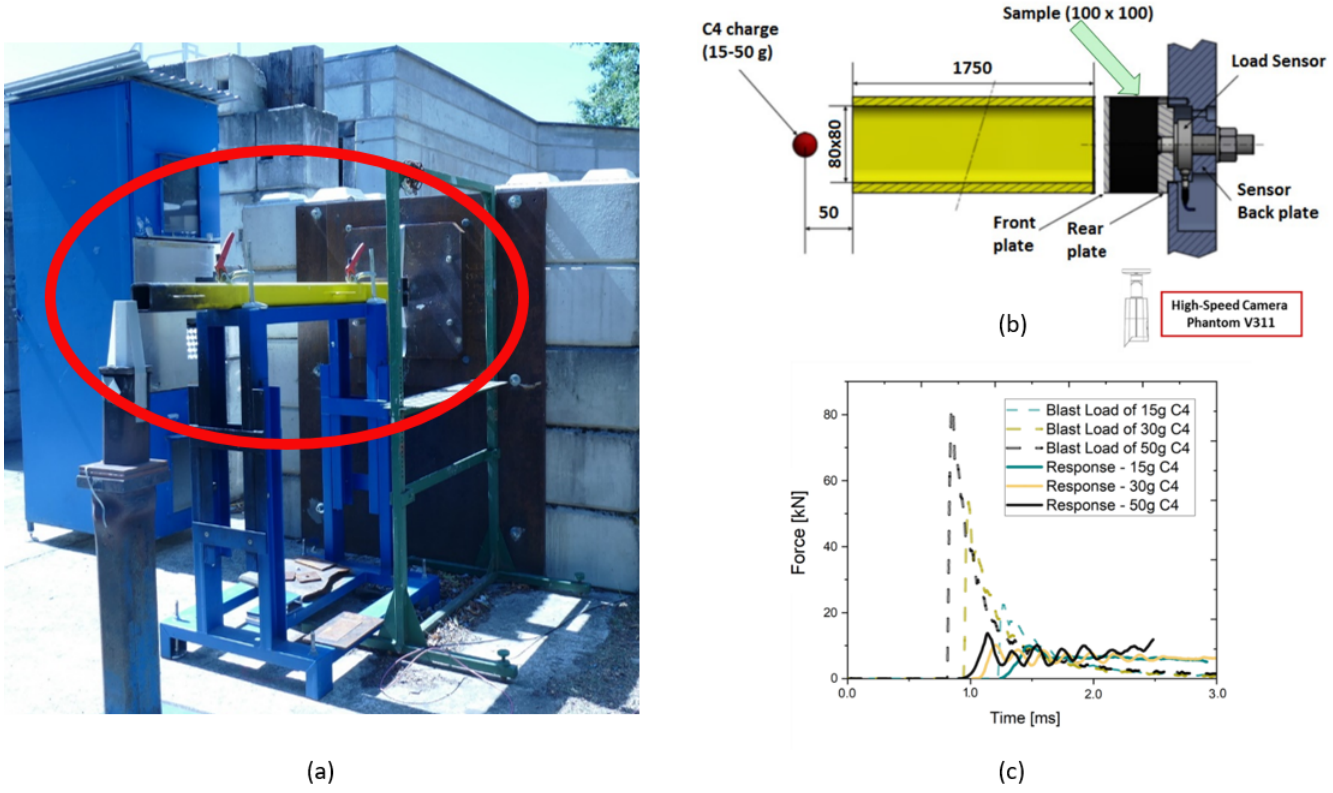

Figure 6: *Explosive Driven Shock Tube (EDST) (a) photographie du banc* d'essai *de souffle prise sur le terrain* d'essai *de* l'Institut *de recherche franco-allemand de Saint-Louis (ISL), (b) schéma de* l'EDST, *(c) comparaison entre les profils de charge de souffle avec et sans structure de protection pour différentes quantités de charge explosive.*

Les échantillons présentés à la Figure 3 sont soumis aux effwts de souffle. Les éprouvettes ont subi une compression dynamique à l'aide d'un banc d'essai EDST (Explosive Driven Shock

Tube) (Fig. 6a). L'EDST assure la propagation d'une onde plane après l'explosion d'une petite quantitè de C-4. L'échantillon testé est situé à l'extrémité du tube et inséré entre deux plaques d'acier (Fig. 6b). La plaque avant est accélérée par la pression générée lors d'une détonation −son mouvement comprime l'échantillon testé. La plaque doit être arrêtée avant la densification complète de la structure. Si la structure testée est entièrement densifiée, une augmentation soudaine de la charge transmise se produit et l'échantillon est considéré comme inefficace pour atténuer une charge de souffle donnée. Le capteur de force PCB 206C enregistre la charge transmise à travers l'échantillon testé à la plaque arrière (Fig. 6c). Le test est instrumenté avec une caméra ultra-rapide Phantom V311 positionnée à 0,5 m de l'échantillon qui enregistre le déplacement de la plaque avant [14].

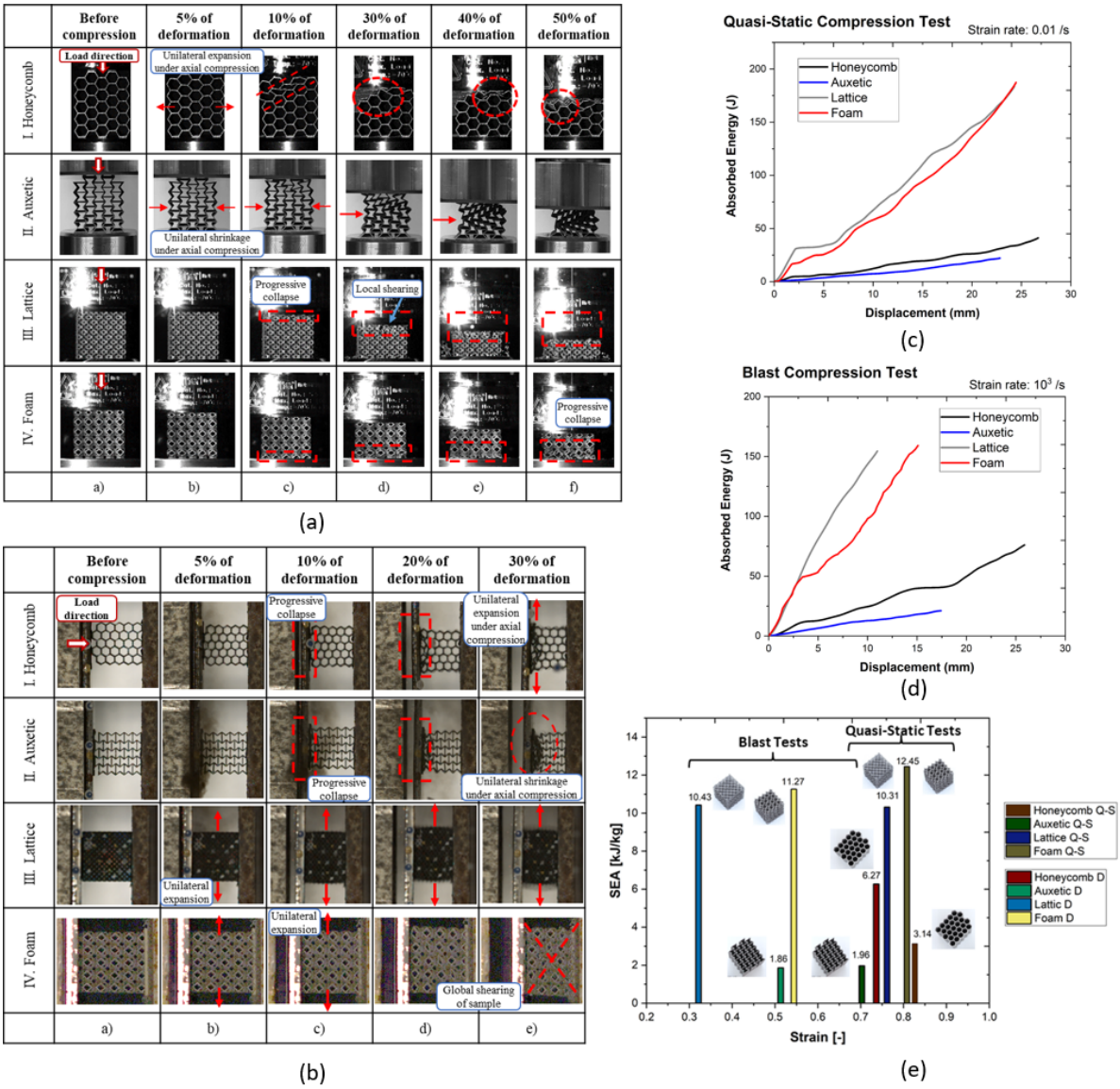

Figure 7: *Principales étapes de déformation enregistrées pendant (a) les essais quasi-statiques et (b) explosifs, et les résultats de (c,d)* l'énergie *absorbée, respectivement ; (e) propriétés résumées de* l'absorption d'énergie *spécifique pour chaque structure.*

IV Résultats des tests expérimentaux

La force transmise à travers l'échantillon testé dépend de la densité de la structure, de sa taille et des propriétés du matériau [10]. Pour comparer les résultats obtenus lors des essais de souffle EDST, les valeurs d'interdépendances entre force et- déplacement enregistrées sont converties en contraintes équivalentes $\sigma_{eq}(t)$ et en déformations équivalentes $\varepsilon_{eq}(t)$. De plus, l'évaluation des réponses structurelles est rapportée concernant l'absorption d'énergie par unité de masse (SEA) ou l'efficacité de course de chaque échantillon.

Les résultats sont présentés dans 7. Ils prouvent une influence considérable d'une topologie structurée sur le processus de déformation. Les structures caractérisées par des cellules unitaires 3D (mousse et réseau), par rapport aux structures avec des cellules 2D, présentent une augmentation d'environ dix fois de la contrainte moyenne dans des conditions de souffle.

De plus, les principales étapes des processus de déformation lors des essais de compression quasi-statique et dynamique sont corrélées avec les résultats des mesures. L'analyse prouve que l'augmentation de la vitesse de déformation affecte l'augmentation des résultats de contrainte et le changement des modes de déformation.

De plus, l'influence des conditions aux limites et des propriétés mécaniques a été étudiée pour des échantillons fabriqués par à des méthodes conventionnelles et additives. Il a été observé que les structures AM peuvent absorber au moins deux fois plus d'énergie lorsqu'elles sont soumises à une charge de souffle similaire. Ainsi, la hauteur des structures peut être considérablement réduite.

IV Modélisation numérique

Une analyse plus détaillée des déformations cellulaires est menée à l'aide des simulations numériques dans LS-DYNA. Le développement de la tâche numérique pour chaque structure soumise à l'onde de souffle permet une discussion approfondie des modes de déformation et confirme les résultats expérimentaux.

La corrélation des résultats expérimentaux et numériques montre que le nid d'abeille est caractérisé par l'étirement des cellules vers l'extérieur (Fig. 8). Le mode de déformation pour l'auxétique présente la cellule se repliant vers le centre de la structure. La flexion des entretoises est visible pour la structure en treillis, et le mécanisme de déformation caractérise la mousse qui se produit entre deux coins de la cellule. L'étirement de l'ensemble des structures 3D dans la direction perpendiculaire à la charge explosive et les modes de cisaillement globaux sont également observés.

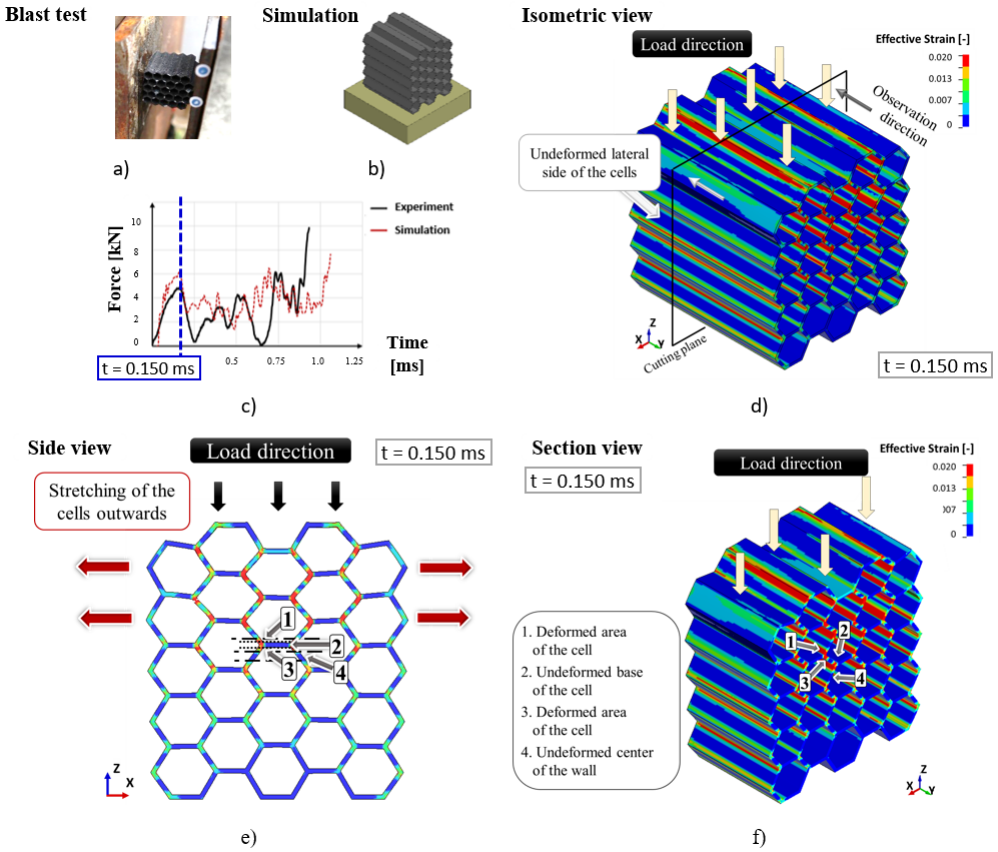

Figure 8: *Mécanisme de déformation de la structure en nid* d'abeille *soumise à* l'onde *de choc, analysé sur la base de la comparaison entre le travail expérimentale et la simulation (a) échantillon testé, (b) tâche numérique dans LS-DYNA, (c) comparaison de la force mesurée dans le temps avec les résultats numériques obtenus.* L'analyse *des résultats de déformation effective présentés dans (d) vue isométrique, (e) latérale et (f) en coupe.*

V Conclusion

Les travaux montrent clairement que les structures 3D ont la capacité d'absorber plus efficacement les effets d'une explosion que les structures 2D testées. Il est prouvé qu'ils peuvent transmettre une force plus élevée, répartie uniformément. De plus, les résultats contrainte-déformation, les paramétres EA et SEA ont montré que les structures en mousse et en treillis provoquent une augmentation de la capacité d'absorption d'énergie et permettent d'atténuer les effets de souffle.

L'analyse numérique examine plus en détail les modes de déformation. La structure composée d'entretoises (qui sont le résultat de leur flexion) permet à un échantillon d'être globalement étiré dans le sens opposé à la force appliquée. Alors que les structures 2D chargées dans la direction dans le plan sont caractérisées par un pliage progressif des cellules, réduisant les déformations internes. Par conséquent, la résistance des structures diminue.

De plus, il a été prouvé, sur la base de l'exemple de la géométrie en nid d'abeilles, que les structures produites de manière additive peuvent obtenir des résultats bien plus avantageux par rapport à celles produites par les procédés conventionnels.

Bibliography

[1] X. Dang and Ph.C. Chan. Design and test of a blast shield for boeing 737 overhead compartment. *Shock and Vibration*, 13:629–650, 2006.

[2] J. Malachowski and T. Niezgoda. Research of elastomeric protective layers subjected to blast wave. *Applied Mechanics and Materials*, 82:680–685, 07 2011.

[3] L. Yang, O. Harrysson, D. Cormier, H. West, H. Gong, and B. Stucker. Additive manufacturing of metal cellular structures: Design and fabrication. *JOM*, 67, 03 2015.

[4] M. Ali, A. Qamhiyah, D. Flugrad, and M. Shakoor. Compact energy absorbing cellular structure. pages 413–420, 06 2006.

[5] H. Ousji, B. Belkassem, M.A. Louar, B. Reymen, J. Martino, D. Lecompte, L. Pyl, and J. Vantomme. Air-blast response of sacrificial cladding using low density foams: Experimental and analytical approach. *International Journal of Mechanical Sciences*, 128-129(C):459–474, 2017.

[6] M. Stanczak, T. Fras, L. Blanc, P. Pawlowski, and A. Rusinek. Blast-induced compression of a thin-walled aluminum honeycomb structure—experiment and modeling. *Metals*, 9(12), 2019.

[7] L. Blanc, A. Jung, S. Diebels, A. Kleine, and M. Sturtzer. Blast wave mitigation with galvanised polyurethane foam in a sandwich cladding. *Shock Waves*, 31:1–16, 09 2021.

[8] D. Mohr. *Experimental investigation and constitutive modeling of metallic honeycombs in sandwich structures.* PhD thesis, Massachusetts Institute of Technology, 2003.

[9] J. Klepaczko, A. Rusinek, J.A. Rodriguez-Martinez, R. Pecherski, and A. Arias. Modelling of thermo-viscoplastic behaviour of DH36 and Weldox 460-E structural steels at wide ranges of strain rates and temperatures, comparison of constitutive relations for impact problems. *Mechanics of Materials*, 41:599–621, 05 2009.

[10] M. Suceska. *Test methods for explosives.* Springer Science and Business Media, 2012.

[11] J. Malachowski. Effect of blast wave on chosen structure – numerical and experimental study. *International Journal of Mathematics and Computers in Simulation*, 2:238–245, 01 2008.

[12] CMI. Cellular materials. blast protection., 2019. http://www.cellularmaterials.net/blast-protection.html [Online; accessed 28.01.2020].

[13] T. Wierzbicki. Crushing analysis of metal honeycombs. *International Journal of Impact Engineering*, 1(2):157–174, 1983.

[14] L. Blanc, T. Schunck, and D. Eckenfels. Sacrificial cladding with brittle materials for blast protection. *Materials*, 14(14), 2021.

Chapter 1

Protection systems against blast wave

This chapter is dedicated to a literature review on the main issues related to protection systems against blast waves. The thesis aim is to analyze the behavior of the structure under blast loading. Therefore, the fundamental knowledge about the principles accompanying the explosion and the comparative parameters is crucial to achieving the goal.

Consequently, the literature review is divided into the part concerning the research of the explosion physic and the section describing the energy absorbers. First, a description of the blast phenomena and the possibility of studying them is presented. The next part focuses on analyzing the cellular metallic structures subjected to blast loading. This chapter highlights the most important parameters that should be considered during the research on the structures under blast loading.

1.1 Explosive and ballistic protection

1.1.1 Blast wave characteristics

The detonation of the explosive charge causes the large and sudden release of energy contained initially in a small volume. It generates mechanical waves in the ambient field, whose characteristics depend on the energy released by the explosive. These mechanical waves are called blast waves characterized by a shock front followed by an expansion wave. The shock front is a thin layer (less than 200 nm) usually represented by a discontinuity that propagates faster than the local sound speed. It causes the fluid to undergo sudden changes in its initial properties: the Mach number decreases across the shock front, along with a sudden rise in density, pressure, and temperature. The blast wave is an irreversible process because of the extreme reactions produced by the collisions of the particles. An example of detonation in the air and a representation of the shock front generated by the phenomena are shown in Figure 1.1a $-$ 1.1b, respectively. In addition, Figure 1.1b also shows a shock front which is reflected by the ground, originally discovered by Mach in 1878 [1].

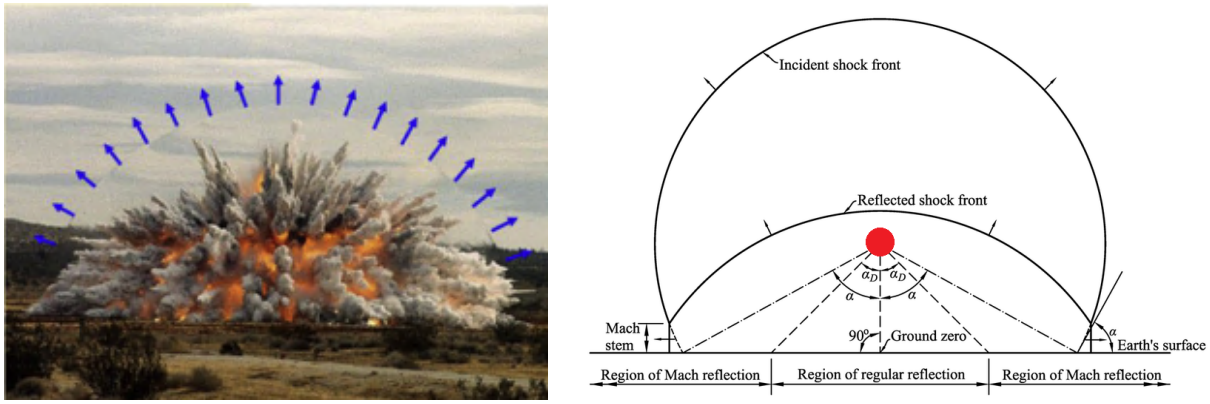

(a) (b)

Figure 1.1: *Illustration of (a) the hemispherical symmetric isotropic blast wave propagation from a point source [2] (b) process of creating the incident and reflected shock wave [3].*

In the field of threats against explosions, knowing the variation of pressure generated by the blast wave is necessary to develop an adequate protection solution. Despite being complex, the blast waves can be approximated by the Friedlander model (Fig. 1.2). When the shock wave arrives at the point under consideration, the pressure increases suddenly and reach the maximum peak of the overpressure (p_{max}) in nanoseconds. Then, the pressure starts to decrease, over a positive phase duration (t_d). The value of the positive impulse transmitted by the blast wave is the integral of the pressure curve over the positive phase duration. In addition to the positive phase, the profile can also be characterized by a negative one, where the pressure is lower than atmospheric pressure. In terms, the pressure reaches the reference value p_0, e.g. the atmospheric pressure. Analytically, the blast wave overpressure of this idealized model is estimated with the Friedlander waveform function (Eq. 1.1).

$$p(t) = p_{max} \cdot e^{-\frac{t}{t_d}} \cdot \left(1 - \frac{t}{t_d}\right) \tag{1.1}$$

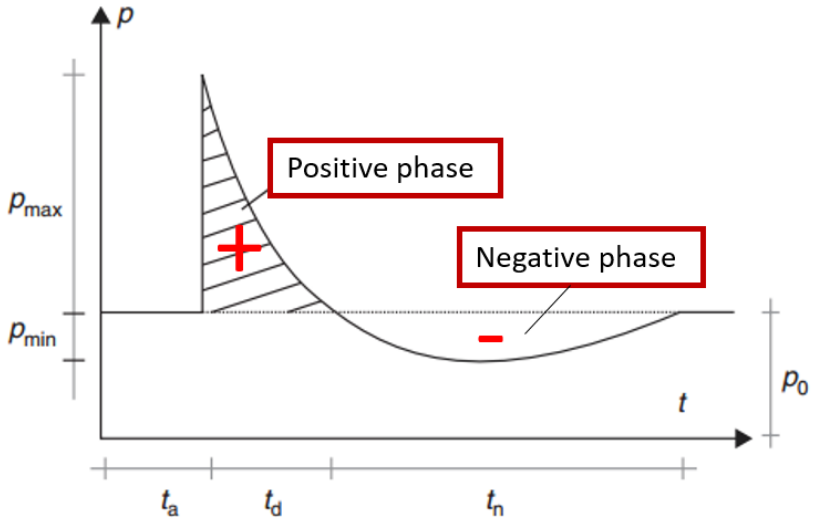

Figure 1.2: *The idealized Friedlander waveform form of a blast wave [4].*

1.1.2 Research methods for blast wave phenomena

The influence of an explosion on a structure may be analyzed experimentally by a few test techniques. It can be split into the study on mitigation of the explosions or the physic phenomena accompanying the blast loading [5]. The first one can be related directly to the charge, and the second one is each solution acting on the blast propagation and interaction with the protection.

The experimental investigations on the structured response to shock and blast waves are performed in "free-air" [6, 7], or by means of blast and shock tubes [8, 9]. "Free-air" tests allow studying the effects of interactions in real structure-explosion configurations. They can provide information on the blast impulse value, as well as peak of the pressure by the means of pressure gauge, ballistic pendulum and other metrological devices. The analysis of large-scale explosively generated shock waves may also aid in an assessing air-blasts propagation and their interaction with the surrounding environment (e.g. dust, granular, liquid or other media). "Free-air" explosion tests, similar to those in Figure 1.1a are considered difficult in instrumentation and have limited repeatability. In addition, the high-cost can effect the number of the performed tests.

On the contrary, traditional shock tubes are used mainly for academic purposes and generate shock waves in a more simple and safe way. Therefore, it allows to enlarge the range of applications. The application examples of classical shock tubes can be found in papers [10–12]. Authors provide the experimental data and results of numerical modeling confirming the correct flow and pressure profiles, whether a shock front or a blast wave is expected. In addition, Figure 1.3 presents Shock Tube Test Facility, one of test stand developed by ABS Group in San Antonio. The experimental setup is used to test the blast capacity of different absorbers in a controlled environment.

(a)

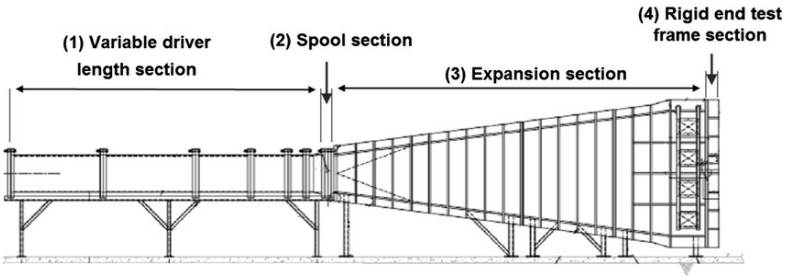

(b)

Figure 1.3: *(a) ABS Group Shock Tube Test Facility in San Antonio, Texas, (b) geometry of the shock tube.*

Specific improvement of the traditional shock tubes had been found at the University of Cape Town in South Africa. The small tube is placed in front of the ballistic pendulum [13]. As a result, the experimental setup has been significantly minimized. A condensed explosive charge is placed inside the tube, which allows to reduce the curvature of the generated shock wave. Then, further improvements and simplifications of the test equipment led to the development of the Explosive Driven Shock Tubes (EDST) at the Royal Military Academy of Brussels in 2017 [14]. The similar experimental set up is used in the French-German Research Institute of Saint-Louis (ISL), which allows explosive tests to be carried out for this thesis. Due to the EDST, a blast wave is obtained by an explosion of a charge located in front of the tube [15]. The wave propagates inside the tube, creating a localized planar pressure front. Compared to a "free-air" detonation, the EDST is a test setup used to generate and measure the effects of blast waves on a small surface. However, this technique has better repeatability, enabling more accurate pressure measurements.

The phenomena accompanying the explosion causes the wide changes in the pressure, temperature, density and particle velocities. Mechanisms of pressure wave propagation are complex, consisting of several physical phenomena such as a burning effect, heat transfer and air compression [16]. The conditions surrounding the explosion make blast testing a challenging experimental technique, constantly developed in various research centers.

1.2 Literature review on energy absorbing structures against explosion treat

Different types of energy absorbers are used to minimize the pressure peak, thereby extending the duration of the load. Due to the way of the dissipate the energy under load, the absorbers can be divided into:

1. passive – are characterized by the constant mechanical properties that determine their behavior under a considered load;
2. adaptive – allow for optimal adjustment of the stiffness to the dissipated kinetic energy. Whereby, it can distinguish:
   a) semi-active – the absorber adjusts its parameters once to the loading;
   b) active – is able to change the features in real-time during the dissipation process.

The hereby thesis focused on the passive absorbers placed in the sandwich cladding. The deliberations start with analyzing cellular structures, ending with modern metamaterials.

1.2.1 Cellular structures

Ashby and Gibson defined the cellular solid as an interconnected network of solid struts or plates composed of the edges and faces. They can be divided into two-dimensional (2D) or three-dimensional (3D) cellular materials. The first ones are composed with the array of polygons which is sufficient to characterize the area to be filled (Fig. 1.4a). The open-cell 3D materials are characterized by the polyhedral cells packed in three dimensions to fill the space, and the adjacent cells are connected through the edges (Fig. 1.4b). Wherein the closed-cell 3D materials are joined by the solid faces of the cells (Fig. 1.4c) [17].

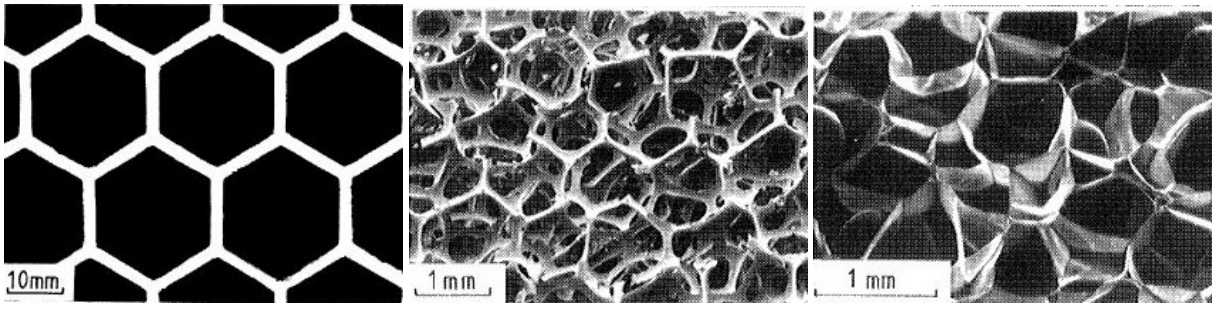

(a) (b) (c)

Figure 1.4: *Cellular materials with (a) the dwo-dimensional, (b) open-cell three-dimensional and (c) closed-cell three-dimensional geometry [17].*

Cellular structures are well-known for their good energy absorption capacity due to their ability to convert effectively kinetic energy into other forms like elastic-plastic energies in permanently deformable solids [18]. The arrangement of the internal cells and their local geometry mainly influence the mechanical response of cellular structures. They are characterized by high specific strength and stiffness, as well as good heat capabilities. Because of their excellent absorptive properties in relation to mass, they are used in automotive, aerospace, personal protective equipment, or defense [19, 20]. Most of the energy-dissipating structures are made of metals. These absorbers are characterized by considerable dissipation capacity as well as they can be used to transfer loads efficiently. The dissipation mechanism of the metal structures consists mainly in the formation of large plastic deformations, often located in plastic joints. The most energy-efficient of the progressive plastic crushing is achieved by the axial loading. The absorbers can perform their function of minimizing the transmitted load level due to the cost of the structure height [21].

Since the last century, extensive research on metallic cellular structures can be noted. Due to their wide applicability as absorbers, the studies has been conducted to define the principal process operation. In the 1960s, Alexander derived an expression for the mean axial load during the compression process of thin cylindrical shells [22]. The collapse mode called "concertina folding" has been described as the formation of straight-sided convolutions. In-depth studies were carried out by Ashby and Gibson [17], who determined the basic mechanical properties of cellular materials. The quasi-static and dynamic behavior of elementary cells under compression was considered, e.g., Abramowicz and el. [23], McFarland [24], or Wierzbicki [25]. Through empirical and analytical approaches, they provided both descriptions of the kinematics of the plastic collapse process and the formulas of the effective crushing distance, the instantaneous and mean crushing force, or the length of the local folding wave. The local plastic bucking, along with the high of the absorber and the deformation on the mesoscale level, provides good stability and favorable crush characteristics while significantly reducing the weight of the absorber.

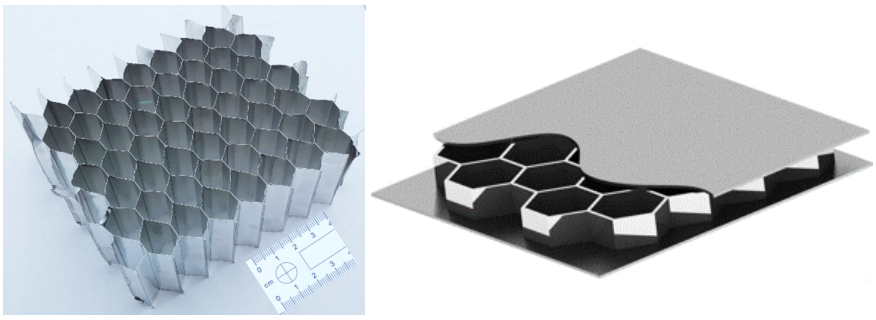

(a) (b)

Figure 1.5: *Thin-walled hexagonal aluminum honeycomb structure: (a) example of real sample and (b) a scheme of its application to sandwich panels.*

Among the cellular structures, a thin-walled hexagonal aluminum honeycomb is considered as one of an excellent blast energy absorber (see examples in Fig. 1.5) [26]. Therefore, its behavior under loading has been the subject of wide research interest [27, 28]. These metallic honeycombs are efficient in protective applications because their deformation mechanism is used to dissipate the energy of a load. They have been designed to buckle and fold in a controlled manner under an axial compressive load, which decreases and distributes the initial load over a more extended time. Honeycombs are characterized by an exceptionally good weight-to-energy ratio of absorption capacity, are very cost-effective, and are simple to manufacture [17]. However, traditional honeycombs provide optimal performance only when axially compressed. Moreover, a strained structure must be replaced after a single use as their folding and buckling are irreversible. Nevertheless, aluminum honeycombs are often used in various industrial sectors thanks to their properties, ensuring reliable performance under dynamic loading. As early as the 1960s, experimental programs were launched evaluating and optimizing metal honeycomb elements as axial energy absorbers [29, 30].

Another group of materials used in the construction of energy absorbers is porous structures, e.g., metallic foams. A similar dissipation mechanism can characterize them as the honeycomb. The advantages are low weight, high energy absorption capacity during plastic deformation, and high stiffness. These materials also have good mechanical and acoustic damping, are closed porosity and can be fully recyclable [31].

1.2.2 Energy absorbers tested under blast loading

In addition, various structural components have already been tested and analyzed under blast loading. The results of the conducted tests using the EDST technique can be found in [14] or [15]. Ousji at el. focus on mitigating blast effects by a sacrificial cladding with polyurethane (PU) as a crushable core. Influences of the front plate mass and the material and geometrical properties of the PU sample on the absorption of a given shock are investigated and modeled.

In [32] authors have performed the studies on the cellular materials of the cardboard hexagonal honeycomb, polystyrene and polyethylene foams under blast loading (Fig. 1.6). The structures were subjected the blast compression due to the explosion of 15 g of C-4 load.

(a) (b) (c)

Figure 1.6: *Tested cellular material under blast wave due to EDST of (a) polystyrene foam, (b) polyethylene foam and (c) cardboard hexagonal honeycomb [32].*

Figure 1.7a shows the transmitted load to the target without any absorber as well as the evolutions of the force courses when the tested samples were placed in a sandwich cladding. The transmitted force is significantly reduced, and the force oscillates around the mean force over a more extended time than the force course without an absorber. Then, the tested structures achieve the densification phases after 2.5 ms in case of foams and after 3 ms for the honeycomb.

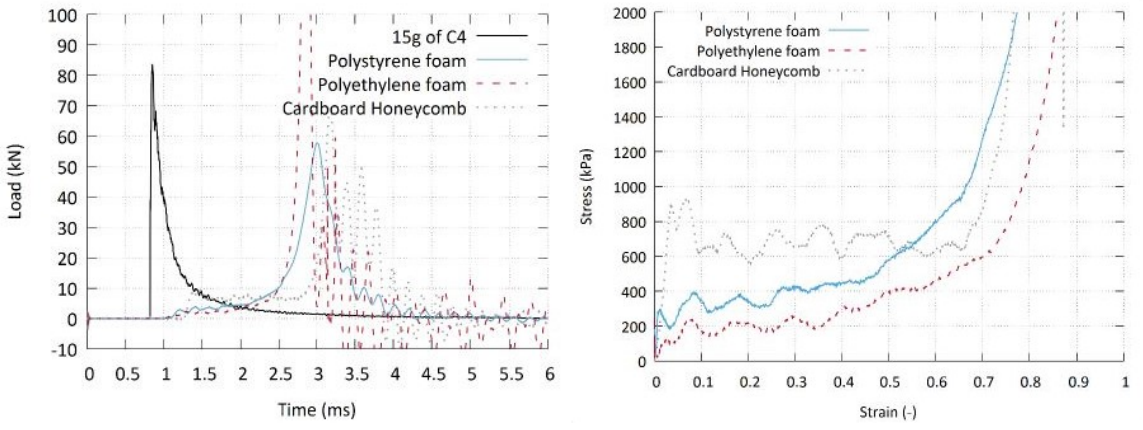

(a) (b)

Figure 1.7: *(a) Transmitted load to the target with and without cellular material (b) stress-strain curves of the tested structures under blast compression [32].*

Table 1.1: *Key parameters of the tested cellular structure in [32].*

Parameter	ρ [kg/m^3]	ε_d [-]	σ_{mean} [kPa]	T [kJ/m^3]	E_k [J]	E_{abs} [J]	E_{abs} / E_k
Polystyrene foam	33	0.52	390	203	476	100	21 %
Polyethylene foam	40	0.63	277	175	476	81	17 %
Cardboard honeycomb	90	0.66	683	451	476	267	57 %

Figure 1.7b and Table 1.1 allow to accurately compare the absorption properties of the tested structures. The results prove that the cardboard honeycomb structure has absorbed more than two and a half times more energy than the foams. However, the polyethylene structure is more efficient than polystyrene.

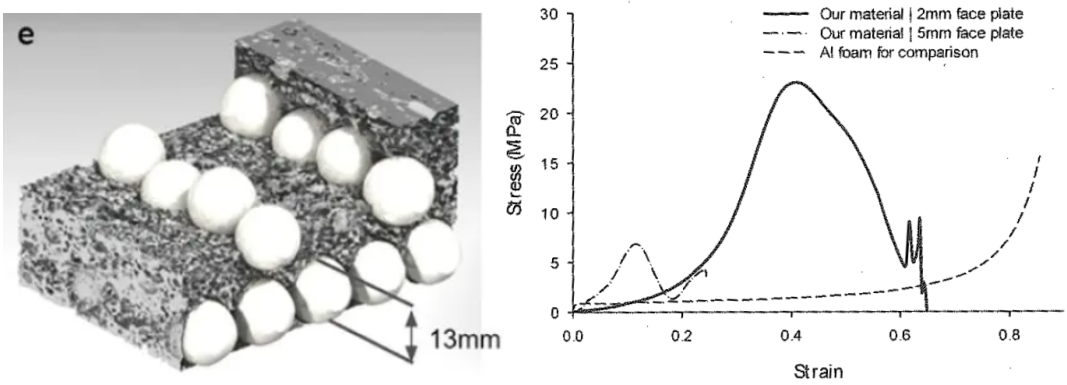

(a) (b)

Figure 1.8: *(a) Tested Proteus^{TM} cellular material (b) stress-strain curves of the foam at static loading compared with the dynamic performance of metallic foam with one layer of ceramic sphares [33].*

In [33] authors tested the developed by themselves the Proteus$^{\text{TM}}$ material. The aluminum foam with the embedded ceramic segments subjected the blast load. However, the response was not easily controlled by the dynamic compression, the face deformation was non-uniform, and the sample was characterized by the early achievement the densification phase (after 5 % using 5 mm panel and after 25 % with 2 mm plate). Authors have supposed that the developed cellular material can undergo partially hardened by using the ceramic spheres. In addition, they have pointed out that the wave phenomena may influence the observed deformation processes.

1.2.3 Metamaterials

Metamaterials are artificially manufactured materials that are often inspired by nature. "Meta" in Greek means "go beyond" or "after". In the context of the discussed thesis, it refers to the possibility of designing structures with unique properties, beyond those found in natural materials. The metamaterials can be designed as a periodically repeating network of major cells or a dense network of cells placed in their nodes.

The hexagonal unit cell can characterize honeycomb as well as auxetic structures. Both geometry are classified for the basic group of the two-dimensional (2D) cellular materials [34]. The difference in the topology of the unit cell mainly affects the sign of the Poisson's coefficient which mechanism is shown in Figure 1.9. The honeycomb are characterized by the positive

ratio that means that when the specimen is stretched then the elongation sample takes place in the direction to the load direction. At the same time, the sample undergoes a contraction, perpendicular to the tensile load. The auxetic, also called "re-entrant honeycomb" is the example of the structure with the negative Poisson's ratio. The sample expands transversely to the stretching direction.

According to [35], the auxetic metamaterials are characterized by resistance to the indent (such as notches, grooves, holes) therefore they could be used against the blast threats. In order to mitigate mechanical shocks, the honeycomb structure were used, among others, in the Douglas C-47 Skytrain "Dakota" aircraft fuel tanks [34].

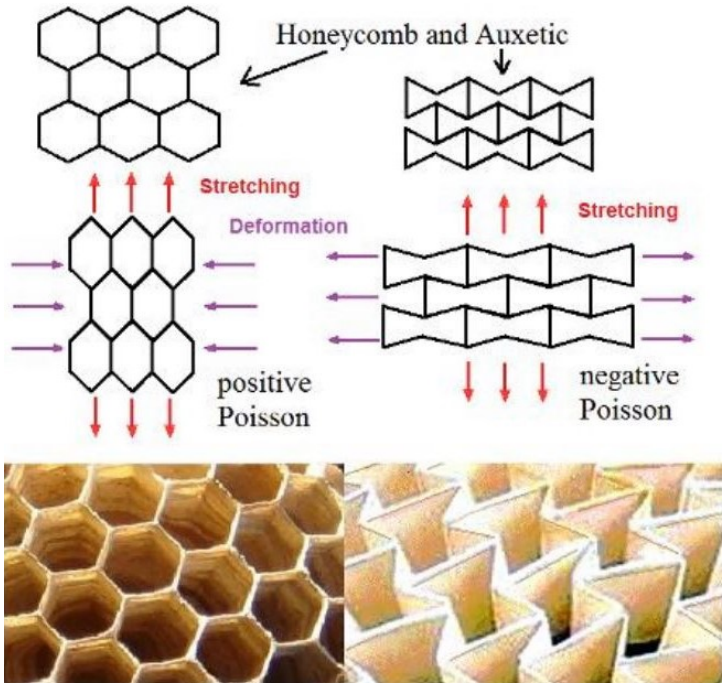

Figure 1.9: *Comparison of the deformation mechanism of the honeycomb and auxetic structure under stretching [34].*

Table 1.2: *The specific properties of the honeycomb and auxetic structure.*

Honeycomb	**Auxetic**
Expands longitudinally when stretched	Expands transversely when stretched
Positive Poisson's ratio	Negative Poisson's ratio
Good strength-weight ratio	Vibration absorption
Saddle-shaped surfaces	Dome-shaped surfaces

The lattice and foam have established the most well-known structures among the three-dimensional (3D) cellular materials [36]. Lattice consists of a connected network of struts. Their architecture depends on the different intersections of the beam connections, examples of which are presented in Fig. 1.10. This approach allows the adjustment of the metamaterial properties to the required needs. In [37], the octet truss lattice has been designed to increase the energy absorption capacity. Therefore, the structure proves the constant plateau stress and zero plastic Poisson's ratio.

Historically, foams were regarded as a particular subset of lattice materials. They are composed of the open or close unit cell. The first one consists of the struts connected at low connectivity joints. They are characterized by effective moisture absorption, but they lend to breakdown easily. Wherein the closed-cell foams achieve higher cushioning but may contain undesirable chemicals or particles inside the cells. The foams are often used for thermal and acoustic insulation, filtration of the pollutants, or solid particles [36].

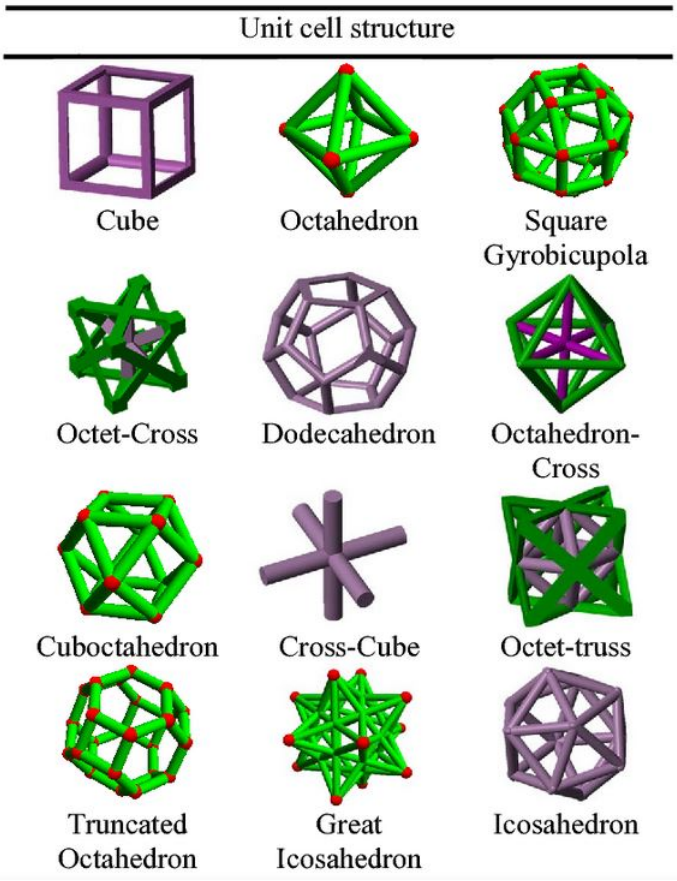

Figure 1.10: *The unit cells library for the the three-dimensional (3D) lattice metamaterials [38].*

Table 1.3: *The specific properties of the lattice and foam structure.*

Lattice	**Foam**
Network of struts	Open or closed cell
Stretch-dominated	Bending-dominated
Stiff, strong load-bearing, lightweight, high specific strength, good impact absorption	Lower stiffness and strength

The second group of the metamaterials includes structures with the periodically repeating network, such as the hierarchical, chiral and anti-chiral, presented in Fig. 1.11, [39]. Hierarchy is achieved by conserving the rotational and reflective symmetries of the beams. This can be done by replacing the nodes in a periodic network of cells with the original cells, albeit smaller. The hierarchical architectures allow to design the structure to increase the specific stiffness [40–42], toughness [43], strength [40,41], buckling strength [39], negative or complex Poisson's ratio [44].

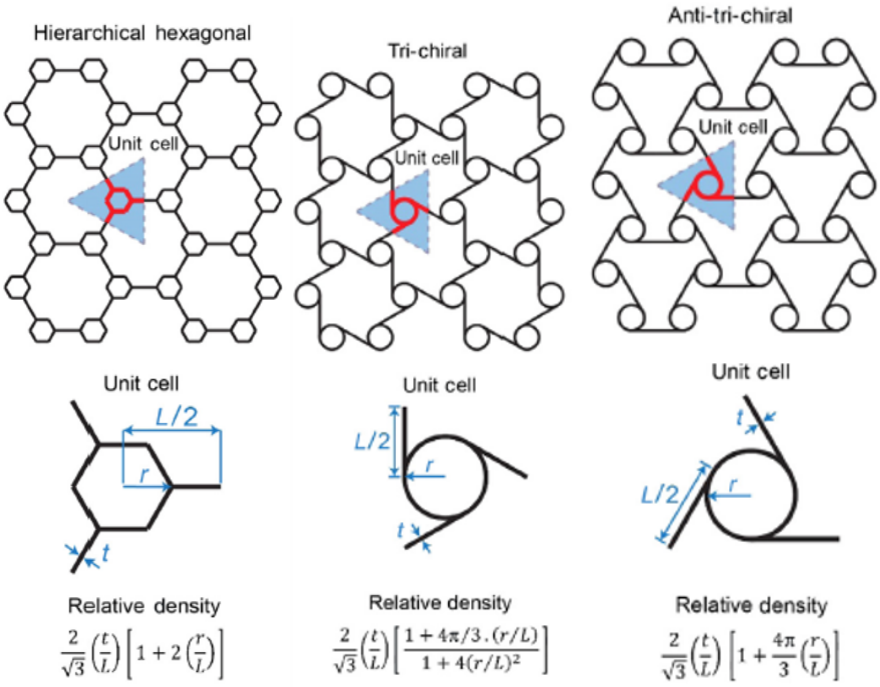

Figure 1.11: *The scheme of the hierarchical, chiral and anti-chiral architectures [39].*

The periodic chiral metamaterials can be constructed by attaching the circular nodes on different sides of the ligament. The trichiral, hexachiral or n-chiral structures are generated by adding three, six, or n ligaments connected to the central node, respectively. They are dominated by the bending response under axial loading and auxetic behavior. The samples with a chiral structure can be useful for the application to mitigate energy and noise. To achieve anti-chirality architecture, the nodes must be joined by a ligament on the same side - they cannot cross the line that joined the centers of two connected nodes. The antitetra-chiral structures are characterized by the anisotropy, but exhibit auxeticity and low shear modulus as the magnitude of the chirality of the unit cell increas [39].

1.2.4 The generalized response of compressed cellular metallic structures

The fundamental issue in the analysis of the dynamic compression loads a protective object is the dissipation of kinetic energy into its other forms. For example, the dissipation mechanisms can take place by the plastic flow of metals, formation of cracks, delamination, or friction.

A schematic, generalized response of a metallic cellular structure to compression is presented in Figure 1.12. The curve may vary depending on a structure type, strain rate, or due to the different external conditions. The three main parts are usually recognizable if the structure is fully compressed. After the linear elastic range of the structure deformation, the registered peak stress represents the plastic collapse stress, i.e., the maximum load that the structure can bear. In case of large deformations in the energy absorbed systems, the elastic part of the deformation energy is negligible low in relation to the energy dissipated in the subsequent phases. In the plateau regime, the constant mean stress can represent the generalized load transmitted to the

protected object. The structures absorb large amounts of energy due to different mechanisms of energy dissipation. The length of the plateau determines the moment in which the structure attains the densification phase. The further large plastic deformation is no longer possible.

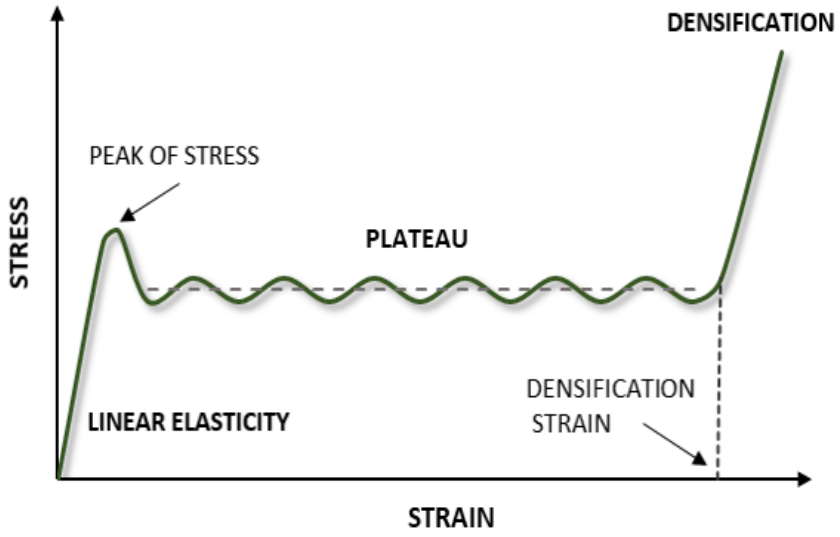

Figure 1.12: *The generalized stress-strain curve representing the response of a metallic cellular structure to a compressive load.*

The analysis of the diagram allows to conclude that the desired characteristics of the efficient absorber should be:

1. minimization of the transmitted force peak in relation to the average value;
2. adjusting the value of the transmitted force to the strength of the protected structure;
3. extending the plateau range by a later achievement the densification phase.

The parameters which enable the comparison of the structural performance are discussed following Section.

1.2.5 Comparison of the mechanical properties of the cellular structures under compressive loading

In the first approach to compare the absorbing properties of the considered cellular structures, the measured force over the time F(t) or the displacement of the structure F(x) can be taken into account. Based on the measured force-displacement courses, the dissipated energy EA inside the absorber in volume Ω can be calculated based on the equation Eq.(1.2). From Newton's second law, the change of the energy EA must be equal to the work W done by the external force, regardless of the kind of processes taking place into the absorber.

$$W = \int_0^{x_{max}} F(x)dx = \int_\Omega EAd\Omega \tag{1.2}$$

To simplify the above Equation, the work can be expressed as the average force F_{mean} multiplied by the maximum displacement x_{max}, Eq.(1.3).

$$W = F_{mean} \cdot x_{max} \tag{1.3}$$

To consider the mass of the structure, the specific absorbed energy (SEA) is often compared. SAE is the absorbed energy per unit of the crushed specimen mass, defined by Equation (1.4).

$$SEA = \frac{\int_0^{x_{max}} F(x)dx}{m} = \frac{EA}{m} \tag{1.4}$$

The following Equation allows comparing the absorbed energy to the initial volume (V) of the structure. Then, based on Equation (1.5), the dissipated energy density (VEA) is determined.

$$VEA = \frac{EA}{\rho_s} \tag{1.5}$$

SEA and VEA are often determined based on the part of the structure directly involved in the dissipation process. High values of SEA and VEA prove the compact and light absorbers. In addition, the mean crushing force is calculated as:

$$F_{mean} = \frac{\int F(x)dx}{l} \tag{1.6}$$

where l is the initial length of the structure.

The crush force efficiency (CFE) is defined as the ratio of the peak load F_{max} to the mean crushing load F_{mean}. CFE values close to 1 characterize absorbers with a very beneficial, flat crush curve.

$$CFE = \frac{F_{max}}{F_{mean}} \tag{1.7}$$

Stroke efficiency (SE) allows to define the post-crush displacement x_{max} to the total length of specimen l.

$$SE = \frac{x_{max}}{l} \tag{1.8}$$

However, often the comparison of the energy absorption properties of the different structures are based only on the stress-strain characteristics (as shown in Fig. 1.12). The parameter of the maximum compressive strength $\sigma_{\max}$ defined as the peak load, $F_{\max}$ to the initial cross-section area of the sample A_0.

$$\sigma_{max} = \frac{F_{max}}{A_0} \tag{1.9}$$

Moreover, the material toughness T gives the information of the total energy per unit volume consumed by the cellular material that a sample can dissipate before densification.

$$T = \int_0^{\epsilon_d} \sigma \epsilon d\epsilon = \sigma_{mean} \cdot \epsilon_d \tag{1.10}$$

1.3 Chapter summary

The phenomena accompanying the blast wave in the air are a complex issue in which both the shock wave and the followed expansion wave must be taken into account, as discussed in Section 1.1.1. The absorbing properties of the structural designs can be tested in "free-air", or by means of blast and shock tubes. A beneficial solution for the laboratory studies can be obtained due to the EDST set-up, which allows to carry out small-scale tests.

Section 1.2.4 gives insight into the general structure responses and points out the crucial properties of the cellular structure under compression loading. In addition, Section 1.2 shows the advantages of using metamaterials. According to the literature review, the most known metamaterials of the honeycomb, auxetic, foam and lattice have been analyzed analytically [45], experimentally [46], as well as numerically [47]. The tests were performed under different conditions like: thermal [48], quasi-static and dynamic tensile [49], shear [50], or compression [51]. However, to the best of the author's knowledge, there is no data summarizing the structures' behavior described above after an explosive. Such an approach made it possible to analyze the absorbing properties of a selected class of elementary unit cells. In addition, the use of advanced manufacturing technology allows studying the possibilities of AM structures dedicated to military applications.

Bibliography

[1] Q. Wan, H. Jeon, R. Deiterding, and V. Eliasson. Numerical and experimental investigation of oblique shock wave reflection off a water wedge. *Journal of Fluid Mechanics*, 826, 06 2017.

[2] J. Haber, J. Chrostowski, and R. Nyman. Chapter 5 - other launch safety hazards. In F. A. Allahdadi, I. Rongier, and P. D. Wilde, editors, *Safety Design for Space Operations*, pages 187–253. Butterworth-Heinemann, Oxford, 2013.

[3] J. Shin, A. Whittaker, A. Aref, and D. Cormie. Air-blast effects on civil structures. 11 2014.

[4] N. Gebbeken and T. Krauthammer. Understanding the dynamic response of concrete to loading: practical examples. In J. Weerheijm, editor, *Understanding the Tensile Properties of Concrete*, Woodhead Publishing Series in Civil and Structural Engineering, pages 338–369. Woodhead Publishing, 2013.

[5] L. Blanc, A. Jung, S. Diebels, A. Kleine, and M. Sturtzer. Blast wave mitigation with galvanised polyurethane foam in a sandwich cladding. *Shock Waves*, 31:1–16, 09 2021.

[6] X. Dang and Ph. C. Chan. Design and test of a blast shield for boeing 737 overhead compartment. *Shock and Vibration*, 13:629–650, 2006.

[7] K. Spranghers, I. Vasilakos, D. Lecompte, H. Sol, and J. Vantomme. Identification of the plastic behavior of aluminum plates under free air explosions using inverse methods and full-field measurements. *International Journal of Solids and Structures*, 51(1):210–226, 2014.

[8] A. Tyas. Experimental measurement of pressure loading from near-field blast events: techniques, findings and future challenges. In *Multidisciplinary Digital Publishing Institute Proceedings*, volume 2, page 471, 2018.

[9] B. D. Henshall. The use of multiple diaphragms in shock tubes. *British Aeronautical Research Council*, page 291, 12 1955.

[10] A. Lloyd, E. Jacques, M. Saatcioglu, D. Palermo, I. Nistor, and T. Tikka. Capabilities of a shock tube to simulate blast loading on structures. *ACI Symposium Publication*, 281:629–650, 2011.

[11] R. Andreotti, M. Colombo, A. Guardone, P. Martinelli, G. Riganti, and M. di Prisco. Performance of a shock tube facility for impact response of structures. *International Journal of Non-Linear Mechanics*, 72:53–66, 2015.

[12] V. Aune, E. Fagerholt, M. Langseth, and T. Borvik. A shock tube facility to generate blast loading on structures. *International Journal of Protective Structures*, 7(3):340–366, 2016.

[13] M. Downey. Design, build and commission a shock tube apparatus for autoinition research., December 2009.

[14] H. Ousji, B. Belkassem, M.A. Louar, B. Reymen, J. Martino, D. Lecompte, L. Pyl, and J. Vantomme. Air-blast response of sacrificial cladding using low density foams: Experimental and analytical approach. *International Journal of Mechanical Sciences*, 128-129(C):459–474, 2017.

[15] M. A. Louar, B. Belkassem, H. Ousji, K. Spranghers, D. Kakogiannis, L. Pyl, and J. Vantomme. Explosive driven shock tube loading of aluminium plates: experimental study. *International Journal of Impact Engineering*, 86:111–123, 2015.

[16] Ch. E. Needham. *Blast Waves (Shock Wave and High Pressure Phenomena)*. Springer, 2010.

[17] L. J. Gibson and M. F. Ashby. *Cellular Solids: Structure and Properties*. Cambridge Solid State Science Series. Cambridge University Press, 2 edition, 1997.

[18] M. Ali, A. Qamhiyah, D. Flugrad, and M. Shakoor. Compact energy absorbing cellular structure. pages 413–420, 06 2006.

[19] F. Mostert. Challenges in blast protection research. *Defence Technology*, 14, 05 2018.

[20] S. Mckown, Y. Shen, W. K. Brookes, Ch. Sutcliffe, W. J. Cantwell, G. Langdon, G. Nurick, and M. Theobald. The quasi-static and blast loading response of lattice structures. *International Journal of Impact Engineering*, 35:795–810, 08 2008.

[21] P. K. Pawlowski. Systemy adaptacyjnej absorpcji obciążeń udarowych. identyfikacja udaru, sterowanie absorberów, dyssypacja energii, 2011.

[22] J. M. Alexander. An approximate analysis of the collapse of thin cylindrical shells under axial loading. *The Quarterly Journal of Mechanics and Applied Mathematics*, 13(1):10–15, 1960.

[23] W. Abramowicz and N. Jones. Dynamic axial crushing of square tubes. *International Journal of Impact Engineering*, 2(2):179–208, 1984.

[24] R. Farland. Hexagonal cell structures under post-buckling axial load. *AIAA Journal*, 1:1380–1385, 06 1963.

[25] T. Wierzbicki. Crushing analysis of metal honeycombs. *International Journal of Impact Engineering*, 1(2):157–174, 1983.

[26] D. Kwan and B. O'Toole. Energy absorbing sandwich structures under blast loading. 05 2004.

[27] H. Bornstein and K. Ackland. Evaluation of energy absorbing materials under blast loading. *WIT Transactions on Engineering Sciences*, 77:125–136, 2013.

[28] A. G. Hanssen, L. Enstock, and M. Langseth. Close-range blast loading of aluminium foam panels. *International Journal of Impact Engineering*, 27(6):593–618, 2002.

[29] L. Cao, Y. Lin, F. Lu, R. Chen, Z. Zhang, and Y. Li. Experimental study on the shock absorption performance of combined aluminium honeycombs under impact loading. *Shock and Vibration*, 2015(1070-9622):1–8, 2015.

[30] R. K. McFarland. The development of metal honeycomb energy-absorbing elements. Technical Report 32-639, Jet Propulsion Laboratory, California Institute of Technology, Pasadena, CA, USA, July 1964.

[31] S. T. Taher, R. Zahari, S. Ataollahi, F. Mustapha, and S.N. Basri. A double-cell foam-filled composite block for efficient energy absorption under axial compression. *Composite Structures*, 89(3):399–407, 2009.

[32] L. Blanc, T. Schnuck, D. Eckenfels, and J.-F. Legendre. *Screening of absorbing materials for blast mitigation technology based on sandwich claddings.*, chapter New materials for ballistic protections and blast attenuation, pages 260–271. Proceedings of the Light-Weight Armour Group for Defense and Security, ENSAIT, Roubaix, France, October 2019.

[33] S. Szyniewski, R. Vogel, L. Blanc, T. Jankowiak, T. Fras, F. Bittner, H. J. Endres, T. Hipke, and E. Jakubczyk. *Use of wave refractions and reflections to reduce transmitted shock and to fragment bullets in metallic foam ceramic architected material PROTEUS TM*, chapter New materials for ballistic protections and blast attenuation, pages 296–305. Proceedings of the Light-Weight Armour Group for Defense and Security, ENSAIT, Roubaix, France, October 2019.

[34] A. C. Sparavigna. Paper-based Metamaterials: Honeycomb and Auxetic Structures. *International Journal of Sciences*, 3(11):22–25, November 2014.

[35] Z.-D. Ma, H.-T. Bian, C. Sun, G. M. Hulbert, K. Bishnoi, and F. Rostam-Abadi. Functionally-graded npr (negative poisson's ratio) material for a blast-protective deflector. 2010.

[36] M. F Ashby. The properties of foams and lattices. *Philosophical Transactions of the Royal Society A: Mathematical, Physical and Engineering Sciences*, 364(1838):15–30, 2006.

[37] T. Tancogne-Dejean and D. Mohr. Elastically-isotropic truss lattice materials of reduced plastic anisotropy. *International Journal of Solids and Structures*, 138:24–39, 2018.

[38] D. S. Nguyen and F. Vignat. A method to generate lattice structure for additive manufacturing. In *2016 IEEE International Conference on Industrial Engineering and Engineering Management (IEEM)*, pages 966–970, 2016.

[39] D. Mousanezhad, B. Haghpanah, R. Ghosh, A. M. Hamouda, H. Nayeb-Hashemi, and A. Vaziri. Elastic properties of chiral, anti-chiral, and hierarchical honeycombs: A simple energy-based approach. *Theoretical and Applied Mechanics Letters*, 6(2):81–96, 2016.

[40] R. Lakes. Materials with structural hierarchy. *Nature*, 361:511–514, 1993.

[41] R. Oftadeh, B. Haghpanah, J. Papadopoulos, A.M.S Hamouda, H. Nayeb-Hashemi, and A. Vaziri. Mechanics of anisotropic hierarchical honeycombs. *International Journal of Mechanical Sciences*, 81, 04 2014.

[42] R. Oftadeh, B. Haghpanah, D. Vella, A. Boudaoud, and A. Vaziri. Optimal fractal-like hierarchical honeycombs. *Physical Review Letters*, 113:104301, Sep 2014.

[43] F. Barthelat and H. D. Espinosa. An experimental investigation of deformation and fracture of nacre–mother of pearl. *Experimental Mechanics*, 47:311–324, 2007.

[44] F. Song, J. Zhou, X. Xu, Y. Xu, and Y. Bai. Effect of a negative poisson ratio in the tension of ceramics. *Physical review letters*, 100:245502, 06 2008.

[45] A. A. S. M. Ashab, D. Ruan, G. Lu, and A. A. Bhuiyan. Finite element analysis of aluminum honeycombs subjected to dynamic indentation and compression loads. *Materials (Basel, Switzerland)*, 9(3), March 2016.

[46] U. Dar, H. Mian, M. Abid, A. Topa, Z. Sheikh, and M. Bilal. Experimental and numerical investigation of compressive behavior of lattice structures manufactured through projection micro stereolithography. *Materials Today Communications*, 25:101563, 08 2020.

[47] Y. Amani, S. Dancette, P. Delroisse, A. Simar, and E. Maire. Compression behavior of lattice structures produced by selective laser melting: X-ray tomography based experimental and finite element approaches. *Acta Materialia*, 159:395–407, 2018.

[48] C. Petit, S. Meille, and E. Maire. Cellular solids studied by x-ray tomography and finite element modeling - a review. *Journal of Materials Research*, 28, 09 2013.

[49] J. Zhang, G. Lu, D. Ruan, and Z. Wang. Tensile behavior of an auxetic structure: Analytical modeling and finite element analysis. *International Journal of Mechanical Sciences*, 136:143–154, 2018.

[50] N. Denkov, S. Tcholakova, K. Golemanov, K. Ananthpadmanabhan, and A. Lips. Role of surfactant type and bubble surface mobility in foam rheology. *Soft Matter*, 5, 09 2009.

[51] Z. P. Sun, Y. B. Guo, and V. P. W. Shim. Static and dynamic crushing of polymeric lattices fabricated by fused deposition modelling and selective laser sintering – an experimental investigation. *International Journal of Impact Engineering*, 160:104059, 2022.

Chapter 2

Description of the Additive Manufacturing technology

Additive Manufacturing (AM) is a technology that allows much freedom in designing parts, thus being beneficial for researching various types of samples on a laboratory scale. Therefore, this chapter focuses on understanding the fundamental principles of the technique and identifies the basic printing methods. A large part is devoted to discussing the Direct Metal Laser Sintering (DMLS) method used to manufacture samples for the studying in this thesis. In addition, the main process parameters are discussed, which affect the quality of printed components. Finally, state of art in research of AM technology is presented.

2.1 Additive Manufacturing - General knowledge

The production landscape is ever-changing. One of the most significant drivers of the development is the appearance of advanced manufacturing technologies that enable more cost-efficient, and resourcefulness small-scale [1]. Additive Manufacturing (AM) is an advanced technology that has achieved the status of one of the leading production processes nowadays. It can be observed that interest in AM technology has increased rapidly in recent years. It contributes to a growing number of relevant studies and published results. According to the SCOPUS database, in 2012, there were published 621 articles related to AM topic; whereas, in 2017, this number increased to 4040, reaching 8485 in 2020 [2]. This tendency shows that AM technology becomes increasingly attractive, not only for the scientific world but also for industrial applications.

It is worth noting that AM contributed to the establishment of another technological development period, called the Third Industrial Revolution (TIR) [3]. One of the first TIR triggers was the development of the Advanced Research Projects Agency Network (ARPANET) in 1969. Over 15 years later (in 1986), Charles Hull patented the first AM method - stereolithography (SLA) (patent number: 4,575,330 [4]). The revolution of AM technology resulted from the fact that the manufacturing process relies on the material addition, not its removal, as it is in the traditionally used subtractive manufacturing methodologies. Due to the many potential sustainability benefits and wide application possibilities, AM technology has achieved the status of one of the most promising modern production processes.

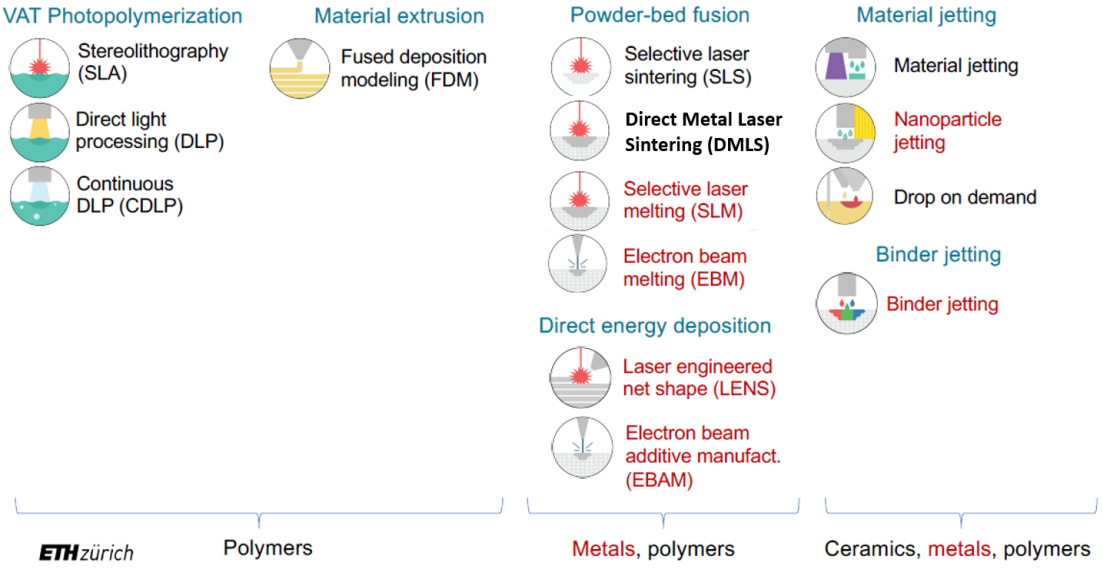

Figure 2.1: *Classification of Additive Manufacturing methods (based on [5]).*

The first patented method (SLA) has been based on UV lasers curing liquid photopolymer resin [6]. Then, in the early 90s, many technologies were introduced, such as Fused Deposition Modeling (FDM) from Stratasys or Selective Laser Sintering (SLS) from DTM. The extrusion methods (such as FDM) are currently the most common and cheapest method for rapid prototyping using thermoplastic materials. SLS method, along with Selective Laser Melting (SLM), Direct Metal Laser Sintering (DMLS), as well as Electron Beam Melting (EBM), belongs to the Powder-Bed Fusion process. It is based on the melt, and fusion layer-by-layer of a metal powder using a high power laser or electron beam [7]. Material jetting methods can be compared

to a traditional two-dimensional inkjet printer. Material is deposited from a nozzle that moves horizontally across the build platform. Then, each layer is hardened using ultraviolet (UV) light. The division of the described above methods is shown schematically in Figure 2.1.

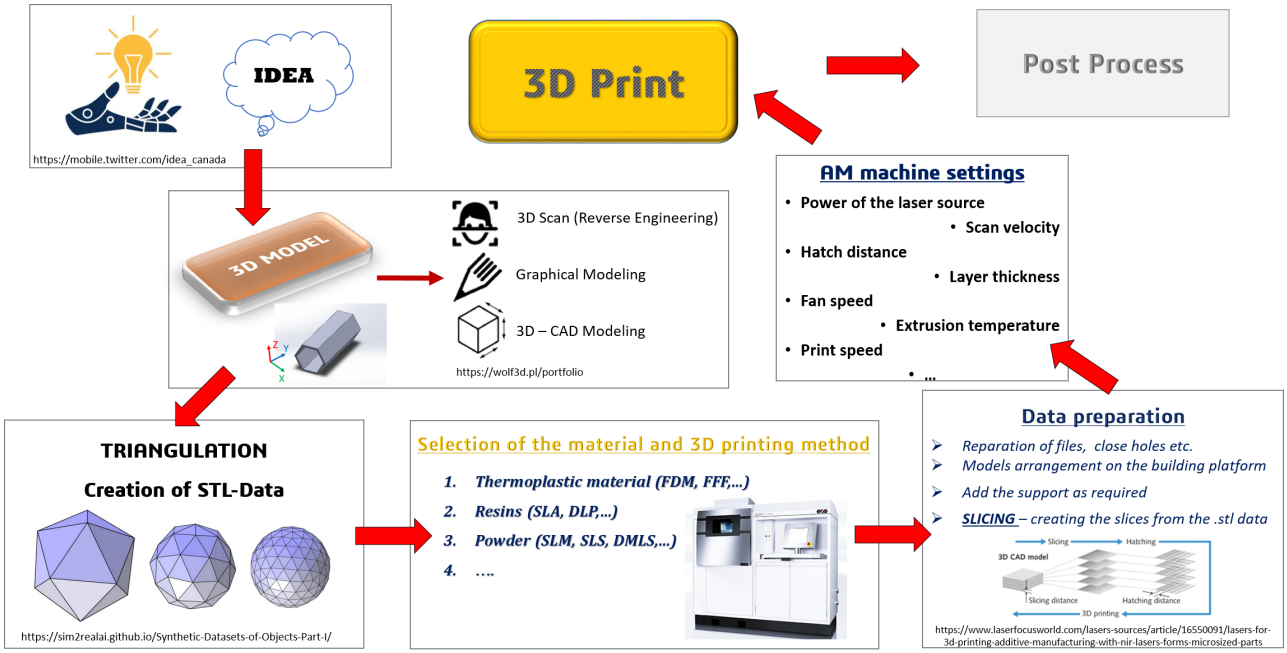

Figure 2.2: *Additive manufacturing process chain.*

The manufacturing process with the use of AM technology begins with the 3D modeling of the part that will be then printed, as schematically shown in Figure 2.2. It can be realized by the 3D scan, graphical, or CAD modeling. Then, a design model must be converted to "STL" file ("Standard Triangle Language"). The STL format describes a raw and unstructured triangulated surface of the CAD model. It is based on the unit normal and vertices of the triangles due to using a three-dimensional Cartesian coordinate system. After preparing the model, the focus should be on choosing the manufacturing method – analysis of available printing possibilities, technological limitations, and further use of the printed part.

Depending on the shape, complexity, and number of printed objects, the parts should be placed appropriately on the build platform. Since layering techniques often require additional parts below the printed area to avoid collapse of the construction, the additional "supports" (printed part with the lower density or other material) is often used. However, breakaway 3D printing support is hard to remove and may potentially damage the model. Their correct addition requires knowledge and experience to ensure a successful print.

The STL model should be sliced to prepare a new file using suitable slicer software, for example, Cura for FDM, ChiTuBox for SLA, or Magics RP for the DMSL method. The new file's format must be based on code that is compatible with the printer being used. The task of the slicer program is to create a file for printing layer by layer. Before preparing the AM machine, the last stage is to set the appropriate process parameters, i.e., extrusion temperature, scan velocity, fan speed. Parameters will differ from the chosen printing method, material, quality of the part obtained [8]. Often, the printed object also needs post-processing, which will be discussed in detail in Section 2.2.2.

2.2 Description of the Direct Metal Laser Sintering (DMLS) method

The specimens for this thesis have been manufactured based on the DMLS method from AlSi10Mg aluminum powder, which provides good dynamic properties. Furthermore, the used method enables printing parts with complex geometry. DMLS was developed by EOS GmbH and Rapid Product Innovations (RPI) in 1994. Compared to the well-known SLM method, DMLS fuses metal alloys powder in lower temperatures. The production of the AM samples necessary for the tests is based on an EOSINT M 280 3D printer. Considering the above, this section focuses on the description of the DMSL method and the key factors influencing the manufacturing process.

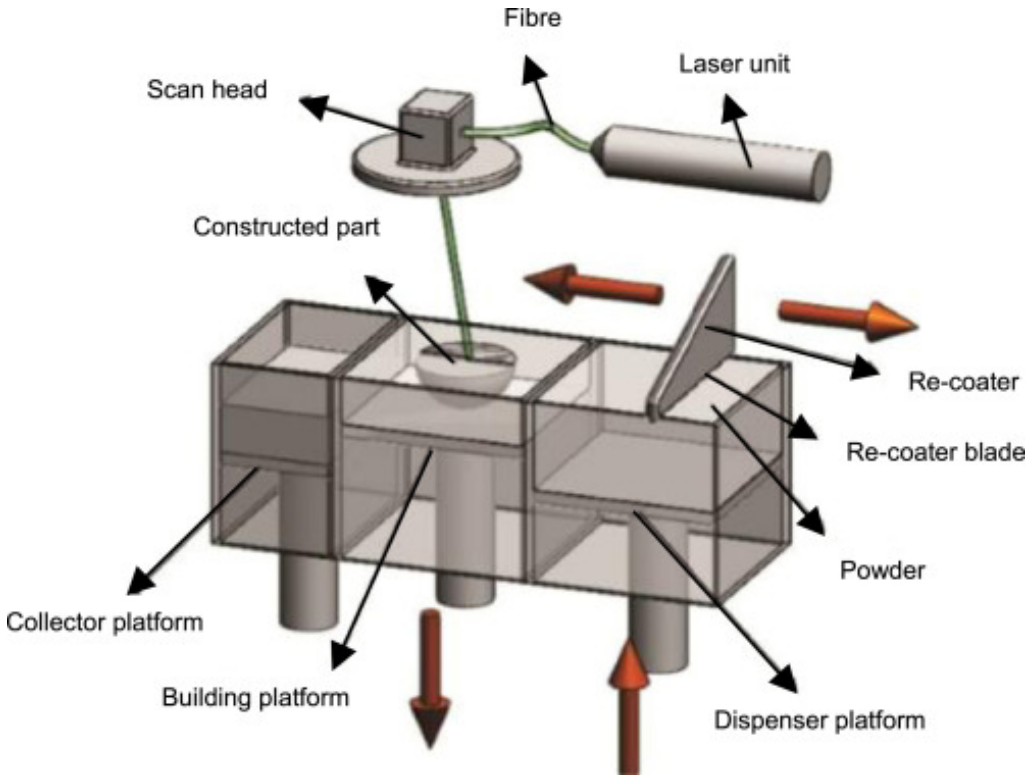

Figure 2.3: *Schematic of the DMSL process [9].*

Figure 2.3 presents the DMLS process principle schematically. Firstly, the re-coater moves across the surface to pick up excess material from the dispenser platform with the unmelted powder. Next, the blade spread a thin layer of the powder evenly on the building platform. Then the laser selectively fuses powder according to the generated code of the 3D model. EOSINT M 280 involves the use of a Yb fiber laser with the wavelength of 1060−1100 nm and nominal power of 200−400 W. The laser beam affects the mirror system, which allows for efficient welding of particle surfaces due to reflection and scanning. The diameter of the laser beam in the building area varies between 100−500 µm. Depending on the laser power, the beam melts about three layers of powder into the depth (20−60 µm). Although the exposure speed of the scanner can be up to 7000 $\mathrm{mm\,s^{-1}}$, the laser in the EOSINT M 280 requires time-consuming cooling. After completion of the sintering process of the first layer, the build platform is lowered by one layer height, making room for the next powder (20−100 µm). The linear drive moves the recoater's

arm in the horizontal direction with the travel speed of 40−500 $\mathrm{mm\,s^{-1}}$. The excess powder goes to the collector platform, which can be reused after sifting. Then, the laser beam melts an applied layer of material, allowing the repeating of the whole print operation of the new cross-section of the 3D model. The EOSINT M 280 system requires argon or nitrogen inert gas with a minimum purity of 99.996 % air volume.

2.2.1 Process parameters

It is essential to produce high-density parts with optimal surface quality to achieve the required mechanical properties. It is realized by the minimization defects, e.g., by optimizing process parameters. The critical factor is an energy density that affects the microstructure, physical and mechanical properties, and the quality of the manufactured parts. For example, sufficient energy density is needed to melt powder particles of the layer being processed and of the previous layer to assure a correct binding between successive layers and avoid lack of fusion and porosity. On the other hand, excess energy can cause material vaporization, creating defects and reducing material density.

The defined set of process parameters allows obtaining a working window where parts with high densities and low roughness are achieved. According Equation 2.1 the volumetric energy density is defined as a function of laser power P_{Laser}, scanning speed v_{scan}, layer thickness t_{Layer}, and hatch spacing h_s.

$$E_{density} = \frac{P_{Laser}}{v_{scan} \cdot h_s \cdot t_{Layer}} \tag{2.1}$$

The power of the laser P_{Laser} (expressed in W) influences the density of the printed part. P_{Laser} is the amount of energy converted per unit time of the laser from the machine of additive manufacturing. When the laser power increases, the energy density also increases. The maximum power for the EOSINT M 280 can be equal to 400 W. It is worth mentioning that too high laser power may affect the appearance of various defects, e.g., "key holes".

In contrast to the laser power, when the scanning speed v_{scan}, layer thickness t_{Layer}, and hatch spacing h_s increase, the $E_{density}$ decreases. The velocity of the laser displacement v_{scan} is a dependence of the distance between two laser exposure points (expressed in mm) on the exposure time of these points (in s). When v_{scan} is too high, the unmelted powder can form some droplets, influencing the decreasing the accuracy and strength of the obtained part. Wherein too low-velocity results in a ball effect. It influences the higher porosity and surface roughness. The velocity of the laser displacement during the melting is defined as below:

$$v_{scan} = \frac{x_{dist}}{t_{expo}} \tag{2.2}$$

The exact difference between hatch spacing h_s and layer thickness t_{Layer} (slicing distance) is shown in Figure 2.4. The h_s parameter is the distance between two parallel paths of laser track on one layer. It is also called scanning spacing. An overlap of the melting pool can be created for a low hatch distance. Too high scan spacing contributed to a lack of fusion during the melting, by creating voids between two laser paths. The layer thickness t_{Layer} is the distance of the two layers which are generated during the slicer process. It determines the thickness of the powder, which is spread on the building bed by the recorder before the laser melting. The parameter influences not only the time of the printing process but also the mechanical properties and the surface roughness. High layer thickness provides high porosity and the worst surface quality.

If two layers are too far from each other, the material may not be melted in deeper. Therefore, a balling phenomenon can cause weak bonding inside the sample. However, by increasing the layer thickness, the time of the print process can be significantly decreased [10].

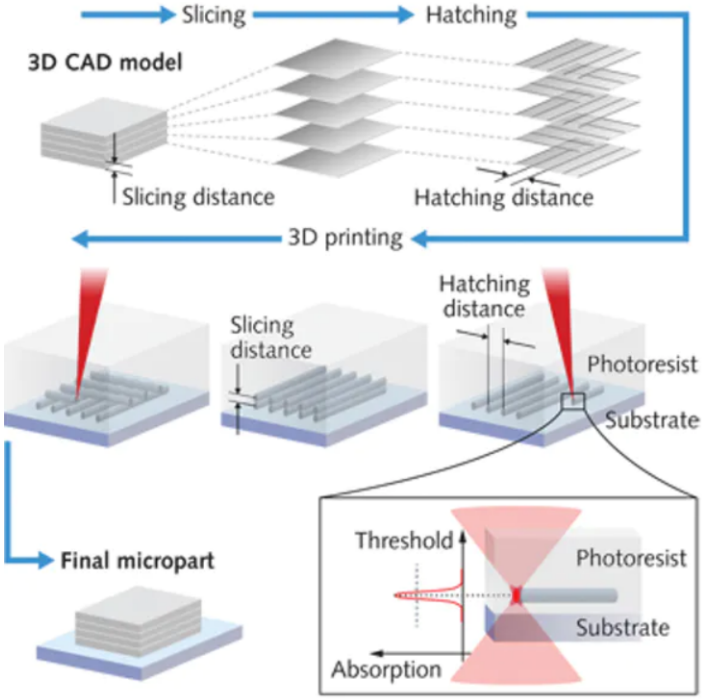

Figure 2.4: *Schematic of the hatch spacing h_s and layer thickness t_{Layer} parameters [10].*

Apart from the process parameters mentioned above, the scanning strategy particularly influences the quality of printed parts. The geometrical pattern, followed by the energy beam, influences the thermal gradient and, therefore, the part's quality. Many defects are the result of the significant residual stresses or balling effects. The adjusted scanning strategy in the AM process controls densification, microstructure, and mechanical property of three-dimensional parts [11]. Figure 2.5 shows the schematics of different types of scanning strategies. The uni-directional (Fig. 2.5a), bi-directional (Fig. 2.5b), as well as island scanning (Fig. 2.5c) are the most common scanning strategies. The uni-directional and bi-directional are characterized by a long path of the laser working distance. The difference between them lies in the direction of the scanning vector. For the uni-directional scanning, the laser beam moves in one way. In the bi-directional scan, also called zigzag scan, the laser works in the opposite direction. The third one, called a chessboard strategy, is based on dividing the building platform into small square areas. It reduces the scan vector length and increases performance in certain situations. Comparison of the uni-directional (Fig. 2.5c), bi-directional (Fig. 2.5d) and helix scanning strategy (Fig. 2.5f) present the way of reducing the length of the scanning vector. The contour scanning strategy (Fig. 2.5g) is based on continuous laser scanning of a predefined contour and hatching the area inside the contour [11].

Figures 2.5h–2.5i distinguish the double pass of laser beam scan on the subsequent layers. It influences the defining microstructure and mechanical properties of the obtained part. Figures 2.5i–2.5m demonstrate that the rotation of scan vectors between or inside layers. In addition, Figure 2.5n shows an example of the distribution of points where the melting focuses.

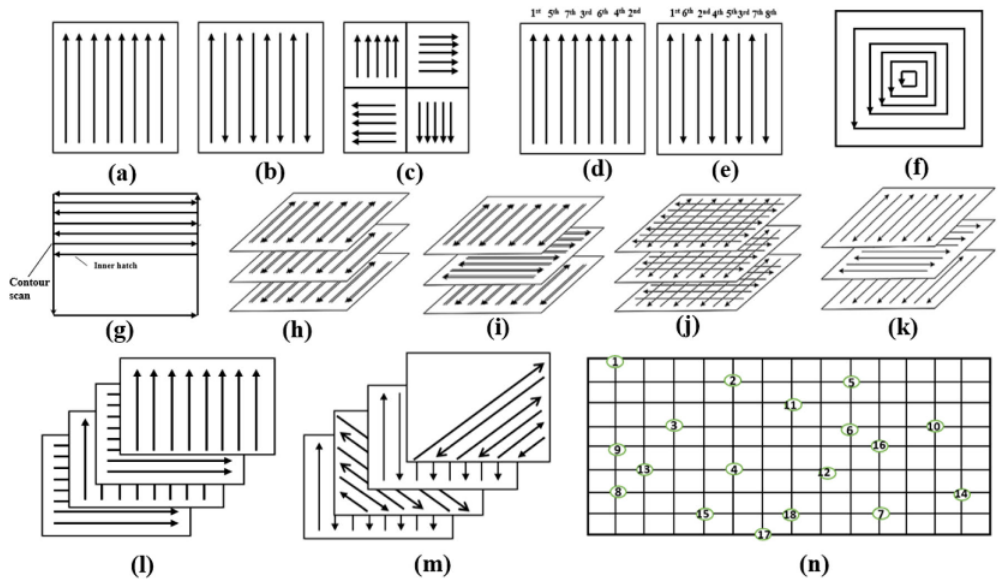

Figure 2.5: *Different types of scanning strategies: (a) uni-directional, (b) bi-directional - zigzag, (c) island scan; (d) variation of scanning sequences based on uni-directional scan, and (e) bi-directional scan; (f) helix scan, (g) contour, (h) bi-directional, double pass of laser beam; (i) bi-directional, double pass of laser beam,* 90° *rotation scan vector between layers; (j) cross-scan; (k) bi-directional, single pass of laser beam,* 90° *rotation of scan vector between layers, (l)* 90° *rotation of uni-directional scan between successive layers; (m)* 45° *rotation of scan vector; (n) point melting scan [11].*

2.2.2 Post-processing

Additional post-processing is often needed for AM parts to meet more advanced manufacturing requirements. Firstly, removing support and raft structure is often necessary on DMLS parts. Typically, it takes place by using wire EDM or a band saw. However, additional machining processes may be beneficial to improve the properties of the final part, get closer to required tolerances, or prepare a complex component. In general, the DMLS process can produce parts with tolerances of ± 0.003 in. (0.076 mm) [12], in which a layer thickness may vary between 20-60 µm [13]. However, basic CNC machining can increase the tolerances up to ± 0.03 mm [14].

The rapid heating and cooling of the metal material during the DMLS process results in a buildup of internal stresses. Therefore, additional heat treatments can influence mechanical properties such as hardness, elongation, or fatigue strength. Heat treatment is the process of heating metal without letting it reach the molten or melting stage, and then cooling the metal in a controlled way to select desired mechanical properties. A T6 cycle of heat treatment is often used for conventionally cast components, composed of solution annealing, quenching, and age hardening. However, for laser-sintered parts, it is recommended to use the stress-relieving cycle of 2 hours at 300 °C (572 °F). It is caused by an anisotropy which is a result of the layered way of manufacturing [14]. In the literature [15], it can be found the studies on the samples after the heat treatment at 530 °C for 6 h, which, despite the annealing, can cause a formation of stable intermetallic phase from supersaturated one. As well as, in [14] is proposed to perform a shorter solution annealing for 30 minutes in 530 °C followed by immediate quenching to water. The artificial aging process should take part of 6 hours at 165 °C followed by cooling in air.

2.2.3 Materials in DMSL method

DMLS is a well-known technology for sintering aluminum, titanium, nickel alloys, steel, or stainless-steel powder, which enables reliable and repeatable part quality [14]. EOS' portfolio offers over 20 different alloys and over 70 validated processes for the DMLS systems. The materials are available as premium products - highly validated data with high repeatability or core products that are under testing.

Table 2.1: *Metal materials for EOS 3D printers using DMLS technology [16].*

Material		Ultimate Tensile Strength	Yield Strength	Elongation / Break	Usage examples
Aluminum	AlSi10Mg	460 MPa	245 MPa	5 %	Conflux Heatexchanger
	AlF357	330 MPa	260 MPa	11 %	EOS Coral Heatsink
	Al2139	520 MPa	460 MPa	4 %	-
Case Hardening Steel	20MnCr5	1250 MPa	900 MPa	10 %	Gear Wheel
Cobalt Chrome	MP1	1100 MPa	600 MPa	min 20 %	Stent
	SP2	1350 MPa	850 MPa	3 %	Dental bridge
	RPD	1100 MPa	550 MPa	7 %	Dental Partials
Copper	Cu	190 MPa	140 MPa	20 %	Heatexchanger Demopart
	CuCP	165 MPa	235 MPa	45 %	-
	CuCrZr	300 MPa	200 MPa	30 %	Combustion Chamber
Nickel Alloy	IN625	920 MPa	670 MPa	40 %	Combuster
	IN718	1020 MPa	710 MPa	29 %	Euro-K Burner
	IN939	1510 MPa	1115 MPa	12 %	-
	HX	750 MPa	590 MPa	33 %	TUM Solid Fuel Burner
Precious metals	-	-	-	-	Cufflinks
Refractive materials	W1	-	-	-	Tungsten Anti Scatter Grid
Stainless Steel	316L	590 MPa	500 MPa	47 %	Watch case
	316L VPro	530 MPa	410 MPa	13.5 %	GKN manifold
	17-4PH	1340 MPa	1235 MPa	13,5 %	Medical Device
	254	700 MPa	600 MPa	30 %	Austenitic 3D printing material
	CX	1720 MPa	1650 MPa	6 %	Mold insert
	PH1	1440MPa	1300 MPa	13 %	EOS Packaging Sieve
	GP1	min 980 MPa	min 550 MPa	min 29 %	Kappius rear hub
Titanium	Ti64	1055 MPa	945 MPa	13 %	Gear Harness Bracket
	Ti64ELI	1055 MPa	945 MPa	13 %	Permedica Acetabular Cups with porous surface
	Ti64 Grade 5	1080 MPa	980 MPa	14 %	Gear Harness Bracket
	Ti64 Grade 23	1050 MPa	940 MPa	14 %	Permedica Acetabular Cups with porous surface
	TiCP Grade 2	570 MPa	445 MPa	26 %	Skull Implant
Tool Steel	MS1	2080 MPa	2000 MPa	4 %	Linde HYDROPOX burner
	CX	1720 MPa	1650 MPa	6 %	Mold insert
	1.2709	2250 MPa	2160 MPa	3.5 %	Pipe mold

Detailed data obtained following the manufacturer's datasheet [14] and possible applications are presented in Table 2.1. The EOS aluminum family of powders are aluminum-silicon alloys, often used for many applications in industries, e.g., aerospace and automotive. Among others, the EOS Aluminum AlSi10Mg alloy is one of the most used powders. It is characterized by a good strength to weight, height hardness, as well as offers corrosion resistance and dynamic properties. The particle size of powder is in range 10-45 µm and the density of the material is equal to $2.67\,\mathrm{g/cm^3}$. Stainless steel alloys are commonly used in medical, oil, gas, or ship-

building applications. The material behavior characteristics of copper alloy (e.g., Cu, CuCP, and CuCrZr) indicate that it can be ideal for heat exchangers, rocket engine parts, induction coils, or electronics. In addition, the behavior indicates good conductivity properties. Nickel alloys can be used in gas turbines for both aerospace and energy industries, process industry, or shipbuilding [14]. Precious metals are not commonly offered powder available in the portfolio of companies intended for the DMLS method. However, these materials are characterized by unique properties such as high resistance to corrosion and good malleability. Therefore, they can be applied for jewelry and watches and in dental, electronics, and other industries. It should be taken into account that the presented data in Table 2.1 may differ depending on the parameter's settings in the 3D printing machine. In addition, as mentioned in the section above, both physical and mechanical properties will be affected by the post-process.

2.3 Literature review on AM research

Focusing on properties of structures manufactured by sintering metal powders, numerous works mainly concern the study of various types of powders and the mechanical properties of the parts obtained from them. Understanding the effect of anisotropy on the mechanical properties of the layered parts can be crucial. Therefore, in [17] have been presented the results from compression tests of AlSi10Mg aluminum samples to define the material deformation behavior. The obtained results indicate that the build direction and heat treatment significantly affect the obtained stress value. Furthermore, the results increase together with the slope of the printed sample to the build platform, and the annealing process (2h at 300 °C) causes a significant decrease in stress level (up to 100 MPa) compared to the as-fabricated samples.

An essential issue for materials manufactured by melting metal powder is a microstructure. In the case of the powder-bed fusion methods, it can be distinguished two primary types of solidification [18]. First, pure metals or alloys (like Ti6Al5V, which occurred a stable planar front) are characterized by grains growing over several layers. Then they form large and columnar grains. In the second case, the grains are directed toward the center of the melt pool, like for 18Ni300 maraging steel or AlSi10Mg aluminum. The finer microstructure of AlSi10Mg allows obtaining a higher strength than material produced by conventional casting methods. However, the material's microstructure is one of many factors affecting the properties of the manufactured parts. Therefore, it is necessary to carry out additional studies under different conditions to gain more knowledge of the tested samples.

The quasi-static experiments of honeycomb structures manufactured from Ti-6Al-4V alloy powder were performed by Baranowski et al. [19]. They proved that a heat treatment causes a lowering of the yield point, and the fracture is less brittle than the structures without any treatment. Su et al. [20] investigated the mechanical properties of AlSi10Mg sandwich structures with the origami cores under quasi-static compression in out-of-plane load direction. They found a dependence between the dihedral angle and compressive strength, although the performance of the tested cores proved similar. Al-Saedi et al. [21] showed that the functionally graded lattice structures made of Al-12Si aluminum powder exhibit a higher value of the total cumulative energy absorption per unit volume than the uniform lattice structures. Kohnen et al. [22] investigated mechanical properties and deformation behavior of additively manufactured Ti-6Al-4V structures lattice and hollow spherical structures subjected to tension, compression, and cyclic tests. They proved that the stretching mode dominates the deformation of the lattice structures, and they achieve a higher energy absorption capacity than a bending-dominated mode of deformation of

the hollow spherical structures. Another group of structures that is increasingly in the industry is microstructures. In [23], different types of AlSi10Mg aluminum microlattices fabricated by the SLM method were subjected to quasi-static compression loads. The tested structure with a cubic fluorite unit cell achieved higher strength concerning weight than most known metallic and non-metallic microlattices.

In parallel, many investigations concern dynamic behavior of additively manufactured structures [24–27] because cellular materials exhibit excellent absorption properties during dynamic compression. Ozdemir et al. [28] proved that the Ti-6Al-4V lattice structure could be useful in protective systems. Harris et al. [29] investigated the dynamic deformation of an additively-manufacture square honeycomb with solid and lattice truss walls. The energy absorption efficiency of the hybrid structure achieved higher values when the collapse was in a regime dominated by dynamic buckling. In [30], two kinds of AM lattice structures were subjected to quasi-static and blast loading. They have shown that although the deformation mechanisms were similar in both tests, the structure geometry, relative density, and material properties significantly affect energy-absorbing characteristics at two strain rate regimes.

The literature mentioned above shows that the study of the AM structures with different topologies is a leading topic both in science and industry. Such printed structures should be tested at different strain rate conditions, load direction, or temperatures. In order to perform the deep analysis and enable the drawing of broad-reaching conclusions, material studies should be also performed.

2.4 Chapter summary

As proven in Chapter, AM is a forward-looking technology that contributed to distinguishing the TIR technological period. AM includes many methods, classification of which may be based on the material used and its way of bonding. Section 2.1 distinguishes the most well-known types, i.e., VAT Photopolymetrization, Material Extrusion, Powder-bed Fusion, Direct Energy Deposition, and Material Jetting. Then the principles of the DMLS method (belonging to the Powder-bed Fusion class) are described in detail in Section 2.2. This method was developed by EOS GmbH and Rapid Product Innovations (RPI) and allows the use of multiple powders to match the material properties with the required properties of the printed component. Section 2.2.3 summarizes the most popular materials currently are offered by the company.

The solidification in laser melting methods belongs to the rapid process and can be controlled using different combinations of print parameters. The most important aspects of machine setup must be included: the power of the laser, scanning speed, the thickness of the scanned powder layers, or hatch distance of the laser scan tracks. Increasing the laser power or decreasing the scanning speed, layer thickness, and hatch spacing enhance energy density. However, too high laser power may contribute to internal defects. In addition, it is necessary to adapt the scanning strategy to the considered task.

The post-processing discussed in Section 2.2.2 is often used to remove support structures or increase the accuracy of the printed part. In addition, heat treatment affects stress-relieving inside the sample. In Section 2.3 it is proved that intensive research on AM technology is underway. The studies are performed on both the material and the different structures in order to obtain better properties than those currently offered on the market. Following the current science direction, conducting an experimental investigation focused on the AM structures under different conditions is warranted.

Bibliography

[1] S. Ford and M. Despeisse. Additive manufacturing and sustainability: an exploratory study of the advantages and challenges. *Journal of Cleaner Production*, 137:1573–1587, 2016.

[2] Scopus database. Additive manufacturing, April 2021. https://www.scopus.com [Online; accessed 15.04.2021].

[3] B. Roberts. The third industrial revolution: Implications for planning cities and regions. *Workiing Paper Urban Frontiers*, 1, 06 2015.

[4] Ch. W. Hull. Apparatus for production of three-dimensional objects by stereolithography, 1986.

[5] L. De Lorenzis, O. Boolakee, and S. Jose. An introduction to modeling of selective laser melting. CISM, 12-16 April, 2021, 2021.

[6] L. Yang, K. Hsu, B. Baughman, D. Godfrey, F. Medina, M. Menon, and S. Wiener. *Additive Manufacturing of Metals: The Technology, Materials, Design and Production.* Springer Series in Advanced Manufacturing. Cambridge University Press, 1 edition, 2017.

[7] N. S. Moghaddam, A. Jahadakbar, A. Amerinatanzi, and M. Elahinia. *Laser-Based Additive Manufacturing of Metal Parts: Modeling, Optimization, and Control of Mechanical Properties*, chapter Recent Advances in Laser-Based Additive Manufacturing, pages 1–23. CRC Press by Taylor and Francis Group, Boca Raton, 1st edition, 2018.

[8] S. A.M. Tofail, E. P. Koumoulos, A. Bandyopadhyay, S. Bose, L. O. Donoghue, and C. Charitidis. Additive manufacturing. scientific and technological challenges, market uptake and opportunities. *Materials Today*, 21(1):22–37, 2018.

[9] R. Singh, S. Singh, and M. S. J. Hashmi. Implant materials and their processing technologies. In *Reference Module in Materials Science and Materials Engineering.* Elsevier, 2016.

[10] F. Niesler, M. Hermatschweiler, and A. Werner. Lasers for 3d printing: Additive manufacturing with nir lasers forms micro-sized parts, 2014.

[11] H. Jia, H. Sun, H. Wang, Y. Wu, and H. Wang. Scanning strategy in selective laser melting (slm): a review. *The International Journal of Advanced Manufacturing Technology*, 113, 04 2021.

[12] Protolabs. Getting started with metal additive manufacturing, 2021. https://www.protolabs.com/resources/design-tips/how-to-design-and-manufacture-metal-3d-printed-parts/ [Online; accessed 09.01.2022].

[13] R. Ferrari. Met e-manufacturing itech metal, 2021. http://www.e-manufacturing.it/ [Online; accessed 12.01.2022].

[14] EOS GmbH. Dmls metal materials, 2021. https://www.eos.info/en/additive-manufacturing/3d-printing-metal/dmls-metal-materials [Online; accessed 02.08.2021].

[15] N. Takata, H. Kodaira, K. Sekizawa, A. Suzuki, and M. Kobashi. Change in microstructure of selectively laser melted alsi10mg alloy with heat treatments. *Materials Science and Engineering: A*, 704:218–228, 2017.

[16] Robert-Stirling-Ring 1. Eos aluminium alsi10mg, 2020. https://fathommfg.com/wp-content/uploads/2020/11/EOS 07.04.2020].

[17] E. Segebade, M. Gerstenmeyer, S. Dietrich, F. Zanger, and V. Schulze. Influence of anisotropy of additively manufactured AlSi10Mg parts on chip formation during orthogonal cutting. *Procedia CIRP*, 82:113–118, 2019.

[18] J.-P. Kruth, S. Dadbakhsh, B. Vrancken, and K. Kempen. *Additive manufacturing: innovations, advances, and applications*, chapter Additive Manufacturing of Metals via Selective Laser Melting Process Aspects and Material Developments, pages 69–99. CRC Press by Taylor and Francis Group, Boca Raton, 2016.

[19] P. Baranowski, P. Platek, A. Antolak-Dudka, M. Sarzynski, M. Kucewicz, T. Durejko, J. Malachowski, J. Janiszewski, and T. Czujko. Deformation of honeycomb cellular structures manufactured with Laser Engineered Net Shaping (LENS) technology under quasi-static loading: Experimental testing and simulation. *Additive Manufacturing*, 25:307–316, 2019.

[20] L. Z. Su, Z. Li, Z. X. Ge, Y. Zhou, and K. J. Wang. *Automatic Control, Mechatronics and Industrial Engineering: Proceedings of the International Conference on Automatic Control, Mechatronics and Industrial Engineering (ACMIE 2018)*, chapter Mechanical properties of an AlSi10Mg sandwich structure with different origami patterns under compression, pages 251–256. CRC Press by Taylor and Francis Group, Boca Raton, 2018.

[21] D. S. J. Al-Saedi, S.H. Masood, M. Faizan-Ur-Rab, A. A., and P. Ponnusamy. Mechanical properties and energy absorption capability of functionally graded f2bcc lattice fabricated by slm. *Materials and Design*, 144:32–44, 2018.

[22] P. Kohnen, C. Haase, J. Bultmann, S. Ziegler, J.H. Schleifenbaum, and W. Bleck. Mechanical properties and deformation behavior of additively manufactured lattice structures of stainless steel. *Materials and Design*, 145:205–217, 2018.

[23] T. Yu, H. Hyer, Y. Sohn, Y. Bai, and D. Wu. Structure-property relationship in high strength and lightweight AlSi10Mg microlattices fabricated by selective laser melting. *Materials and Design*, 182:108062, 2019.

[24] A. Antolak-Dudka, P. Platek, T. Durejko, P. Baranowski, J. Malachowski, M. Sarzynski, and T. Czujko. Static and dynamic loading behavior of Ti6Al4V honeycomb structures manufactured by Laser Engineered Net Shaping (LENSTM) technology. *Materials*, 12(8), 2019.

[25] K. Davami, M. Mohsenizadeh, M. Munther, T. Palma, A. Beheshti, and K. Momeni. Dynamic energy absorption characteristics of additively-manufactured shape-recovering lattice structures. *Materials Research Express*, 2019.

[26] T. Tancogne-Dejean, A. B. Spierings, and D. Mohr. Additively-manufactured metallic micro-lattice materials for high specific energy absorption under static and dynamic loading. *Acta Materialia*, 116:14–28, 2016.

[27] L. Xiao and W. Song. Additively-manufactured functionally graded Ti-6Al-4V lattice structures with high strength under static and dynamic loading: Experiments. *International Journal of Impact Engineering*, 111:255–272, 2018.

[28] Z. Ozdemir, E. Hernandez-Nava, A. Tyas, J. Warren, S. Fay, R. Goodall, I. Todd, and H. Askes. Energy absorption in lattice structures in dynamics: Experiments. *International Journal of Impact Engineering*, 89:49–61, 11 2015.

[29] J. A. Harris, R. E. Winter, and G. J. McShane. Impact response of additively manufactured metallic hybrid lattice materials. *International Journal of Impact Engineering*, 104:177–191, 2017.

[30] S. McKown, Y. Shen, W. K. Brookes, C. J. Sutcliffe, W. J. Cantwell, G. S. Langdon, G. N. Nurick, and M. D. Theobald. The quasi-static and blast loading response of lattice structures. *International Journal of Impact Engineering*, 35(8):795–810, 2008. Twenty-fifth Anniversary Celebratory Issue Honouring Professor Norman Jones on his 70th Birthday.

Chapter 3

Material behavior

The hereby chapter is devoted to analyzing the behavior of AlSi10Mg material manufactured by the DLSM method. The tension and compression tests are performed to study the influence of the print direction, strain rate, and temperature sensitivity. In addition, the given studies include the analysis of the effect of the heat treatment or its lack of AM samples on the obtained results. To complete the experimental part of the material investigation, the tests under quasi-static conditions are complemented by the tests carried out through a Split Hopkinson Pressure Bar (SHPB). They allow for the extension of the material investigation of the strain rate sensitivity. In addition, the experimental setup equipped with the heating chamber makes it possible to study the temperature dependencies at the dynamic range.

Furthermore, the microstructural analysis of the samples before and after the annealing allows conducting observations of the discrepancies in the arrangement of the particles, which affect the material behavior. It also confirms the influence of the printing direction on the resultant structural anisotropy. The samples printed additively from the AlSi10Mg powder have a more refined microstructure and improved strength and hardness compared to structures produced by the conventional casting methods [1]. Since the tested alloy is characterized by a good strength-to-weight ratio, high hardness, and offers high corrosion resistance [2–5], therefore, the printed AlSi10Mg aluminum has also become an interesting topic in the field of material modeling science. The test results are used to identify a constitutive model and calibrate the material parameters. The modified Johnson-Cook model accounting for the phenomenological observations is identified and validated on the experimental loading cases. The provided discussion on the microstructure and mechanical behavior is useful for further designing and manufacturing the components from the AlSi10Mg aluminum powder.

3.1 Introduction

In the case of AM technology, selecting the metal alloy type is as important as choosing print settings, process conditions, or post-treatment of parts. The whole fabrication process affects the properties of a final product. The changing parameters can influence, e.g., the roughness, strength, ductility, or microstructure. As the technology is relatively new compared to casting or welding, the technical aspects of the DMLS technique have still being analyzed. The [6, 7] papers report on different laser processing conditions and their influence on the thermal behavior of AlSi10Mg powder during printing and the resultant microstructure. When the laser power increases, the maximum temperature gradient and the size of the melted pools also increase. The process parameters determine an energy density model correlated with pores and internal defects in the manufactured part [8]. The higher porosity was related to the insufficient obtained energy density and an increase in the non-melted grains. Furthermore, the deposition in a precise volumetric energy density (VED) window, which is related to the laser's diameter dependence, can lead to fully dense parts [9]. To find the optimal process condition, various print settings were tested in the reference [1]. They proposed a relationship between the laser power and the scanning speed to the obtained porosity. The manufactured samples were characterized by the lowest obtained porosity, below 10 %, when the laser energy varied between 50 J/mm^3 – 75 J/mm^3 and higher than 120 J/mm^3. However, the energy density of 120 J/mm^3 was correlated with the additional defects, e.g., the keyholes resulting from higher vaporization [10].

In the laser sintering methods, the authors [11] distinguished two main types of solidification. The epitaxial growth [12] takes place along the direction of the maximum thermal gradients. The microstructure may be characterized by long and columnar grains formed over the printed layers. The solidification mechanism requires stable planar fronts without local perturbations in the material structure. Therefore, this is typically for pure or low-alloy metals (e.g., Ti6Al5V) in which an additional amount of the alloying elements is limited. In the second case, the grains are directed toward the center of the melt pool for the structures of medium- and high-alloy metals (such as the 18Ni300 maraging steel or AlSi10Mg aluminum). The solidification process is characterized by the expulsion of hemispherical grains, forming a fine cellular structure. Different combinations of the print parameters, e.g., a scanning strategy, can strongly influence the solidification process of the melted powder. For certain powders, a unidirectional scan can lead to the strongest texture. However, it can also generate tilts of the texture perpendicular to the scan vectors. A rotation between printed layers results in better grains and a more substantial texture for the structures manufactured from pure and low-alloy metal powders. Since anisotropy characterizes the additively manufactured samples, the rotation and overlapping of layers are often applied to increase the randomness of the adjacent tracts. Thus, it contributes to the improvement of the homogenization of properties.

Another topic extensively discussed in the literature is understanding the effects of structural anisotropy and residual stresses on the mechanical properties of the layered-built samples. Segebade et al. [13] or Maconachie et al. [14] performed tension tests of AlSi10Mg aluminum samples to define the material behavior. The obtained results indicate that the building direction has no significant effect on hardening curves. However, it was observed that the horizontally built samples reached a slightly higher strain limit, which was attributed to the heat treatment process. This post-process allows the stresses to be relieved and can lead to softening of the material, improving ductility and creep resistance. Entirely different conclusions on the influence of the printed direction were drawn by [15–18]. The conducted research correlates the obtained results with the position of the sample on the build platform. Delcuse et al. tested the effect of the

build orientation on the porosity and mechanical properties of an auxetic structure made from Inconel alloy IN718. The studies prove that the horizontally printed auxetic structures exhibit higher yield stress, stiffness, and plastic work during the tensile tests. However, the Poisson's ratio is independent of the sample position on the build platform.

The effect of heat treatment is often discussed in the literature concerning AM technology. Post-processing can introduce changes to the microstructure; therefore, the manufactured objects can obtain customized mechanical properties, e.g., increased hardness or ductility. Zygula et al. [19] compared the mechanical properties and microstructure of the AlSi10Mg samples as-built and after heat treatment. Then, the characteristics of the samples printed additively were confronted with the values describing samples made from a cast alloy. In both cases, the heat treatment results in a reduction of the porosity. In [20], the microstructure of as-fabricated and after heat treatment samples made from AlSi10Mg alloy was discussed in detail. It was concluded that the annealing at 300 °C for 2 hours caused the increase in the precipitation of the fine Si phase within the columnar Al matrix. The treatment at the temperature of 530 °C for 6 hours resulted in the formation of a stable intermetallic phase and microstructural equilibrium. It has been observed that each subsequent heat treatment increases the ductility and reduces the stress values obtained during tensile tests.

3.2 Material and specimens

The samples for the material testing are manufactured from AlSi10Mg aluminum powder. Table 3.1 presents the chemical composition of the powder and the main material properties. The presented parameters in the material datasheet from EOS GmbH−Electro Optical Systems [3] are confirmed by the Scanning Electron Microscope (SEM) and Energy Dispersive Spectroscopy (EDS) observations, using the ZEISS Gemini 350 VP FE-SEM machine (Fig. 3.1). The particle size of powder is in range 10−45 µm and the density of the material is equal to 2.67 g/cm^3.

Table 3.1: *(a) Selected material parameters and (b) chemical composition of the AlSi10Mg aluminum powder.*

(a)	Material			ρ	E	ν
	AlSi10Mg			2.67 [g/cm^3]	70 [GPa]	0.33 [−]
(b)	Alloy Elements (wt %)					
	Al	Si	Mg	Fe	Mn	Ti
	Bal.	9-11	0.2-0.45	⩽0.55	⩽0.45	⩽0.15

The bidirectional scanning method, used by an EOSINT M 280 3D printer during the manufacturing process (see Section 2.2) contributes to the unified macro properties of the final part. As shown in Table 3.2, the processing parameters have been selected to obtain the laser energy density of 50 J/mm^3, allowing almost solid components and neglecting the negative influence of the porosity [1].

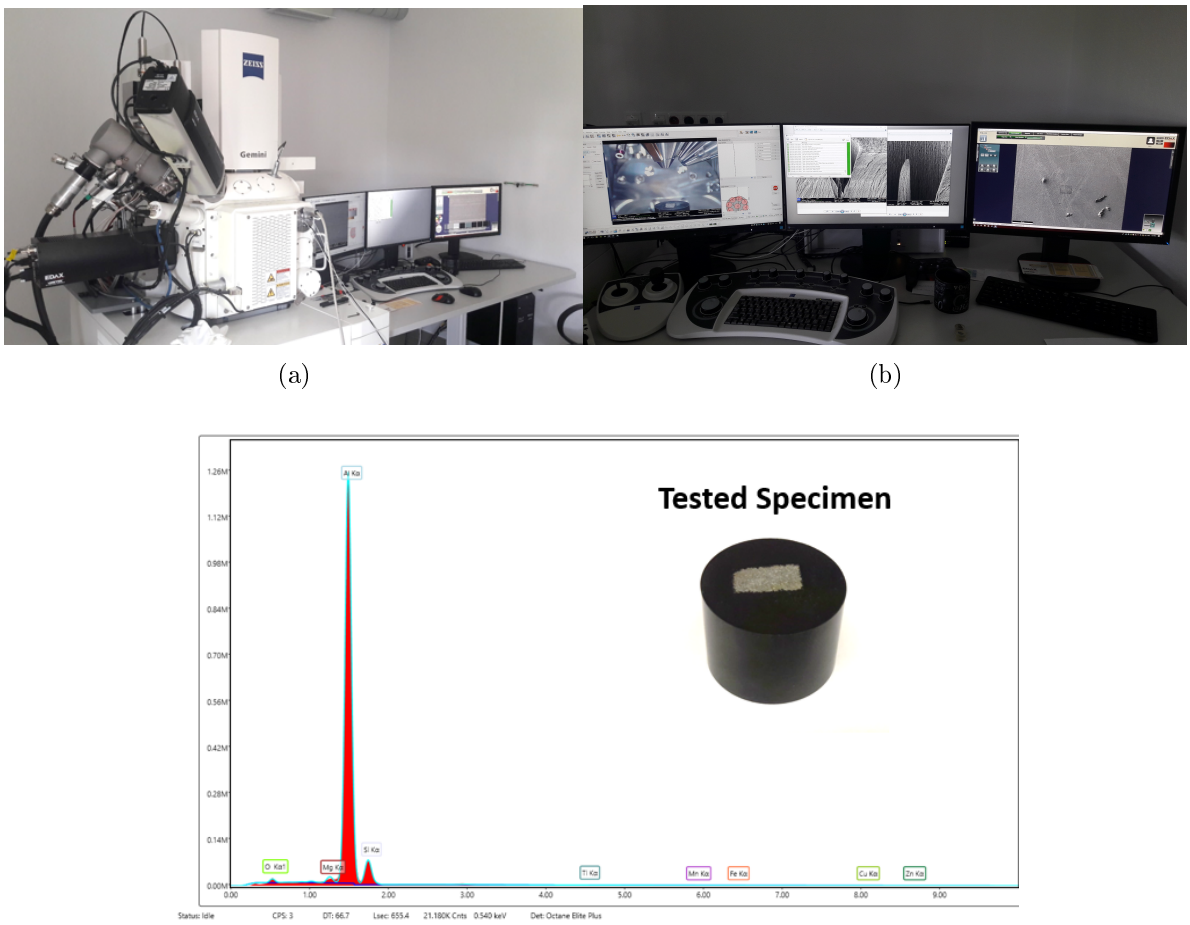

(a) (b)

(c)

Figure 3.1: *SEM and EDS observations (a,b) ZEISS Gemini 350 VP FE-SEM machine, (c) chemical composition of AlSi10Mg.*

Table 3.2: *Basic parameters used for manufacturing tested structures by the DMLS method. The EOSINT M 280 3D printer, developed by EOS is used to print the metal structures.*

Parameter of printing process	**Value**
Power of the laser source	370 W
Scan velocity	1300 mm·s^{-1}
Hatch distance of the laser scan tracks	190 µm
Thickness of the powder layers to be scanned	30 µm
Energy density	50 J·mm^{-3}

The manufactured samples have been subjected to tensile and compression loads under quasi-static and dynamic conditions. In order to investigate the influence of the print direction on the results, nine different possibilities for the slop sample were considered, depending on the test. The print directions of the manufactured samples are presented in Figure 3.2a. The samples are distributed at 45 degrees apart in the Euclidean space. Whereby, the flat specimens for the tensile tests were positioned at an angle of 0 ° and 90 ° in the XY horizontal and XZ

vertical planes. Their geometry is shown in Figure 3.2b. The quasi-static compression tests are performed using cylinders with dimensions of $\Phi = 6$ mm and h = 9 mm. In the dynamic compression tests performed using the Split-Hopkinson Pressure Bars, the cylindrical samples of $\Phi = 5.8$ mm and h = 3 mm are tested. To verify the effects of material anisotropy, the specimens for compression tests were printed along three directions in XZ plane – a horizontal print [0°], vertical [90°] and at the angle of 45° to the build platform [45°] Fig. 3.2c. This approach follows the assumption of transversal isotropy of the printed material.

The printed samples were lathed and subsequently cut by Electrical Discharge Machining (EDM) to the required dimensions. The study concerns the samples as-fabricated and after heat treatment, due to which internal stresses are relieved [21, 22]. The heat treatment is carried out for 120 minutes at 300°C, following indications in the powder datasheet [3].

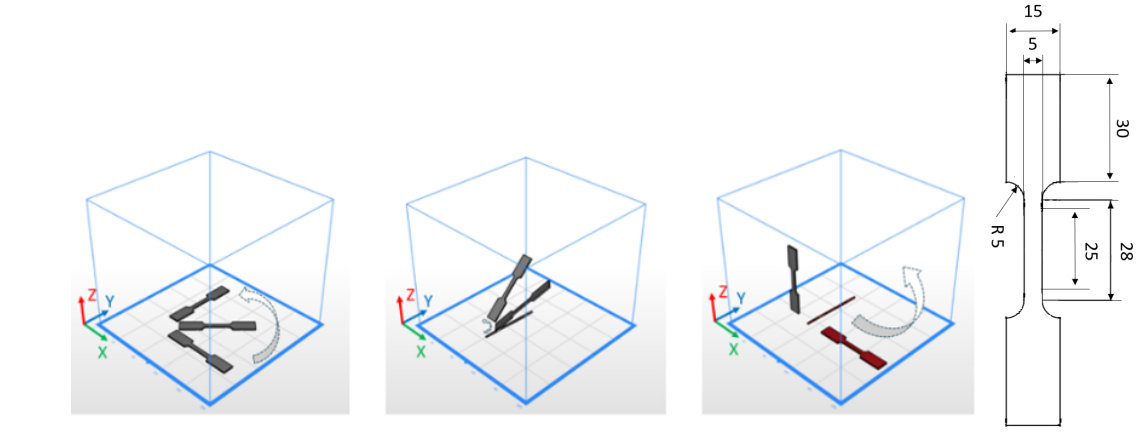

(a) (b)

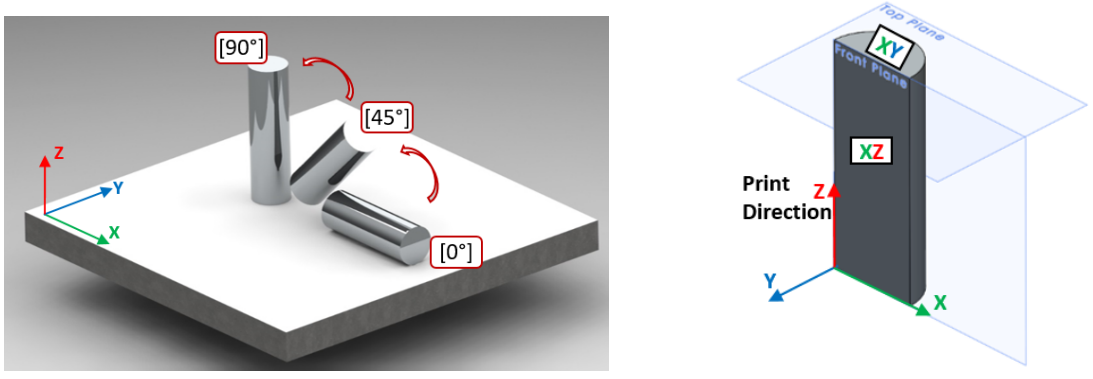

(c) (d)

Figure 3.2: *(a) Orientation of the samples versus the build platform; (b) dimensions of the sample for the tensile tests; (c) considered print directions for the compression testing scheme; (d) observed sample surfaces for the microstructural analysis.*

3.3 Microstructure analysis of the as-fabricated and heat-treated samples

The microstructure observation was performed on the polished and adequately etched samples using the Olympus DSX 510 optical microscope. The observed surfaces aligned along the building direction [XZ] and the transverse surface [XY] are schematically shown in Fig. 3.2d. The comparison of the microstructure is based on the specimens as-fabricated (Fig. 3.4a-3.4c) and after the annealing process (Fig. 3.4d-3.4e).

The formation of the optically observed melt pools (Fig. 3.3b-3.3c) is presented schematically in Fig. 3.3a. The melt pools can be related to manufacturing and the cooling process of the melted areas [23]. Visible melt pools with distinct boundaries characterize the observed surfaces for as-fabricated (Fig. 3.4a) and annealed samples (Fig. 3.4d). As a result of differences in the cooling rate, three distinct areas are formed: a fine cellular structure, a coarse cellular structure, and a heat-affected zone (HAZ) (Fig. 3.3a, Fig. 3.3c). The first zone was created towards the melt pool centre due to a slower solidification process. The region with the coarse cellular structure is the intermediate zone between the center and the boundaries of the melt pool. The long Si particles are formed in heat-affected zones that contact a previously solidified melt pool. The visible bright eutectic Al/Si phase of the micrographs in Fig. 3.4c is precipitated during the solidification process and included in the Al matrix of melt pools [24]. It can be observed in Fig. 3.4f that after the heat treatment, the Si particles become larger and more visible in the fine cellular structure. During the annealing process, the Si particles diffused from the supersaturated Al/Si matrix. As a result, the precipitated grains of Si are similar in shape and size to the grains in the heat-affected zone region (Fig. 3.3c). The greater amount and larger size of other particles across the aluminium matrix may reduce the strength and influence the behavior of the manufactured samples.

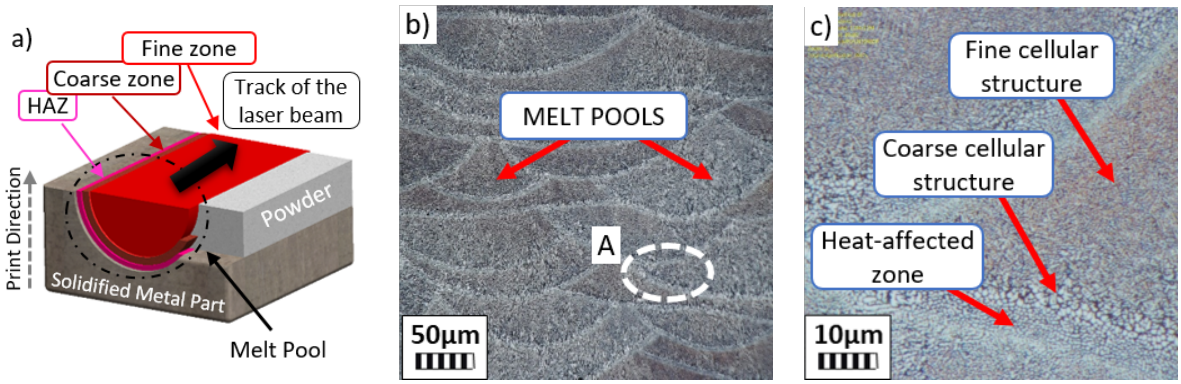

(a) (b) (c)

Figure 3.3: *(a) The schemes of melt pool forming and (b) the optical micrographs of the AlSi10Mg as-fabricated sample, (c) enlarged area marked "A".*

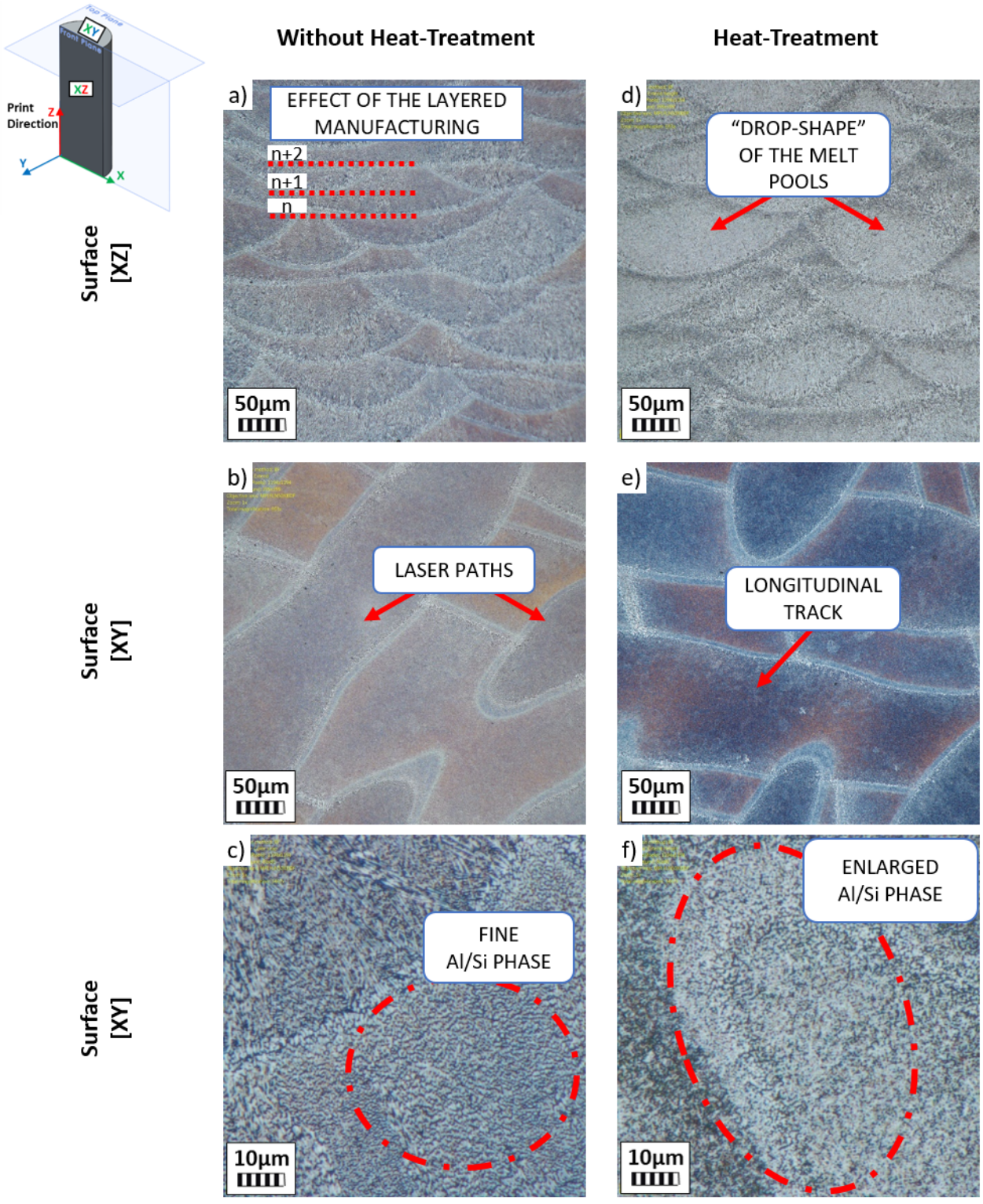

Figure 3.4: *The optical micrographs showing microstructures of the AlSi10Mg samples without heat treatment (a, b, c) and annealed (d, e, f).*

In addition, the microstructures of samples before and after the compression process were compared. Figure 3.5 shows the results from the observations of the XZ surface (Fig. 3.2d) of the vertically printed samples [90°] with and without heat treatment. The undeformed sample, before heat treatment is characterized by long fibers of the Si network (Fig. 3.5a). After annealing, the finer mesh is visible. Due to the diffusion of Si grains from the supersaturated Al/Si matrix, the longitudinal fibers form a smaller and and more circular network (Fig. 3.5b). After compression, both samples exhibit high porosity around the entire crack path. The voids arrange themselves in such a way that one of the possible further fracture paths can be supposed (see Fig. 3.5b-3.5d). In addition, it is observed that the as-fabricated sample is characterized by a sharp end of the crack, (Fig. 3.5b). The head of the crack of the sample presented in Figure 3.5d is more rounded. On the surface after the heat treatment process, it is observed to be less porous, which may affect the strength and ductility of the material.

A deeper analysis focuses on the observation of the phenomena occurring in the microstructure during the compression process. Figure 3.6 presents the surface of two samples after 20 % of deformation. In Figure 3.6a is shown the specimen printed at 45° angle to the building platform and in Figure 3.6b is the vertically printed sample after heat treatment. The first one is characterized by a non-unified network of round and oval shapes within the Si network. The second one consists of very long fibers directed horizontally. The circular network before deformation (Fig. 3.5c) forms into one area and does not create a fine mesh like it does for the [45°] specimen (Fig. 3.6a). This observed phenomena may affect the mechanical response of the sample, e.g., increasing the ductility and the material softening occurrence, due to the connection of the Si network. The formation of long Si fibers may also have the effect of reducing the porosity observed compared to the [45°] sample (Fig. 3.6a).

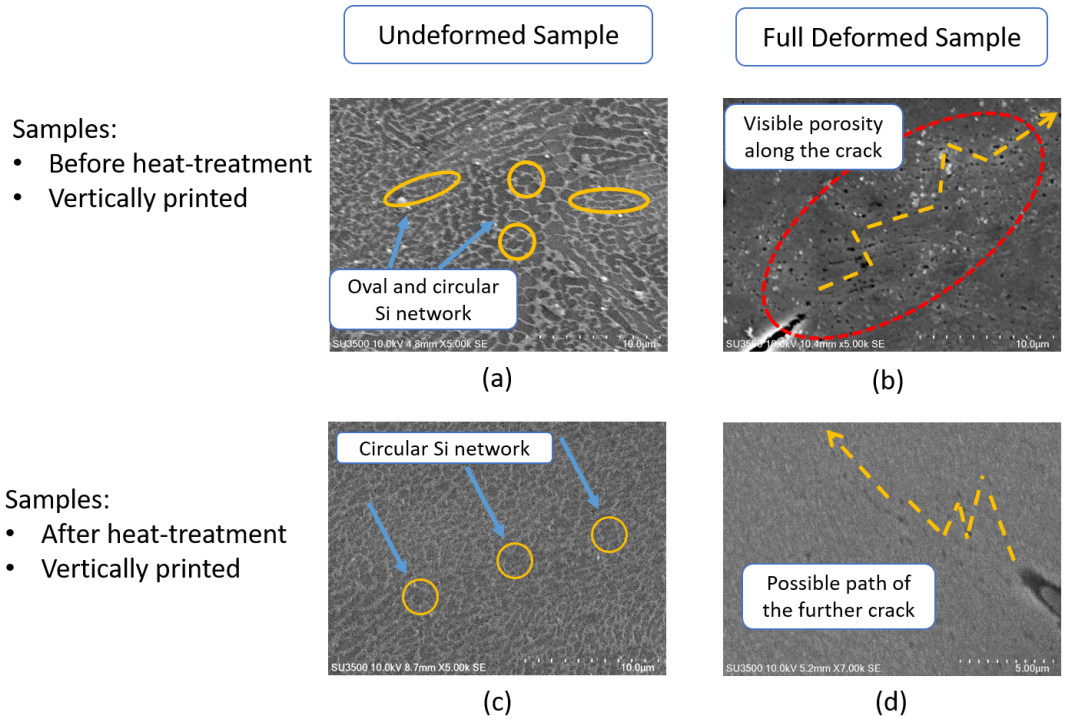

Figure 3.5: *Microstructure observations of undeformed and full compressed samples before and after the heat treatment process at the strain rate of 0.001/s.*

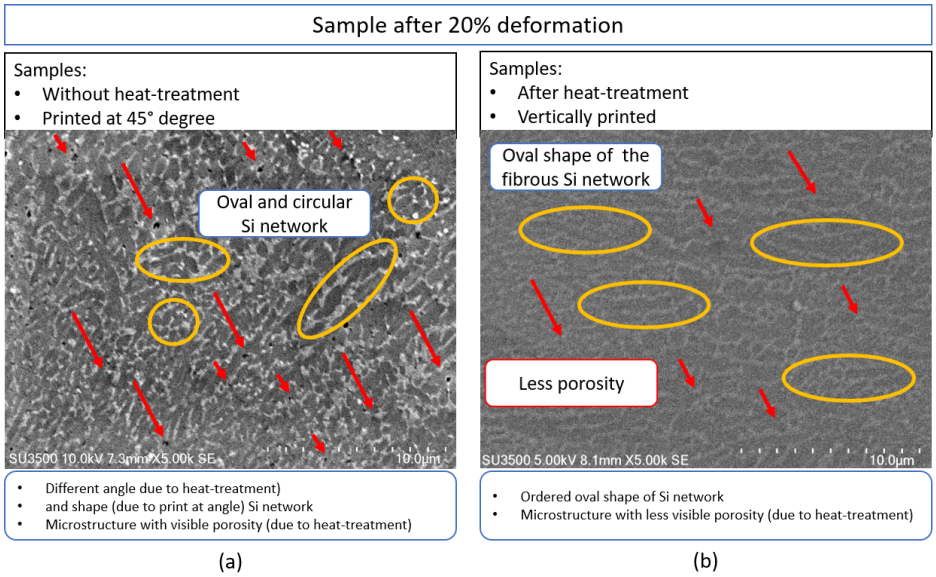

Figure 3.6: *Microstructure after 20 % compression of the samples (a) printed at* 45° *without heat treatment and (b) printed at* 90° *with heat treatment.*

3.4 Measurement of the Vickers hardness

The hardness of the as-fabricated and annealed samples is studied with the Vickers method. The tests are performed using a Buehler's microhardness tester machine Wilson VH1202 [25]. First, an indentation mapping is performed using a 0.2 kg load with a hold time of 10 s to obtain the homogeneity along the longitudinal axes in the material. Then, to determine an average hardness value, the tests are repeated five times.

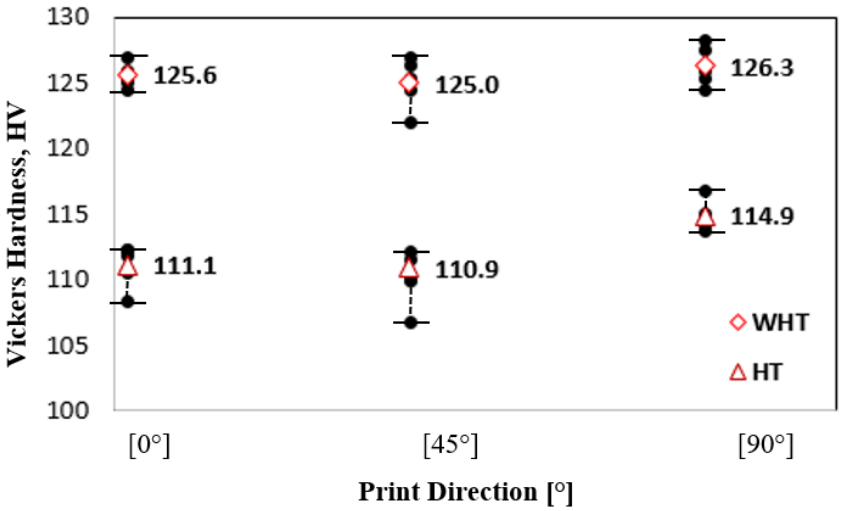

Figure 3.7: *The Vickers hardness results of the AlSi10Mg aluminium alloy for the samples without the heat treatment (WHT) and after the heat treatment (HT), printed at* 0°, 45° *and* 90° *angles to the build platform.*

Figure 3.7 shows the comparison of the values obtained in the hardness tests for six types of the samples (three printing directions [0°], [45°], [90°]; heat-treated (HT) and as-fabricated (WHT)). The hardness of the HT samples decreases in comparison to the samples WHT. The vertically printed specimens in both conditions exhibit slightly higher HV hardness values. Moreover, the samples without heat treatment are characterized by constant hardness values, close to 125 ± 3 HV. After the heat treatment, the hardness varies from 110 ± 4 HV (for [45°] sample) to 115 ± 2 HV (for [90°] sample).

3.5 Experimental testing of the manufactured samples

The samples described in Section 3.2 are subjected to quasi-static and dynamic tensile and compression loadings to evaluate the material properties of AlSi10Mg aluminum alloy in terms of strain rate and temperature sensitivity.

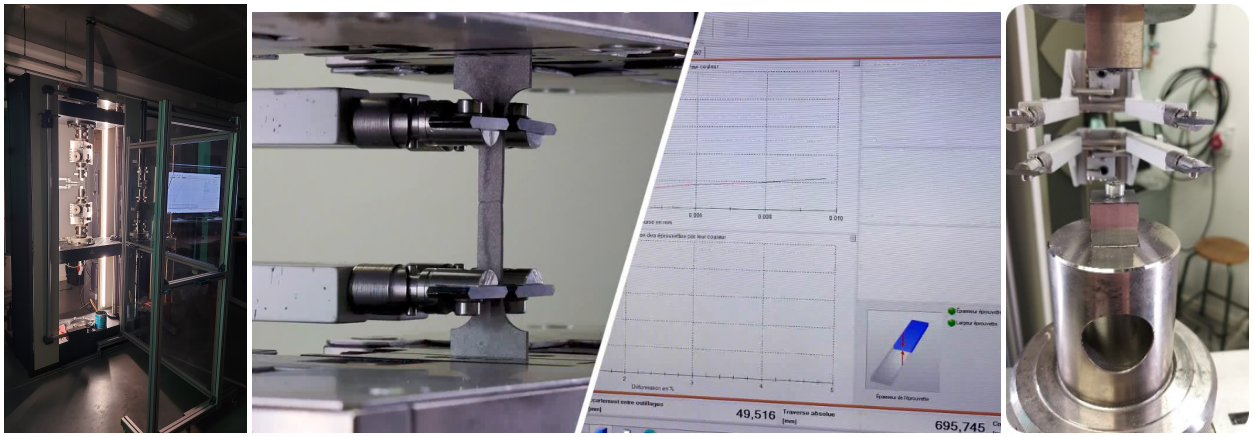

(a) (b) (c)

Figure 3.8: *(a) The hydraulic universal testing machine Zwick 1476 used to perform the quasi-static tests, (b) the example of the dog-bone shaped sample under tensile loading with the measured force-time results, and (c) the cylindrical sample after performed compression test.*

3.5.1 Tests performed in a quasi-static regime

The quasi-static tensile and compression tests were performed using a hydraulic universal testing machine Zwick 1476 with a 100 kN load cell (Fig. 3.8a). The horizontally and vertically printed samples were tested under tensile loading. The dog-bone shaped specimens were placed into the machine jaws (Fig. 3.8b). The cylindrical samples used in compression tests were inserted between two rigid high-strength steel blocks to avoid plastic deformation of the machine's grips (Fig. 3.8c). In addition, a high-pressure grease with molybdenum disulphide ISO140 allows minimalising friction effects [26]. The tests are performed under three constant loading velocities at the strain rates: 0.001 s^{-1}, 0.01 s^{-1} and 0.1 s^{-1}. To measure the sample displacement, the test stand is equipped with an extensometer. At the same time, the load sensor provides values of the force over time. Each test is repeated at least twice for each sample type. The details are summarized in Tables 3.3–3.5.

Table 3.3: *Summary of the conditions of the quasi-static tension tests to study the printing direction influance and strain rate sensitivity.*

Printing Direction	Strain Rate	Temperature	Stress Relieve
XY [0°] XY [90°] XZ [0°] XZ [90°]	10^{-3} 10^{-2} 10^{-1}	T_{room}	Heat treatment

Table 3.4: *Summary of the conditions of the quasi-static tension tests to study temperature sensitivity.*

Printing Direction	Strain Rate	Temperature	Stress Relieve
XY [0°] XZ [0°]	10^{-3}	T_{room} 100°C 150°C 200°C	Heat treatment

Table 3.5: *Summary of the conditions of the quasi-static compression tests to study the printing direction influance and strain rate sensitivity.*

Printing Direction	Strain Rate	Temperature	Stress Relieve
XZ [0°] XZ [45°] XZ [90°]	10^{-3} 10^{-2} 10^{-1}	T_{room}	Without Heat treatment Heat treatment

Based on the trivial equations (Eq. 3.1-Eq. 3.2), the measured values of the force $F(t)$ over displacement $l(t)$ from the performed quasi-static tensile tests are converted on the nominal stress - nominal strain.

$$\sigma_{nom} = \frac{F(t)}{A_0} \tag{3.1}$$

$$\varepsilon_{nom} = \frac{l(t) - l_0}{l_0} \tag{3.2}$$

Where A_0 is the initial cross-section of the sample and l_0 is initial gage length.

Due to the error resulting from the calibration and backlash of the machine jaw, the strain is corrected according to Equation 3.3. The reduction of the stiffness error resulting from the experimental technique imperfections requires comparing the Young's modulus E_{mean} from the considered test with the Young's modulus E_{theor} from the literature.

$$\varepsilon_{cor} = \varepsilon_{nom} - \sigma_{nom} \frac{E_{theor} - E_{mean}}{E_{theor} E_{mean}} \tag{3.3}$$

It is worth noticing that the cross-section does not remain constant during the test. In addition, the current elongation state affects the further development process. Therefore, the nominal stress - nominal strain must be converted into true stress - true strain according to

Equations 3.4 - 3.5 for the tension and following Equations 3.6 - 3.7 for the compression tests [27]. The changes of the curves are shown schematically in Fig. 3.9b.

$$\sigma_{true} = \sigma_{nom}(1 + \varepsilon_{nom}) \tag{3.4}$$

$$\varepsilon_{true} = ln(1 + \varepsilon_{nom}) \tag{3.5}$$

$$\sigma_{true} = \sigma_{nom}(1 - \varepsilon_{cor}) \tag{3.6}$$

$$\varepsilon_{true} = -ln(1 - \varepsilon_{cor}) \tag{3.7}$$

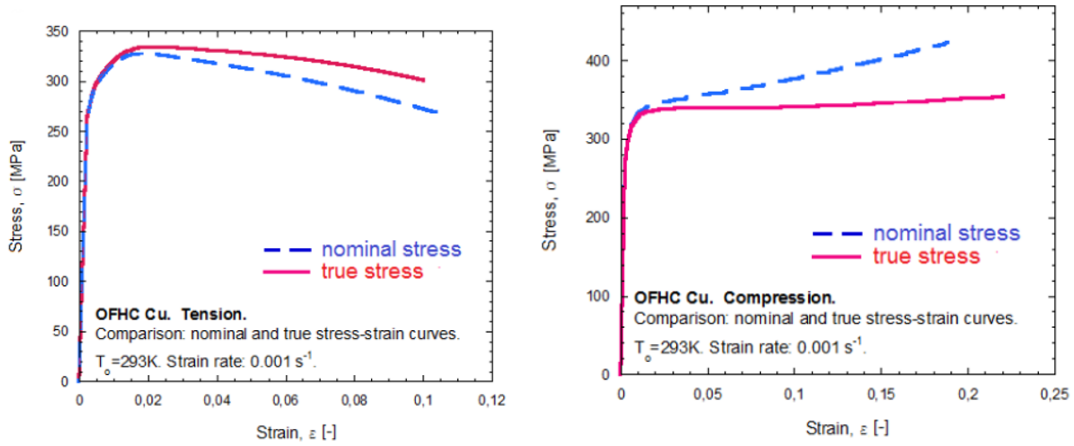

(a) (b)

Figure 3.9: *Schematically shown changes between engineering and true stress-strain curves for (a) tension and (b) compression test [27].*

Results of the quasi-static tensile tests

The true stress - true strain results from quasi-static tensile tests performed at the room temperature are presented in Figure 3.10. The horizontally printed sample obtains the ultimate tensile strength of 388 MPa at the strain rate of 0.001 s^{-1}. It increases up to 411 MPa when the strain rate is equal to 0.1 s^{-1} (see Fig. 3.11). The maximum increasing of the ultimate tensile strength for the horizontally printed samples is 23 MPa and 9 MPa for the vertically printed samples. The obtained results prove that AlSi10Mg aluminum is only slightly sensitive to strain rate changes.

Figure 3.12 shows the comparison of the print direction on the obtained results. The horizontally printed samples, in contrast to vertically oriented, obtained about 70 MPa higher results at each considered strain rate. However, the exact position on the build platform, both for the horizontal and vertical directions, is of negligible importance. It can be observed that the samples positioned at [90°] to the platform have been slightly stiffer than those printed at [0°]. The mean values of the Young's Modulus are equal to 71.5 GPa for the XY [90°], 72.0 GPa for the XZ [90°] and 70.0 GPa for the XY [0°], 70.5 GPa for the XZ [0°]. Thereby, the stress results of the [90°] samples are, on average, 4 MPa higher.

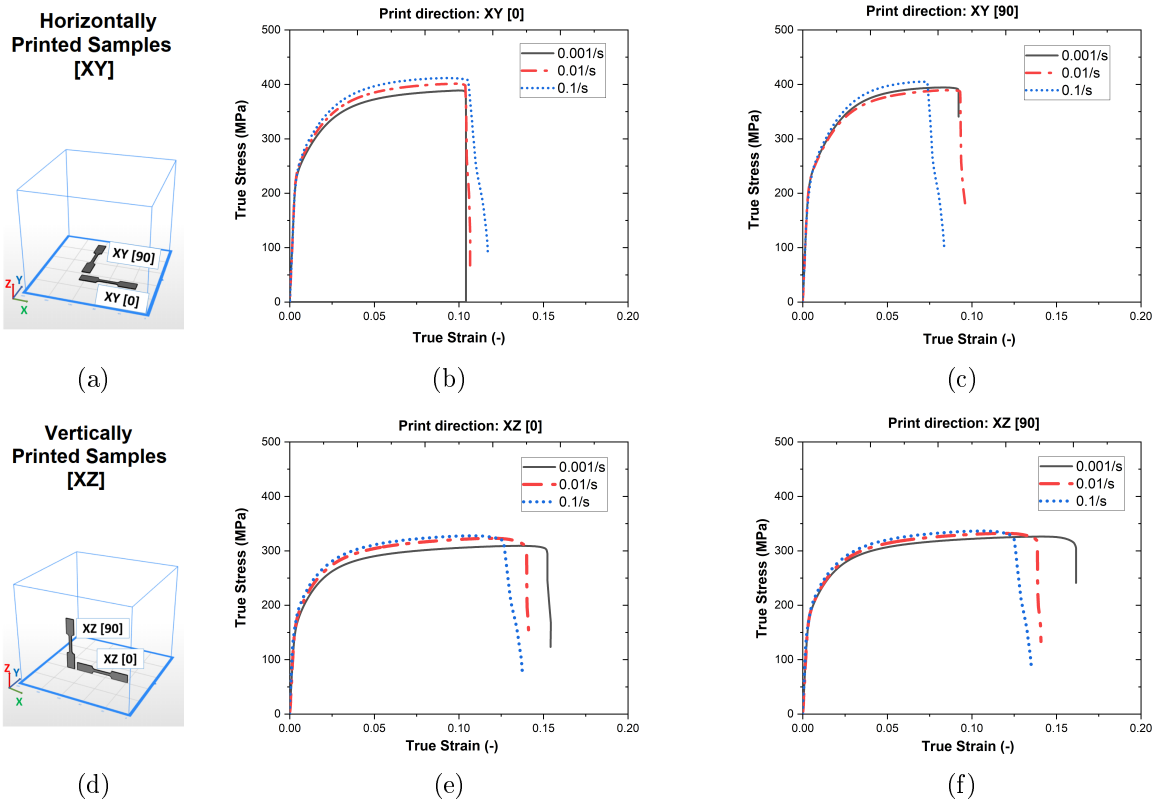

Figure 3.10: *The true stress - true strain results from the tensile tests carried out at room temperature and the strain rates of 0.001/s, 0.01/s and 0.1/s. The heat treated samples were printed (a) horizontally (b, c) at 0° and 90° an angle to the build platform, respectively and (d) vertically (e, f) at 0° and 90° an angle to the build platform, respectively.*

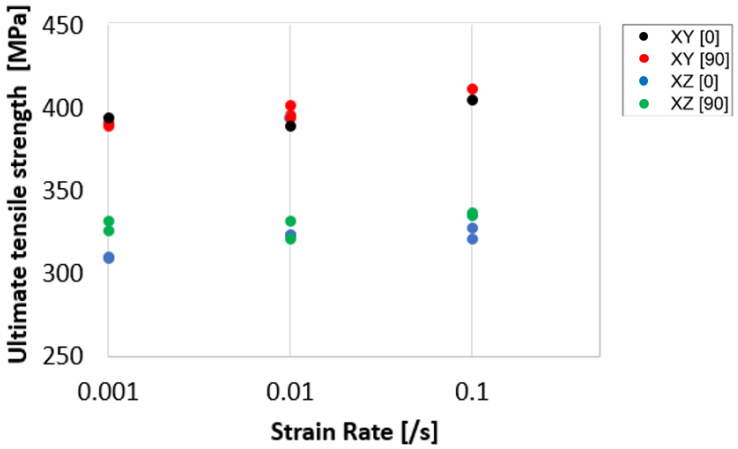

Figure 3.11: *The ultimate tensile strength at the different strain rates for the heat treated samples printed horizontally and vertically*

Although, the strength of the vertically printed samples is lower to 87 MPa lower, the elongation at failure is much higher. The XZ [90°] samples have obtained the highest value of the elongation at failure equaled to 16.04 %. Whereby, the mean value for the XZ samples is 13.5 %

and for the XY samples is about 9.8 %. The obtained results prove that print direction significantly influences on the obtained microstructure, the effects of which are clearly visible in the results (Fig. 3.12). The longer path of the laser beam causes the increase of the tensile strength. As it takes place for the horizontally printed samples (Fig. 3.12). At the same time, the samples undergo the smaller elongations at failure compared to the vertically printed ones. This may be a result of the melt pool dislocation.

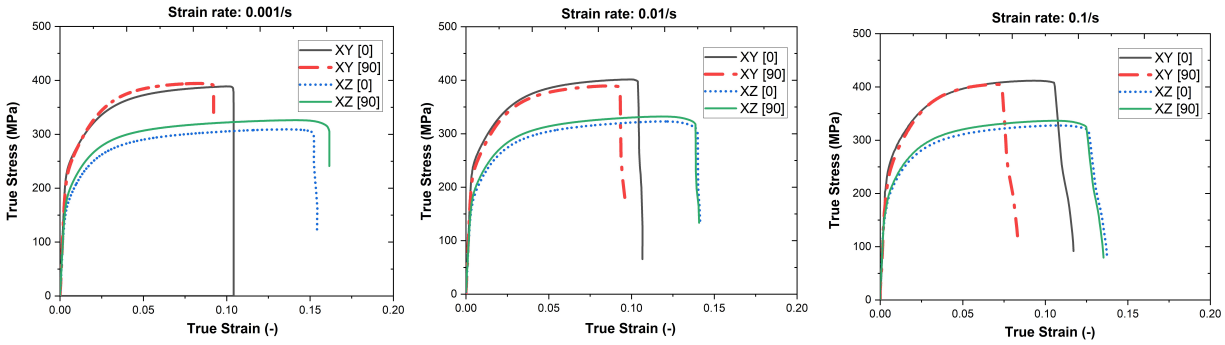

(a) (b) (c)

Figure 3.12: *Influence of the print direction on the true stress - true strain results. The quasi-static tensile tests were performed at different strain rates on the heat treated samples printed horizontally and vertically to the build platform at [0°] and [90°] directions.*

The quasi-static tensile tests - temperature sensitivity

To study the temperature sensitivity, the quasi-static tests have been performed at the strain rate of 0.001 s^{-1}. The comparison of the stress-strain results takes place at the room temperature, 100 °C, 150 °C and 200 °C. The tested XY [0] and XZ [0] samples were subjected to the heat treatment.

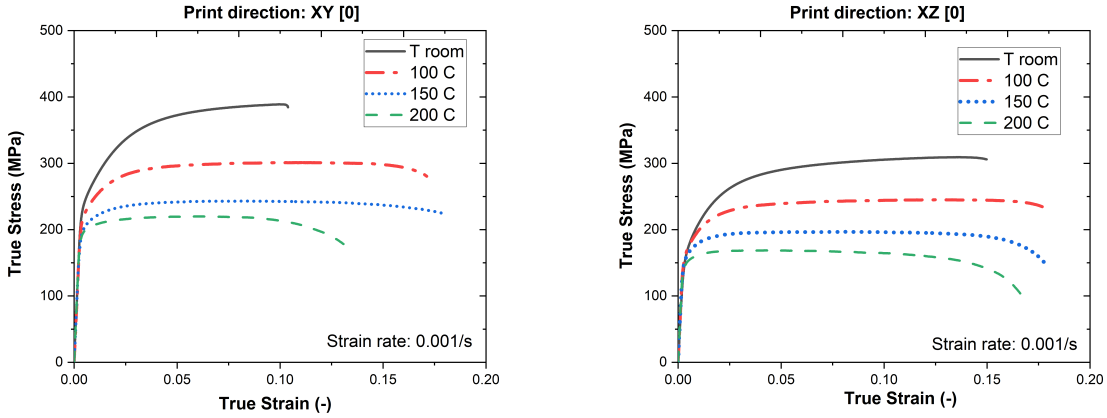

(a) (b)

Figure 3.13: *Temperature sensitivity of the AlSi10Mg aluminium alloy based on (a) horizontally and (b) vertically printed samples printed at [0°] to the build platform. The test performed at 0.001* s^{-1}*)*

Figure 3.13 presents the stress-strain results obtained from the quasi-static tensile tests. When the temperature increases from room conditions to 200 °C, the ultimate tensile strength decreases two time for both case of the samples. The AlSi10Mg aluminum alloy is highly sensitive to temperature changes. It is worth noting that the elongation at break increases when the tests are performed at the temperature higher than the room conditions. At room temperature, the horizontally printed samples failures at 9.8 % of strain. When the temperature rises to 150 °C, the elongation can be equal to 17.5 %. For XZ samples, the increase in elongation ranges from 13.5 % at room temperature to 16 % at 100 °C.

Results of the quasi-static compression tests

The tensile tests proved that the greatest impact on the obtained results was the orientation of the sample to the building platform. Therefore, the compression tests focus on three printing directions. The specimens have been positioned along the Z axis and printed at [0°], [45°], [90°]. Furthermore, the influence of the post-processing has been investigated, based on the heat-treated (HT) and as-fabricated (WHT) samples.

The obtained true stress over true strain curves at the room temperature for different quasi-static strain rates are reported in Fig. 3.14. For each presented case, the influence of the printing direction is observed. The vertically printed samples [90°] are characterized by increased stress and smaller strains to fracture. The [90°] samples and those printed at the angle of 45° to the build platform show a similar behavior during the compression process, which is confirmed by the shape of the resulting true stress - true strain curves. The material softening may be observed after the deformation reached the value of the true strain of 0.15 for the samples without heat treatment and of 0.1 for the samples after the stress-relieving.

The strain rate dependency is more visible using the samples after the heat treatment. However, increasing the strain rate in the quasi-static range does not increase the stress level significantly. Therefore, the studied AlSi10Mg aluminum alloy is considered not strain rate sensitive in the quasi-static range. Comparing the results obtained for samples without heat treatment (Fig. 3.14(1)) and after it (Fig. 3.14(2)) compressed at the same strain rate, it can be observed that the annealing process causes a decrease of the obtained stress values by an average of 100 MPa and a longer deformation process. Moreover, softening in the plastic range is much more noticeable.

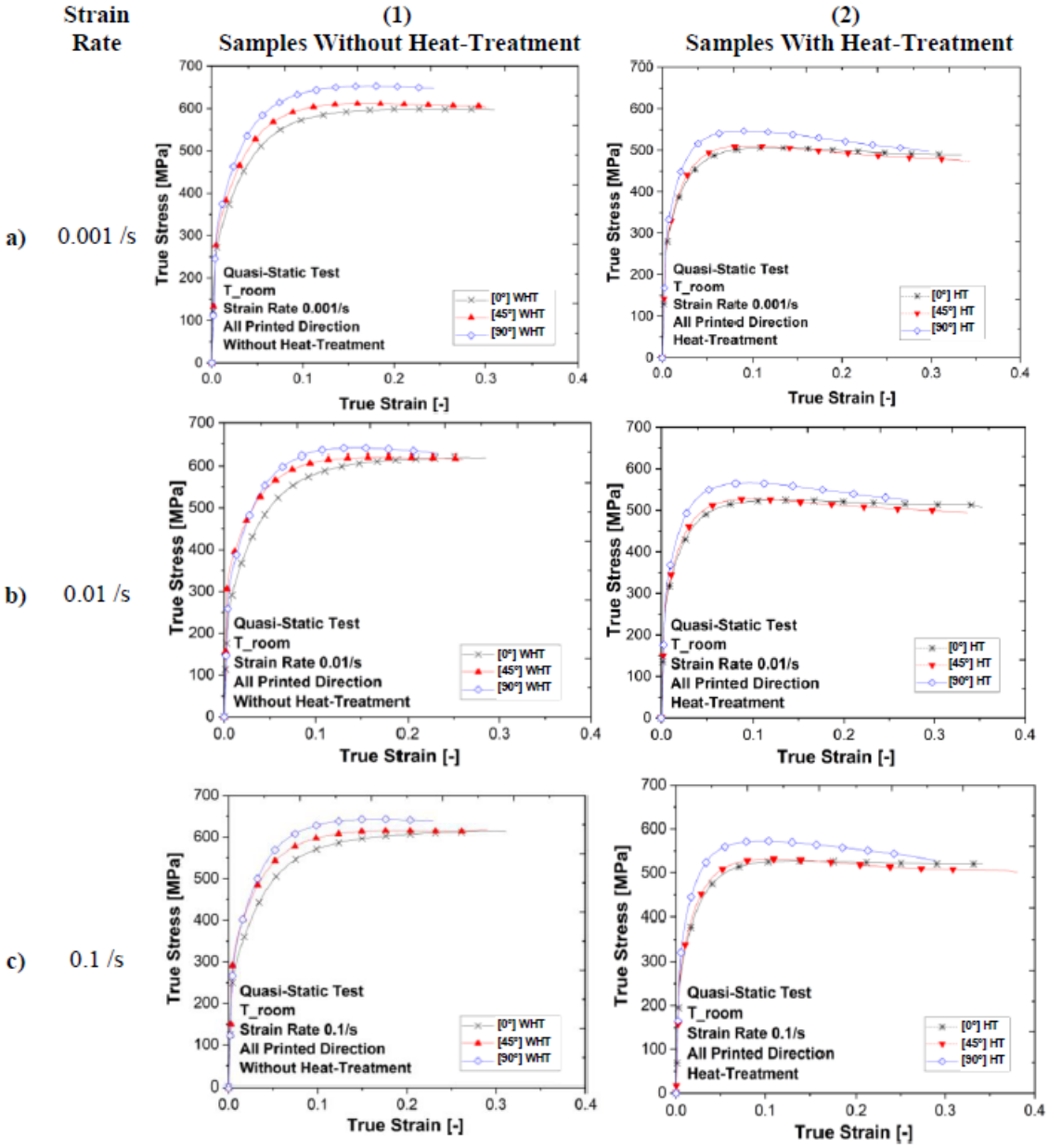

Figure 3.14: *Summary of the quasi - static compression test of the AlSi10Mg aluminium alloy given in the true stress over true strain curves.*

3.5.2 Results of the dynamic compression tests

The dynamic response of the studied material is investigated using a Split Hopkinson Pressure Bar (SHPB) test stand, presented in Fig. 3.15. The projectile impacts a 1.5 m long input bar, which generates an elastic incident wave $\varepsilon_I(t)$. When the incident wave reaches the bar-specimen interface, it is split into a reflected wave $\varepsilon_R(t)$ and a transmitted wave $\varepsilon_T(t)$. The first one goes back through the incident bar, and the second one propagates through the tested sample and then through the output bar. A full-bridge of four strain gauges and a Vishay conditioner are

used to measure the response of the propagated waves. Further analysis is performed using the Waves Analysis and Study Program WASP based on the characteristics of the registered waves.

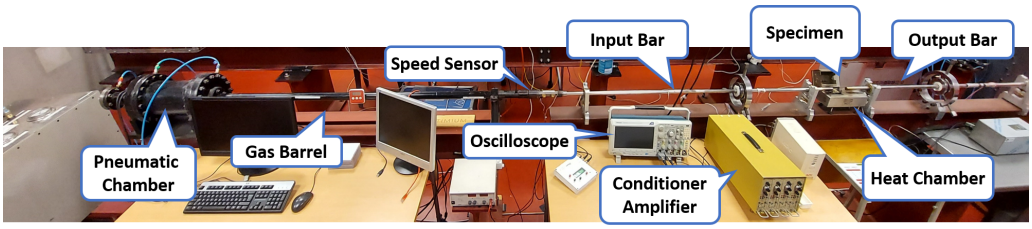

(a)

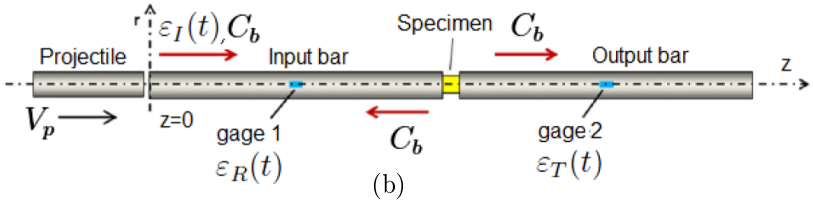

(b)

Figure 3.15: *Split Hopkinson Pressure Bar (a) the used experimental stand at the LEM 3 at the Lorraine University (b) the schematic illustration showing its working principles.*

The physical principles of the SHPB are based on the one-dimensional approach towards the uniaxial plane wave propagation modeling, characterized by Eq. (3.8).

$$\frac{\partial^2 U}{\partial t^2} = C_b^2 \frac{\partial^2 U}{\partial x^2} \tag{3.8}$$

The force equilibrium on the two end faces of the specimen is necessary to validate the performed tests. Based on the Hooke's law, Ravichandran and Subhash proposed the $R(t)$ parameter [28]. $R(t)$ should obtain a value close to zero to achieve the force equilibrium during the test. Eq. 3.8 allows evaluating the difference of the two acting forces ($F_1(t)$ and $F_2(t)$) on the end faces of the specimen $\Delta F(t)$ to the average forces $F_{avg}(t)$. The example of the R parameter evolution, presented in Fig. 3.16, shows that the R parameter is almost equal to zero beyond the beginning of the performed test.

$$R(t) = \left| \frac{\Delta F(t)}{F_{avg}} \right| = 2 \left| \frac{F_1(t) - F_2(t)}{F_1(t) + F_2(t)} \right| \tag{3.9}$$

$$F_1(t) = E_b A_b (\varepsilon_I(t) - \varepsilon_R(t)) \tag{3.10}$$

$$F_2(t) = E_b A_b \varepsilon_T(t) \tag{3.11}$$

Where E_b and A_b are the Young Modulus and a cross-sectional area of the bars.

In addition, the energy balance W_{exp} (3.12) and the quantity of movement Q_{exp} (Eq. (3.13)) must be achieved. The obtained values for the signal of incident waves (Eqs. 3.12-3.13) are compared with the initial energy and momentum values for the projectile (Eqs. 3.14-3.15).

$$W_{exp} = A_0 \rho C_b^3 \int_0^t \varepsilon_I(\xi)^2 d\xi \tag{3.12}$$

$$Q_{exp} = A_0 E \int_0^t \varepsilon_I(\xi) d\xi \tag{3.13}$$

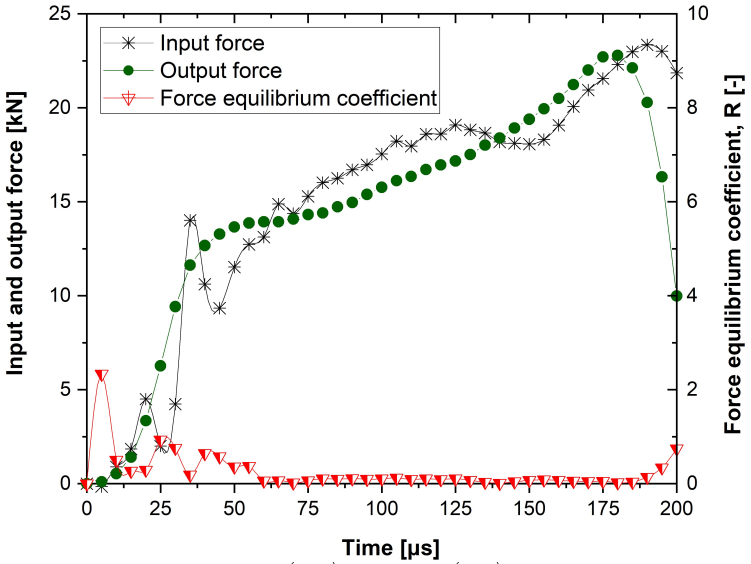

Figure 3.16: *Evolution of the force input (F1), output (F2) and force equilibrium coefficient (R).*

$$W_P = \frac{M_P V_0^2}{2} \tag{3.14}$$

$$Q_P = M_P V_0 \tag{3.15}$$

Where M_P and V_0 are mass and initial velocity of the projectile.

If the force equilibrium, energy balance and quantity of movement are achieved, the nominal stress $\sigma_{nom}(t)$, the nominal strain $\varepsilon_{nom}(t)$ and the nominal strain rate $\dot{\varepsilon}_{nom}(t)$ can be calculated using the registered forces imposed on the samples and the resulted displacements of the bars (Eqs. 3.16-3.18).

$$\sigma_{nom}(t) = \frac{E_b A_b \varepsilon_T(t)}{A_S} \tag{3.16}$$

$$\varepsilon_{nom}(t) = \frac{2C_b}{L_S} \int_0^t \varepsilon_R(t) dt \tag{3.17}$$

$$\dot{\varepsilon}_{nom}(t) = \frac{C_b \varepsilon_R(t)}{L_S} \tag{3.18}$$

Where A_s and L_s are a cross-section and length of specimens. The elastic wave speed C_b in a bar with the Young's modulus E_b and the density ρ_b can be described by Eq. 3.19.

$$C_b = \sqrt{\frac{E_b}{\rho_b}} \tag{3.19}$$

3.5.3 Adiabatic-isothermal correction

The performed tests confirmed that the deformation of the AlSi10Mg aluminium alloy is sensitive to temperature changes. Therefore, the adiabatic heating effect on the strains softening for the large deformation in the dynamic region is included. Knowing the temperature sensitivity ν, the true stress under adiabatic conditions $\sigma_{Adiabatic}$ are corrected to achieve the required isothermal results $\sigma_{Isothermal}$, according to Eq. 3.20 [29–31].

$$\sigma_{Isothermal} = \sigma_{Adiabatic} + |\nu| \, \Delta T \tag{3.20}$$

The temperature increment ΔT during the plastic work concerning the initial temperature T_0 can be estimated based on the following equations:

$$T = T_0 + \Delta T \tag{3.21}$$

$$\Delta T(\varepsilon_p) \approx \frac{\beta}{\rho \cdot C_p} \int \sigma(\varepsilon_p, \dot{\varepsilon}_p, T) d\varepsilon_p \tag{3.22}$$

Where β, ρ, C_p are the Taylor-Quinney coefficient, the density and the specific heat at a constant pressure of the material.

The Taylor-Quinney β coefficient corresponds to the plastic work converted into heat and depends on the strain rate of a deformation process. It is worth noticing that the estimation of this coefficient is a challenge and different methods exist to determine it correctly. In this paper, β is assumed as equal to 0.9, as it is usually used for metals [32–34]. The temperature sensitivity parameter $\nu = \partial\sigma/\partial T$ is determined based on the quasi-static tensile tests at different temperatures for horizontally printed samples. Fig. 3.17a shows the linear curve slopes of the true stress over temperature at 6 %, 8 % and 10 % of deformation. The performed analysis allows determining the average temperature sensitivity parameter equal to $\nu \approx -1.004\,\mathrm{MPa\,K^{-1}}$. Then, the experimental curves of the true stress at the high strain rate ranges are corrected based on Eq. 3.20. The example of the adiabatic-isothermal correction of the equivalent stress-equivalent strain at the different strain rates is shown in Fig. 3.17b.

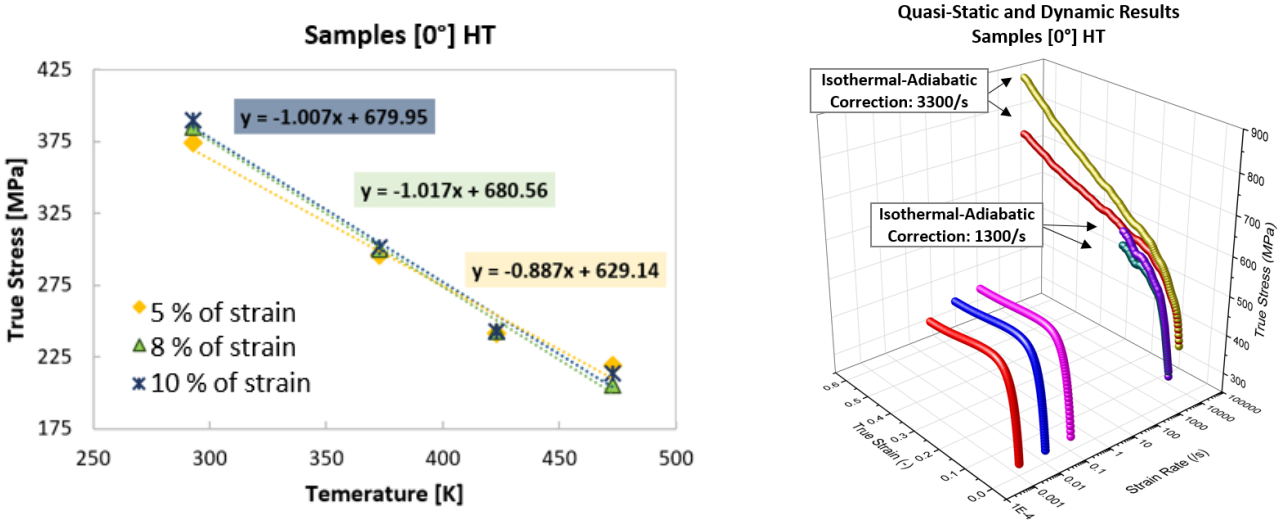

(a) (b)

Figure 3.17: Results for horizontally printed samples [0°] from the AlSi10Mg aluminium alloy: a) temperature sensitivity of the flow stress at the 5 %, 8% and 10% strain. b) Material behaviour at different strain rates under the adiabatic and isothermal conditions.

The final results in terms of material behavior for different strain rates are reported in Fig. 3.18. It can be observed that in dynamic range and quasi-static regime, the AlSi10Mg aluminum alloy exhibits only a slight strain rate dependence. In addition, in the first stage of deformation (up to ≈ 0.15 of strain), the horizontally printed samples [0°] obtain the lowest results in terms of the stress level, then [45°] samples. The vertically printed [90°] specimens are characterized as the highest obtained values. The stress for [45°] samples without heat

treatment are similar to vertical ones and, after heat treatment, closer to horizontally printed samples. The high hardening increase characterizes the [45°] and [90°] samples after crossing the references strain. Moreover, it is observed that after the compression, the cross-sections for [0°] and [45°] samples are more oval than for the vertically printed samples [90°], in which cross-sections remain circular. It is an effect of anisotropy resulting from the specificity of layered manufacturing. In the case of [90°] samples, the load is applied along with the melt pools arrangement and perpendicular to the longitudinal tracks (see Fig. 3.4).

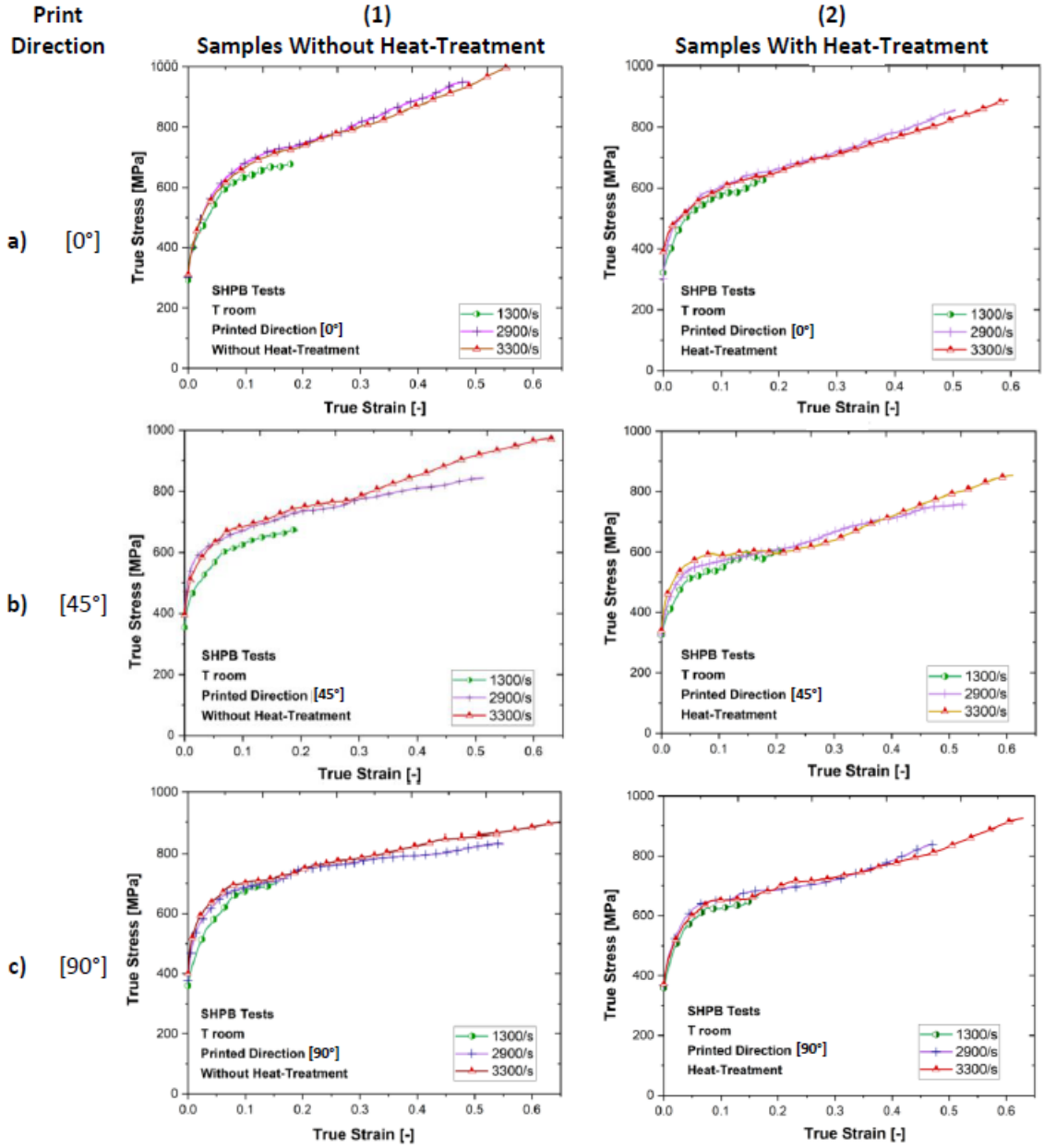

Figure 3.18: *Summary of obtained average results of true stress over true strain of a compression test on an AlSi10Mg aluminium alloy sample at 1300/s – 3300/s strain rates and room temperature.*

3.5.4 Strain-rate sensitivity of the AlSi10Mg manufactured additively

The SHPB dynamic compression tests prove the slights strain rate sensitivity of the AlSi10Mg aluminium alloy. The comparison of the quasi-static and dynamic results presented in the values of the true stress read for the true strain of 0.1 is presented in Fig. 3.19. The strain rate dependence for the tested alloy differs between the quasi-static and dynamic region, which can be seen on the slopes of the true stress-strain rate curves (Tables 3.6-3.7). The AlSI10Mg aluminium becomes more susceptible to the strain rate in the dynamic regimes.

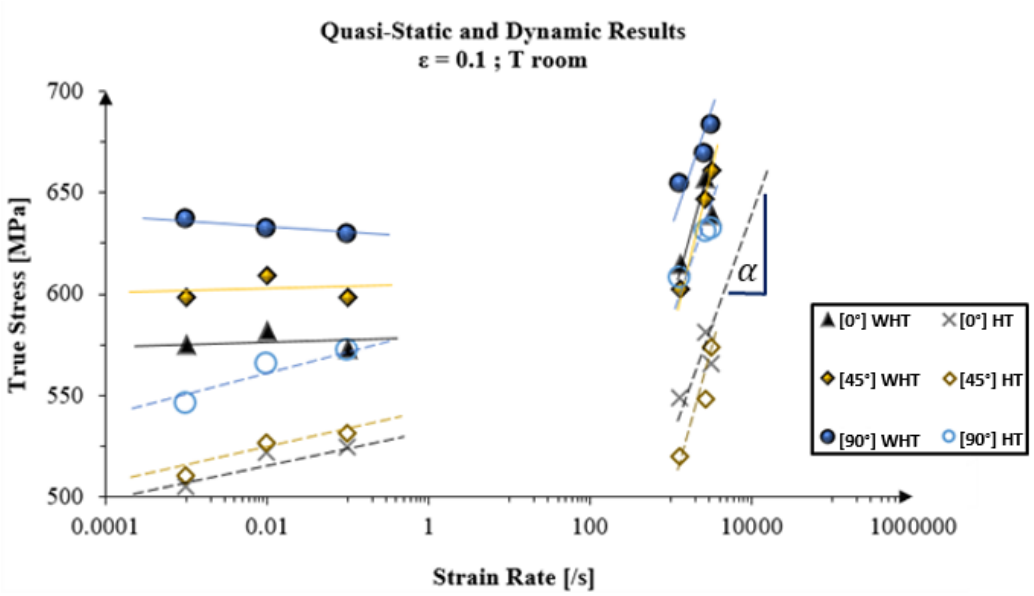

Figure 3.19: *Summary of the true stress values at 0.1 true strain for different printing directions, before heat treatment (WHT) and after stress relieving (HT).*

Table 3.6: *The slope of the true stress-strain rate curves at the quasi-static range.*

Equations of the slope curves in the static region $y = a \cdot log(x) + b$		
Print Direction	**WHT**	**HT**
[0°]	$y = -1.06x + 571$	$y = 9.67 + 534$
[45°]	$y = 0.13x + 599$	$y = 10.18x + 541$
[90°]	$y = -3.67x + 625$	$y = 13.21x + 586$

Table 3.7: *The slope of the true stress-strain rate curves at the dynamic range.*

Equations of the slope curves in the static region $y = a \cdot log(x) + b$		
Print Direction	**WHT**	**HT**
[0°]	$y = -61.7x + 422$	$y = 43.8 + 413$
[45°]	$y = 150.9x + 132$	$y = 137.4x + 92$
[90°]	$y = 73.1x + 427$	$y = 62.3x + 414$

Figures 3.14 and 3.19 show that the print direction and the performed post-processing affects the material behavior. The stress-relieving causes an about 80 MPa decrease of the obtained stress level. The strain rate sensitivity is more distinctly seen for the heat-treated samples in the quasi-static region (Tables 3.6-3.7). It can be related to an arrangement of grains in the microstructure after the annealing process. In the dynamic regime, the heat treatment slightly affects the slope curves of the strain rate sensitivity. The highest susceptibility characterizes the samples printed at the angle of 45° to the build platform to the strain rate.

3.5.5 Temperature sensitivity of the AlSi10Mg manufactured additively

The SHPB dynamic compression tests are performed at 100 °C, 150 °C and 200 °C. The constant temperature level during the test is assured by a mounted heat chamber (Fig. 3.15). The sensor is connected to a controller regulating the temperature in the chamber so that the sample reached the initial temperature [35]. The compression tests are performed with an average strain rate of 2900 s^{-1}.

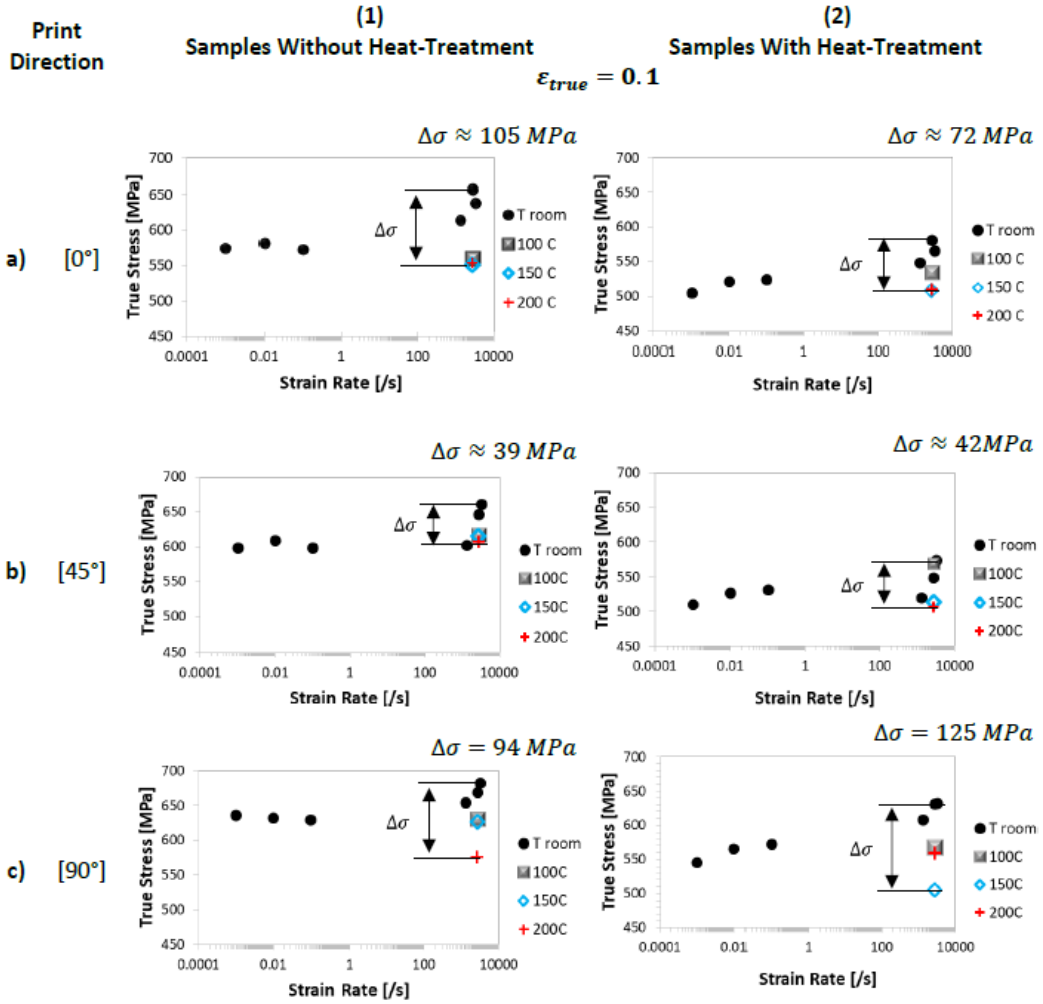

Figure 3.20: *The true stress at the true strain of 0.1 as a function of temperature and the strain rate (a-c) for different printing direction and (1-2) before and after the annealing process.*

Figure 3.21 presents the obtained results after adiabatic−isothermal correction (see paragraph 3.5.3) It is shown that with the temperature increases, the hardening stage takes place at lower stress values. However, the [0°] HT and [45°] HT samples become an exception as the obtained curves of true stress are similar for the highest temperature. This effect may be explained by a too low temperature obtained during the tests at 200 °C. The highest temperature sensitivity is noticed for the horizontally printed samples [0°], whereas the lowest is register for the samples printed at an angle of 45°.

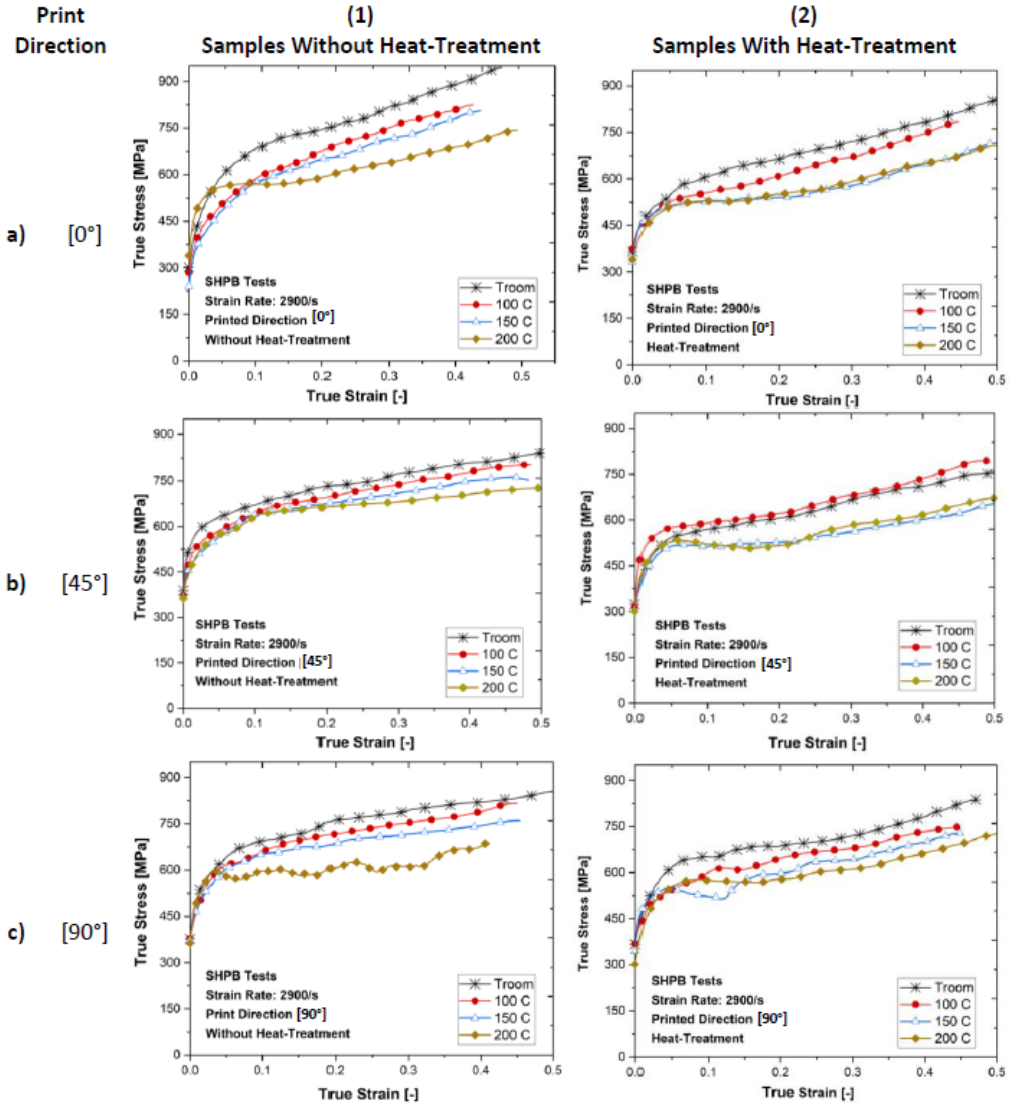

Figure 3.21: *Summary of obtained average results of true stress over true strain of dynamic compression tests at 2900* s^{-1} *strain rate for an AlSi10Mg aluminium alloy from 20* °C*−200* °C.

Separately for each printed direction, the values of true stress at the true strain of 0.1 are collected in Fig. 3.20. The graphs summarize all the results obtained from the compression tests, accounting for both strain rate and temperature influences. It is worth noticing that at dynamic rates, an increase of the temperature to 100 °C causes decreasing in the stress level to those observed at quasi-static tests.

3.6 Material model

The aim of the carried out tests is to describe the behavior of AlSi10Mg aluminum alloy at different strain rates and temperatures. Based on these experimental observations, a proposed constitutive model of the tested material describes the flow stress in the plastic range.

In many branch like aerospace, the yield point determines the moment when a material may be applicable. However, in the last few decades, interest in the plastic region has also become an industrial focus e.g. in automotive. Therefore, many developed models descriptive the parameters affecting the deformation e.g. influence of strain hardening. Due to the derivation from the fundamental laws of physics or mathematical approach; the phenomenological, semi-physical and physical models can be distinguished.

3.6.1 Phenomenological models

Phenomenological models are based on the empirical observations. The flow stress over the strain can be described by the mathematical functions which takes into account the change of the main parameters e.g. strain rate, temperature. Comparing with other models, phenomenological ones are widely use as they are simply and have a limited number of material parameters which are necessary for using this constitutive model. They describe the empirical phenomena based on the fundamental theory, however, they do not directly derive from "first principle".

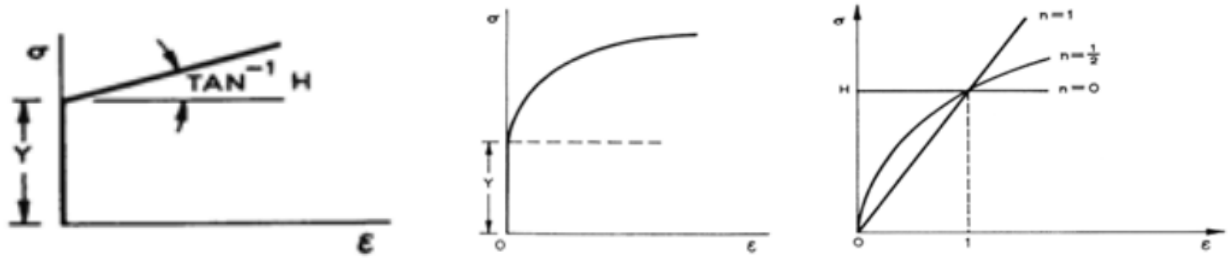

(a) (b) (c)

Figure 3.22: *Basic examples of the hardening models (a) rigid linear work , (b) Ludwig power law, (c) influence of the work hardening power (n) on the model curve shape [36].*

Ludwig Power Law

The hardening constitutive models allow to neglect the elastic part of deformation and describe the plastic range. Figure 3.22a shows one of the most basic example of the rigid linear work models. In this approach, after reaching the yield point, stress varies linearly with plastic strain. This model can be applied to plastic bending analysis of beams [36]. However, when the hardening regime cannot be described by the linear function, the Ludwig Power Law allow to introduce the different work hardening power values. Equations 3.23 - 3.24 and Figure 3.22c show the changes in the curve shape depending on the coefficient n – the transition from the rigid linear work model when $n = 1$ to the Ludwig Power Law model when $0 < n < 1$.

$$\sigma = Y + H\bar{\varepsilon_p} \tag{3.23}$$

$$\sigma = Y + H\bar{\varepsilon_p}^n \tag{3.24}$$

where $\sigma -$ the flow stress, $\varepsilon_p -$ the equivalent plastic strain, $Y -$ yield strength, $H -$ material dependent strength coefficient and $n -$ work hardening power.

Johnson-Cook (JC) model

Among other phenomenological models, the Johnson-Cook (JC) model is often use e.g. in the numerical calculations. The individual expressions in three brackets (Eq.3.25) represent: the strain hardening, strain rate hardening, and thermal softening. It is calibrated separately using experimental data of the stress-strain at different strain rates and temperatures.

$$\sigma = \left[A + B\varepsilon_p^n\right]\left[1 + C\, ln\left(\frac{\dot{\varepsilon}}{\dot{\varepsilon}_0}\right)\right]\left[1 - \left(\frac{T - T_0}{T_f - T_0}\right)^m\right] \tag{3.25}$$

The flow stress σ at the strain rate $\dot{\varepsilon}$ and at temperature T is calculated based on the equivalent plastic strain ε_p and the material constants A, B, n, m. Whereby $\dot{\varepsilon}_0$, T_f and T_0 are the reference strain rate, the melting temperature and the reference temperature, respectively. The reference values often correspond to the lowest strain rate and temperature values at which tests are performed.

JC model is a simple and requires relatively few number of material constants. Therefore, it has been widely applied to various materials for different temperatures and strain rates. However, the drawback of the JC constitutive model is that they only fit in with uncomplicated experimental results (see Fig. 3.23). Therefore, modifications in the original JC model have been incorporated. The developed models allow to predict the deformation material behavior of with different strain rate and temperature sensitivity.

Arrhenius equation

The Arrhenius equation was proposed by Svante Arrhenius and Jacobus Henricus van 't Hoff in 1884. Then, Sellars and Mc Tegart in [37] have used the dependence to develop the material model for describing the mechanical behavior during hot deformation of the metallic materials (Eq. 3.26). Successive modifications of the model and introduction of the Zener-Holomon parameter Z (Eq. 3.28) allow to define the dependence of the temperature T, the strain rate $\dot{\varepsilon}$ and the effective activation energy Q under different process conditions [38].

$$\dot{\varepsilon} = A \cdot F(\sigma) \cdot exp(\frac{-Q}{RT}) \tag{3.26}$$

where:

$$F(\sigma) = [sinh(\alpha\sigma)]^n \tag{3.27}$$

$$Z = \dot{\varepsilon} \cdot exp\left(\frac{QR}{T}\right) \tag{3.28}$$

where A, α , n are the material constants.

The final Arrhenius model can be expressed by the following equation:

$$\sigma = \frac{1}{\alpha} ln \left[\left(\frac{Z}{A} \right)^{\frac{1}{n}} + \left[\left(\frac{Z}{A} \right)^{\frac{2}{n}} + 1 \right]^{\frac{1}{2}} \right] \tag{3.29}$$

3.6.2 Semi-physical models

Semi-physical model description may take into account the type of material, microstructure, stress, temperature etc. They may link the microstructure description, its evolution with the macroscopic properties. In addition, the models can depend on the different chemical compositions, influence of a heat treatments, welding or post weld heat treatment. The semi-physical models can be useful for studying changing creep properties based on the starting microstructure. Although these models can be more advanced than phenomenological ones, they often require more computational time in numerical modeling. In addition, due to the microstructure complexity, some physical phenomena can be omitted during modeling [39].

3.6.3 Physical models

Physical models describe the mechanical phenomena within a material on the basis of actual physics and not just the fit parameters. It allows to insight into the underlying mechanisms behind the fundamental theory. It provides an overview of the deformation mechanisms and material microstructure e.g. dislocation mechanism, the dynamic recrystallization, thermal activation. These models increase the use of modeling as they allow to take into account the extreme conditions. The physical models requires an extensive testing campaign combined with the microstructural observations [40]. So far, Zerilli-Armstrong (Z-A), Bonder-Partom (B-P) or Rusinek-Klepaczko models have been developed.

Zerilli-Armstrong (Z-A) model

Z-A model is characterized by the high accuracy and relatively simple forms. The final flow stress (Eq. 3.30) contains the thermal σ_{th} and athermarmal σ_a components.

$$\sigma = \sigma_a + \sigma_{th} \tag{3.30}$$

Z-A model has been derived to characterize the deformation behavior of the Face Centered Cubic (FCC) and Body Centered Cubic (BCC) metals. This is due to the fact that the FCC alloys prove the thermal activation which is depended from the plastic strain. For the BCC atom organization, the thermal yield stress is strongly dependence from the strain rate and temperature. The activation volume is almost independent of the plastic strain [41].

For the FCC metals like copper or aluminum, the Z-A athermal (Eq. 3.31) and thermal (Eq. 3.32) flow stress can be express:

$$\sigma_a = c_6 \tag{3.31}$$

$$\sigma_{th} = c_2 \varepsilon_p^{1/2} exp \left[-c_3 T + c_4 T ln \left(\frac{\dot{\varepsilon_p}}{\varepsilon_{p0}} \right) \right] \tag{3.32}$$

For the BCC metals e.g. pure iron, tantalum, molybdenum, niobium:

$$\sigma_a = c_5 \varepsilon_p^n + c_6 \tag{3.33}$$

$$\sigma_{th} = c_1 exp\left[-c_3 T + c_4 T ln\left(\frac{\dot{\varepsilon_p}}{\varepsilon_{p0}}\right)\right] \tag{3.34}$$

where c_1, c_2, c_3, c_4, c_5, c_6 and n are material constants. In addition, the deformation behavior of Z-A model depends on the strain hardening ε_p, strain rate hardening $\dot{\varepsilon_p}$ and thermal softening T.

Rusinek-Klepaczko (R-K) model

The R-K model [42] is a result of the development of the works, among others Klepaczko [43–45] or Klepaczko and Chiem [46]. The visco-plastic model has been determined as the mechanical response of the cold-rolled Al-calmed sheet steel. The flow stress is a function of strain $\bar{\varepsilon}^p$, strain rate $\dot{\bar{\varepsilon}}^p$ and temperature T (Eq. 3.35). However, the influence of the history of strain rate and temperature has been neglected.

$$\bar{\sigma} = f(\bar{\varepsilon}^p, \dot{\bar{\varepsilon}}^p, T) \tag{3.35}$$

The R-K model is based on the dislocation theory and consists of internal $\sigma_\mu\left(\bar{\varepsilon}^p, \dot{\bar{\varepsilon}}^p, T\right)$ and effective $\sigma^*\left(\dot{\bar{\varepsilon}}^p, T\right)$ stress components. The multiplication by a parameter $E(T)/E_0$ allows to link the temperature dependence with the Young's modulus – based on physical considerations in [44]. The internal stress is a results of the new immobile dislocations creations which are responsible for the strain hardening. The thermal activation process is introduced by the second component of the effective stress.

$$\bar{\sigma}(\bar{\varepsilon}^p, \dot{\bar{\varepsilon}}^p, T) = \frac{E(T))}{E_0}\left[\sigma_\mu\left(\bar{\varepsilon}^p, \dot{\bar{\varepsilon}}^p, T\right) + \sigma^*\left(\dot{\bar{\varepsilon}}^p, T\right)\right] \tag{3.36}$$

$$\frac{E(T))}{E_0} = 1 - \frac{T}{T_m} exp\left[\theta^*\left(1 - \frac{T_m}{T}\right)\right] \tag{3.37}$$

where E_0 is Young's modulus at 0 K, T_m is melting temperature and θ^* is the characteristic homologous temperature of the tested material.

The internal stress is dependent from stain rate and temperature changes. The presented Equation 3.38 is based on the Swift law.

$$\sigma_\mu\left(\bar{\varepsilon}^p, \dot{\bar{\varepsilon}}^p, T\right) = B\left(\dot{\bar{\varepsilon}}^p, T\right)\left(\varepsilon_0 + \bar{\varepsilon}^p\right)^{n\left(\dot{\bar{\varepsilon}}^p, T\right)} \tag{3.38}$$

where $B\left(\dot{\bar{\varepsilon}}^p, T\right)$ is plasticity modulus:

$$B\left(\dot{\bar{\varepsilon}}^p, T\right) = B_0\left[\left(\frac{T}{T_m}\right) log\left(\dot{\varepsilon_{max}}\right)\right]^{-\upsilon} \tag{3.39}$$

and $n\left(\dot{\bar{\varepsilon}}^p, T\right)$ is strain hardening parameter:

$$n\left(\dot{\bar{\varepsilon}}^p, T\right) = n_0\left\langle 1 - D_2\left(\frac{T}{T_m}\right) log\left(\frac{\dot{\bar{\varepsilon}}^p}{\dot{\varepsilon}_{min}}\right)\right\rangle \tag{3.40}$$

$$n\left(\dot{\bar{\varepsilon}}^p, T\right) = n_0\left\langle x\right\rangle \tag{3.41}$$

$$\begin{cases} \langle x \rangle = 0, & x \leq 0 \\ \langle x \rangle = x, & x > 0 \end{cases} \tag{3.42}$$

where ε_0 is yield point at the quasi-static test, $\dot{\varepsilon}_{max}$ and $\dot{\varepsilon}_{min}$ are the experimentally value of the maximum and minimum strain rate at which the material is tested. B_0 and D_2 are material constants, ν is the temperature sensitivity parameter, n_0 is the strain hardening parameter at 0 K, x is the mathematical operator.

The effective stress $\sigma^*\left(\dot{\bar{\varepsilon}}^p, T\right)$ is similar to the Arrhenius equation in terms of describing a thermally activated process.

$$\sigma^*\left(\dot{\bar{\varepsilon}}^p, T\right) = \sigma_0^* \left\langle 1 - D_1 \left(\frac{T}{T_m}\right) log\left(\frac{\dot{\varepsilon}_{max}}{\dot{\bar{\varepsilon}}^p}\right) \right\rangle^{m^*} \tag{3.43}$$

where σ_0^* is the referenced effective stress at 0 K, D_1 and m^* are the material constants.

Although the R-K model is more complex, it may be more accurate than the simpler phenomenological J-C model for some type of material. The comparison of these models has been performed for the DH-36 steel at the different strain rates (Fig. 3.23).

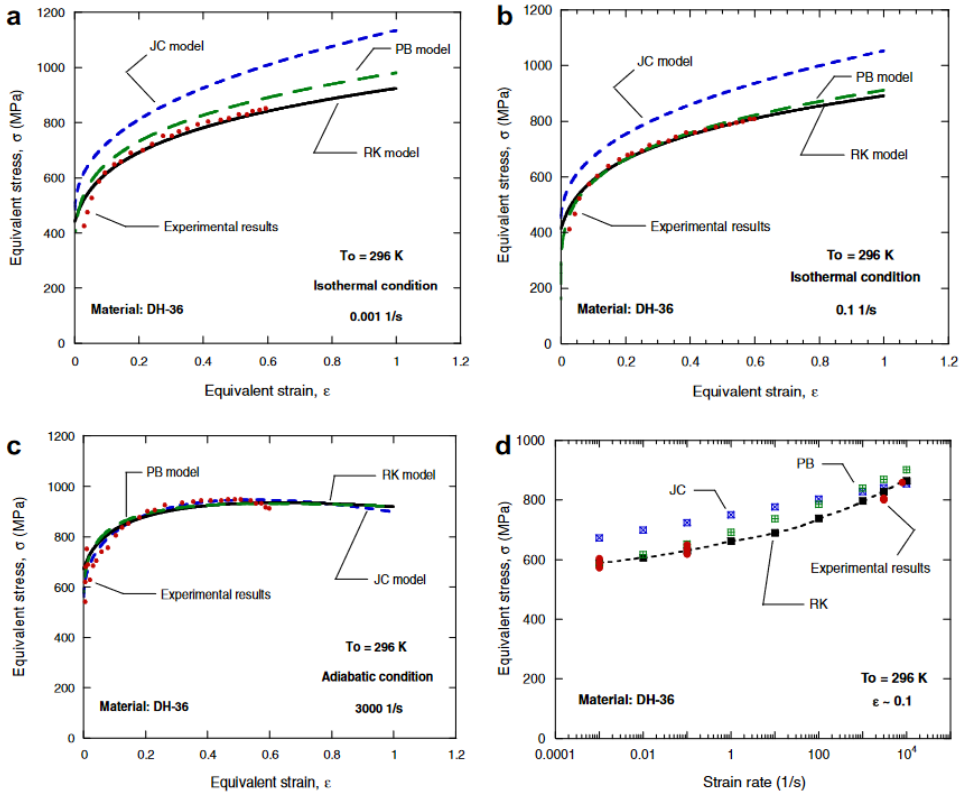

Figure 3.23: *Comparison of Rusinek-Klepaczko (RK model) constitutive relation with Johnson–Cook (JC model) and Physical Base (PB model) constitutive model in relation to the experimental results for DH-36 steel [47].*

3.6.4 Modified Johnson-Cook (MJC) model for the printed AlSi10Mg aluminum alloy

In the first approach, the thermo-visco-plastic behavior of AlSi10Mg alloy for each printed direction are approximated using well known Johnson-Cook (JC) model. The fundamental equation and the description of the constitutive model is presented in Section 3.6.1.

Taking into account that the compression tests were carried out in a wider range in terms of strain rate, thermal conditions and the number of tests performed, the material model is based on the obtained results, presented incl. in Section 3.5.2.

The reference values in Equation 3.25 referring to the lowest strain rate of 0.001 s^{-1} and room temperature The reference static yield stress A is obtained at the strain rate hardening becomes unity. It takes place only when the plastic strain is equal to 0 and at the references values of the strain rate and temperature. Similarly, the C parameter is obtained at the reference temperature, but when the strain rate is different for each test. One of the biggest challenges when getting the C parameter may be the lack of a distinct constitutive dependency. These may be the results of experimental errors, e.g. no the force equilibrium in the SHPB test or the complex characteristics of the tested material. By following the procedure of determining the C parameter, the parameter m relating to the temperature sensitivity is obtained analogously. Considering the above, the material parameters have been obtained for two sets of the sample. It allows to distinguish the samples with and without heat treatment. The results are presented in Tables 3.8−3.9.

Table 3.8: *The material parameters of the Johnson-Cook model for AlSi10Mg aluminium alloy developed for the samples without heat treatment.*

WHT	A [MPa]	B [MPa]	n [-]	C [-]	m [-]	MAPE [%]
[0°]	220	1184	0.437	0.0001	1.26	14.4
[45°]	235	1231	0.424	0.007	1.52	21.06
[90°]	267	1455	0.466	0.0002	1.40	23.17

Table 3.9: *The material parameters of the Johnson-Cook model for AlSi10Mg aluminium alloy developed for the samples after heat treatment (2h at 300°C).*

WHT	A [MPa]	B [MPa]	n [-]	C [-]	m [-]	MAPE [%]
[0°]	189	801	0.304	0.0009	1.33	12.92
[45°]	237	639	0.284	0.00014	1.34	17.56
[90°]	263	824	0.341	0.0018	1.31	10.49

Due to the limitations of the JC model, the constitutive model is often modified to fit the registered material behavior or to minimize material constants, e.g. necessary in the simulation approach [48, 49]. The verified parameters of the JC material modeling. Tables 3.8 - 3.9 allows describing the AlSi10Mg material behavior with the mean absolute percentage error (MAPE) between 10 % - 23 % (Eq. 3.44).

$$MAPE = \frac{1}{N}\sum_{i=0}^{N} \left| \frac{\sigma_{exp} - \sigma_{mod}}{\sigma_{exp}} \right| \cdot 100\% \tag{3.44}$$

where σ_{exp} is the experimental stress values, σ_{mod} is the predicted stress value, and N is the number of the fitted points.

Due to the complexity of the obtained experimental characteristics of the printed alloy, the JC model has allowed determining with good accuracy only at the first stage of the plastic work. However, the tested alloy is characterized by the softening in the second plastic range at the quasi-static condition (Fig. 3.14). To take this phenomenon into account, the JC constitutive model has been modified, and softening parameter P is introduced (Eq. 3.45) to agree with experimental observation (Fig. 3.14).

$$f(\varepsilon_p) = 1 - P\varepsilon_p \tag{3.45}$$

Figure 3.19 shows that the AlSi10Mg alloy is characterized by two ranges of strain rate sensitivity for the quasi-static and dynamic regions. However, the classic JC model does not take into account a nonlinear strain rate sensitivity. Therefore, the nonlinearity of the strain rate influence is extended by the following equation.

$$f_P(\dot{\varepsilon}) = 1 + C_1 ln\left(\frac{\dot{\varepsilon}}{\dot{\varepsilon}_0}\right) + C_2 ln\left(\frac{\dot{\varepsilon}}{\dot{\varepsilon}_0}\right)^k \tag{3.46}$$

As the dynamic process is related to converting the part of the plastic work into heat and cannot be dissipated along with the specimen, the isothermal-adiabatic corrections are introduced (see Section 3.5.4). Therefore, the softening visible in the quasi-static range is not observed for the dynamic results. However, this phenomenon is also not neglected, and the developed model allows to distinguish the material behavior at different strain rates. Eq. 3.47 presents the final constitutive model for the AlSi10Mg aluminum alloy, in which the flow stress is a sum of the two ranges of the equivalent stress: σ_I (up to the reference strain under a visible softening) and σ_{II} (in which the hardening in the dynamic region occurs).

$$\sigma_f = \sigma_I + \sigma_{II}\langle\varepsilon_p - \varepsilon_{ref}\rangle^0 \tag{3.47}$$

Where ε_p is the equivalent plastic strain and ε_{ref} is the reference strain for which the softening does not occur in the dynamic region. The Macaulay notation is defined by using Eq. 3.48.

$$\begin{cases} \langle\bullet\rangle^0 = 0, & \bullet < 0 \\ \langle\bullet\rangle^0 = 1, & \bullet \geq 0 \end{cases} \tag{3.48}$$

Then the first part of Eq. 3.47 can be described as the relations presented by Eqs. 3.49-3.52.

$$\sigma_I = f_I(\varepsilon_p) \cdot f(\dot{\varepsilon}) \cdot f(T) \tag{3.49}$$

$$f_I(\varepsilon_p) = [A + B_1\varepsilon_p^n][1 - P\varepsilon_p\} \tag{3.50}$$

$$f(\dot{\varepsilon}) = 1 + C_1 ln\left(\frac{\dot{\varepsilon}}{\dot{\varepsilon}_0}\right) + C_2 ln\left(\frac{\dot{\varepsilon}}{\dot{\varepsilon}_0}\right)^k \tag{3.51}$$

$$f(T) = 1 - \left(\frac{T - T_0}{T_f - T_0}\right)^m \tag{3.52}$$

Where A, B_1, C_1, C_2, P, n, m, k are material constants, $\dot{\varepsilon}$ – the strain rate, $\dot{\varepsilon_0}$ – the reference strain rate, T_f – the melting temperature and T_0 is the reference temperature.

After exceeding the value of the reference strain, the second part of Eq. 3.47 describes the equivalent flow stress as presented by Eqs. 3.53–3.54. The material constant B_2 determines the

second hardening stage, visible at the dynamic conditions. The function $\tanh(\dot{\varepsilon})$ allows not to consider the effect of the material hardening in the quasi-static region.

$$\sigma_{II}(\varepsilon_p, \dot{\bar{\varepsilon}}) = f_{II}(\varepsilon_p) \cdot f(\dot{\bar{\varepsilon_0}}) \cdot (\varepsilon_p - \varepsilon_{ref}) \cdot \tanh(\dot{\varepsilon}) \tag{3.53}$$

$$f_{II}(\varepsilon_p) = B_2 \cdot \varepsilon_p \tag{3.54}$$

The final equation describing the characteristics of the printed AlSi10Mg aluminum alloy can be present by Eq. 3.55.

$$\sigma_f = f_I(\varepsilon_p) \cdot f(\dot{\bar{\varepsilon}}) \cdot f(T) + f_{II}(\varepsilon_p) \cdot f(\dot{\bar{\varepsilon}}) \cdot \tanh(\dot{\varepsilon}) \cdot \langle \varepsilon_p - \varepsilon_{ref} \rangle \tag{3.55}$$

Table 3.10: *The material parameters of the proposed constitutive model for AlSi10Mg aluminium alloy developed for the samples without heat treatment.*

WHT	A **[MPa]**	B_1 **[MPa]**	B_2 **[MPa]**	**n [-]**	C_1 **[-]**	C_2 **[-]**	**k [-]**	**m [-]**	**P [-]**	**MAPE [%]**
[0°]	220	1184	2109	0.437	0.0001	0.0005	2.164	1.26	1.23	**2.34**
[45°]	235	1231	2505	0.424	0.007	0.0001	2.006	1.52	1.40	**3.20**
[90°]	267	1455	2854	0.466	0.0002	0.0003	2.247	1.40	1.61	**2.67**

Table 3.11: *The material parameters of the proposed constitutive model for AlSi10Mg aluminium alloy developed for the samples after heat treatment (2h at 300°C).*

WHT	A **[MPa]**	B_1 **[MPa]**	B_2 **[MPa]**	**n [-]**	C_1 **[-]**	C_2 **[-]**	**k [-]**	**m [-]**	**P [-]**	**MAPE [%]**
[0°]	189	801	1728	0.304	0.00094	0.00073	1.906	1.33	1.12	**2.94**
[45°]	236	639	1594	0.284	0.00014	0.0067	1.510	1.34	1.04	**2.70**
[90°]	263	824	2209	0.341	0.0017	0.0176	0.898	1.31	1.51	**3.11**

The obtained material constants are seen in Tables 3.10− 3.11. They have been obtained due to comparing the forecast values with the experimental stress values using the root mean square error (RMSE) approach. Figures 3.24a− 3.24b present the curves modelled using the JC model and the curves obtained after the correction due to the proposed model. The modified JC model allows for ten times less error between the model and the experimental data (Table 3.12). To determine the material model parameters that characterized AlSi10Mg alloy, the observation that the aluminum exhibits different mechanical properties dependent on the post−processing must be considered. In addition, the melt pools arrangement influences the obtained stress results. Therefore, the constitutive parameters must be distinguished for each print direction. For a simplification, it is assumed that the reference strain ε_{ref} is equal to 0.15 for the structures without heat treatment and 0.1 for the heat−treated structures.

Table 3.12: *Comparison of the MAPE between the JC Model and the modified JC Model based on the experimental data obtained for [0°] WHT samples.*

Strain Rate	**0.001/s**	**0.01/s**	**0.1/s**	**1300/s**	**2900/s**	**3300/s**
MAPE - JC Model	9.65 %	11.56 %	10.79 %	33. 28 %	17.33 %	10.56 %
MAPE - Modified JC Model	1.62%	2.04%	1.76%	5.46%	1.79%	1.35%

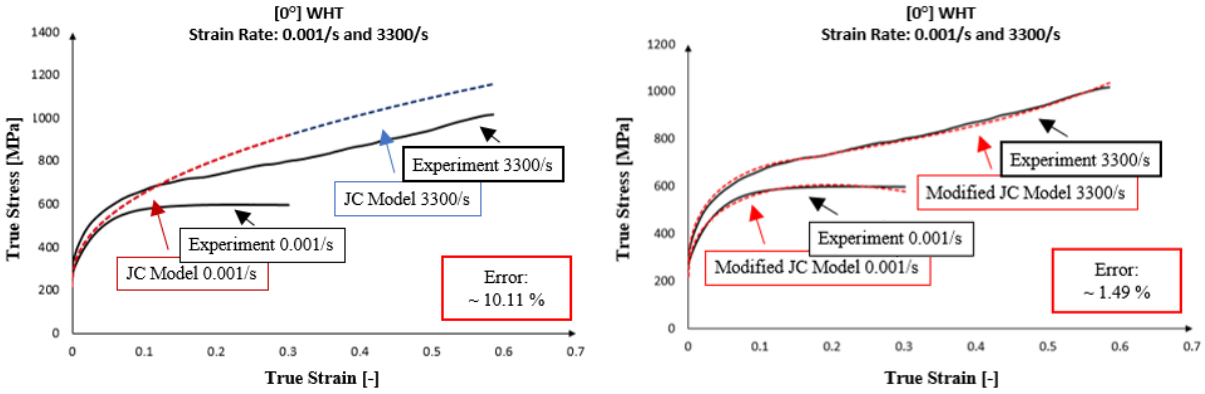

(a) (b)

Figure 3.24: *Comparison of the experimental data for the horizontally printed samples with the curves resulted from a) JC modelling and b) modified JC modelling.*

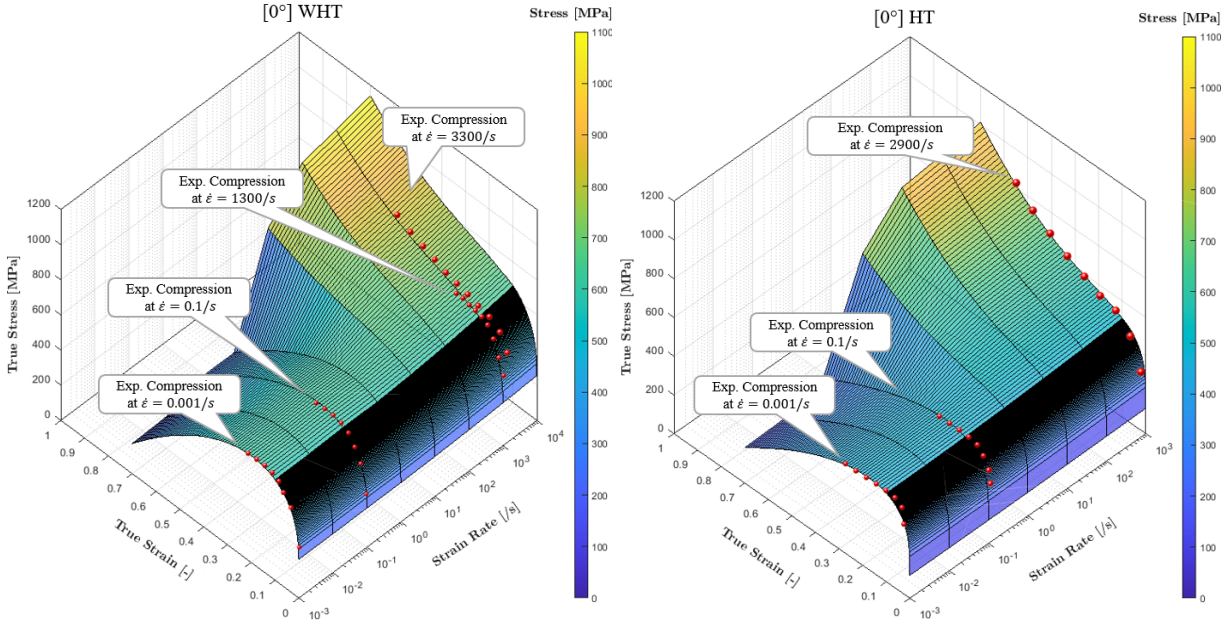

(a) (b)

Figure 3.25: *Effects of strain rate on the equivalent stress over plastic strain at the room temperature based on the modified JC model parameters obtained for the horizontally printed samples a) without the heat treatment and b) with the heat treatment.*

Consequently, the new material model describes the material behavior with an average error of 3 % compared to the experimental data (Tables 3.10−3.11). The mean absolute percentage error is about one order of magnitude lower than that obtained based on the JC modeling. Figure 3.25 presents the development of the equivalent stress surfaces depending on the equivalent strain and strain rates for the horizontally printing direction.

3.7 Chapter summary

The presented chapter analyses the mechanical behavior of the AlSi10Mg aluminium alloy intended for components manufactured additively. The samples printed by the DMLS method are subjected to the tensile and compression tests performed at the quasi-static and dynamic conditions. The material tests are carried out at the strain rate from $0.001/s$ to $3300/s$ and the temperatures up to 200 °C. The experimental investigation evaluates the influence of the printed direction and the applied heat treatment on the material's behavior.

The obtained results prove that the orientation of the sample to the build platform influences the stress-strain results significantly. The obtained stress during compression increases together with the slope of the printed sample to the build platform. The opposite phenomenon is observed for samples subjected to a tension load. Horizontally printed samples obtain the highest stress values. Furthermore, changing the position of the sample in the direction of the Z axis causes an increase of up to 33 % of the obtained stress values, while the change of the orientation in the XY plane influences the results by no more than 4 MPa. It can be noted that after reaching the reference strain during the compression process, the samples exhibit a change in the hardening (from softening in the quasi-static regime to a stronger hardening in the dynamic region).

The used heat treatment is another significant factor affecting the behavior of the printed AlSi10Mg alloy. The analysis of the obtained results from the compression tests on samples with and without heat treatment prove that the annealing process (2h at 300 °C) causes a decrease in stress level (up to 100 MPa). The influence of the heat treatment on the mechanical results can be the effect of the observed changes in the microstructure. The stress relaxation after the post-processing can cause the precipitation of the Si-phase within the Al/Si matrix. Before the annealing, the Al matrix supersaturated by Si particles contributes to a higher strength of the aluminum alloy. The Vickers hardness tests have confirmed the decreased hardness. It was verified that the as-fabricated samples are characterized by 125 HV, whereas the samples's hardness decreased to 110 HV after the annealing process.

The experimental approach to investigations of the behavior of the AlSi10Mg aluminum under compression proves that the material properties differ with the print direction and the chosen post-processing. These phenomena have been taken into account by the proposed modified JC constitutive model. Furthermore, the approach towards modeling considers the distinction between hardening and softening phenomena, two ranges of strain rate and temperature dependence. Consequently, the average error between the experiments and analytically results was minimized to an average error of 3 %. However, much worse modeling results were obtained when the classical JC plasticity model was used, in which MAPE reaches about 15 %.

The performed tests prove the complexity of the behavior of the AlSi10Mg alloy manufactured additively. Based on the compression testing and its modeling, the obtained results complement a gap in the research on this alloy applied to the additive techniques. The presented study analyses the effects observed experimentally, providing a detailed discussion on the material performance, which can be useful for industrial applications and further optimization of the manufactured parts.

Bibliography

[1] N. Read, W. Wang, K. Essa, and M. M. Attallah. Selective laser melting of alsi10mg alloy: Process optimisation and mechanical properties development. *Matereials and Design*, 65:417–424, 2015.

[2] A. Stwora, G. Skrabalak, and J. Maszybrocka. To enhance mechanical properties of parts produced from alsi10mg powder with use of sls/slm methods by densification of the product surface. *Mechanik*, 90:426–431, 2017.

[3] *EOS GmbH-Electro Optical Systems. Material data sheet. EOS Aluminium AlSi10Mg.*, 05.2014. https://fathommfg.com/EOS/Aluminium/AlSi10Mg/en/ [Online; accessed 23.01.2020].

[4] C. Zhang, H. Zhu, H. Liao, Y. Cheng, Z. Hu, and X. Zeng. Effect of heat treatments on fatigue property of selective laser melting alsi10mg. *International Journal of Fatigue*, 116:513–522, 07 2018.

[5] M. Tang and P. Ch. Pistorius. Oxides, porosity and fatigue performance of alsi10mg parts produced by selective laser melting. *International Journal of Fatigue*, 94:192–201, 2017.

[6] Y. Li and D. Gu. Parametric analysis of thermal behavior during selective laser melting additive manufacturing of aluminum alloy powder. *Materials and Design*, 63:856–867, 2014.

[7] Y. Li and D. Gu. Thermal behavior during selective laser melting of commercially pure titanium powder numerical simulation and experimental study. *Additive Manufacturing*, 1:99–109, 2014.

[8] J. Kluczynski, L. Sniezek, K. Grzelak, J. Janiszewski, P. Platek, J. Torzewski, I. Szachogluchowicz, and K. Gocman. Influence of selective laser melting technological parameters on the mechanical properties of additively manufactured elements using 316l austenitic steel. *Materials*, 13:1449, 2020.

[9] U. S. Bertoli, A. J. Wolfer, M. J. Matthews, J.-P. R. Delplanque, and J. M. Schoenung. On the limitations of volumetric energy density as a design parameter for selective laser melting. *Matereials and Design*, 113:331–340, 2017.

[10] Eyitayo Olatunde Olakanmi. Selective laser sintering/melting (sls/slm) of pure al, al-mg, and al-si powders: Effect of processing conditions and powder properties. *Journal of Materials Processing Technology*, 213:1387–1405, 2013.

[11] J.-P. Kruth, S. Dadbakhsh, B. Vrancken, K. Kempen, J. Vleugels, and J. Van Humbeeck. *Additive Manufacturing of Metals via Selective Laser Melting Process Aspects and Material Developments*, pages 69–99. CRC Press by Taylor and Francis Group, 2016.

[12] Vemuru V Krishnamurthy. *Additive Manufacturing of Rare Earth Permanent Magnets*, pages 413–429. CRC Press by Taylor and Francis Group, 2016.

[13] E. Segebade, M. Gerstenmeyer, S. Dietrich, F. Zanger, and V. Schulze. Influence of anisotropy of additively manufactured alsi10mg parts on chip formation during orthogonal cutting. *Procedia CIRP*, 82:113–118, 2019.

[14] T. Maconachie, M. Leary, J. Zhang, A. Medvedev, A. Sarker, D. Ruan, G. Lu, O. Faruque, and M. Brandt. Effect of build orientation on the quasi static and dynamic response of slm alsi10mg. *Materials Science and Engineering A*, 788:139445, 2020.

[15] L. Hitzler, Ch. Janousch, J. Schanz, M. Merkel, B. Heine, F. Mack, W. Hall, and A. Ochsner. Direction and location dependency of selective laser melted alsi10mg specimens. *Journal of Materials Processing Technology*, 243:48–61, 2020.

[16] D. Murphy, O. Fashanu, M. Spratt, J. Newkirk, K. Chandrashekhara, H. Misak, and D. Klenosky. Compressive and bending performance of selectively laser melted alsi10mg structures solid freeform fabrication. In *Proc. of the 30th Annual International Solid Freeform Fabrication Symposium An Additive Manufacturing Conference*, pages 2177–2187, 2019.

[17] M. Kristoffersen, M. Costas, T. Koenis, V. Brotan, Ch. O. Paulsen, and T. Borvik. On the ballistic perforation resistance of additive manufactured alsi10mg aluminium plates. *International Journal of Impact Engineering*, 137:103476, 2020.

[18] L. Delcuse, S. Bahi, U. Gunputh, A. Rusinek, P. Wood, and M. H. Miguelez. Effect of powder bed fusion laser melting process parameters, build orientation and strut thickness on porosity, accuracy and tensile properties of an auxetic structure in in718 alloy. *Additive Manufacturing*, 36:101339, 2020.

[19] K. Zygula, B. Nosek, H. Pasiowiec, and N. Szysiak. Mechanical properties and microstructure of alsi10mg alloy obtained by casting and slm technique. *World Scientific News*, 104:462–472, 2018.

[20] N. Takata, H. Kodaira, K. Sekizawa, A. Suzuki, and M. Kobashi. Change in microstructure of selectively laser melted alsi10mg alloy with heat treatments. *Materials Science and Engineering A*, 704:218–228, 2017.

[21] M. Rafieazad, M. Mohammadi, A. Gerlich, and A. Nasiri. *Impacts of Friction Stir Processing on Microstructure and Corrosion Properties of DMLS-AlSi10Mg*, pages 239–248. Springer International Publishing, 02 2020.

[22] M. Robinson, Q. Han, H. Gu, S. Soe, and R. Setchi. The effect of heat treatment of alsi10mg on the energy absorption performance of surface-based structures. pages 395–402, 2021.

[23] F. Trevisan, F. Calignano, M. Lorusso, J. Pakkanen, A. Aversa, E. P. Ambrosio, M. Lombardi, P. Fino, and D. Manfredi. On the selective laser melting (slm) of the alsi10mg alloy: Process, microstructure, and mechanical properties. *Materials*, 10(1), 2017.

[24] Y. Zhou, F. Ning, P. Zhang, and A. Sharma. Geometrical, microstructural, and mechanical properties of curved-surface AlSi10Mg parts fabricated by powder bed fusion additive manufacturing. *Materials and Design*, 198:109360, 2021.

[25] Buehler:. https://www.buehler.com/wilson-vh1102-1202-micro-hardness-tester.php, March 2021.

[26] T. Fras, A. Rusinek, R.B. Pecherski, R. Bernier, and T. Jankowiak. Analysis of friction influence on material deformation under biaxial compression state. *Tribology International*, 80:14–24, 2014.

[27] T. Fras. *Modelling of plastic yield surface of materials accounting for initial anisotropy and strength differential effect on the basis of experiments and numerical simulation.* PhD thesis, Universite de Lorraine and Akademia Gorniczo-Hutnicza im. Stanislawa Staszica w Krakowie, 2013.

[28] G. Subhash and G. Ravichandran. *Mechanical Testing and Evaluation*, chapter Split-Hopkinson pressure bar testing of ceramics, page 497–504. eighth ed. ASM International, 2000.

[29] M. Nasraoui, P. Forquin, L. Siad, and A. Rusinek. Influence of strain rate, temperature and adiabatic heating on the mechanical behaviour of poly-methyl-methacrylate: Experimental and modelling analyses. *Materials and Design*, 37:500–509, 05 2012.

[30] A. Rusinek, R. Bernier, R. M. Boumbimba, M. Klosak, T. Jankowiak, and G. Z. Voyiadjis. New devices to capture the temperature effect under dynamic compression and impact perforation of polymers, application to PMMA. *Polymer Testing*, 65:1–9, 2018.

[31] A. Rusinek and J. R. Klepaczko. Shear testing of a sheet steel at wide range of strain rates and a constitutive relation with strain-rate and temperature dependence of the flow stress. *International Journal of Plasticity*, 17(1):87–115, 2001.

[32] A. Rusinek and J. R. Klepaczko. Experiments on heat generated during plastic deformation and stored energy for TRIP steels. *Materials and Design*, 30(1):35–48, 2009.

[33] Y. Coget, Y. Demarty, and A. Rusinek. Characterization of the mechanical behavior of a lead alloy, from quasi-static to dynamic loading for a wide range of temperatures. *Materials*, 13(10), 2020.

[34] D. Rittel, L. H. Zhang, and S. Osovski. The dependence of the Taylor-Quinney coefficient on the dynamic loading mode. *Journal of the Mechanics and Physics of Solids*, 107:96–114, 2017.

[35] A. Bendarma, T. Jankowiak, A. Rusinek, T. Lodygowski, B. Jia, M. H. Migurlez, and M. Klosak. Dynamic behavior of aluminum alloy Aw 5005 undergoing interfacial friction and specimen configuration in split hopkinson pressure bar system at high strain rates and temperatures. *Materials*, 13(20), 2020.

[36] A. C. S. Reddy, B. C. Reddy, and D. V. Paleswar. Review on different hardening models for computation of deep drawing process simulation. pages 2333–2338, 01 2020.

[37] C. M. Sellars and W. J. McTegart. On the mechanism of hot deformation. *Acta Metallurgica*, 14:1136–1138, 1966.

[38] A. Mosleh, A. Mikhaylovskaya, A. Kotov, and V. Portnoy. Arrhenius-type constitutive equation model of superplastic deformation behaviour of different titanium based alloys. *Defect and Diffusion Forum*, 385:45–52, 07 2018.

[39] B. Krenmayr and B. Sonderegger. Physical modeling of dislocation creep in high temperature steels. In *4th International ECCC Creep & Fracture Conference*, 2017.

[40] N. Kotkunde, H. N. Krishnamurthy, P. Puranik, A. K. Gupta, and S. K. Singh. Microstructure study and constitutive modeling of ti–6al–4v alloy at elevated temperatures. *Materials and Design (1980-2015)*, 54:96–103, 2014.

[41] F. Abed and G. Voyiadjis. A consistent modified zerilli-armstrong flow stress model for bcc and fcc metals for elevated temperatures. *Acta Mechanica*, 175:1–18, 03 2005.

[42] A. Rusinek and J. R. Klepaczko. Shear testing of sheet steel at wide range of strain rates and a constitutive relation with strain-rate and temperature dependence of the flow stress. *International Journal of Plasticity*, 17:87–115, 01 2001.

[43] J. R. Klepaczko. An experimental technique for shear testing at high and very high strain rates. the case of a mild steel. *International Journal of Impact Engineering*, 15:25–39, 1994.

[44] J. R. Klepaczko. Thermally activated flow and strain rate history effects for some polycristalline fcc metals. *Materials Science and Engineering: A*, 18:121–135, 1975.

[45] J. R. Klepaczko. A practical stress-strain-strain rate-temperature constitutive relations of the power form. *Journal of Mechanical Working Technology*, 15:143–164, 1987.

[46] J. R. Klepaczko and G. C. Y. Chiem. On rate sensitivity of fcc metals, instantaneous rate sensitivity and rate sensitivity of strain hardening. *Journal of the Mechanics and Physics of Solids*, 34:29–54, 1986.

[47] J. R. Klepaczko, A. Rusinek, J. A. Rodriguez-Martinez, R. B. Pecherski, and A. Arias. Modelling of thermo-viscoplastic behaviour of dh-36 and weldox 460-e structural steels at wide ranges of strain rates and temperatures, comparison of constitutive relations for impact problems. *Mechanics of Materials*, 41(5):599–621, 2009.

[48] S. Dey, T. Borvik, O. Hopperstad, and M. Langseth. On the influence of fracture criterion in projectile impact of steel plates. *Computational Materials Science*, 38:176–191, 11 2006.

[49] M. Stanczak, T. Fras, L. Blanc, P. Pawlowski, and A. Rusinek. Blast-induced compression of a thin-walled aluminum honeycomb structure—experiment and modeling. *Metals*, 9(12), 2019.

Chapter 4

Experimental investigation

The main aim of this Chapter is to investigate the energy absorption efficiency of the metallic structure, which is characterized by the different geometry of a unit cell. The task starts with familiarizing the absorption capabilities of the currently used protection systems against blast waves. Based on the thin-walled aluminum honeycomb structures, the fundamental knowledge of the deformation mechanisms and experimental phenomena are defined.

The conducted research has allowed for further studies of the absorption efficiency of the structures obtained by the DMLS method. Four representative types of the printed structures are tested during quasi-static and blast compression. The experimental campaign is performed on the hexagonal honeycomb, auxetic, rhomboidal lattice, and regular foam structures. The performed tests allow comparing the influence of the sample dimensions, the relative density, or the cells' arrangement on the absorption properties. In addition, the damage process of the AM structures is analyzed, which allows correlating the measured results with the recorded structure response.

4.1 Description of used technique

The blast experimental campaign is conducted using the Explosive Driven Shock Tube (EDST) test stand, built at the French-German Research Institute of Saint-Louis (ISL) (Fig. 3.1). The EDST ensures the propagation of a planar wave after the explosion of a small amount (15−50 g) of the C-4 charge, placed 50 mm in front of the shock tube. The tube has an internal square cross-section of A_0 = 80 x 80 mm^2 and a length of 1750 mm, as presented schematically in Figure 3.1a.

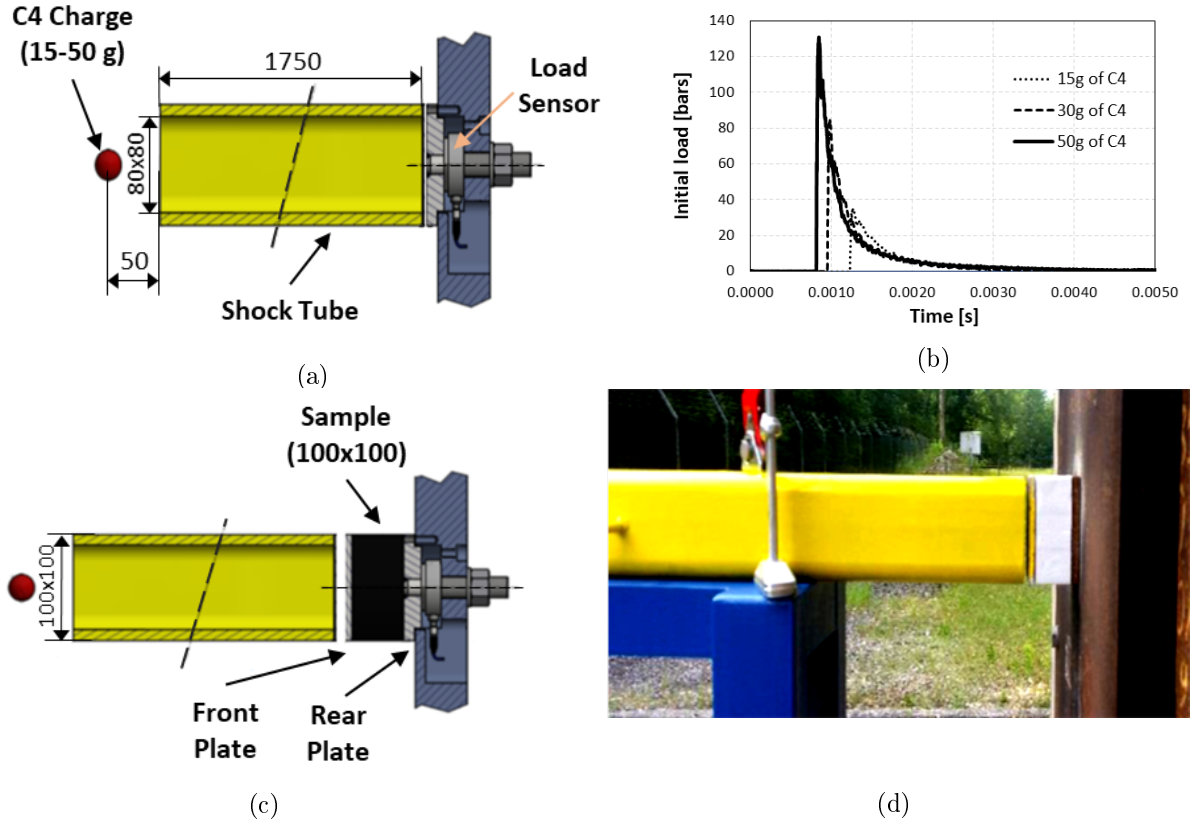

Figure 4.1: *Explosive-driven shock tube: (a) scheme of the experimental configuration used to measure a blast wave pressure without application of an energy-absorbing structure (dimensions in [mm]), (b) measured blast wave pressures p(t) generated by detonation of several C-4 charges, (c) scheme of a test with an energy-absorptive structure (dimensions in [mm]), and (d) a photo from the blast test at the ISL's training ground.*

The C-4 charge is an explosive material based on a nitramide RDX, which is considered more energetic than Trinitrotoluene (TNT) [1]. C-4 is stable and insensitive to most physical shakes. Moreover, it cannot be detonated by a gunshot or by dropping it onto a hard surface, which reduces the risk of accidental detonation. When detonated, C-4 decomposes rapidly to release nitrogen, water, carbon oxides, and other gases with high temperature and pressure. Then, the shock wave propagates inside the tube of the EDST set-up. Due to the length of the tube and internal reflections, the spherical shock wave forms a planar front. As a result, the planar wave may evenly load the plate behind the tube compared to a curved shock wave.

The load applied to the tested sample is directly related to the gas pressure at the end of the tube. Figure 3.1b presents the time evolution of the pressure generated by the detonation of charges with three different masses. The pressure profiles are measured directly using a Kulite HKS-375 pressure transducer in the configuration, in which the shock tube is placed directly in contact with the backplate. Presented in Fig. 3.1b results of the loads may deviate less than 7 %. The main origins of the discrepancies are the molding of the C-4 sphere and the influence of a detonator when put inside a small charge.

The sample is mounted using an adhesive between two steel plates during the blast test, as presented in Fig. 3.1c − 3.1d. The blast wave interacts directly with the front plate; hence the sample is not directly affected by the blast wave. The plate is accelerated by the blast wave and its movement converts the blast energy into the kinetic energy. As a result, the plate compresses the tested sample. During the deformation process, the load transmitted to the rear plate is measured by a force transducer PCB 206C mounted between the rear steel plate and the rigid, concrete wall of the bunker (Figs. 3.1a − 3.1c). The PCB 206C is a quartz force ring sensor with a sensitivity of 13.5 mV/kN and a frequency range of 0.3 mHz − 40 kHz. Both plates are made with the medium carbon, low alloy 4340 steel (36CrNiMo4/1.6511), also known as the S235 steel. The thickness of the front plate can be changed in order to adjust the strain rate and the energy transmitted to the tested material. The compression process is recorded using a Phantom V311 high-speed camera positioned at 0.5 m from the sample and equipped with f85/1.4 lens, providing exposure time lower than 8 µs, which guarantees a sufficient luminosity during the recording. Furthermore, the frame rate of 31 kfps with the total recording time of 2 s ensures an adequate time discretization to measure the displacement of the front plate by means of image analysis.

Assuming there are no fluid-structure interaction effects, the front plate velocity can be estimated using Eq. 3.1. It is based on the momentum conservation law and dependent on the plate mass M_{plate} and the load impulse I_r. The impulse is obtained during the experiment without a sample (as shown in Fig. 3.1a).

$$v = \frac{I_r \cdot A_{tube}}{M_{plate}} \tag{4.1}$$

where: A_{tube} is the shock tube internal cross-section. The reflected impulse I_r is estimated based on the the measured gas pressure over time $p_{trans}(t)$ (see Fig. 3.1b), expressed by Eq. 3.2.

$$I_r = \int_0^{t_{trans}} p_{trans}(t)dt \tag{4.2}$$

The value of impulse transmitted by the blast wave to a front plate can be more accurately estimated by using Taylor‘s acoustic analysis of fluid structure interaction [2]. The advantage of this approach is that it can also include the nonlinear regime [3]. The Taylor‘s acoustic analysis describes the reduction of the transmitted impulse due to the plate movement induced by the blast, but in the water environment. In addition, this effect is more dominant for lighter structures [4], which are accelerated faster. The solution of this problem is characterized by a non-dimensional coefficient being the ratio of time scales of the incident blast wave duration and the characteristic time of the fluid-structure interaction. In the analyzed case, for the front plate not backed by the sample, this coefficient is about of 0.01. This value represents the heavy plate regime, and the solution corresponds to the case of the reflection of a linear wave on a rigid boundary [3].

The measurements of the force and displacement over time are used to calculate the equivalent stress and strain for the tested structures, according to Eqs. 3.3 – 3.4. They are the key parameters for the comparison of different structures. Based on the curve obtained from the stress-strain correlation, the characteristics of the structure response to the blast may be determined as described in Chapter 1. The values of the peak and plateau stress or densification strain are crucial for further analysis [5].

$$\sigma_{eq}(t) = \frac{F_{trans}(t)}{A_{ref}} = \frac{p_{trans}(t) \cdot A_{tube}}{A_{ref}} \tag{4.3}$$

$$\varepsilon_{eq}(t) = \frac{x(t)}{L_0} \tag{4.4}$$

where: F_{trans}(t) – total force transmitted to the backplate, A_{ref} – reference cross-section area of the sample, $x(t)$ – displacement of the front plate, L_0 – the initial height of the sample.

The reference cross-section A_{ref} can be chosen either as the exact area covered by cells or as an area of a rectangle circumscribed on it. The A_{ref} should not be confused with the exact cross-section area of the structure walls which is in direct contact with plates [6, 7].

In reality, event lower velocity of the front plate is recorded due to the reaction of the structure core reacting against the induced displacement. The actual velocity of the front plate, needed to compute the strain rate, cannot be determined before the test if the material parameters and architecture influence are unknown. Because of the character of the experimental technique, the strain rate may only be estimated. It is assumed that it may vary between 500 s^{-1} – 1000 s^{-1} for the studied detonations. The strain rate is also not constant, except during the plastic phase of the sample. Considering the test in which 50 g C-4 is exploded and no absorptive structure is inserted to the configuration, the velocity of the plate is calculated as 38 m/s, according to Eq. 3.1. If a 50 mm high absorber is used, the initial strain rate would be 760 s^{-1}. On this basis, the obtained energy to mitigate equally to 473 J is determined. The presented case is discussed in detail in the following Sections.

4.1.1 Results of the conventionally used, thin-wall metallic honeycomb structures under blast compression loading

The fundamental phenomena occurring during the blast compression test has been explored based on the well-known structure in the blast protective system of the thin-walled 3000 series aluminum honeycomb, presented in Fig. 3.2. Furthermore, the impact of the main factors such as the mass amount of the used explosive charge, geometric dependence, and reference to the quasi-static responses is analyzed.

The tested honeycombs are manufactured by bonding together thin, corrosion-resistant sheets of aluminum foil, which are then expanded to form a cellular hexagonal configuration. According to the producer, the structures have the generalized cell size described by a diameter of 12 mm and the thickness of a single wall of 70 µm, which results in a density close to 40 kg m^3 [8]. The structures subjected to the tests have a height of 50 mm and consist of 7, 19, and approximately 53 cells. However, the structures are slightly differ from sample to sample and also contain single "orphan" walls at their edges resulting from partitioning of the full cells while cutting. Therefore, in order to obtain consistency in comparison of results, to determine values of the experimental stresses, the A_{ref} is taken based on averaged measurements of real samples (36 x 42 mm^2, 50 x 50 mm^2, 100 x 100 mm^2 for 7-, 19- and 53-cells, respectively).

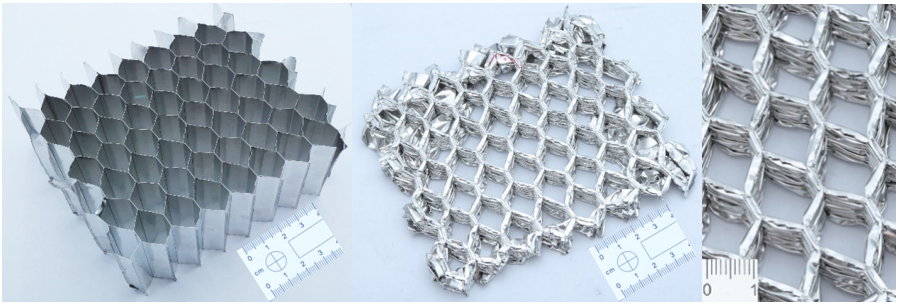

(a) (b) (c)

Figure 4.2: *The tested 53-cell honeycomb structure under blast wave by the EDST (a) non-deformed specimen and (b,c) fully compressed.*

Figure 3.3 presents the frames from the performed blast test using the EDST test facilities. The shown subsequent phases depict the example of the deformation, when the 50 mm high honeycomb is placed between two 100 x 100 mm^2 steel plates. The front surface of the sample is in contact with the 8 mm thick plate with a mass of 655 g, whereas its rear surface contacts the 11 mm thick plate under which the load sensor is located. After detonation of 50 g of the C-4 charge, the visible shock wave in Fig. 3.3, causes the movement of the front plate. In the presented example, the progressive folds formation begins from the rear plate side (Fig. 3.3b). After 30 % of strain the folds are created from the front plate side (Fig. 3.3c), followed by folding on both sides until densification (Fig. 3.3d– 3.3e). The mechanism of fold creating is considered random and is characterized by a number of schematics. The comparison of the sample before and after dynamic compression is shown in Figure 3.2.

The plate displacement and the force transmitted through the structure are registered by the load sensor and the image analysis. Finally, the obtained experimental results are presented in Figure 3.4. The force over time is compared with the initial load from the experiment without the absorbing structure (Fig. 3.4a). It is clearly visible that the use of the absorber significantly reduces the first peak of the transmitted force (see Fig. 3.4a). The force decreases more than four times (from 80 kN to about 20 kN) in the case of the discussed 53-cells structure. In addition, Figure 3.4 compares of the results obtained from the detonation of 15 g, 30 g, and 50 g of the C-4 charge. The lower amount of explosive charge has resulted in a decrease in the response of the tested absorber (Fig. 3.4b). However, it is observed that a bigger structure can transmit a greater amount of load, despite the detonation of a smaller amount of the used explosive charge.

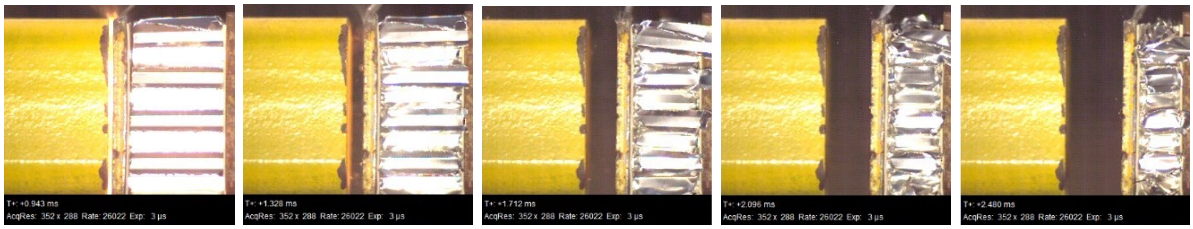

(a) t = 0.81 ms ; x = 50 mm (b) t = 1.38 ms ; x = 43 mm (c) t = 1.71 ms ; x = 35 mm (d) t = 1.89 ms ; x = 29 mm (e) t = 2.39 ms ; x = 22 mm

Figure 4.3: *Subsequent frames depicting the compression of the structure on the example of a honeycomb core during the EDST blast test.*

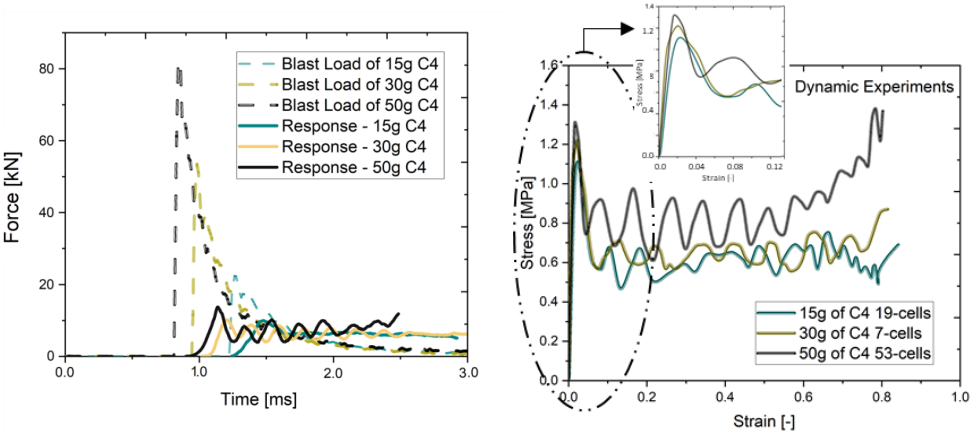

(a) (b)

Figure 4.4: *(a) Comparison between the blast load profiles and the structural responses, (b) stress-strain curves for the various honeycomb structure size compressed due to the detonation of 15* g*, 30* g*, and 50* g *of the C-4 explosive charge used in the EDST blast tests.*

4.1.2 Quasi-static compression tests of the thin-walled honeycomb structures

The compression tests in quasi-static conditions are performed to complete the overview of the behavior of the tested structures under the axial loading. The compression process of the thin-wall metallic honeycomb structures with a height of 50 mm, composed of 7- and 53-cells are analyzed. The tests are performed by means of hydraulic universal testing machine Instron 5982 equipped with 100 kN load (Fig. 3.6). The loading velocity is adjusted to the height of the structure resulting in a constant strain rate of 0.01/s. The compression experiments are registered by a camera and stopped after the onset of densification.

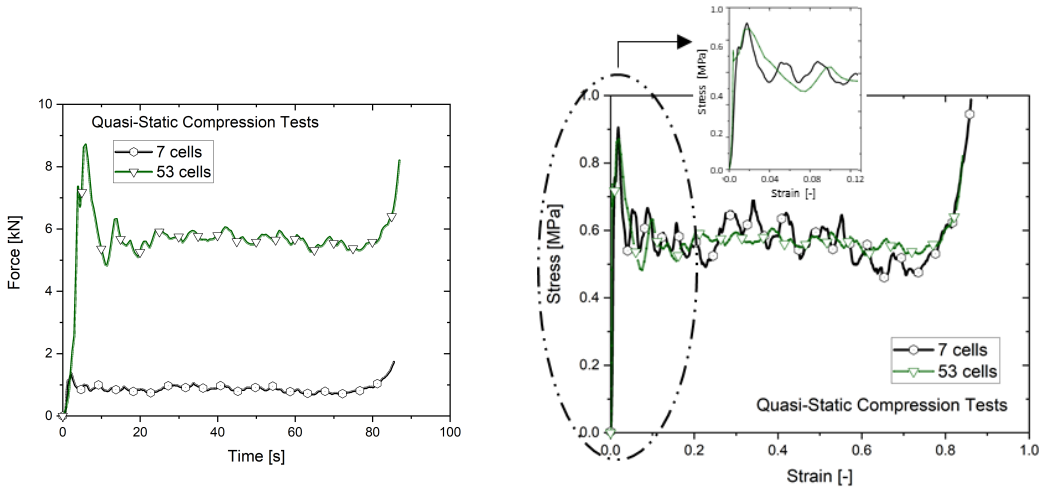

(a) (b)

Figure 4.5: *Quasi-static compression of 53-cells and 7-cells honeycombs: (a) force over time, and (b) stress over strain.*

Figure 3.5 shows the measured force-time curves and the resulting engineering stress-strain dependencies. It is observed that despite the difference in the registered forces, two structures with different numbers of cells are characterized by similar values of the peak stresses (about 0.9 MPa) and the mean stresses (about 0.56 MPa), Fig. 3.5b. Therefore, the number of cells at the quasi-static conditions plays a secondary role, as the scaling effect can be noted for the tested honeycomb structure. The representative number of unit cells can be used to minimize the studied structures. The issue is described in detail in the following Chapter 5.

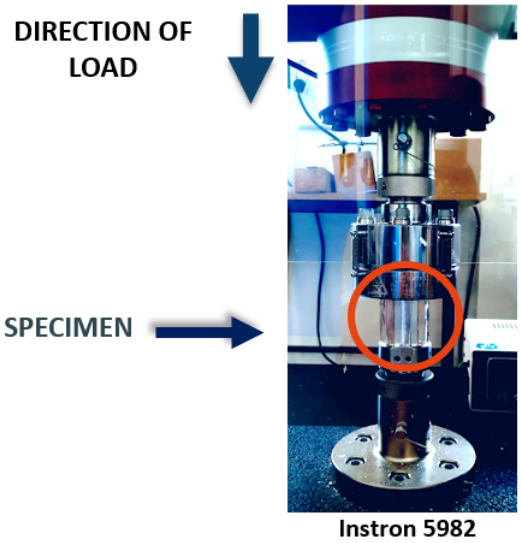

Figure 4.6: *Quasi-static compression test performed on the 7-cells, thin-walled metallic honeycomb structure by means of hydraulic universal testing machine Instron 5982 equipped with a maximum load of 100* kN.

4.1.3 Comparison of the results between quasi-static and blast compression of the honeycomb structures

The characteristics of forces and stresses resulted from the discussed above quasi-static and blast tests are collected in Table 3.1. This summary allows observing changes in the structure responses depending on their sizes and the acting loads. The comparison between the stress-strain curves resulted from the blast-induced compression and the quasi-static one is given in Fig. 3.7. The stress-strain curves are calculated according to Eqs. 3.3 and 3.4. The structure responses resemble the idealized compression curve given in Chapter 1. The characteristic phases of peak, plateau and densification are noticeable, however not as distinctly as in the idealized case in Figure 1.12 (see Chapter 1).

Table 4.1: *Experimental summary of the results of thin-walled metal honeycomb structures subjected to quasi-static and explosive loading.*

Structure	**7 Cells**				**19 Cells**				**53 Cells**			
Loading	F_{max} [kN]	F_{mean} [kN]	σ_{peak} [MPa]	σ_{mean} [MPa]	F_{max} [kN]	F_{mean} [kN]	σ_{peak} [MPa]	σ_{mean} [MPa]	F_{max} [kN]	F_{mean} [kN]	σ_{peak} [MPa]	σ_{mean} [MPa]
Quasi-Static	1.37	0.85	0.91	0.56	-	-	-	-	8.85	5.63	0.88	0.56
15 g of C-4	1.66	0.96	1.10	0.64	2.74	1.55	1.10	0.62	10.0	6.19	1.00	0.62
30 g of C-4	1.83	0.99	1.21	0.66	2.48	1.64	0.99	0.66	10.2	6.26	1.02	0.63
50 g of C-4	-	-	-	-	-	-	-	-	13.6	8.18	1.36	0.82

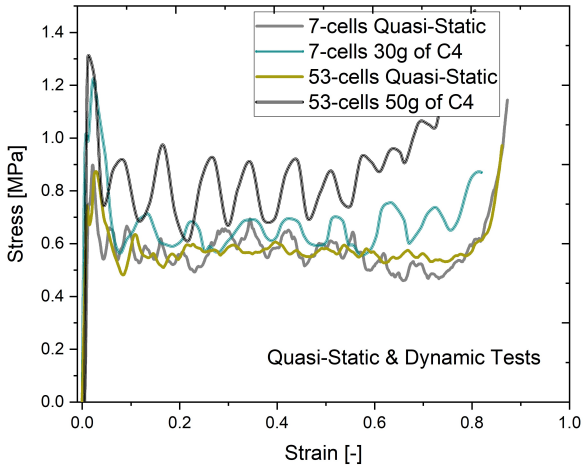

Figure 4.7: *Comparison of the stress-strain curves resulted from quasi-static and blast-induced compression.*

Based on the obtained results, it may be noted that the peak stresses calculated in the dynamic compression are higher than those obtained in the quasi-static tests. For example, the 7-cells structures reached the peak stress of 0.91 MPa in the quasi-static test. It increases to 1.1 MPa in the compression imposed by the detonation of 15 g C-4. Then, the response increases to 1.21 MPa when a higher mass of 30 g of C-4 explodes. This effect can be attributed to strain rate hardening of the aluminum alloy and/or to dynamic compression of the air trapped inside cells of the structure. The peak and mean stresses for the curves describing the responses of the honeycombs with 7- and 53-cells remain on a similar level. Fluctuations, visible in the curve presenting the behavior of the dynamically compressed honeycombs (Fig. 3.7), are much more distinct than those occurring in the quasi-static compression. These superiors oscillations are added to the oscillations originating from the folding of the structures.

The analysis of the traditionally manufactured structures from thin aluminum sheets under blast loading shows the fundamental knowledge about the experiment. Therefore, the studies provide background for further investigations of structures manufactured using advanced techniques.

4.2 Additively manufactured structures

As the AM process offers an opportunity to create new structures quickly and at a comparatively low cost, compared with conventional types of production, the AM has received a large amount of press in recent studies. Therefore, the advanced technology can play a significant role in enhancing innovative solutions in military applications and provides a new way of increasing the energy absorption capacity of structures. The key reason for investigations on regular cellular structures is the relationship between structure topology and its mechanical response in terms of energy mitigation.

Well-known structure in industrial applications is the geometry of the honeycomb, analyzed in the previous Section 3.1.1. As is described in Chapter 1, the honeycomb structures are characterized by a high strength-to-weight ratio. In addition, the well-known traditional honeycombs can be manufactured in a relatively simple method [6, 9, 10]. However, the properties of in-of-plane and out-of-plane, such as stiffness or strength, are significantly different. The cell walls in the plane indicate a bend-dominated mode during an axial load application, compared to the extension or compression of walls in the out-of-plane load direction.

On the other hand, the auxetic structures can be applied to enhance the shear and indentation resistance, or ensure the high fracture toughness (according to [11]). They are characterized by a negative Poisson's ratio and a deformation mode of dome-shape double-curved surfaces, which can increase absorptive properties [12, 13]. These structures are applied where it is necessary to convert compressive planer stress into a compressive longitudinal stress [14]. The two types mentioned above of cellular structures consist of the unit cells that can be characterized in two dimensions, here called "2D structures", and a unit cell is called "2D unit cell". Instead, the lattice and foam structures represent a class of cellular structures composed of unit cells that need to be characterized in three dimensions. In the thesis, this group is called "3D structures", and a unit cell is called "3D unit cell".

Compared to the auxcetics and honeycombs of the same dimensions, the "3D structures" can be characterized by a significantly lower relative density while maintaining high mechanical strength. Moreover, their response to loading is not limited to one direction as in the structures with 2D unit cells. Therefore, it ensures greater freedom of application. It is worth noting that an innovative or more complex structure may require a more complicated production process [15]. Therefore, AM methods are the optimal production techniques to manufacture the samples necessary for laboratory studies.

The experimental investigation of different energy absorption mechanisms is based on four different types of cellular structures. Figure 3.8 shows the tested structures of: hexagonal honeycomb (Fig. 3.8a), 2D re-entrant hexagons honeycomb – auxetic (Fig. 3.8b), cross-cube rhomboidal lattice (Fig. 3.8c), and dodecahefron regular foam (Fig. 3.8d), respectively. One of the experimental campaigns was carried out on the basis of the presented cubic samples which are characterized by a similar relative density. They are consisted of 5 unit in each direction and an edge is equal to 30 mm.

Additionally, structures with higher relative densities of about 0.3 are tested. In this case, the honeycomb and auxetic samples are characterized by the dimensions of 17 x 18 x 20 mm^3, and consist of 6 x 7 and 5 x 9 unit cells, respectively. The thickness of the walls is equal to 0.5 mm. The obtained results of the performed tests are discussed below sections.

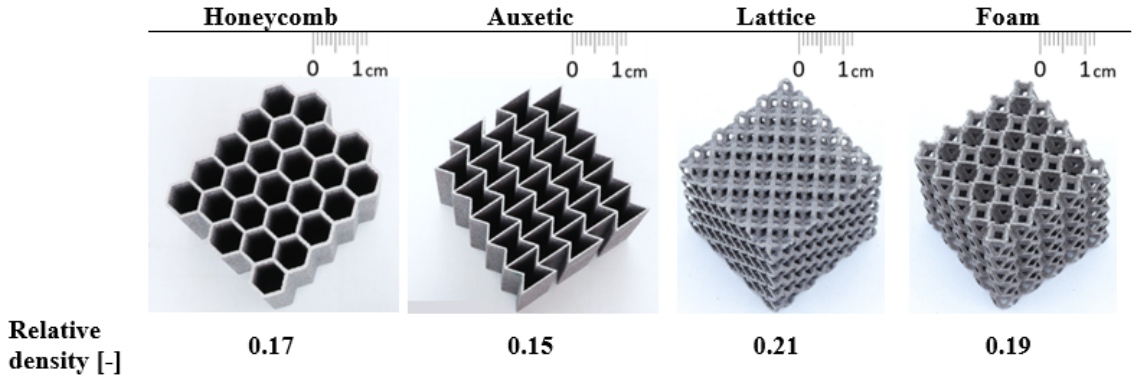

Figure 4.8: *Photographs of the additively manufactured structures from AlSi10Mg aluminum powder used in the quasi-static and dynamic tests in related to relative density.*

Based on the described in Section 3.1 technique, the quasi-static and blast tests on the AM structures have been performed. The compression of the experimental results allow the evaluation of the leading mechanical properties and mechanisms of deformation for each one type of the AM structure.

4.2.1 Results of the quasi-static compression tests of the AM structures

First, the quasi-static tests are carried out similarly as is done for conventionally used, thin-wall metallic honeycomb structures (Section 3.1.2). The analysis of the obtained results has been possible due to the data collected in Table 3.2. The developed curves are shown in Figure 3.9a. They are also characterized by the three main phases described in Section 1.3. The first one is a linear elastic deformation that ends a distinct peak, characteristic of the response of a metallic cellular structure during the compression process. The progressive deformation of the structures is visible in the plateau regime, in which the mean value may approximate the transmitted loading. This phase is related to the material yielding and damage mechanisms such as bending, stretching, and collapsing. The tested structures are characterized by the significant force oscillating, Fig. 3.9a. It results from the breaking of the bonds and the ductile-brittle character of the failure mode. When further plastic deformation is no longer possible, the structures are deformed totally and follow the densification stage, causing a sudden sharp increase in the curves.

Figures 3.9a and 3.9b prove a considerable influence of a structured topology on the obtained stress-strain results. The lattice and foam structures are characterized by the above six times increase of the average force (Fig. 3.9a). In addition, the structures characterized with 3D unit cells exhibit much higher energy absorption properties than 2D structures. The absorbed energy values are equal to about 180 J in the case of the lattice and foam structures, compared to 37 J for the honeycomb and 21 J for the auxetic structures. However, the honeycomb structure is characterized by the longest time of the compression process, which results in the greatest densification stroke efficiency up to 15% compared to the other structures (Fig. 3.9a).

The obtained results from experiments and the dimensions of each sample allow calculating the values of the maximum, mean stress, and densification strain, based on Equations 3.3 and 3.4. The quantitative values in Table 3.2 confirm the results in Figure 3.9a that the lattice and foam structures are characterized by the about 5.7 increase of the mean stress compared to the other two. It is worth noting that the auxetic structure exhibits almost equal stress level during

the entire compression process. Therefore, the first stress peak has a slightly lower value than the mean value.

Table 4.2: *Mechanical properties of the tested structures under quasi-static compression loading.*

	Honeycomb	**Auxetic**	**Lattice**	**Foam**
Peak Stress [MPa]	4.29	1.06	19.57	15.21
Mean Stress [MPa]	1.51	1.12	8.28	7.97
Densification Strain [-]	0.82	0.68	0.78	0.76

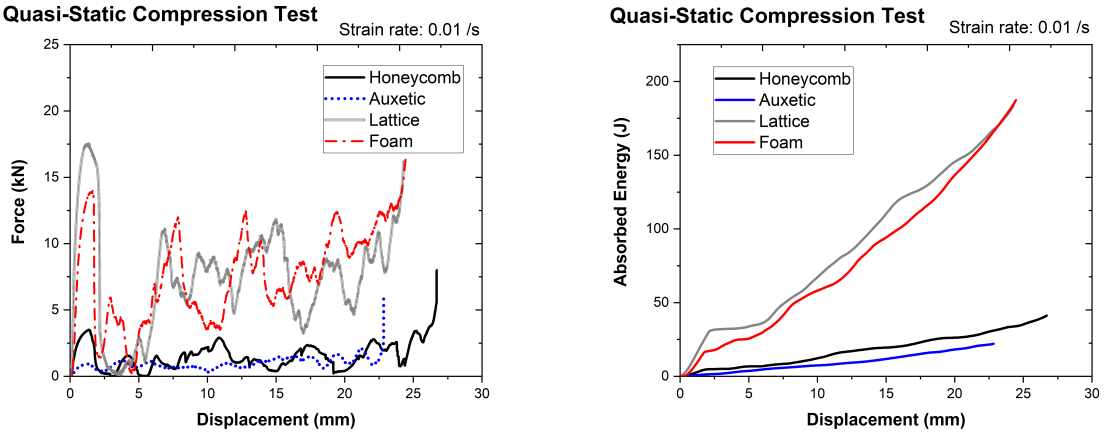

(a) (b)

Figure 4.9: *Results from the quasi-static experiments of uniaxial compression additively manufacturing structures (a) axial force versus displacement, (b) absorbed energy versus displacement.*

The main compression phases of the studied structures were recorded during tests and presented in Figure 3.10. The process registration allows correlating the visual results with the force-displacement curves. It can be observed that the first characteristic peak is related to a significant elasto-plastic deformation of the whole structure (Fig. 3.10a −Fig. 3.10b), followed by the breaking of cell bonds (Fig. 3.10c −Fig. 3.10f). The collapse mechanism occurs after 5% of deformation from the top in case of the honeycomb, auxetic, and lattice structures (Fig. 3.10-I c −Fig. 3.10-III c), and from the bottom for the foam (Fig. 3.10-IV c). It can be an effect of the influence of structured topology and the arrangement of cells. The visible plateau regime, which occurred after the first force peak, is registered about 10 % of the deformation on the force-displacement curves (Fig. 3.9a). However, in the case of honeycomb, it is related to the local shearing mods (Fig. 3.10-I c-f). The auxetic is characterized by the collapse within itself, typically for the metamaterials with the negative Poisson's ratio (Fig. 3.10-II b-c). In the next stage, the structure exhibits the global buckling (Fig. 3.10-II d-f), which corresponds to the almost equal force level during the whole process (Fig. 3.9a). The progressive collapse of the lattice and foam cells is correlated with the achievement of the highest quantitative results (Fig. 3.9a). Despite the fact that the lattice deformation is characterized by the stresses concentration causing a local shearing, visible after 30 % of the deformation (Fig. 3.10-III d). The local deformations may result from possible defects in the manufacturing process.

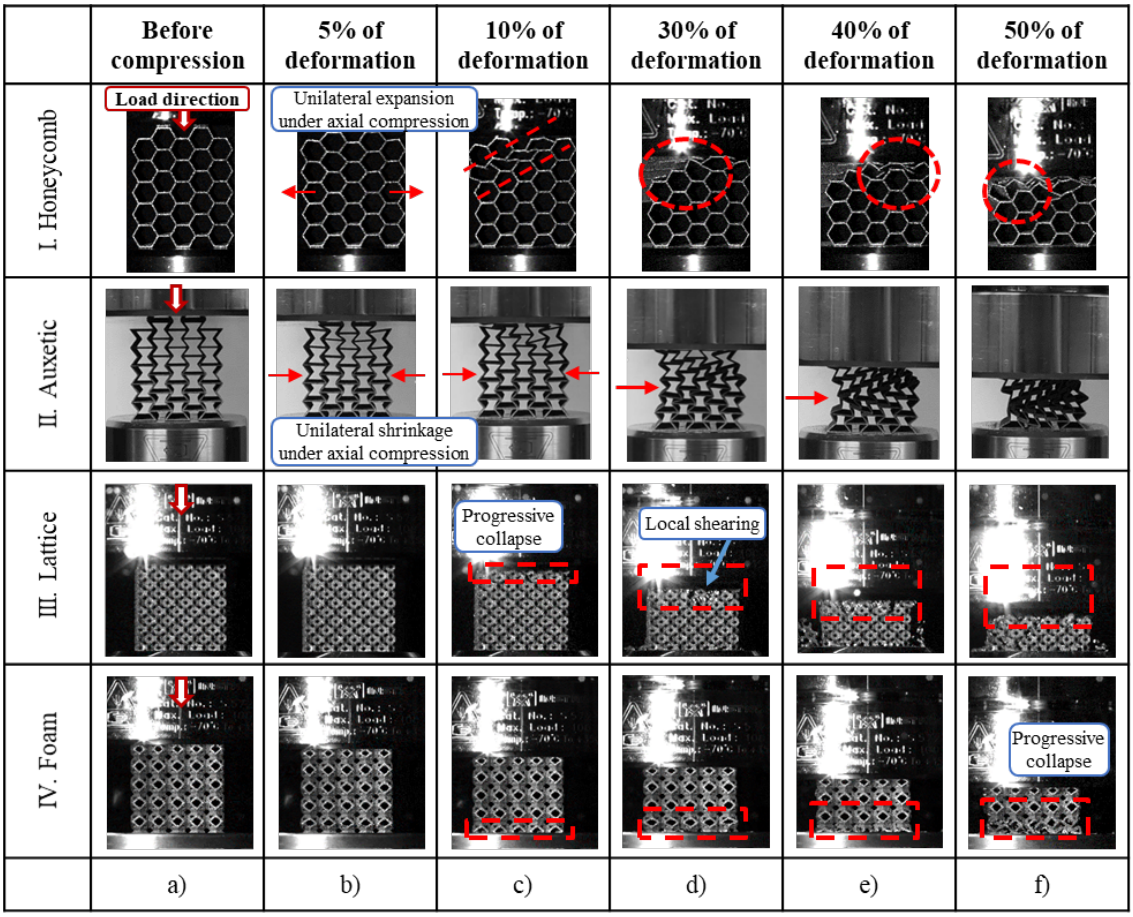

Figure 4.10: *The main stages of the deformation process during the quasi-static compression test (a-f) of the I) honeycomb II) auxetic III) lattice and IV) foam structure.*

Performing the quasi-static tests pose insight into the deformation mechanism, allowed to assume the levels of the transferred force during dynamic tests. Then, the blast tests are performed and the experimental results are discussed in the next section.

4.2.2 Results of the blast compression tests of the AM structures

The tests performed on AM samples (presented in Fig. 3.8) are reported in Figure 3.11. Each structure is shown before (Fig. 3.11a-d) and after (Fig. 3.11e-h) deformation process. The curves of the stress over strain and the absorbed energy over displacement are presented in Figure 3.12. When analyzing the results, it can be noticed that the main phases of the compression process are visible in the honeycomb and auxetic curves, i.e., the peak, plateau, and densification. However, the specimens with 3D geometry absorbed all energy generated during the explosion. Therefore, the stress curves decrease to zero. Furthermore, it should be emphasized that the foam structure has collapsed much more than the lattice structure in order to transfer the same amount of force. On this basis, it can be predicted that the lattice is a more efficient absorber.

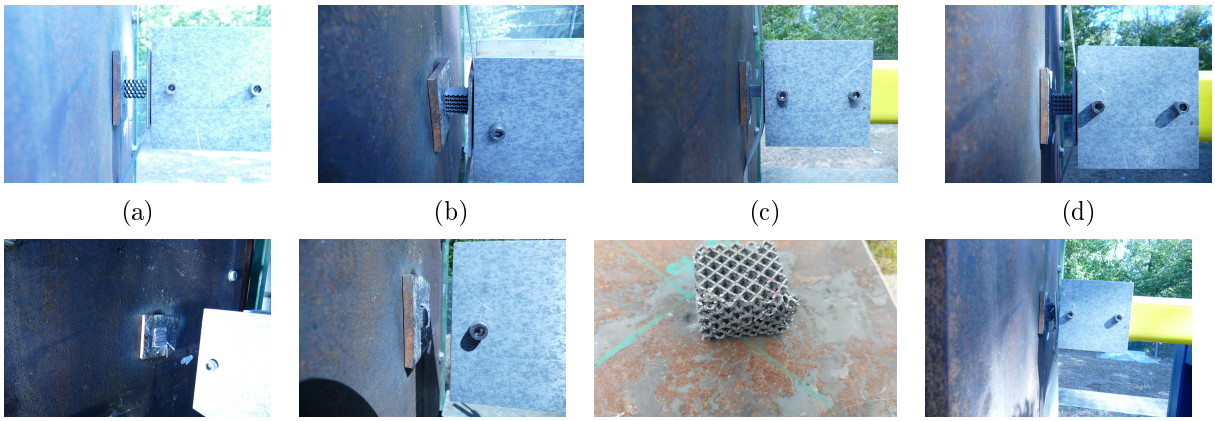

(a) (b) (c) (d)

(e) (f) (g) (h)

Figure 4.11: *Blast tests have been carried out at the training ground of ISL. The tested samples of (a) honeycomb, (b) auxetic, (c) lattice, and (d) foam before deformation and respectively (e,f,g,h) after compression process.*

Table 4.3: *Mechanical properties of the AM structures made from AlSi10Mg alloy during performed blast compression tests. Strain rate of* $1 \cdot 10^3/s$

	Honeycomb	**Auxetic**	**Lattice**	**Foam**
Peak Stress [MPa]	6.01	1.75	21.56	17.43
Mean Stress [MPa]	3.52	1.44	14.18	10.49
Densification Strain [-]	0.76	0.58	0.31	0.52

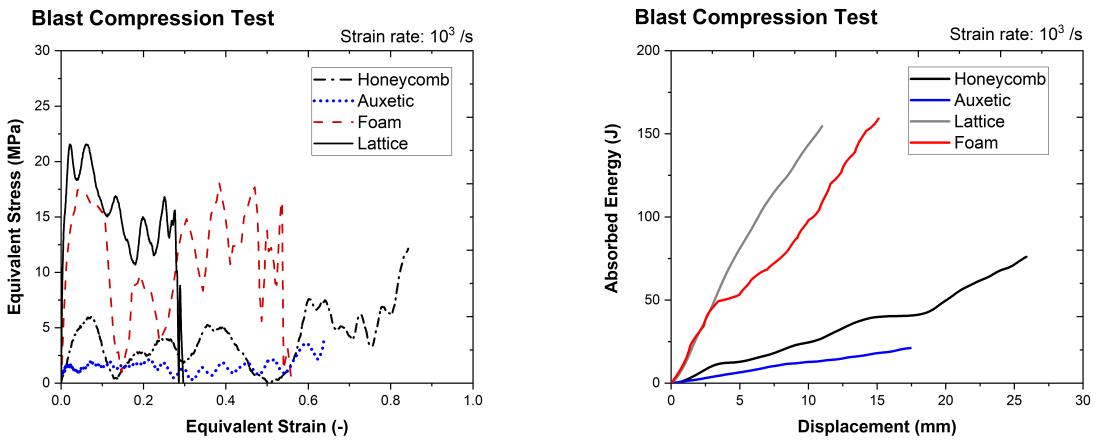

(a) (b)

Figure 4.12: *Results from the blast compression tests of AlSi10Mg additively manufacturing structures (a) stress versus strain (b) absorbed energy versus displacement.*

Each of the curve courses, presented in Fig. 3.12a, are characterized by the large fluctuations that can be correlated with the cell collapses and the bond breaks. The quantitative results presented in Figure 3.12b and Table 3.3 prove that the structures composed of 3D unit cells can

increase, at least double the abortion efficiency when they are subjected to the same explosive load. In addition, it can be noticed that the auxetic structure, characterized by a negative Poisson's coefficient, obtained the lowest stress results. At the same time, the stroke efficiency is 1.4 times lower than that of the honeycomb structure.

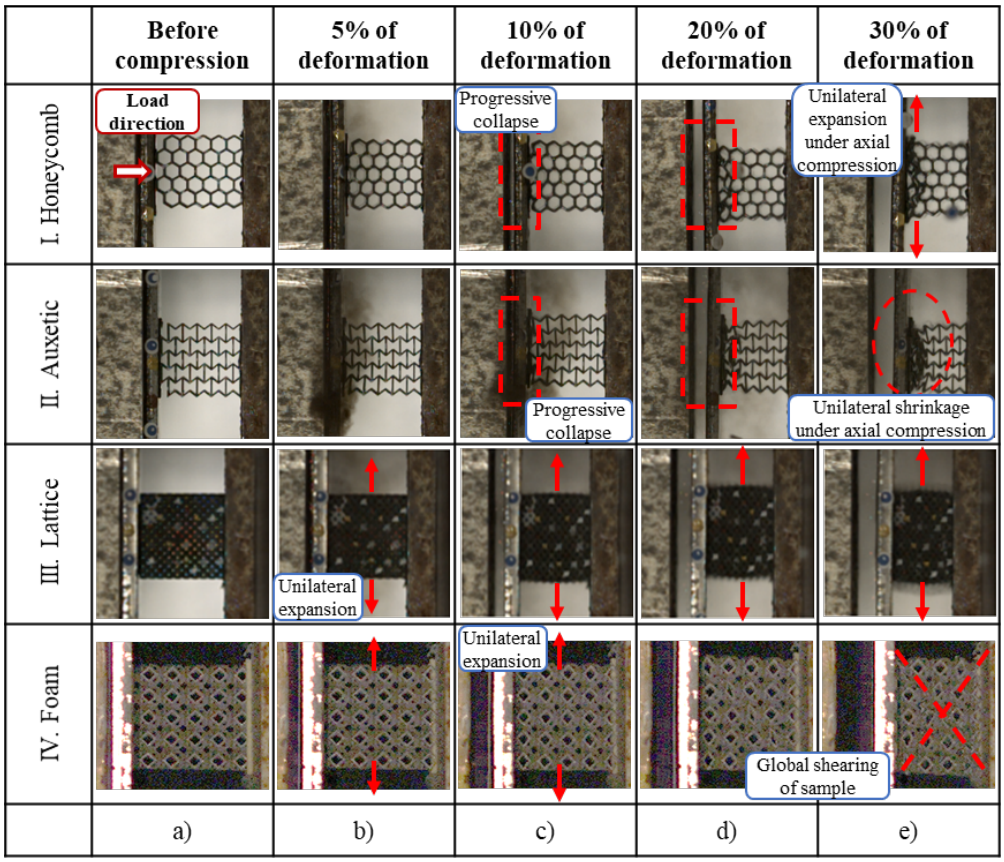

Figure 4.13: *The main stages of the deformation process during the blast compression test (a-f) of the I) honeycomb II) auxetic III) lattice and IV) foam structure.*

The dynamic response of the studied structures is different from the quasi-static one. Figure 3.13 shows the deformation mechanism of the honeycomb (Fig 3.13-I), auxetic (Fig. 3.13-II), lattice (Fig. 3.13-III) and foam (Fig. 3.13-IV) structures subjected to the blast loading. The tested structures composed of a two-dimensional unit cell collapse progressively – row by row (Fig. 3.13-I - Fig. 3.13-II). Wherein, the damage of the honeycomb is characterized by the stretching of the cells outwards (Fig. 3.13-Ie). The deformation of the auxetic at the higher strain rate is stable as opposed to the quasi-static one (Fig. 3.10-II). The synclastic curvature of the deformation indicates the "dome-shape" damage mode. The cells collapse towards inside the structure, visible in Fig. 3.13-II c-e.

The lattice and foam have a similar deformation mechanism in the initial stage of deformation, up to 10 % strain (Fig. 3.13-III a-c - Fig. 3.13-IV a-c). Their collapse processes can be correlated with the absorbed energy results (Fig. 3.12b). Lattice is characterized by cell bending and the stretching of the whole structure during blast compression. The end of the deformation process occurs as a result of shearing the entire structure, which can be seen by analyzing the sample after the test. In the case of the foam structure, the shear mode of the deformation occurs after

10 % of strain (Fig. 3.13-IV d-e). In Fig. 3.12a, the visible flatness of the curve (between 3 mm – 5 mm of the foam displacement) corresponds to the brittle fracture of the cells and breaking bonds in the structure.

The analysis of the deformation processes clearly shows that the boundary conditions, i.e., strain rate, influence the destruction mechanisms taking place. The primary failure mode influences the level of the obtained stress-strain results. In addition, local cell deformation is also observed and correlated with the results in the diagrams. Thus, the discontinuities in the curves have been clarified.

4.2.3 Discussion and comparison of the quasi-static and dynamic results

Specific energy absorption

The results obtained from the performed quasi-static and dynamic tests are referred to the mass of each sample. The energy absorption (EA) and specific energy absorption (SEA) are determined, according to Equation 1.4 (see Chapter 1). Figure 3.14 presents the obtained values of the SEA parameter. These results show the influence of the strain rate on the absorbed energy per unit mass. The samples undergo larger deformations during the quasi-static tests, but they transfer almost two times less force. Therefore, the SEA values for the same structure are similar in the quasi-static and blast regimes.

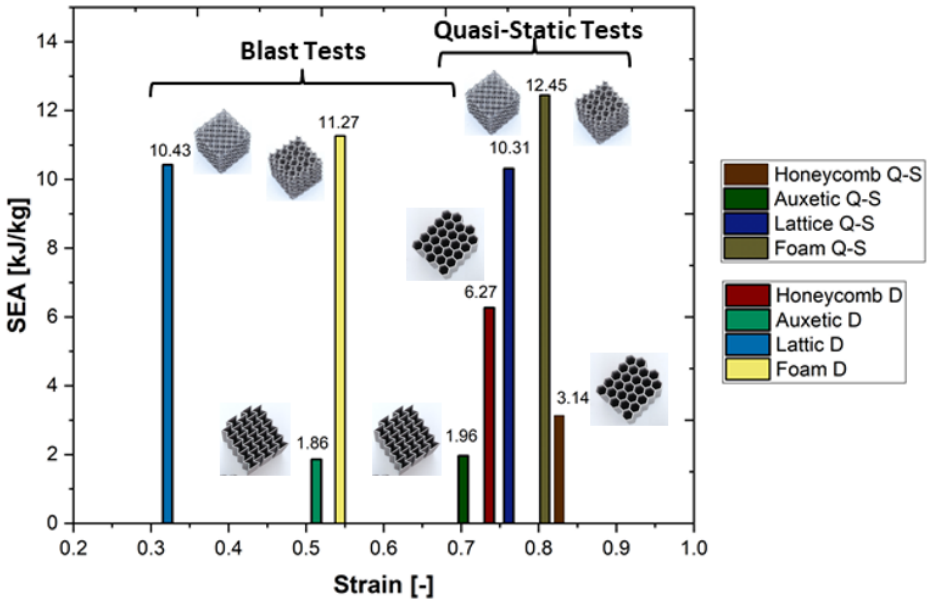

Figure 4.14: *Comparison of the responses depending on the topology of the AM honeycomb structure when loaded with a 30 g C-4 charge.*

The auxetic structure obtains the lowest specific energy absorption of 1.91 ± 0.05 kJ/kg. Then, the SEA value of the honeycomb structure is equal to 3.14 ± 0.05 kJ/kg under quasi-static conditions and of 6.27 ± 0.3 kJ/kg during blast tests. The highest obtained difference characterizes the honeycomb. The structure in the quasi-static range is subjected to local shearing and fracture of the small parts of sample. These internal deformations of the cells are visible as the flattening curve on the EA(x) diagram (Fig. 3.9b). On the contrary, the structure under-

goes a progressive collapse in the blast regime; therefore, it is able to obtain much higher values of the transmitted force.

As it is seen in Figure 3.14, the 3D structures obtain the highest SEA results: lattice of 10.37 ± 0.06 kJ/kg and foam of 11.86 ± 0.6 kJ/kg. The foam's SEA parameter under blast conditions is 45 % to 83 % higher than for honeycomb and auxetic, respectively. Even though the lattice structure achieves slightly lower SEA values, it should be taken into account that it is able to absorb all the generated energy during the explosion, deforming in 31 %. The foam structure needs almost twice the sample's height to mitigate the same amount of the explosive energy. On this basis, it can be concluded that the lattice is at least as efficient absorber as foam structure.

Relative stiffness

In addition, the effect of the structure relative density on the stiffness is characterized using the analytic equations (Eq. 3.5−3.7), developed by Ashby and Gibson [16]. The following equations distinguish the variations for the ideal stretched dominated structure (Eq. 3.6) and for the ideal bending dominated structure (Eq. 3.7).

$$\frac{E}{E_s} = C \cdot \left(\frac{\rho}{\rho_s}\right)^n \tag{4.5}$$

$$\frac{E}{E_s} = \frac{\rho}{\rho_s} \tag{4.6}$$

$$\frac{E}{E_s} = \left(\frac{\rho}{\rho_s}\right)^2 \tag{4.7}$$

where: E and ρ are the structure stiffness and density while E_s and ρ_s represent the solid stiffness and density. The C parameter is a geometry−dependent proportionality constant and n the scaling exponent.

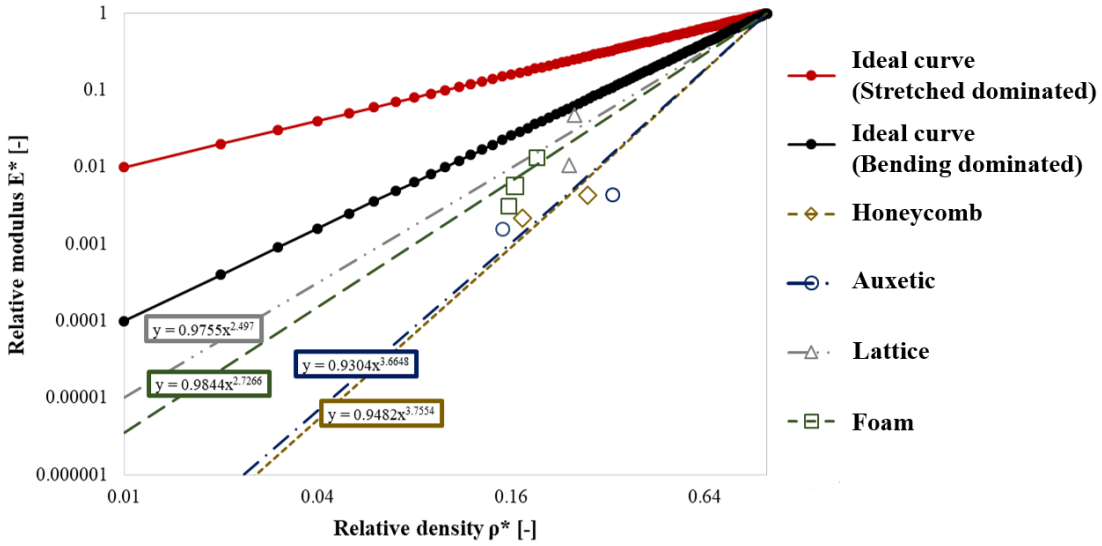

Figure 4.15: *Relative stiffness as a function of relative density.*

A similar relative stiffness can be observed between the foam and the lattice, as well as between the honeycomb and the auxetic (Fig. 3.15). The 3D structures are characterized

by curves that corresponding to the bending-dominated dependencies under the loading. In contrast, the honeycomb and auxetic are characterized by curves with the scaling exponent equal to 3.5. The experimental and numerical (see Chapter 5) analysis of the deformation processes show that the obtained dependencies are related to the stretching / contracting mods. Comparison of the results shows a remarkably higher stiffness for the structures with three-dimensional geometry. It is worth noticing that the relative stiffness results indicate the scaling influence of the relative density on the mechanical properties of the structures.

Plateau stress in different regimes of the strain rate

The stress values at the plateau phase, presented in Tables 3.2 - 3.3 are compared in two regimes: quasi-static and dynamic. Based on the calculated values, the stress ratio SR is calculated according to Equation 3.8 and the results are presented in Figure 3.16a. In addition, the analytical dependencies of the mean stress to strain rate are determined in Figure 3.16b.

$$SR = \frac{\sigma_{PlBlast}}{\sigma_{PlQS}} \tag{4.8}$$

where: $\sigma_{PlBlast}$ and σ_{PlQS} is the average value of the plateau stress in the blast and quasi-static regimes, respectively.

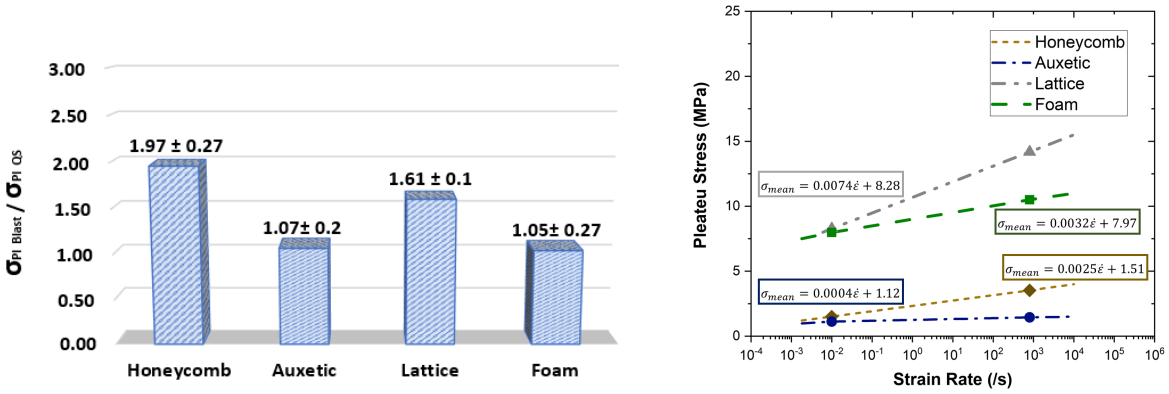

(a) (b)

Figure 4.16: *Stress dependence in the different strain rate regimes of the each tested structures (a) quasi-static and blast relation of the plateau stress (b) slope of the mean stress curves in relation to the strain rate.*

The analysis of the obtained results in Figure 3.16a proves that the honeycomb and lattice structures are much more sensitive (almost two times) to the strain rate changes than the auxetic and foam structures. Additionally, the curve slopes in Figure 3.16b indicate the highest result difference between two regimes for each structure. It is seen that the lattice is characterized by the highest slope equal to 0.007, then foam of 0.032, and honeycomb of 0.0025. Wherein auxetic is characterized by the slightest slope equal to 0.0004. Therefore, an increase in the strain rate slightly increases the ability to transfer force. It is worth noting that the honeycomb structure (characterized by the 2D unit cell) obtains the similar slope of the curve as foam (3D structure).

4.2.4 Influence of the structural topology and boundary condition on the AM structure responses under blast loading

As discussed in Section 3.1.1, the results obtained by thin-walled metallic structures subjected to quasi-static and dynamic compression are influenced by, i.e., cell arrangement, relative density, or the direction of the force application. Considering the above, in this Section, the responses of the AM structures with different designed geometry are analyzed.

Influence of structure size

To investigate the effect of structure size, two types of honeycomb structures with different edge lengths are subjected to blast loading due to the detonations of 30 g C-4 charge. The first cubic sample (called "HC (30 mm") is characterized by the length of 30 mm and consists of 5 x 5 cells. The smaller structure (called "HC (20 mm") is characterized by similar wall thicknesses but higher relative density due to a increase in cell numbers (up to 6 x 7). The geometrical properties of the tested samples are presented in Table 3.4.

Table 4.4: *Specimen properties of the samples subjected to the blast wave caused by the detonation of 30 g of the C-4 explosive charge.*

	HC (20 mm)	HC (30 mm)
Dimensions (mm)	17x18x20	27x32x30
Wall thickness (mm)	0.47	0.42
Cell number	6 x 7	5 x 5
Relative density (-)	0.27	0.17

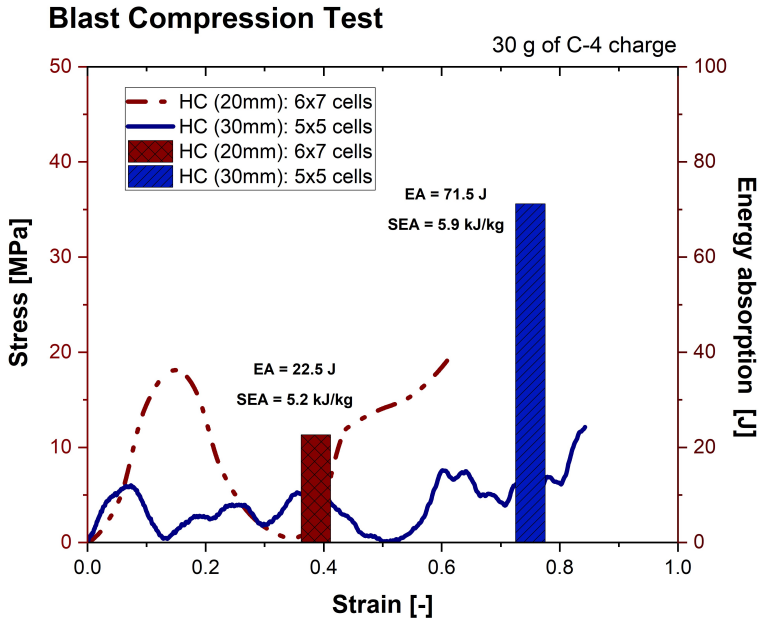

Figure 4.17: *Comparison of the responses depending on the topology of the AM honeycomb structure when loaded due to the blast wave caused by the explosions of 30 g of C-4 charge.*

Figure 3.17 clearly shows that the smaller structure ("HC (20mm)") achieves higher stress and thus a similar SEA value as the structure with a 30 mm edge. Despite the relatively large area under the stress-strain plot of the "HC (20mm)", the crushing force efficiency (CFE) is close to zero (see Chapter 1). The uneven distribution of the transformed force over time resulted in an early transition to the densification phase. The enlargement of the structure and the reduction of the number of cells cause the decrease of the relative density. This approach has allowed the "HC (30mm)" structure to deform the cells internally and to collapse progressively.

The performed tests prove that a smaller structure can achieve higher stress values. However, it still can be classified as a less effective absorber for the load under consideration due to the insufficient amount of internal deformation of the cells.

Load direction

As mentioned in Chapter 1, the behavior of 2D structures depends on the load direction. To investigate the effect of the applied load on the structure responses, two AM samples are compressed from different sides. Their geometrical characteristics are described in Table 3.5. The load direction perpendicular to the cross-section is called in-of-plane. On the other hand, a structure whose deformation is along with the height is loaded in the out-of-plane direction.

Table 4.5: *Geometric properties of the tested AM samples to study the effect of the load direction.*

	HC (Out-of-Plane)	HC (In-of-Plane)
Dimensions (mm)	50x51x30	27x32x30
Wall thickness (mm)	0.6	0.42
Cell number	4 x 5	5 x 5
Relative density (-)	0.07	0.17

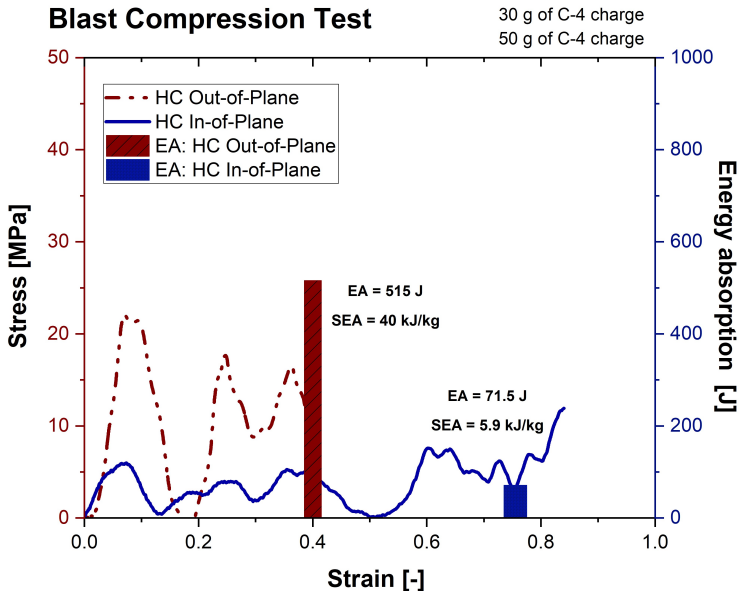

Figure 4.18: *Comparison of the stress-strain curves and energy absorption capacity depending on the load direction of the AM honeycomb structure.*

As shown in Figure 3.18, the structure compressed towards out-of-plane, does not densify, despite being loaded with a higher amount of the explosive charge (50g of the C-4). The lack of the densification phase is because "HC (Out-of-Plane)" structure absorbs all the generated energy. In addition, the "HC (Out-of-Plane)" has used a two times smaller stroke than the "HC (In-of-Plane)" structure, which follows into the densification regime after 27.5 mm of the displacement.

(a)

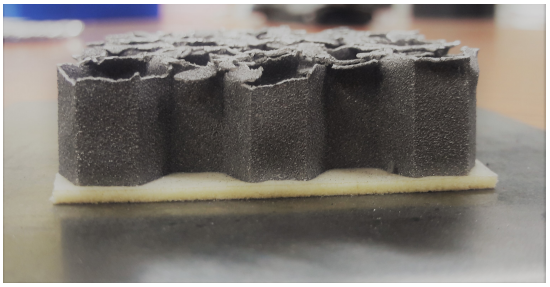

(b)

Figure 4.19: *The photos of the structures loaded in the direction of (b) in-of-plane* "HC (In-of-Plane)" *and (c) out-of-plane* "HC (Out-of-Plane)".

Moreover, both structures undergo a ductile-brittle deformation mode (Fig. 3.19a- 3.19). Wherein, a ductile mechanism of the "HC (In-of-Plane)" structure takes place when the cells expand outwards. The structure then progressively collapses (see Fig 3.13-I). A brittle fracture occurs in the nodes of hexagonal cells. The "HC (Out-of-Plane)" structure, similar to the traditional used, i.e., described in Section 3.1.1 the thin-wall metallic honeycomb, proves the folding mode under blast loading. However, thin-walled metallic honeycombs are characterized by the formation of the sided convolutions. Instead of the concertina folding, the AM "HC (Out-of-Plane)" honeycomb exhibits the wall fracture, which is observed in the middle part of the one fold.

Conventionally vs. additively manufactured structures

Finally, the AM structures are compared with those produced conventionally. The details of four types of specimen geometries that have been used to compare the absorptive properties are shown in Table 3.6. Then, Figure 3.20 presents the stress-strain results obtained during the blast tests caused due to the detonations of 30g and 50g of the C-4 charge.

The tested AM structure loaded in the out-of-plane direction, i.e., "AM HC (Out-of-Plane 50g C4)" absorbs twice as much energy generated under similar experimental conditions as the conventionally produced structure "CM HC (Out-of-Plane 50g C4)". Furthermore, it can be seen that by using AM structures, the size of the component can be reduced in order to absorb the same amount of energy. The phenomenon has also been proven for AM structure loaded in the opposite direction, i.e., in the in-of-plane. The "AM HC (In-of-Plane 30g C4)" structure absorbs a similar amount of energy (71.5 J) as produced conventionally textup"CM HC (Out-of-Plane

30g C4)" (98 J) under the loading generated by 30 g of C-4 charge. Whereby, the displacement of the CM structure is more than 70 mm, and the AM structure needs less than 25 mm.

However, it should be noted that AM is characterized by significant stress oscillations in the plateau regime. It results from the fractures and sudden breaking of the bonds instead of the plastic concertina folding. Thus the structure is unloaded and loaded again by the front plate, visible in the following stress peaks.

Table 4.6: *Specimen properties used in the experimental blast tests, caused by 30 g and 50 g of C-4 explosive charge of the (a) conventionally manufactured* "CM" *and (b) additively manufactured* "AM" *structures.*

(a)	**CM HC (Out-of-Plane 30g C4)**	**CM HC (Out-of-Plane 50g C4)**
Dimensions (mm)	50x50x100	100x100x50
Wall thickness (mm)	0.07	0.07
Cell number	4 x 4	7 x 8

(b)	**AM HC (In-of-Plane 30g C4)**	**AM HC (Out-of-Plane 50g C4)**
Dimensions (mm)	27x32x30	50x51x30
Wall thickness (mm)	0.42	0.6
Cell number	5 x 5	4 x 5

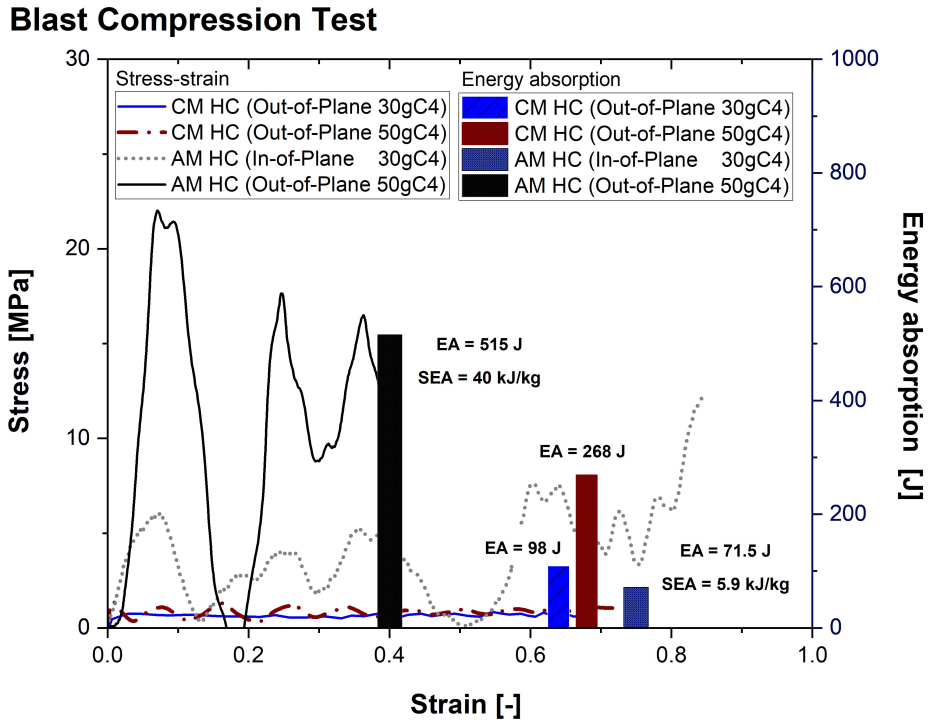

Figure 4.20: *Obtained results of the conventionally manufactured (CM) and additively manufactured (AM) honeycomb structures when loaded in the in-of-plane and out-of-plane direction, caused by the explosions of 30 g and 50 g of C-4 charge.*

4.3 Chapter summary

This chapter focuses on analyzing the absorptive properties of the hexagonal honeycomb, auxetic, rhomboidal lattice, and regular foam structures under quasi-static and blast loading. It is proved a considerable influence of a structured topology on the deformation processes. The structures characterized by 3D unit cells (foam and lattice), compared to the 2D structures (honeycomb and auxetic), exhibit about a six-fold increase in the mean stress under quasi-static loading (Table 3.2) and up to ten-fold under blast conditions (Table 3.3).

In addition, the main stages of the structure destruction during the quasi-static and dynamic compression tests are correlated with the measured results (see Sections 3.2.1 and 3.2.2). The analysis proves that the change of the load conditions (from quasi-static to blast wave) affects the significant increase of the stress results in the case of the honeycomb and lattice structures. However, the auxetic and foam structures are relatively insensitive (Fig. 3.16). The increase in the strain rate also causes the change in the deformation modes (see Figs. 3.10 and 3.13). Section 3.2.3 indicates the effect of scaling moduli corresponding to the structure density (Fig. 3.15). The values of parameter is equal to 2.5 for the 3D structures (lattice and foam) and about 3.5 for honeycomb and auxetic. Furthermore, the influence of the boundary conditions and mechanical properties of the samples produced by conventional methods has been investigated (Section 3.1.1). This approach allows for predicting some issues during the experimental campaign and performing a more profound analysis for the AM structures. Then, in this chapter, the obtained results by structures manufactured by two techniques are compared (Section 3.2.4). It has been observed that AM structures can absorb at least twice as much energy when subjected to similar blast loading. Whereby the dimensions of the structures can be significantly reduced (Section 3.2.4).

The obtained results prove that the AM structures demonstrate a great potential to be designed as ultralight mechanical metamaterials. It is worth noticing that the more beneficial energy absorption capacities characterize the 3D structures, and in addition, their properties do not depend on the load direction as it takes place for 2D structures. A more detailed analysis of cell deformations is possible due to the numerical simulations discussed in the next chapter.

Bibliography

[1] B. Simoens and M. Lefebvre. Influence of the shape of an explosive charge: Quantification of the modification of the pressure field. *Central European Journal of Energetic Materials*, 12(2):195–213, 2015.

[2] G. I. Taylor. *The pressure and impulse of submarine explosion waves on plates.*, volume III. Cambridge University Press, 1963.

[3] N. Kambouchev, L. Noels, and R. Radovitzky. Nonlinear compressibility effects in fluid-structure interaction and their implications on the air-blast loading of structures. *Journal of Applied Physics*, 100:063519 – 063519, 10 2006.

[4] N. Kambouchev, R. Radovitzky, and L. Noels. Fluid-structure interaction effects in the dynamic response of free-standing plates to uniform shock loading. *Journal of Applied Mechanics-transactions of The Asme*, 74, 09 2007.

[5] Q. M. Li, I. Magkiriadis, and J. J. Harrigan. Compressive strain at the onset of densification of cellular solids. *Journal of Cellular Plastics*, 42(5):371–392, 2006.

[6] T. Wierzbicki. Crushing analysis of metal honeycombs. *International Journal of Impact Engineering*, 1(2):157–174, 1983.

[7] T. Wierzbicki and W. Abramowicz. On the crushing mechanics of thin-walled structures. *Journal of Applied Mechanics*, 50(4a):727–734, 12 1983.

[8] CEL COMPONENTS S.R.L. Honeycomb panels, 2019. https://www.honeycombpanels.eu/en/products/honeycomb/aluminium [Online; accessed 28.11.2019].

[9] R. K. McFarland. The development of metal honeycomb energy-absorbing elements. Technical Report 32-639, Jet Propulsion Laboratory, California Institute of Technology, Pasadena, CA, USA,, July 1964.

[10] T. Wierzbicki and W. Abramowicz. On the crushing mechanics of thin-walled structures. *Journal of Applied Mechanics*, 50(4a):727–734, 12 1983.

[11] S. Jin, Y. Korkolis, and Y. Li. Shear resistance of an auxetic chiral mechanical metamaterial. *International Journal of Solids and Structures*, 174:28–37, 11 2019.

[12] W. Wu, W. Hu, G. Qian, H. Liao, X. Xu, and F. Berto. Mechanical design and multifunctional applications of chiral mechanical metamaterials: A review. *Materials and Design*, 180:107950, 2019.

[13] K.W. Wojciechowski. Two-dimensional isotropic system with a negative poisson ratio. *Physics Letters A*, 137(1):60–64, 1989.

[14] M. Mir, M. N. Ali, J. Sami, and U. Ansari. Review of mechanics and applications of auxetic structures. *Advances in Materials Science and Engineering*, 2014, 2014.

[15] J. Sienkiewicz, P. Platek, F. Jiang, X. Sun, and A. Rusinek. Investigations on the mechanical response of gradient lattice structures manufactured via slm. *Metals*, 10(2), 2020.

[16] L. J. Gibson and M. F. Ashby. *The mechanics of honeycombs*, pages 93–174. Cambridge Solid State Science Series. Cambridge University Press, 2 edition, 1997.

Chapter 5

Numerical simulation

The test configuration modeled in the LS-DYNA solver, ver. R9.0.1, intended to analyze the energy absorption mechanisms accompanying structural deformation under a blast loading. The conclusions have reached from the conducted experimental and numerical investigation can be applied to the modeling and optimizing other cellular structures used against the blast treats.

First, the simulations are performed for the conventionally manufactured structure of honeycomb, which is the elementary example for the further investigation of AM structures. This chapter verifies the influence of the numerical results depending on the mesh size, friction conditions, and strain rate sensitivity. Then, the main issues to be considered when developing a simulation with AM structures are presented. The comparison between the values of the load absorbed by the sample crushed numerically and experimentally shows a good agreement, providing insight into the absorption mechanisms of the blast wave.

5.1 Introduction

The finite element method (FEM) simulations are based on either the Eulerian formulation, in which the computational grid is fixed [1] or on the Lagrangian formulation, in which the computational grid is moving with the material [2]. Typically, blast-related problems are modeled by the full Eulerian approach for a volume of air and explosive or by the Arbitrary Lagrangian-Eulerian (ALE) formulation—an intermediate formulation between the two main types, with the capacity of being fully Eulerian or Lagrangian in certain zones of the computational domain [3].

As it is described in Chapter 4, in the EDST blast test, the tested structure is not directly affected by the blast wave. The deformation of the sample results from the movement of the front plate accelerated by a blast wave of a known pressure profile. Therefore, the numerical analysis of the blast energy dissipation may be often modeled using the Lagrangian approach, as it is modeled for the energy absorbers used in automotive or in aviation. For example, NASA Langley Research Center launched the test program of the studies on the composite energy absorbers under the Transport Rotorcraft Airframe Crash Testbed (TRACT) in 2015. The numerical simulations have been based on the Lagrangian approach in LS-DYNA code [4]. Moreover, the numerical models of the car's absorbers are often modeled as both the shell and solid elements in the explicit software package LS-DYNA [5,6]. The crushboxes as thin-walled components allow the use of shell parts, which reduce the calculation time. When the wall thickness to the length of the part increases, the shell elements may not be efficient.

Furthermore, the absorptive properties of additively manufactured structures have become the focus of numerical simulations in recent decades. Baranowski and el. developed the detailed description of numerical modeling for testing honeycomb structures manufactured from Ti-6Al-4V alloy powder using the LENS method. The explicit task in LS-DYNA code has been composed with Multi Parallel Processing, implementation of an erosion criterion, and assuming a prescribed velocity. The eight-mode hexagonal elements with single integration points have been used to represent the honeycomb structure placed between two rigid surfaces. The finite element (FE) analysis allows to defining the relationship between the structure topology and the energy-absorption capabilities.

The FE code offered by LS-DYNA ver. R.9.0.1 is also applied to simulate the deformation of the additively manufactured structures. The experimental processes of the performed blast tests are modeled by using the explicit time integration. The quasi-static compression of the thin-walled metallic honeycomb is also developed but in the implicit formulation. Such an approach allows to thoroughly analyze the discussed task, starting from research on classical structures, following a detailed description of numerical modeling of advanced parts.

5.2 Numerical configuration

In the first approach, the numerical configuration is based on the discussed in Section 4.1 compression behavior of a thin-walled aluminum honeycomb structure. The geometry of the unit cell of the tested structures has been modeled in a CAD program. Then, the experimental set-up has been prepared in Ls-PrePost. The numerical task consisted of the Lagrange solid parts of the tested sample placed between two steel plates. Theoretically, the unit cells have a hexagonal shape with a length of 7 mm and a wall thickness of 0.15 mm. However, it is challenging to manufacture such a structure with assumed geometrical properties. The actual dimensions can be significantly different from the ideal ones, often used in numerical simulations. The solution

to this problem can be using the unit cell dimensions corresponding to the average values, which is discussed in Section 5.4.6.

The measured crushing load is assigned to the nodes of the upper surface of the front plate. The pressure profiles presented in Figure 4.1b are implemented to the numerical task as the initial load, according to the way shown in Figure 5.1. The pressure data over time are taken from the test without the absorbing structure. Then, the calculated initial force is distributed to nodes of the upper surface of the front plate on the area equal to the inner tube cross-section, i.e., 80 x 80 mm ^{2}. The load profile is a crucial initial condition that imposes displacement of the front plate.

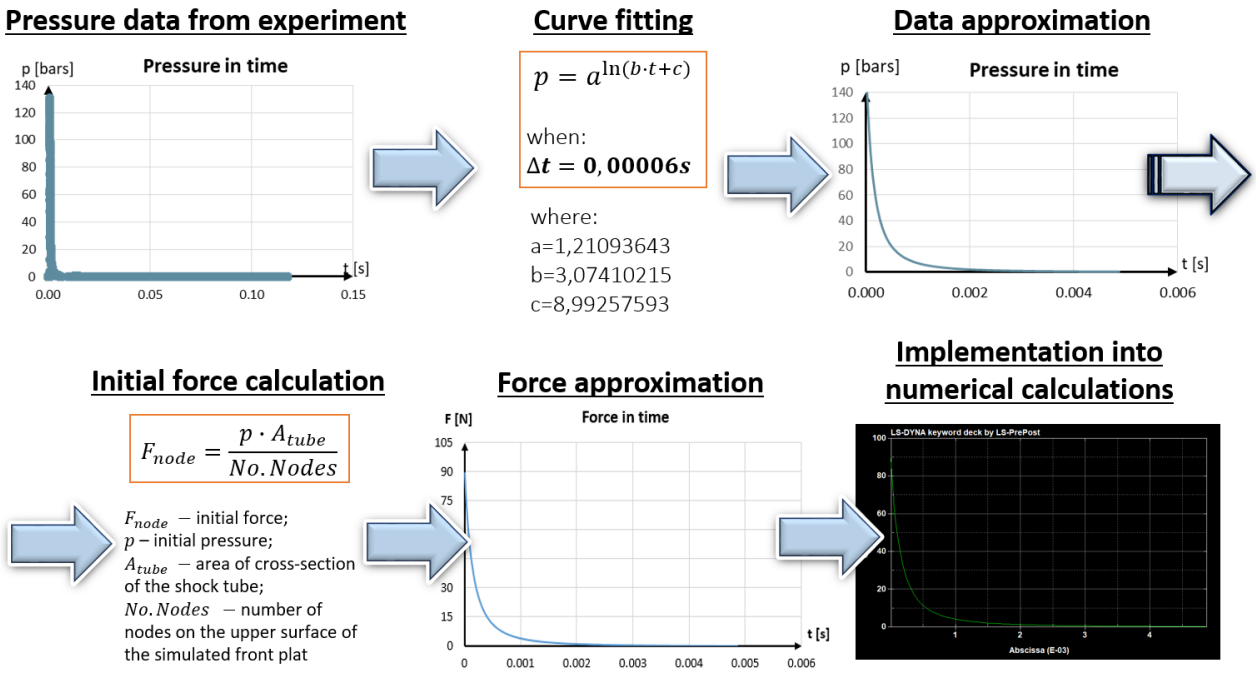

Figure 5.1: *Implementation process of the initial load into a numerical task.*

In order to obtain the output values of the load from the numerical task, the force resulted from the reaction between the bottom plate and the honeycomb is read. Therefore, the transferred force through the structure is determined in a similar way to the experimental measurements. Figure 5.2 shows the contact algorithms based on which the incremental force outputs are calculated. The average value of the resultant force at the point is result of the two output states [7]. Then, the generalized stress is calculated by dividing the determined force by the area which the structure covers. To obtain the strain values, the front plate displacement is divided by the height of the analyzed structure.

To define element formulation in the numerical task, the user chooses between the solid, shell, beam and truss or discrete elements. The section options are shown in Figure 5.3. For the regular solid bodies, hexahedron elements are recommended. However, the tetrahedrons may be more accurate element types when the complex structure increases. They can be appropriate for metals, plastics, and rubber materials. The elements need finer mesh and can not suit large strains. Whereby pentahedras are useful for the transition elements [8].

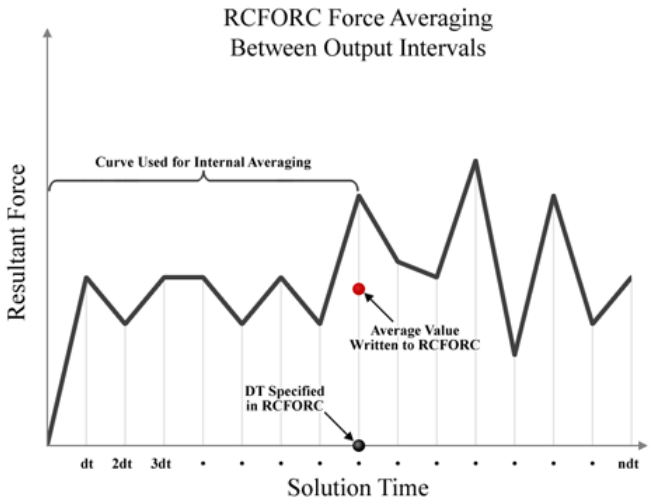

Figure 5.2: *Determination of the contact outputs in LS-DYNA software [7].*

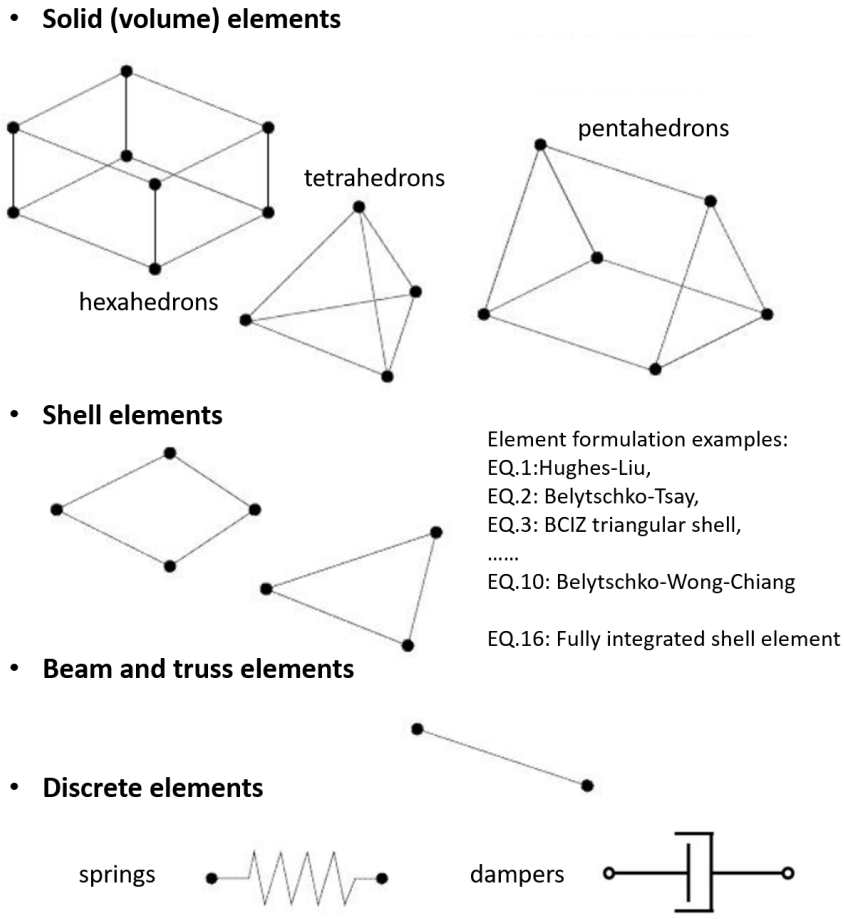

Figure 5.3: *Type of the element formulations in LS-DYNA software [8].*

The way of the node penetration into the opposite segment must be determined by the *CONTROL* card. The potential penetration is achieved by the "slave" nodes which interact with the "master" segment. The contact condition can be applied by using i.e., one-way treatment (Fig. 5.4a), two-way treatment (Fig. 5.4b), single surface contact (Fig. 5.4c) or tied contact (Fig. 5.4d) type. In the one-way treatment the "slave" nodes are checked for penetration through "master" segment. They both are defined via "slave" and "master" list. The similar process is applied in the two-way treatment contact type. However, "master" nodes are additionally checked through the "slave" segments. The single surface contact is defined only for one part via "slave" list. For the tired contact, the "slave" nodes move to the "master" surface during initialization. It takes place by the eliminating gaps between "slave" nodes and "master" segments. The contact conditions can be applied via the penalty or kinematic constraint methods. The penalty function allows to treat the internally penetration by linear springs between the "slave" nodes and "master" segments.

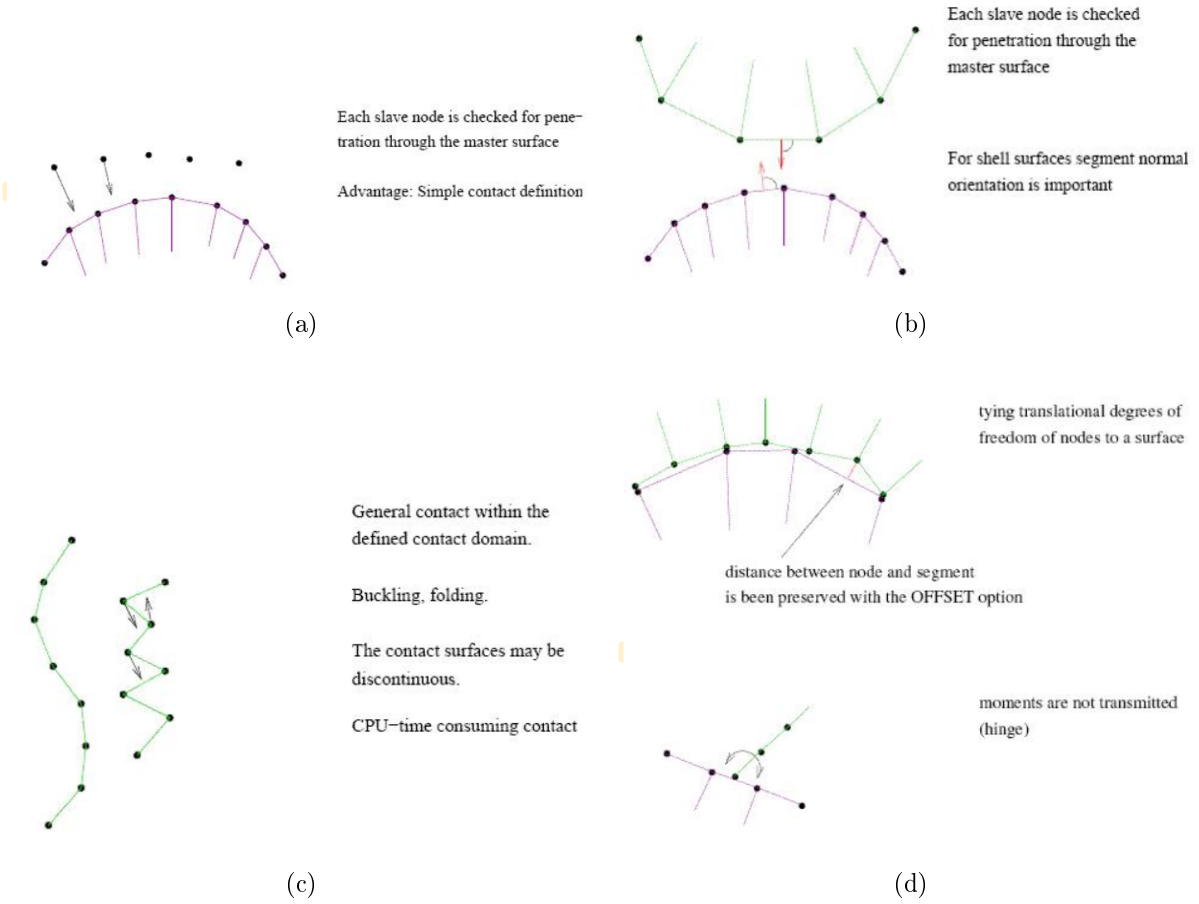

Figure 5.4: *Examples of the contact types (a) *NODES_TO_SURFACE, (b) *SURFACE_TO_SURFACE, (c) *AUTOMATIC_GENERAL_INTERIOR, (d) *TIED_NODES_TO_SURFACE.*

For solid, shell, and thick shell elements which are under-integrated elements with a single integration point, the *HOURGLASS* function may be necessary [9]. The nonphysical, zero-energy mode of deformation causes zero strain and no stress, as it is shown in Figure 5.5. It

ensures the less expensive calculations and stability in large deformations. In addition, the hourglassing affects the less tendency to "shear-lock" than fully-integrated or selectively reduced (S/R) integration formulations [9].

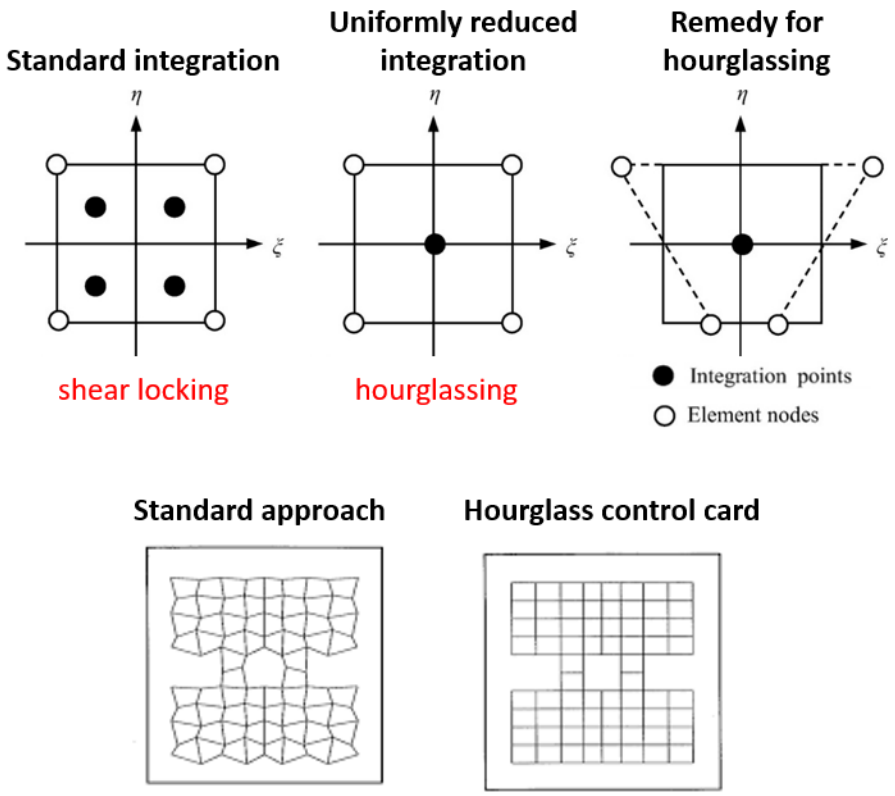

Figure 5.5: *Basic principles of HOURGLASS control function [10].*

Figure 5.6 shows the organization of a numerical task in LS-DYNA software schematically. Only correctly defined input data allow obtaining valuable results. The output data can be read in two different ways. The first is related to the task given by the users, and the second is related to the way of performing the calculations.

Following the criterions presented above, the numerical task of the crushable thin-wall honeycomb core is developed as shown in Figure 5.7. The applied shell part of the structure is characterized by five Gauss integration points through the thickness of the elements. The hourglass viscosity to damp out allows to obtain the zero-energy modes. The shell elements are formulated using the Belytscho-Tsay model. It is worth to note that the tested honeycombs are manufactured by the extrusion of connected aluminum foils. Therefore, a part of the walls is double. This is reproduced by assigning to appropriate walls thickness of 0.15 mm in the $^*SECTION$ field, while the other walls have a thickness of 0.07 mm, as reported in the product datasheet [11]. To ensure that the entire surface of the compressed core is loaded uniformly, the material of the plate is described by the $^*MAT\_Rigid$ 020 material model [12]. The front and rear plates are cuboids with dimensions of 100 mm x 100 mm x 8 mm. To reduce a number of elements and optimize the time calculation, both plates are meshed coarsely. The default solid cuboid elements are applied, which dimensions are equal to 2 mm x 2 mm x 2 mm; thus each plate has 10 000 elements.

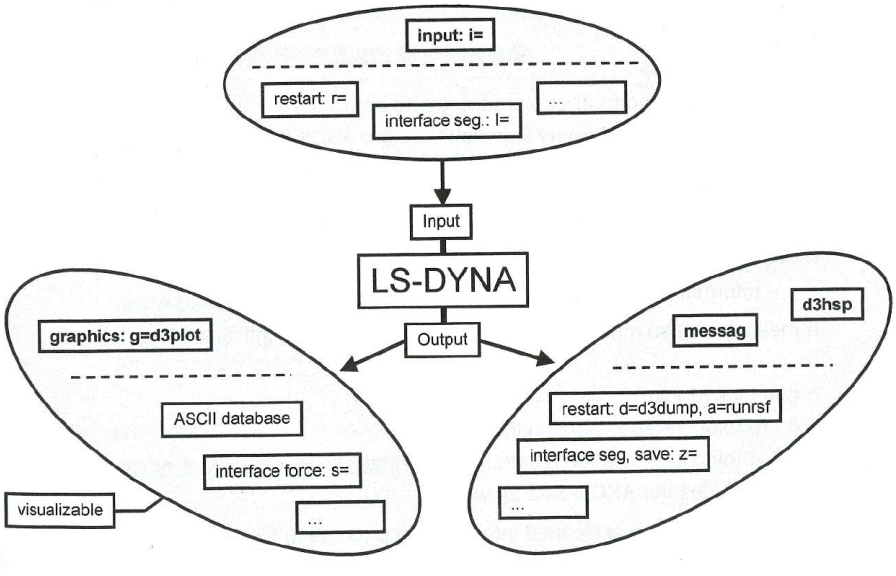

Figure 5.6: *File organization in LS-DYNA software.*

In the discussion task, the contact between the thin-walled structure and the plates is defined by the function *$AUTOMATIC\_SURFACE\_TO\_SURFACE$ and *$SURFACE\_TO\_SURFACE$. The structure's nodes are considered as "slaves" and plate's nodes as "master". The determination of the friction coefficients may be an experimental challenge, but numerically, it has been verified that the frictionless condition does not provide proper results.(see Section 5.4.3) However, the static and dynamic friction parameters must be assumed between the plates and the honeycomb. The boundary conditions are completed by defining the nodes of the bottom surface of the rear steel plate as fully constrained. The introduced assumption blocks the sandwich movement.

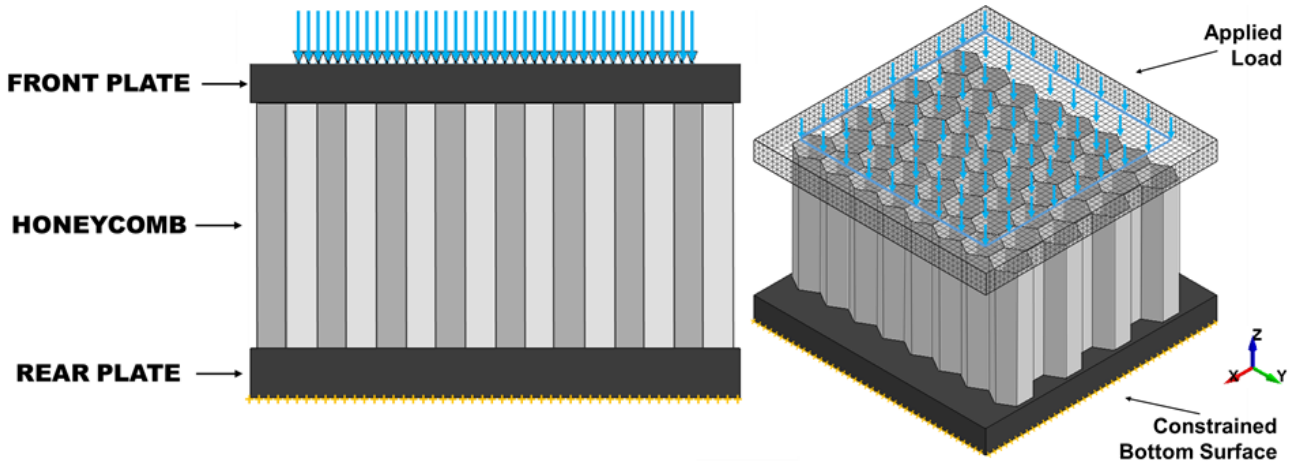

Figure 5.7: *Numerical representation of the tested configuration: (a) side view and (b) isometric view.*

5.3 Material model validation

The conventionally manufactured honeycomb using in this experimental campaign is made with the aluminum alloy AA3003 and consists of 53 cells. To describe the behavior of the AA3003 aluminum alloy in the simulation, the phenomenological flow model proposed by Johnson and Cook is used [13]. Originally, in the Johnson-Cook flow model, it is manipulatively decomposed into three terms which represent the material dependences of strain, strain rate hardening and thermal softening. However, among a few other formulations of the Johnson-Cook model available in the LS-DYNA code, $*MAT\_Simplified\_Johnson\_Cook$ 098 is a simplified function (Eqs. 5.1 - 5.2). The model does not account for temperature effects neither for fracture modeling results in time-efficient calculations [12]. The $*MAT\_098$ is chosen because it is assumed that the thin-walled aluminum honeycombs deform only plastically without damages and it has not been reported that the folding process may be affected greatly by temperature. In addition, this model allows faster calculations, up to 50%, comparing to other Johnson-Cook formulations available in the software [12].

$$\sigma_y = (A + B \cdot \bar{\varepsilon}^{p^n})(1 + C \cdot ln\dot{\varepsilon}^*) \tag{5.1}$$

$$\dot{\varepsilon}^* = \frac{\dot{\bar{\varepsilon}}}{EPSO} \tag{5.2}$$

where: A, B, C – material parameters, $\bar{\varepsilon}^{p^n}$ – effective plastic strain, $\dot{\varepsilon}^*$ – normalized effective strain rate, EPS0 – quasi-static threshold strain rate.

The exact material and mechanical properties of thin AA3003 aluminum foils from which honeycombs are made, had been not availabled in the literature. Depending on a manufacturing method, the alluminium sheets can be characterized by material properties within a wide range [14–18]. Therefore, a reverse engineering method is used, as shown in Figure 5.8. Is enabled an estimation of the parameters for the Johnston-Cook model, Eqs. 5.1– 5.2, based on the results of the quasi-static compression test of the honeycomb structures.

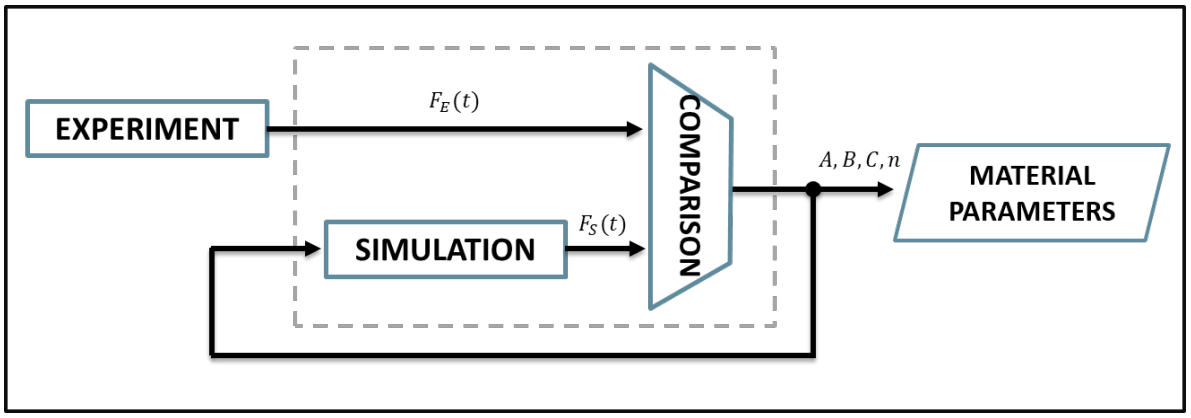

Figure 5.8: *Reverse engineering method*

In absence of material data, the reverse engineering process can be considered as a tool for modeling [19]. Reverse engineering (also known as backwards engineering or back engineering) involves to creating a system, model or device from the sensed data and passing to an

appropriate new model. The studies to derive the material parameters, necessary for the used $^*MAT\_Simplified\_Johnson\_Cook$ 098 Eqs.5.1 - 5.2 have been performed.

The core-competency of LS-DYNA is the highly nonlinear transient dynamic FE analysis which uses explicit time integration. Therefore, the program is applied mainly to model dynamic loading. However, it also may be used to perform implicit, quasi-static calculations. To enable the implicit analysis, several options in the $^*CONTROL$ card must be then activated. The automatic time step control and the optimum equilibrium iteration are added in the option $^*CONTROL\_IMPLICIT\_AUTO$. To solve a linear implicit problem, the *Newmark* type of analysis with the time integration constant values of 0.5 and 0.25 is defined [9]. To find the equilibrium points of the task at each time step the $^*CONTROL\_IMPLICIT\_SOLUTION$ function must be also active. The time step of 0.1 s is set for the implicit analysis in the $^*CONTROL\_IMPLICIT\_GENERAL$ card. Knowing the constant velocity of 0.48 $\mathrm{mm\,s^{-1}}$ in the loading direction, the $^*PRESCRIBED\ MOTION$ function is then chosen with the option $^*VELOCITY\_(RIGID\ BODIES\ AND\ NODES)$. A constant velocity of the front plate is kept, however, each displacement beyond the Z-direction has to be constrained. In the given configuration, the front and rear plates are considered as *RIGID* bodies.

Experimental results of the quasi-static compression test may be used to obtain the optimal fit of the model parameters in a sequence of simulations. The numerical tasks of the quasi-static compression of the 7-cells structure have been performed to validate the Johnson-Cook plasticity parameters for the aluminum AA3003 (Eqs. 5.1 - 5.2). The starting input parameters are assumed based on the material data presented in [20], which were used in the simulations discussed in [21].

The results from the quasi-static compression test have been compared with the results from the implicit numerical simulations in the loop process. Repeating this process has tented the obtained minimization of the error between the numerical and experimental results allows considering the obtained set of the model parameters as adequate. The final values of the material parameters used to model the aluminum are presented in Table 2. These parameters are applied in the numerical analysis of the honeycomb behavior.

Table 5.1: *Parameters of the Johnson-Cook plasticity model.*

Parameters	**Unit**	**AA3003**	**AlSl 4340 [29]**
ρ	g/cm^3	2.7	7.86
E	[GPa]	70	209
A	[MPa]	90	792
B	[MPa]	220	510
n	[-]	0.2	0.26
C	[-]	0.001	0.014

5.4 Numerical investigation

To ensure consistency of the numerical calculation, the influence of the structure geometry, mesh size and friction coefficients are verified that they may affect strongly the results. The hereby provided short discussion is complementary to a more detailed analysis of several other factors influencing numerical results given in the following points.

5.4.1 A number of cells in the honeycomb structure

As the simulation of the 53-cells structure with 1.5 mln elements has required many hours of calculations, the objective is to identify the optimal number of cells allowed an acceptable accuracy of results without extensive time of calculations. For this purpose, subsequent simulations are carried out for the honeycomb modelled with a reduced number of cells, as shown in Figure 5.9.

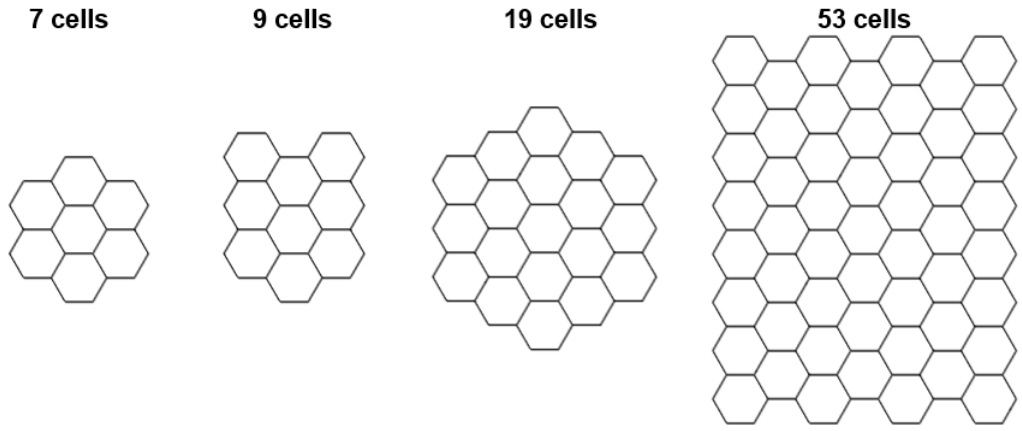

Figure 5.9: *Cross-sections of the honeycomb structure modelled by various number of cells.*

All structures are meshed regularly by elements with the same size 0.2 x 0.2 x 0.2 mm^3, other conditions and parameters are kept as in the simulation of the 53-cells structure. The stress-strain curves for 7, 9 and 19 cells present almost the same values of the peak stress as it is calculated for the 53 cells honeycomb, Table 5.2. Even if a number of cells is reduced, the character of the curves is similar, only the single cell structure differs much from the generally observed trend and does not model the character of the entire structure deformation, Fig. 5.10. The stress fluctuations for multi-cells structures differ slightly because they relate to folds occurring in the different places along the wall height but their approximate value is on a similar level. In consequence, the further parametric study is performed using the 7-cells structure, as it is the minimal number of cells required to perform a representative simulation of the structure behavior.

A difference between the mean plateau stresses calculated for 7 cells and 53 cells is less than 6 % and maximum stress less than 10 %, but the time of calculation is reduced by 20 times. Further reduction of a number of cells in the honeycomb introduces larger errors, Table 5.2. The numerical studies prove that the tested structure should be composed of minimum 7 cells to represent stress-strain response of the larger honeycomb under blast loading.

Table 5.2: *Calculated characteristics depending on a number of cells in the structure.*

Number of cells	**1**	**6**	**7**	**9**	**19**	**53**
Peak stress [MPa]	4.47	2.70	3.10	3.25	3.30	3.31
Mean plateau Stress [MPa]	1.04	0.72	0.78	0.86	0.87	0.85

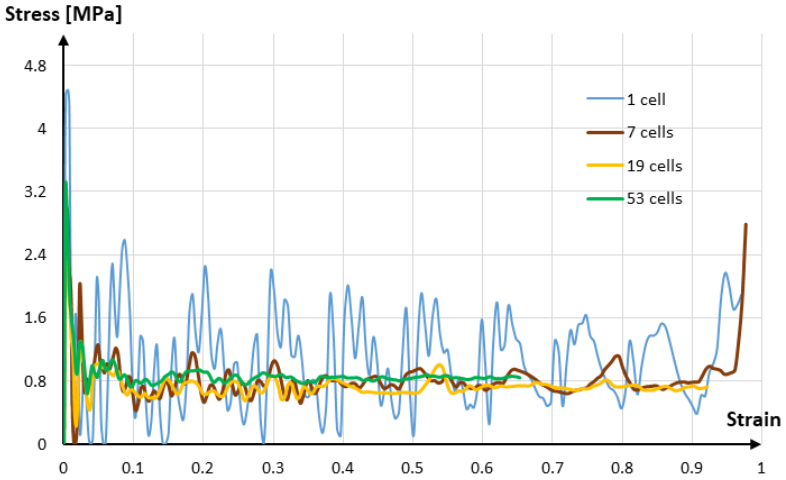

Figure 5.10: *Comparison of the stress-strain curves calculated for the compressed honeycomb structure with different number of cells.*

5.4.2 Mesh size

One of the most important parameters affecting significantly results and the time of calculations is the mesh size. This influence on the calculated results is also verified. If the element size changes from 0.2 mm to 1.0 mm, the difference between the resulted mean plateau stress is close to 50%. For the 7 cells structure, the consistency of results is obtained when the element size is close to 0.4 mm, Fig. 5.11. Calculations with the same solver and at the same settings can be carried out 4 times faster than for the fine mesh with the element size 0.2 mm, which is a reasonable compromise between the results accuracy and calculation time.

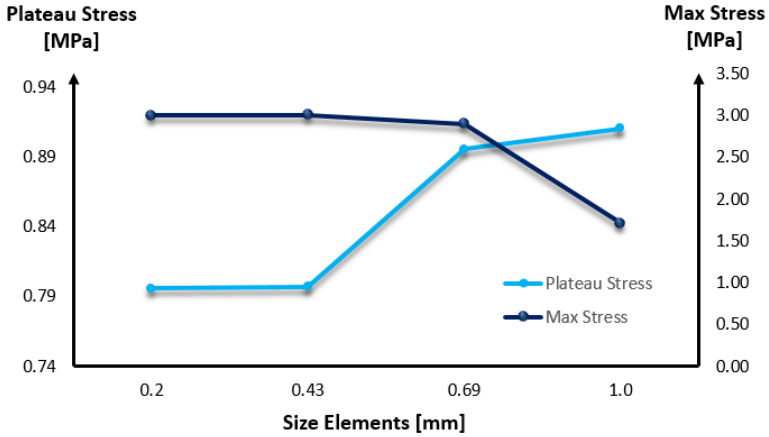

Figure 5.11: *Mesh size influence on the results.*

5.4.3 Friction influence

Characteristics of friction during the uniaxial blast compression tests are challenging to estimate experimentally [22]. The values of the friction coefficient depend on many parameters, like involved materials and quality of surface being in contact. In addition, during the EDST experiment, the honeycomb is assembled with the plates by means of an adhesive tape to prevent it from falling down on the ground. The contact way of the core and plates causes that the friction coefficients are even more difficult to estimate. On the contrary to the experimental test, it is possible to verify numerically if different values of the friction coefficient affect the results.

In LS-DYNA, the compression loads are transferred between the "slave" nodes and the "master" segments. The nodes of part "1" are checked against segment "2", as shown in Figure 5.12. When the contact friction is active, then the tangential loads are transferred. It allows avoiding the sliding after contact for the rigid walls. In other contact surfaces "Coulomb" friction is calculation according to Equation 5.4. The viscous friction limits the friction force, based on Equation 5.6.

$$v_{rel} = v_1^{tan} - v_2^{tan} \tag{5.3}$$

$$F^T \leq \mu F^N \tag{5.4}$$

where:

$$\mu = \mu_d + (\mu_s - \mu_d) exp(-d_c \left| v_{rel} \right|) \tag{5.5}$$

$$F_{lim} = \mu_v A_c \tag{5.6}$$

where: F^N –normal contact force, F^R –fractional force, v_{rel} –relative velocity between two parts v^{tan} –tangential velocity, μ_s –static coefficient of friction, μ_d –dynamic coefficient of friction, d_c –exponential decay factor, μ_v –coefficient for viscous friction, A_c –area of the segment contacted.

Basis of the previously performed investigations, these calculations using the 7-cell structure meshed by elements of 0.4 mm. In the Table 5.3, there are collected values of the friction coefficients assumed between the honeycomb and the front and rear plates. The resulted dependences of the force in time are presented in Fig. 5.13. When the frictionless conditions are applied, the structure slides on the plate surfaces and undergoes strong, non-local buckling which effects are visible in the force evolution. When the non-zero friction coefficients are chosen, better modeling of the structure deformation is obtained. The calculations with various sets of the friction coefficient give similar results but its exact values have a minor influence on the results.

Table 5.3: *Configurations of the friction coefficients between the honeycomb and the plates.*

Friction coefficients	**Set 1**		**Set 2**		**Set 3**		**Set 4**	
	Rear plate	**Front plate**	**Rear plate**	**Front plate**	**Rear plate**	**Front plate**	**Rear plate**	**Front plate**
Static	0.0	0.0	0.2	0.4	0.3	0.5	0.5	0.7
Dynamic	0.0	0.0	0.1	0.3	0.2	0.4	0.4	0.6

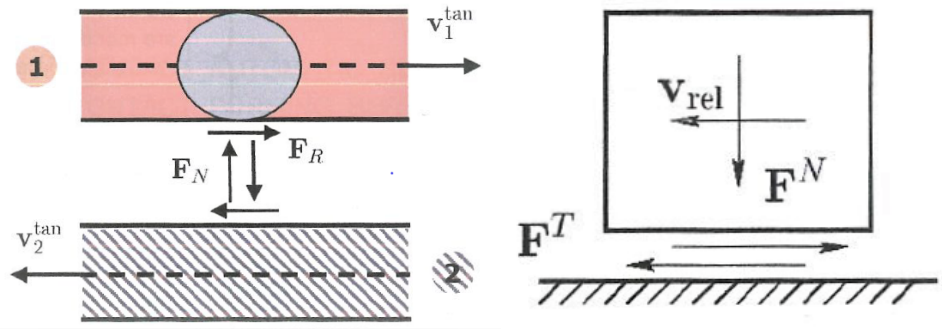

(a) (b)

Figure 5.12: *Definition of friction in LS-DYNA presented as (a) the scheme of the operation mode during the contact and (b) the relation of the relative velocity between two parts.*

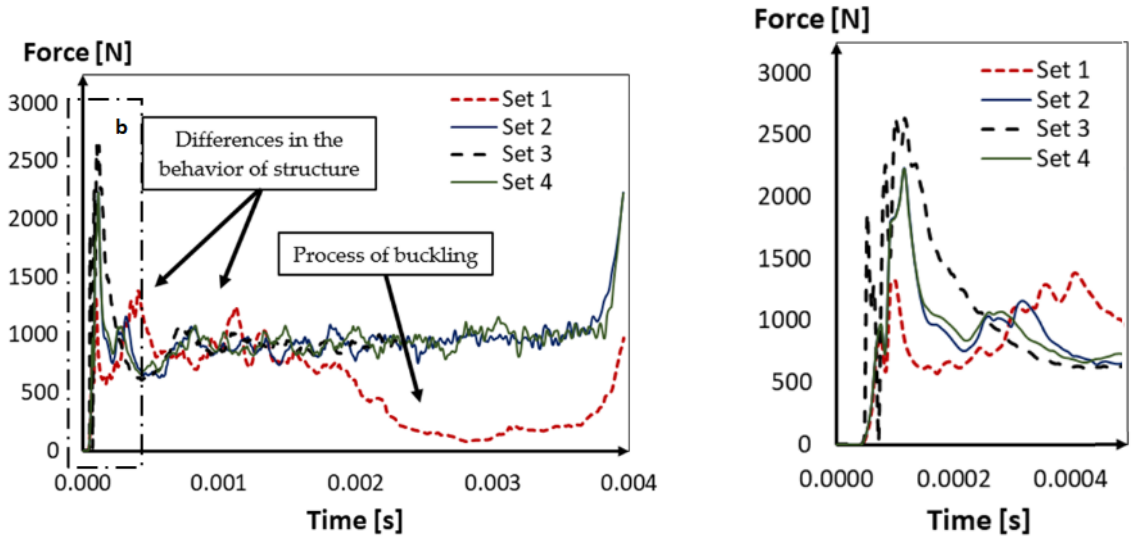

(a) (b)

Figure 5.13: *(a) Comparison of the force-time curves when different friction coefficients are applied (b) close-up of the peak of force.*

Except from the set of frictionless conditions, the other friction sets do not influence the force collected for nodes on the upper surface of the bottom plate. When the frictionless conditions are applied, the structure undergoes strong buckling which effect is seen in the force graph (Fig. 5.13).

5.4.4 Strain rate sensitivity

To describe plastic deformation of the aluminum honeycomb, the Johnson-Cook model was chosen which parameters are fitted to the stress-strain curve. The general influence of A, B, C and n parameters on the shape of curves is presented in Figure 5.14.

$$\sigma = \left[A + B\varepsilon_p^n\right]\left[1 + C\ln\left(\frac{\dot{\varepsilon_p}}{\dot{\varepsilon_0}}\right)\right]\left[1 - (T^*)^m\right]$$

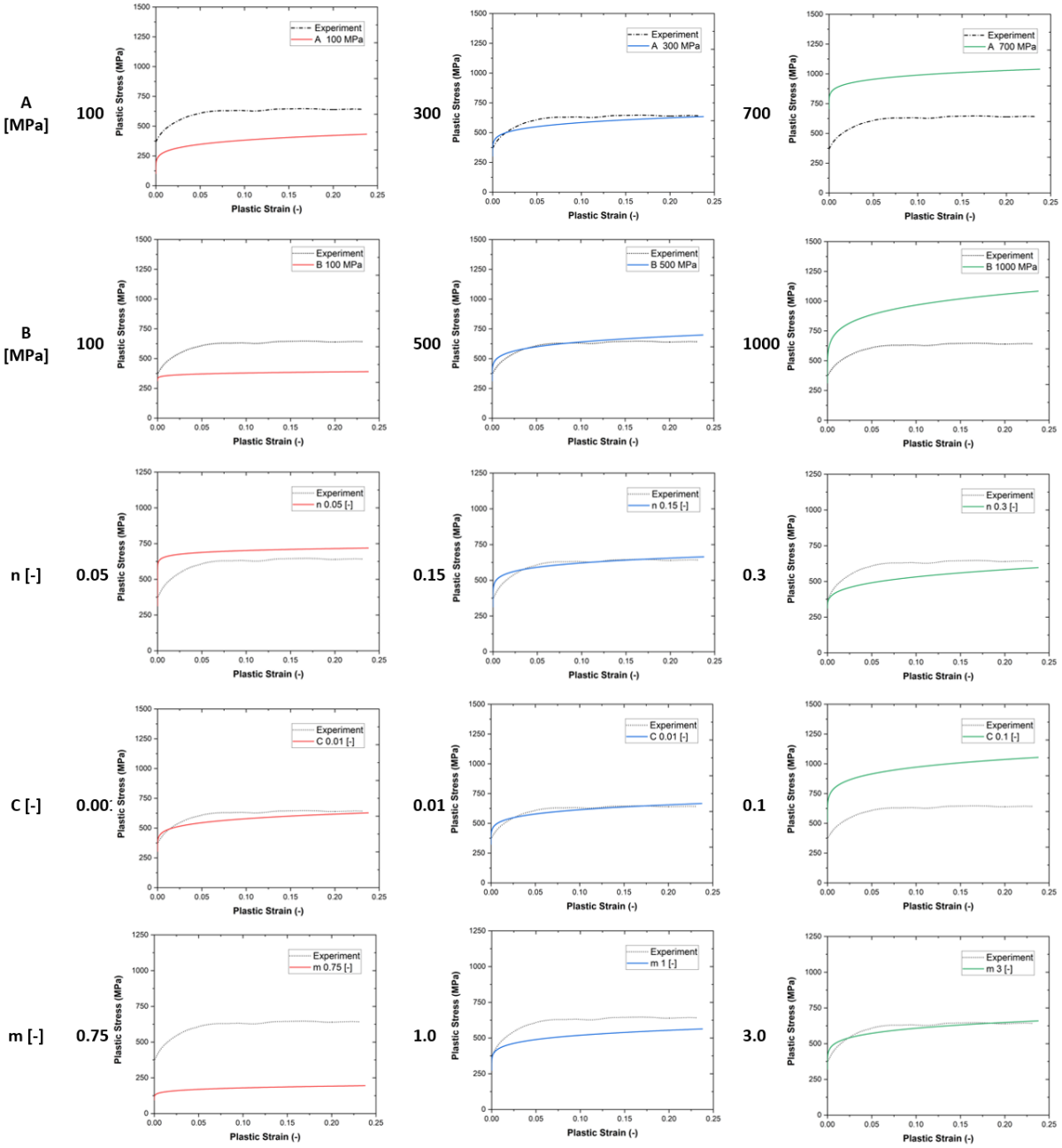

Figure 5.14: *Impact of the individual parameters on Johnson-Cook model.*

For the tested honeycomb made from alloy AA3003, the A, B, C and n parameters are equal to 111.7 MPa, 31.5 MPa, 0.001 and 0.213, respectively [20]. The parameters are obtained by the least square method. The parameter C describes the strain rate sensitivity of a material. Another objective is a verification if changes of the C parameter affects the structure behavior making it more sensitive to strain rates. The simulations for the 7 cells model with 0.4 mm

elements size are carried out for C equals to 0.01 and 0.1, respectively (A, B and n remain unchanged). Increase of the strain rate constant C by 10% and 100 % results in higher value of stresses, about 5 % and 40 %, respectively (Fig. 5.15) but the character of the force curves is similar and mechanism of folding has slight changes, especially at the top and at bottom interior cell.

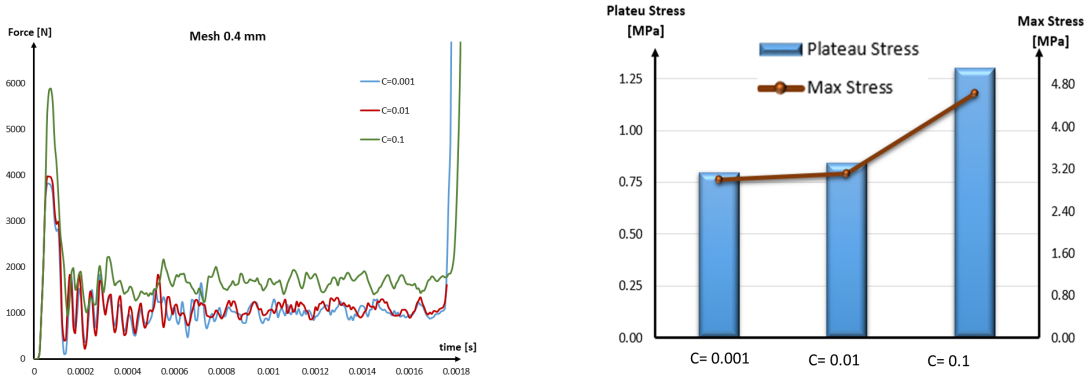

(a) (b)

Figure 5.15: *(a) Force and (b) peak stress and mean plateau stress calculated by means of the JC material model with different values of the C parameter in Eq. 5.1 .*

5.4.5 Thickness of walls

The geometrical parameters of the structure, such as wall thickness, are also checked. This is due to the fact that the real structure is not perfect, and its parameters may be different from the ones assumed. The considered model with wall thickness of 0.15 mm is compared with structures with the thicknesses of 0.07 mm and 0.3 mm. This introduced significant changes, which are shown in Fig. 5.16. When the thickness is increased, the number of folds decreases and the compression process is longer. Thinner walls by half causes decrease results almost three times, and the average wavelength is shorter. Obtained results allow to conclude that further change of dimensions as the length of the edge or angle may introduce significant changes.

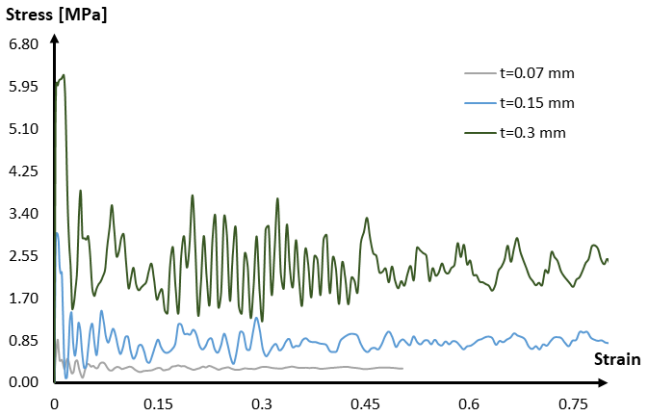

Figure 5.16: *Comparison of the stress-strain curves for different thickness of wall cell.*

5.4.6 Structure geometry

In the first approach, the studies is based on the honeycomb geometry with the ideally dimension of the cells. Figure 5.18b presents the developed honeycomb with the network of a "regular hexagon", which edge length is equal to 7 mm. However, the real structure differs significantly from the assumed idealized one. In reality, the unit cell has two short and four long edges and a range of interior angles varies between [80°] and [145°], Fig. 5.18a. Differences in geometry have led to propose another cell pattern called "hexagon", Fig. 5.18c. The structure is composed with a cell of 6 mm and 8.5 mm long edges and the angle between two longer edges is [90°]. The thickness of ligaments remains as given in the product datasheet [11], i.e. 0.07 mm for single walls and 0.15 mm for double walls.

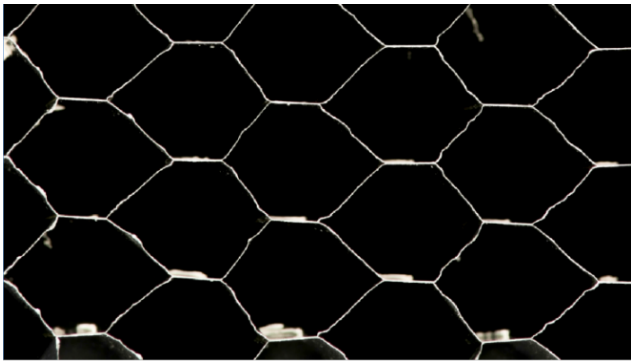

(a)

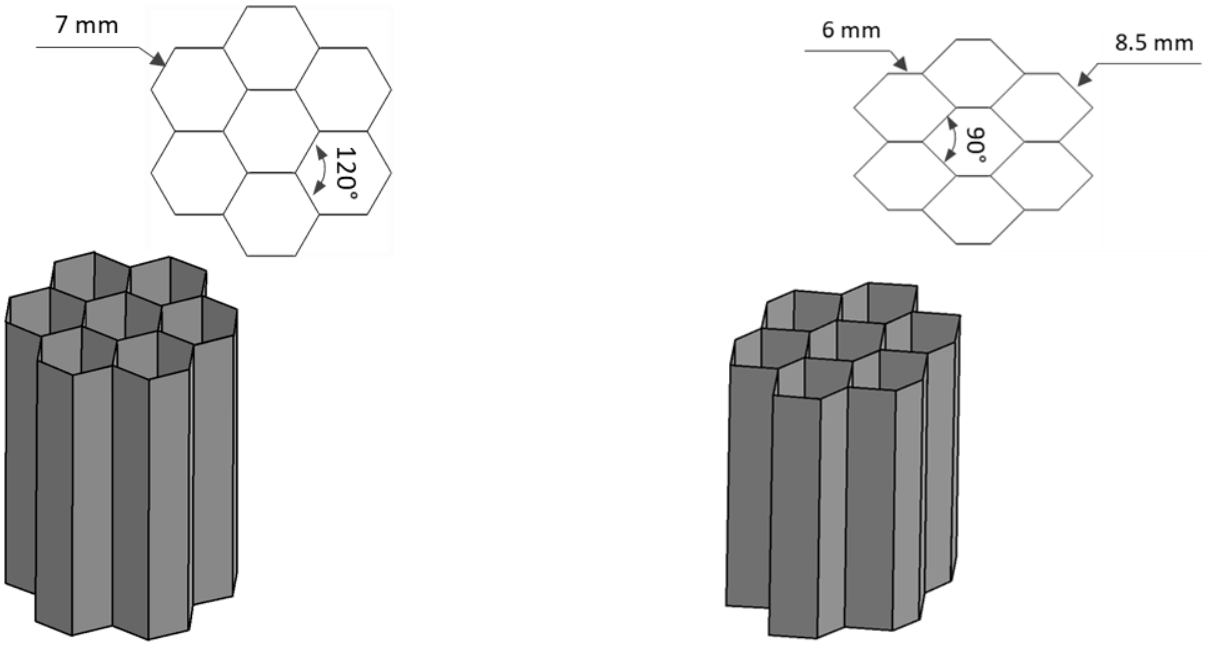

(b) (c)

Figure 5.17: *Comparison of cells of the honeycomb structure: (a) upper-view on the real sample, (b) geometry idealized by regular hexagons cells, (c) hexagonal cells with dimensions closer to real ones.*

The comparison of the obtained numerical results with the experimental values gives a 13% error of the mean force calculated for the idealized structure based on the "regular hexagon", whereas a simulation of the structure with the geometry closer to the real one results in an error reduction to 4%. The peak of the forces has a similar value in both simulations and 34% overestimates the experimental value, Fig. 5.18.

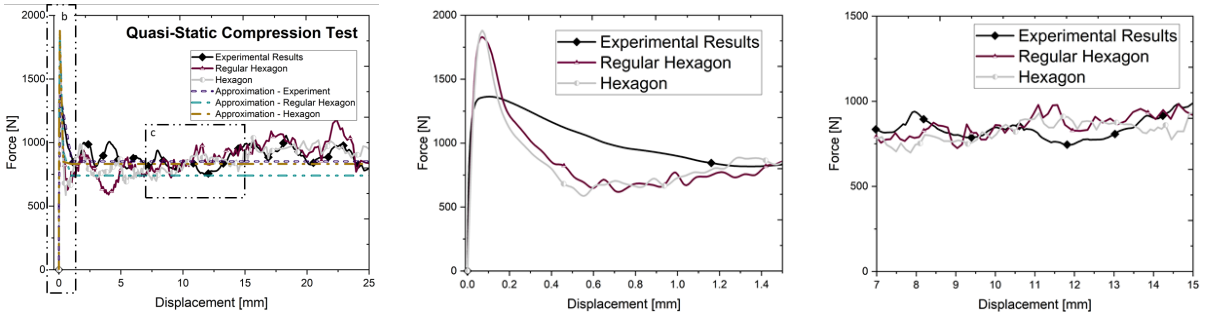

(a) (b) (c)

Figure 5.18: *The results (a) from the implicit simulations with the regular hexagonal and hexagonal cells referenced to force results from the quasi-static experiment (b) close-up of the peak of force (c) close-up of the results in the plateau range.*

5.5 Comparison of results from numerical simulations of traditionally manufactured structures subjected to a blast load

The above-presented verification of numerical conditions proves that the computation model results in the reliable modeling of the structure behavior. On the basis of the model validated by the quasi-static compression test simulation, the modeling of dynamic deformation is prepared. The subsequent section presents its results followed by an analysis and discussion. Experimentally obtained pressure loads resulted from the detonations of 15 g, 30 g, and 50 g of the C-4 charge given in Fig. 4.4 are considered as the initial loading in the numerical model of the blast test configuration. This is possible because in the discussed configuration, no fluid-structure interaction effects occur and the response time of the plate is larger than the blast wave duration. The registered responses of the honeycomb structures to the blast-resulted compression are then compared with those obtained numerically.

Figure 5.19a presents the comparison between the experimentally measured and numerically modeled response of the 53-cells structure to the shock caused by the detonation of 50 g of C-4. In the experimental campaign, the detonation of the charge of 50 g generates the strongest load impulse which leads to the full compression and densification of the 53-cells structure. The registered signal may have been affected by particular dynamics of the set-up, related to the rigidity of the test configuration. These strong fluctuations are not visible in other experimentally obtained curves and the artificiality of this effect is proven by the observation that the calculated values of the peak and mean stresses are close to those obtained in the experiment, i.e. 1.36 MPa vs 1.37 MPa (σ_{peak}) and 0.82 MPa vs 0.71 MPa (σ_{mean}). In the case of the 7-cell honeycomb presented in Fig. 5.19a, the curves have similar tendencies and the amplitudes of stress fluctuations do not differ much. The values of the peak and mean stresses are as follows:

1.1 MPa vs 1.44 MPa (σ_{peak}) and 0.64 MPa vs 0.61 MPa (σ_{mean}), which confirms an acceptable accuracy of the simulation.

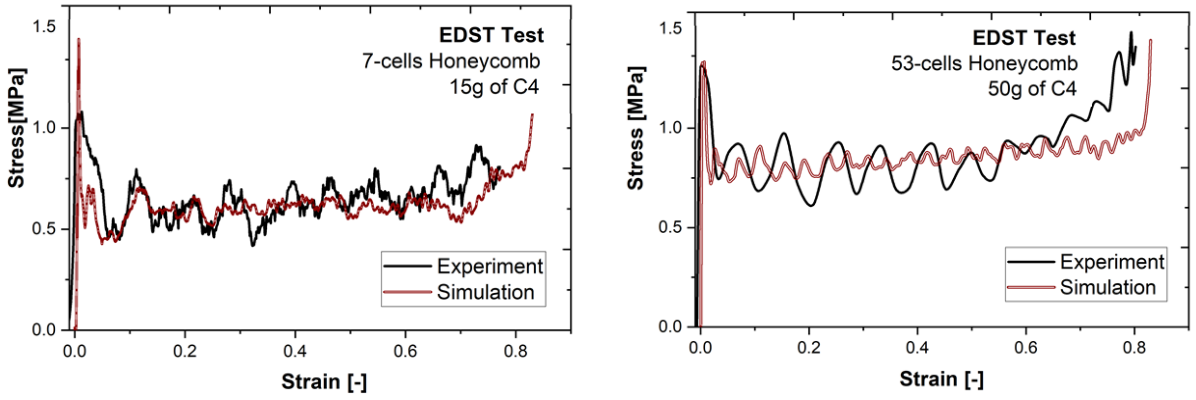

(a) (b)

Figure 5.19: *Comparison between stress-strain curves obtained in the simulation and in the EDST blast test for (a) 53-cell structure compressed in detonation of 50 g C-4 and (b) 7-cells structure compressed in the detonation of 15 g C-4.*

The values characterizing structure responses collected for the 7-, 19- and 53-cells honeycombs are presented in Table 5.4, where the experimental and corresponding numerical results are summarized. Another comparison is presented by the bar graphs in Figure 5.20. On average, in the simulation the mean stresses are correctly foreseen (Figs. 5.20a, 5.20c, 5.20e) but the peak stresses are overestimated (see Figs. 5.20b, 5.20d, 5.20f). The results of mean stresses show similar values for the same amount of charge used, regardless of the number of cells. The greatest discrepancy is occurring for peak values, both in simulations and experiments, however, still remains within the acceptable error limits. It must be emphasized that the numerical model does not account for all features which the real honeycomb structure may have, i.e. imperfections in the material or in ligament joints or irregular cells, which can be the argument explaining the discrepancies between the numerical and experimental results. On the other hand, in the EDST blast test the material response is not directly measured - the data are obtained by the image analysis and from the load sensor fixed on the bunker wall. Therefore, the experimental readings may be affected by the limitations of the measurement techniques, which could be a reason for the difference, not observed in the simulations.

Table 5.4: *Comparison between the numerical (S) and experimental (E) characteristics of structural responses.*

Structure	**7-cells**				**19-cells**				**53-cells**			
	σ_{mean} **[MPa]**		σ_{peak} **[MPa]**		σ_{mean} **[MPa]**		σ_{peak} **[MPa]**		σ_{mean} **[MPa]**		σ_{peak} **[MPa]**	
Load	S	E	S	E	S	E	S	E	S	E	S	E
15g of C4	0.64	0.61	1.10	1.44	0.62	0.57	1.10	1.55	0.62	0.64	1.00	1.53
30g of C4	0.66	0.66	1.21	1.52	0.66	0.63	0.99	1.40	0.63	0.66	1.02	1.59
50g of C4	-	0.71	-	1.78	-	0.64	-	1.43	0.82	0.71	1.36	1.37

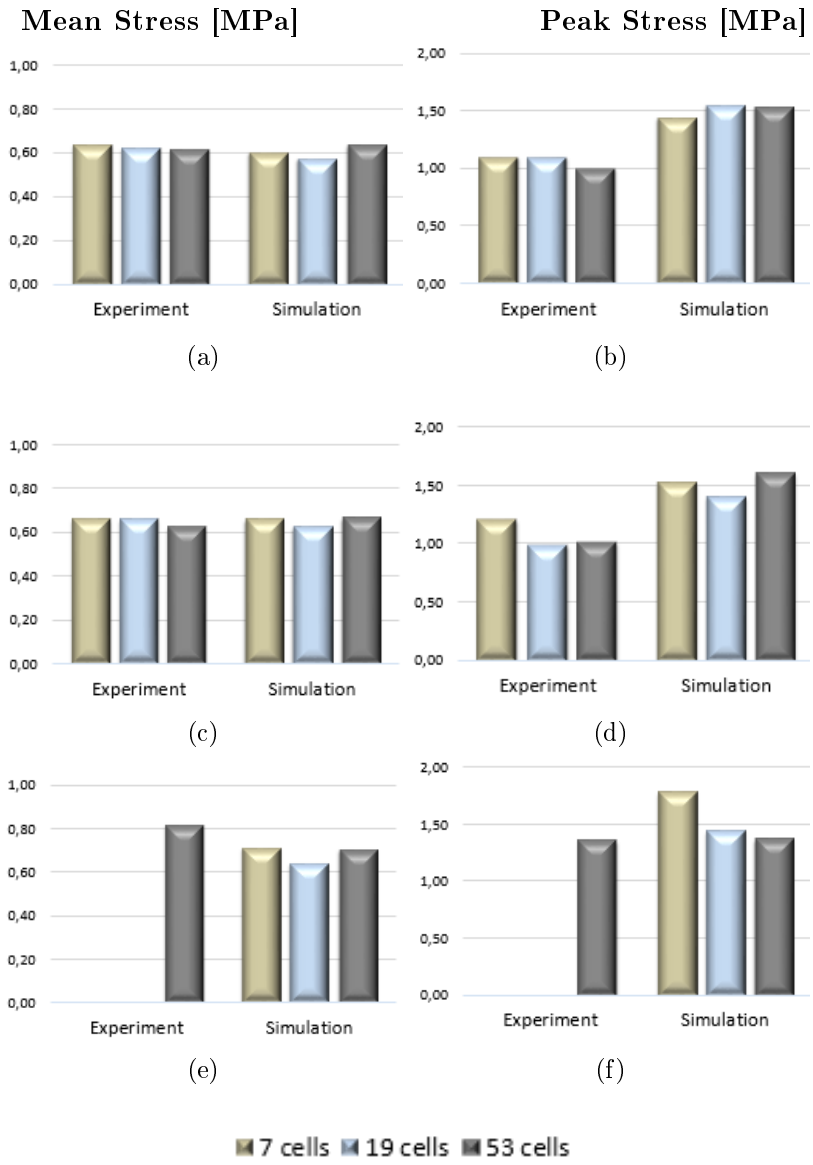

Figure 5.20: *Comparison between the experimental and numerical mean (a, c, e) and peak (b, d, f) stresses characteristic for the structural responses to compression caused by the detonation of various masses of C-4.*

The structural response represented by the stress-strain curves in Fig. 5.19 is complemented by the visualization of deformation, shown in Fig. 5.21. The numerical results may complete the experimental investigation and may add additional analysis to observations provided by means of high-speed camera records (given as an example in Fig. 5.21) The deformation mechanism of the honeycomb consists of the formation of folds. In experimental compression tests, folds are creating very quickly, and finally are strongly compressed and very thin, which makes an analysis of their formation difficult. In the simulation, the compression process may be followed step by step and analyzed in detail. Figure 5.21 shows a sequence of deformation of the 53-cell (Fig. 5.21a and 7-cell (Fig. 5.21b) honeycombs subjected to a load of 50 g and 15 g of C-4, respectively.

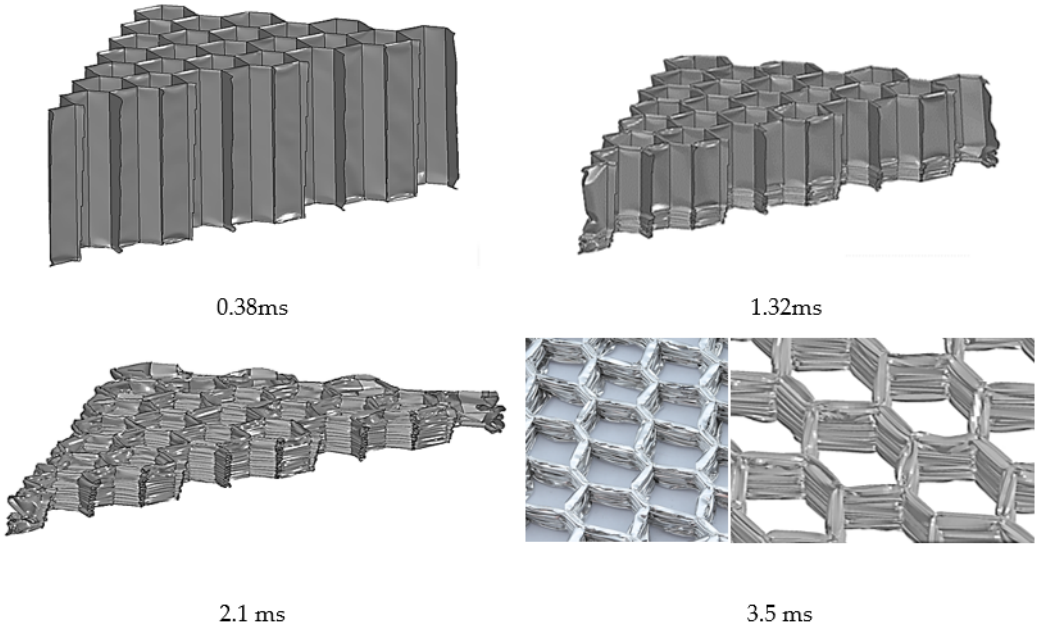

(a)

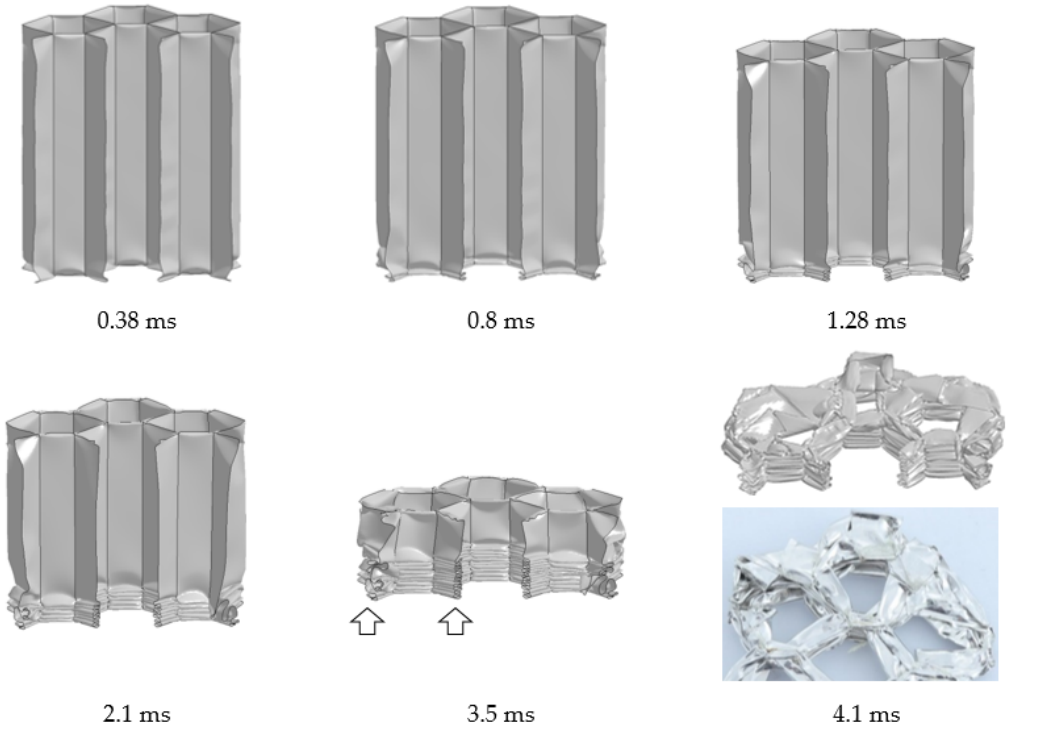

(b)

Figure 5.21: *Subsequent deformation for the cross-sections of (a) 53-cell structure compressed due to detonation of 50 g C-4, (b) 7-cell structure compressed due to detonation of 15 g C-4.*

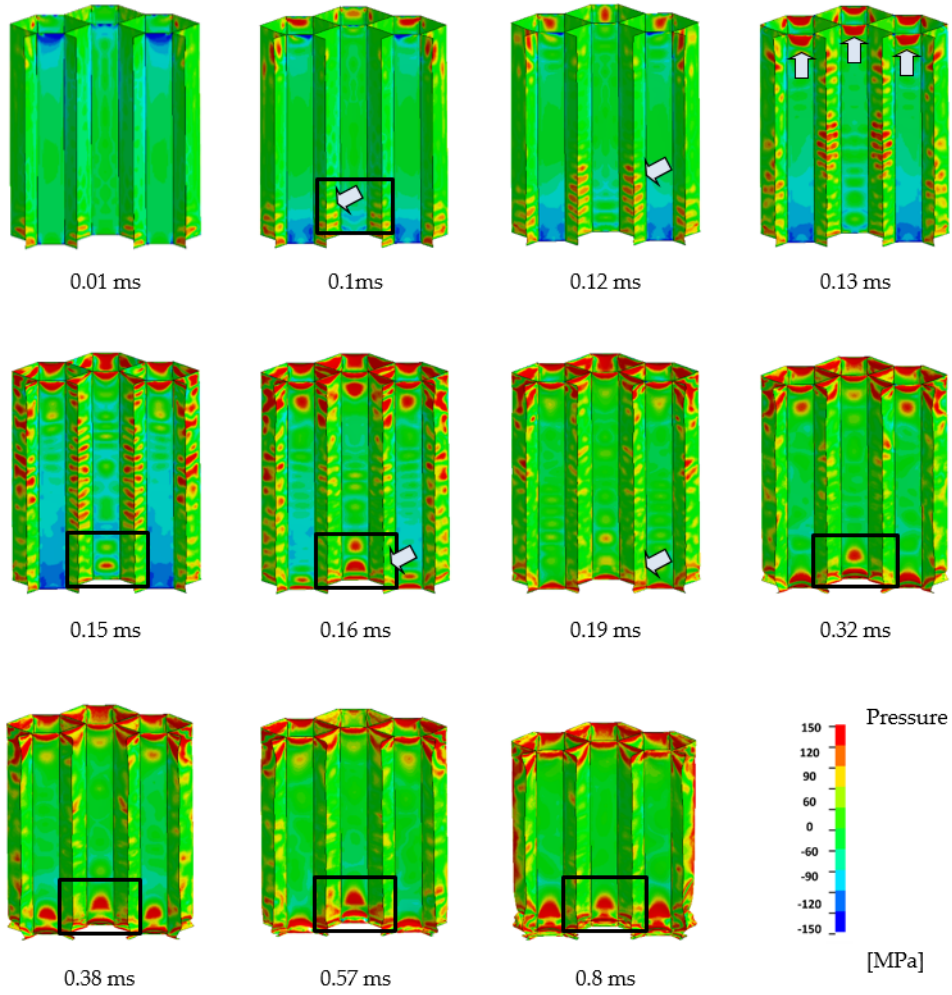

Figure 5.22: *Beginning of compression of the 7-cells structure caused by a detonation 15 g of C-4 charge. Maps of the hydrostatic stresses.*

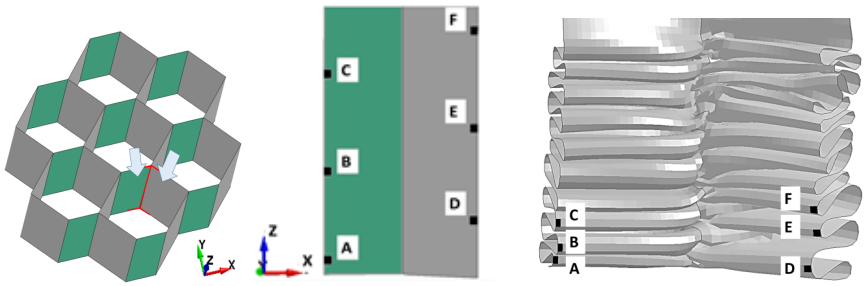

(a) (b) (c)

Figure 5.23: *Formation of the first 3 folds in the 7-cell honeycomb structure: (a) general view of the chosen walls, location of the points: (b) before deformation and (c) after deformation.*

Because of the larger energy of a 50 g explosion, the 53-cell structure is fully compressed faster (in 3.5 ms) than the 7-cell honeycomb due to the detonation of a 15 g charge (in 4.1 ms). For both structures, the folding formation starts from the bottom and in the final stage, they are both fully compressed to 12 (single walls) and 11 (double walls) very thin folds. The boundary cells, not supported by their neighbors, are less stiff so they are more irregularly deformed comparing to the interior cells folded in a more regular manner (Fig. 5.21,time step: 3.5 ms). Like in the experiment, the upper part of the 7-cells honeycomb is partly folded due to the contact with the accelerated plate (Fig. 5.21, time step: 4.1ms). As presented in Fig. 5.21, the modeled deformation of the 7-, and 53-cell structures (as well as of the 19-cell structure not shown here) are similar, so for the further analysis of the folding mechanism, the 7-cells structure is chosen.

Figure 5.22 shows the honeycomb deformation with superimposed maps of the first invariant of the stress tensor (pressure) averaged over the shell thickness. In the early stages of compression, it may be observed that at the moment when the plate hits the structure, the induced stress propagates as a wave to the bottom (0.1 ms) where reflected, starts to travel back (0.12 ms) to the upper part of the honeycomb, where due to the contact with the plate, the structure is already partly strained (0.13 ms). The waves are further reflected and continue their travel again to the bottom part, where the stress concentrates (0.16 ms) forming the first fold. Since then, the deformation is localized behind the fold which is followed by stress concentrations forming subsequent folds, bent "in" and "out" from the middle plane of cell walls.

The mechanism of fold formation may be analyzed closer by looking at the interior cell walls in Fig. 5.24. Three points A, B, and C on the double-wall (marked by green color) are indicated on the three first "bent-out" folds. Accordingly, for the single wall, points D, E and F are chosen. Different stress states which the elements undergo are visualized by the maps of pressure in Fig. 5.24a. Schematically, the first stage of deformation is characterized by an increase of force and elastic deformation of the walls of the honeycomb. During creating the "A" fold, a local peak of force can be seen in 0.21 ms, Fig. 5.24b. It indicates the beginning of the fold formation on a single wall, however in the opposite direction than fold "A". The minimum force in this range indicates the maximum strains, common in two direction (bending "in" and "out") and a starting point for the formation the second-level folds (marked by "D" point). After reaching the maximum force in this range (0.32 ms) the single wall is bending until the minimum force when the folds "B" (0.47 ms) and next "E" (0.7 ms) are starting to deform. In 0.8 ms a new level of folds is occurring (fold "C" and next "F"), according to the schema described above. The process of creating the three first folds ends in 1.3 ms, when the fold "F" is formed.

Figure 5.25 collects the graphs of the time evolution of the hydrostatic stress of the points "A" and "D" and of the equivalent plastic strain for all analyzed points. Numerous fluctuations are observed in the pressure curve featuring the complex elements loading paths, slightly different for the two chosen points. At a certain moment (0.16 ms for "A" and 0.32 ms for "D" −Fig. 5.25b), the stresses are concentrating which localizes a fold and causes a sudden increase of the plastic strain. The stiffer double walls are characterized by higher limit for forces that can be applied without plastic deformation, therefore states of stresses on the yield surface are higher for the point "A" than for "D". The evolution of equivalent plastic strain in time shows the order of fold formation: fold "A" (double wall) and then "D" (single wall) followed by the second folds B and E and finally, folds −"C" and "F". The Fig. 5.25b indicates also that the folds "A", "B" and "C" forming in the similar way, opposite to the folds on the single walls, which are less stiff and therefore may form a different size of folds.

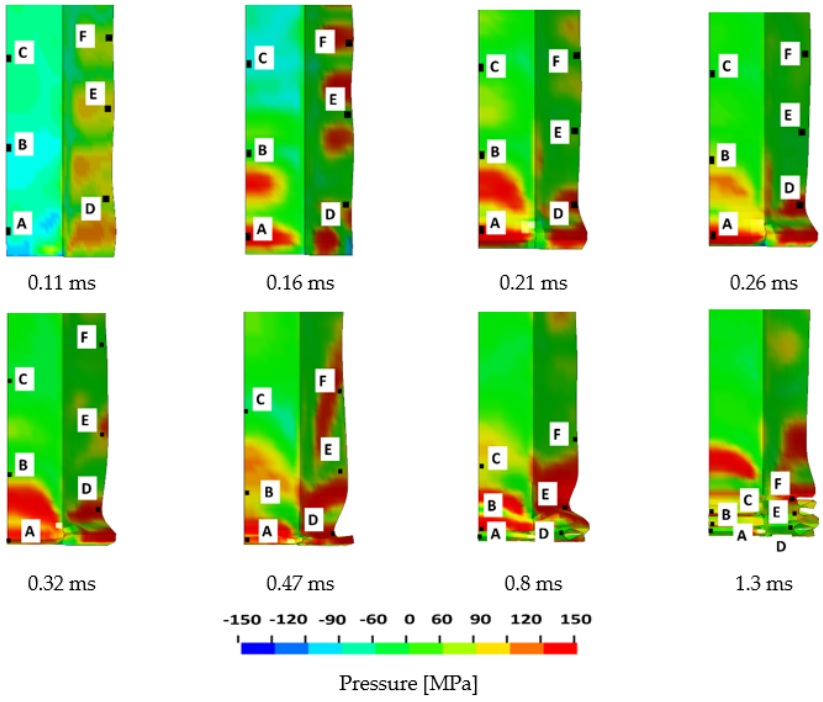

(a)

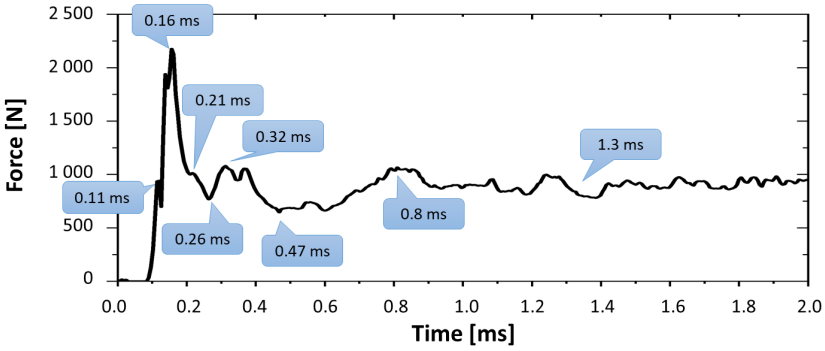

(b)

Figure 5.24: *(a) Deformation in maps of the pressure in the selected time instances of the first 3 folds in the 7-cell honeycomb structure, (b) results of force over time.*

Based on the experimental and numerical tests carried out, it is already known that folding of honeycombs in compressive tests may occur in different order starting from the top or the bottom side of honeycombs or even sometimes originating in the middle [23]. The reasons which determine the stress concentrations are complex and not fully clear. In the discussed blast and quasi-static experimental tests, folds start to form from the bottom side, which is also reproduced in the simulation. It must be emphasized that the above-described simulation models the folding process without any additional numerical techniques used sometimes to impose the first fold (like for example, an artificial structure weakening by deletion of a mesh element in the place of the expected fold). The above-discussed model consists of the shell honeycomb structure regularly meshed by a fine mesh which coupled with the optimized material model is sufficient to obtain correct results.

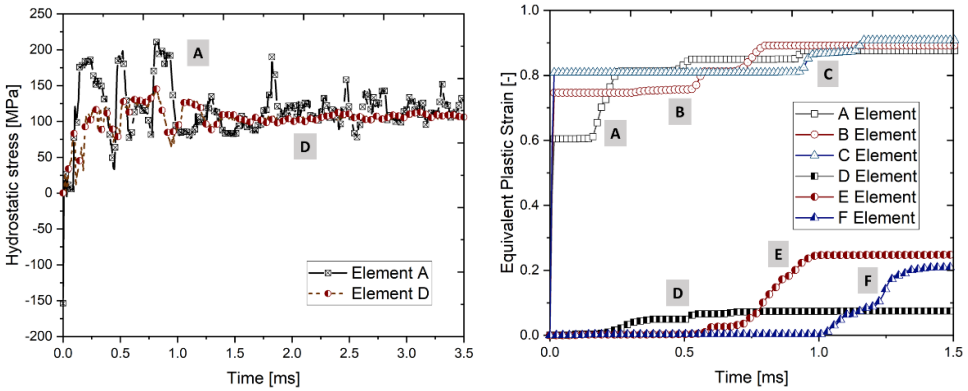

(a) (b)

Figure 5.25: *(a) Hydrostatic stresses in time for the element chosen on the double ("A") and the single wall ("D") from the folds formed as the first and (b) evolution of equivalent plastic strain for 6 chosen elements.*

5.6 Numerical approach for AM structures

The numerical simulations relating to the blast compression tests of the AM structures are developed using explicit modeling and a Lagrange approach in LS-DYNA. It provides the calculation processes at high strain rates. Figure 5.26 shows an example of the developed numerical task for the considered AM structures. The simulations have been created as a result of the development of the previously discussed issues in-deep of the thin-walled honeycomb structures (Section 5.4). However, in this case, the numerical task consists of the solid parts of the AM sample placed between two steel plates. The contact between the components and the boundary conditions are assigned as it takes place in the previous studies (Section 5.4). The steel blocks are modeled according to the description in Section 5.4.3. The $^*MAT\_Linear\_Pleasticity$ 024 allows to the introduction of the in-house obtained characteristics of the AlSi10Mg aluminum alloy (Chapter 3) to describe the material properties of the printed powder. The selection of the set of characteristics depends on the sample orientation to the build platform during manufacturing and the load direction. A maximum effective strain at failure is used to simulate the brittle damage.

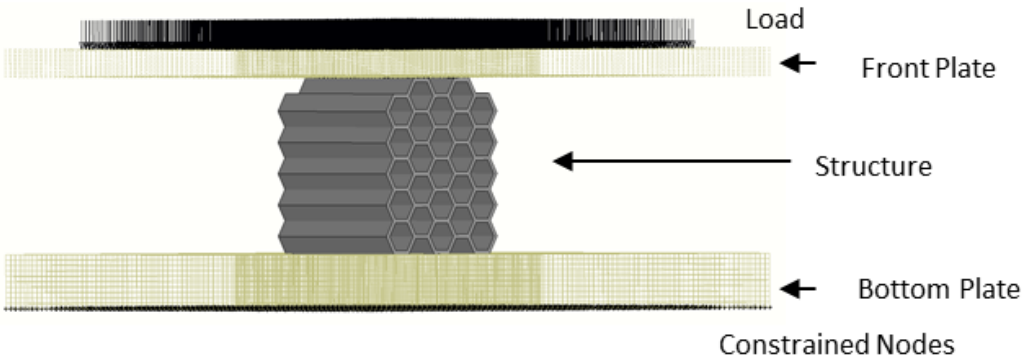

Figure 5.26: *The numerical task in LS-DYNA of the AM structures on the example of the honeycomb structure.*

5.7 Discussion of the main issues of the numerical simulations for AM structures

5.7.1 Geometric accuracy

One of the biggest challenges with the powder−bed fusion methods in the blast protective systems is achieving the required geometric accuracy of the "as-fabricated" components. The shape of the struts or different wall thicknesses affect the stiffness of the structures, which may influence the amount of the transmitted force. Depending on the used powder and the process parameters, the typical part accuracy obtained by the DMLS method should be equal to ± 0.1 mm [24]. Whereby, the minimum wall thickness is 0.3−0.4 mm.

The dimensional accuracy has been taken into account during the study on the manufactured absorbers. The biggest difference between the CAD model and the obtained part has been identified for one of the honeycomb samples. The structure has been design to obtain the wall thickness of 0.72 mm. The performed numerical studies based on the ideal structure geometry exhibit almost two time higher results. As shown in Figures 5.27, which compare the stress-strain (Fig. 5.27a) and toughness-strain (Fig. 5.27b) between the simulation and experiment.

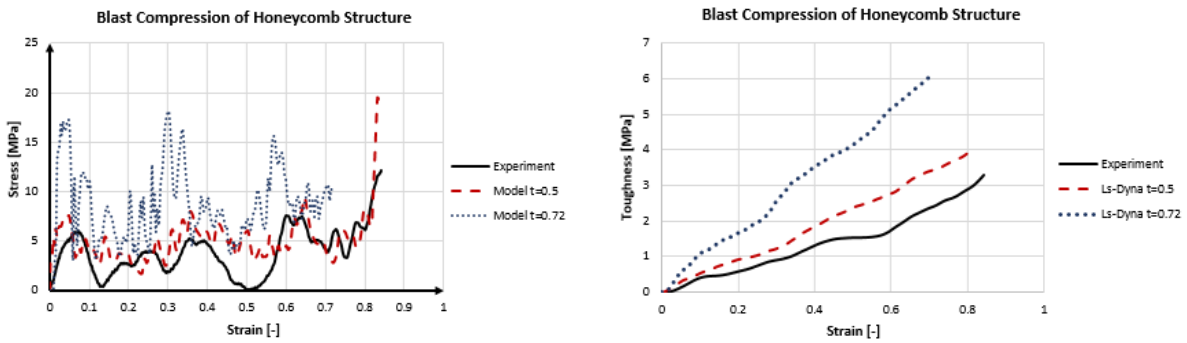

(a) (b)

Figure 5.27: *Comparison between the blast experiment and simulations of the models with the wall thicknesses of 0.5* mm *and 0.72* mm *(a) the stress over strain results, and (b) toughness over strain results.*

The comparison of the assumed mass of the model (Fig. 5.29b) with the actual structure (Fig. 5.29a) indicates that the obtained part is characterized by a significantly lower wall thickness (Fig. 5.29c). The thickness measurements with conventional tools did not give correct results due to the large unevenness of the surface. However, the photogrammetry measurements prove the print inaccuracies and high roughness (Fig. 5.28). Based on the image analysis, the difference in wall thickness is between 0.38−0.56 mm, and the mean value is equal to 0.5 mm. The new model of the honeycomb structure allows obtaining a similar mass to the actual structure. The desirability of the wall thickness correction is also confirmed by the qualitative results presented in the figure (Fig. 5.27) The difference in dimensions of 30 % may be due to the physical limitations of the powder melting and may also indicate technical problems such as with the slicer code. Obtaining high precision of the printed parts is a major challenge for the AM technique, which may limit the use of this production method.

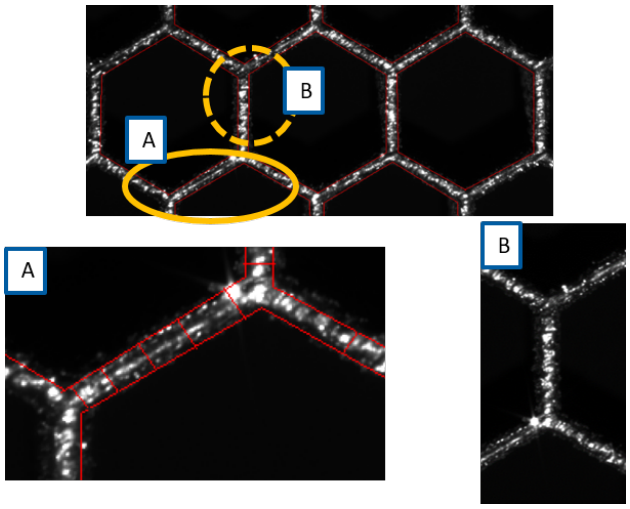

Figure 5.28: *The image analysis if the honeycomb structure.*

$\rho_{AlSi10Mg} = 2.6\ \left[\frac{g}{cm^3}\right]$	Experiment	Model t=0.72	Model t=0.5
Mass of Structure	12.13 g	17.5 g	12.15 g

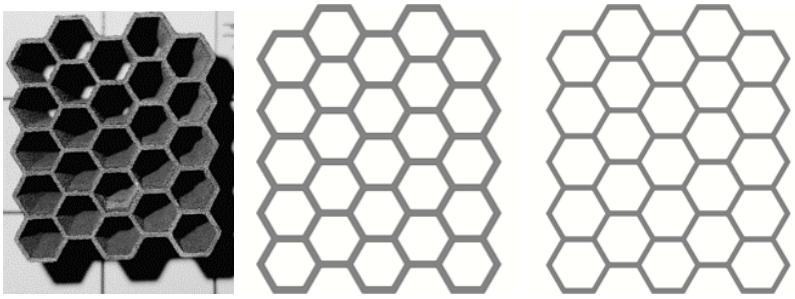

(a) (b) (c)

Figure 5.29: *Mass analysis of (a) the actual structure, (b) CAD model before and (c) after wall thickness improvement.*

5.7.2 Material characteristics

Additive manufacturing is a relatively new technology compared to traditional production methods such as casting. The research into the materials is still at a primary stage. The increase in published results has been visible in recent years. However, it should be mentioned that the literature is still often missing much data. Since numerical simulations require a material model, necessary tests must be carried out independently. As proved in Chapter 3, AM material studies require a large-scale experimental campaign. The performed studies in this thesis indicate the AM material behavior differs depending on the print direction. Therefore, this phenomenon must be considered in numerical simulations. The use of characteristics dependent only on one printing direction may give significant differences in the deformation mode and obtained results.

Moreover, AM material is often much more brittle than the same material used in a production by the traditional methods (as is the case with AlSi10Mg powder [25]). Therefore, additional fracture tests to study stress triaxiality may be useful. However, they are costly and time-consuming. In the LS-DYNA simulations, it is possible to apply non-physical erosion parameters that enable enable simulation of fracture's physical phenomenon. In the discussed examples, the effective plastic strain has been used to introduce the breaking of the bond.

5.7.3 Hardware limitations

The complex geometry of AM structures can be a challenge to properly meshing in numerical programs. The often-used hexahedron elements may prove inefficient and need to be replaced with tetrahedron elements. This increases the possibilities of designing the shapes of the more complex samples. However, the number of elements and nodes also increase significantly. In addition, comparing the tested AM structures to conventional manufactured, the thickness to length ratio has increased by one order of magnitude. Therefore, the shell or beam elements did not allow to simulate of the performed experiments, and the solid parts must be used. The computer's efficiency and calculation time become significant limitations in using more demanding elements.

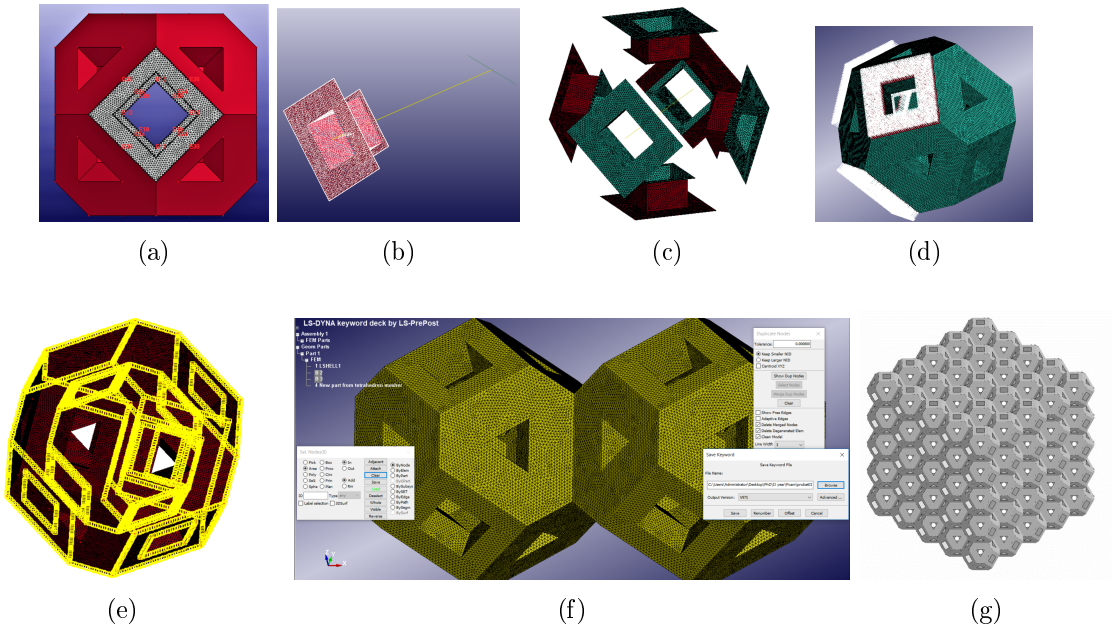

(a) (b) (c) (d) (e) (f) (g)

Figure 5.30: *The formation process of a foam structure in Ls-PrePost: (a) meshing the part of the cell, (b) rotation of a meshed part around the cell center, (c) rotated off the meshed faces, (d) directing the normal vector to the center of the structure, (e) node connection, (f) duplication of the solid cell, (g) obtained structure.*

Complex geometries, such as the tested foam and lattice structures, require a more complicated process to obtain the appropriate FE models than samples with simple geometries. One of the methods of obtaining a mesh for a foam structure is presented in Figure 5.30. First, the unit cells are designed in a CAD program, and then they are subjected to meshing in Ls-PrePost, as shown in Figure 5.30a. In the first step, only part of the cell is meshed by the triangle element type due to the *AutoMesher* function. The meshed part is rotated around the center of the cell, as shown in Figures 5.30b and 5.30c. Therefore, the meshed cell is compatible with successive adjacent cells. After checking the normal vectors that determine the side of the element (Fig. 5.30d), the double nodes have to be connected (Fig. 5.30e). At this stage, the developed cell is a shell part. The *Tetrahedron Meher* function allows the creation of the solid part from a previously formed shell element. This function is demanding and requires an adequately made mesh to connect all nodes. The final step is to duplicate the cells along each axis (Fig. 5.30f), depending on the size of the tested structure (Fig. 5.30g).

5.7.4 Numerical results of the AM structures subjected to blast loading

The developed numerical tasks simulate the ideal conditions of the performed experimental tests when the AM structures are subjected to a blast load caused by the explosion of the 30 g of C-4 charge. Figures 5.31−5.42 compare the dynamic compression processes of the developed simulations with the experimental results. In Fig. 5.31, Fig. 5.34, Fig. 5.37, and Fig. 5.40, it is clearly seen that the behavior of each structure is similar at each stage, and the main deformation modes have been obtained. In addition, the numerical results prove that the structures composed of the 3D unit cell (lattice and foam) are characterized by large strains of the entire structure and exhibit the shear modes during the dynamic compression. At the same time, the deformations of the structures that consist of the 2D unit cell (honeycomb and auxetic) undergo the progressive folding of the cell rows and the band-like stress distributions.

The quantity comparisons between simulations and experiments are presented in Fig. 5.32, Fig. 5.35, Fig. 5.37 and Fig. 5.41. The similar courses of the obtained force-time and stress-strain can be noticed. Due to the many factors affecting the responses of the real structures, the developed numerical tasks can be characterized by slight discrepancies. The inaccuracies may be an effect of the defects of the actual structure, e.g., surface damage, roughness, print accuracy. The results are correlated with the experimental and numerical deformation mods at points "1", "2", "3" in Fig. 5.31, Fig. 5.34, Fig. 5.37, and Fig. 5.40. It is obvious that the previous structural deformation influences further processes of structural destruction and the obtained results. Therefore, the designed ideal conditions in the simulation may omit some experimental issues. For example, the uneven plate load conditions, influence of gravity or sudden compression of the air between the cells can be simulation challenges. The sudden drop in the experimental curves is related to the intensified destruction of the cells inside the structure. In addition, it should be taken into account that the experimental measurements may also be affected by some errors: as a result of the inaccuracy of the sensors or due to the used filters, which average the experimental force results.

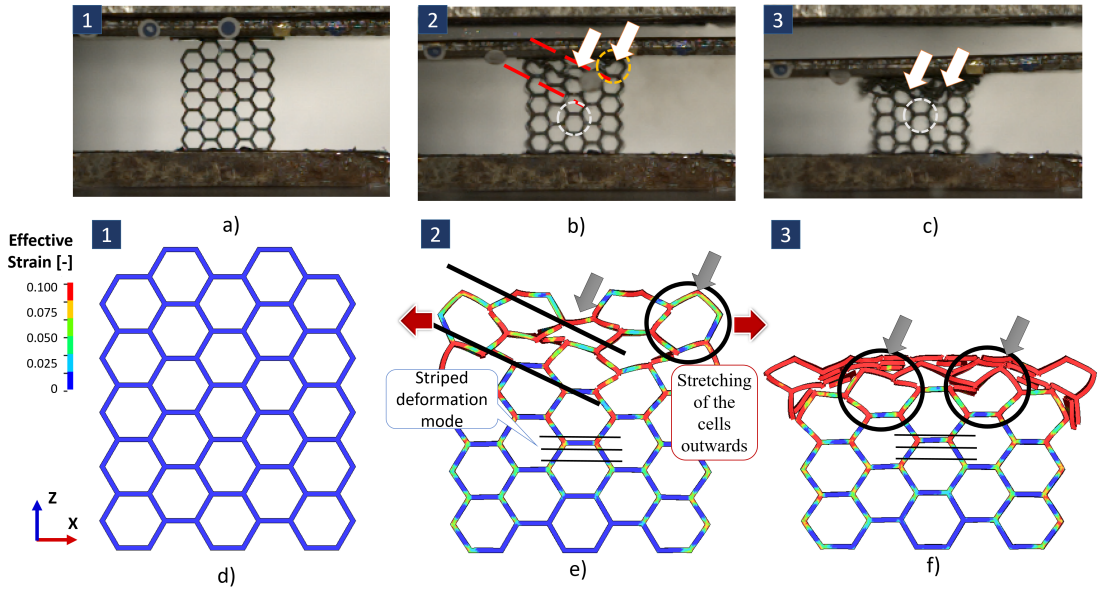

Figure 5.31: *Deformation mechanism correlation of the honeycomb structure between (a-c) experimental photos with (d-f) numerical representation.*

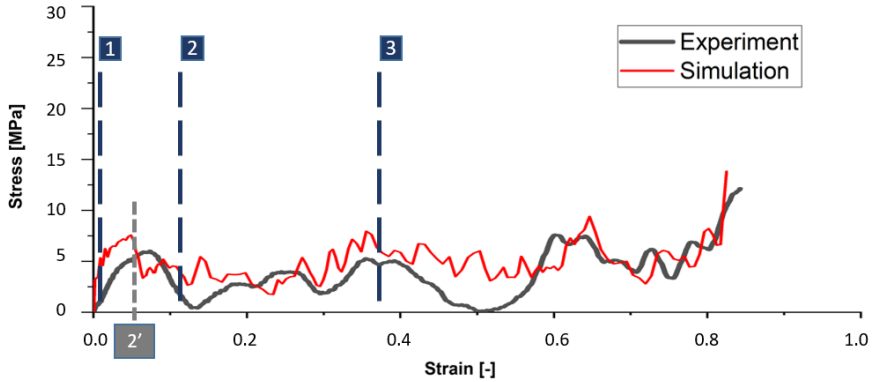

Figure 5.32: *Result comparison for the honeycomb structure between the experiment and simulation with the point indication for Figures 5.31 and 5.33.*

More detailed analyzes of the structure behaviors are presented in Fig. 5.33, Fig. 5.36, Fig. 5.39, and Fig. 5.42. The sample cross-sections at the first peak (“ 2’ ” point on the stress-strain curves) allow to indicate the most strain parts inside each structure. For the structures that consist of the 2D unit cell, equivalent stresses are concentrated mainly at the vertexes of the hexagonal cells (Fig. 5.33c and Fig. 5.36c). The areas around cell corners undergo the strongest deformations. Whereby, the cell bases are almost not deformed and therefore, it can be assumed that partial removal of these areas should not influence of the general structure responses. The similar phenomena is observed for the foam, as shown in Fig. 5.39c. The bases of the cells are almost undeformed, indicating areas that should be optimized to improve the SEA parameter.

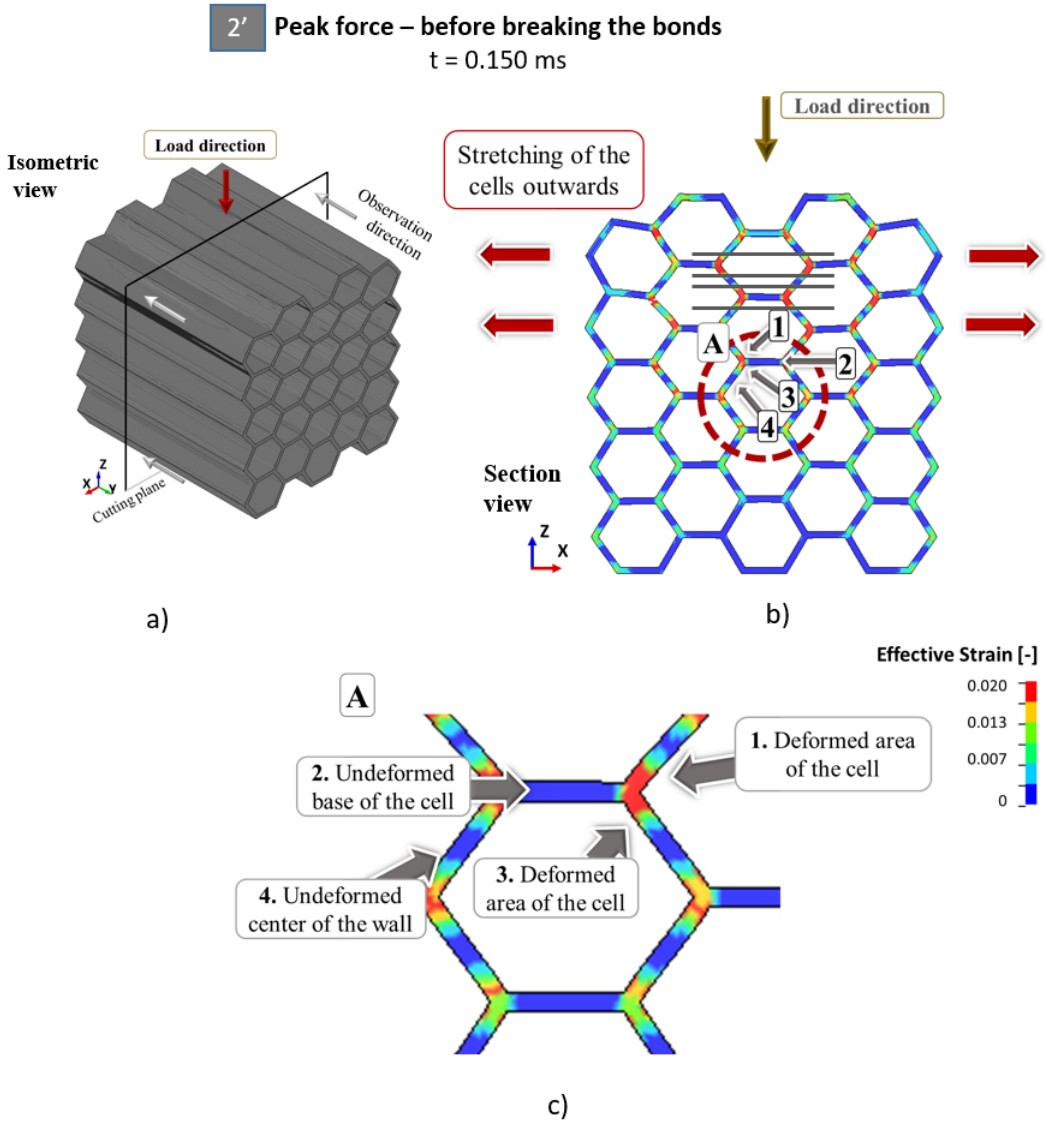

Figure 5.33: *Analysis of the effective strain results, (a) obtained by the honeycomb structure during the blast loading, (b) presented in the cross-section view of the sample, and (c) focusing on the single cell.*

Additionally, it can be seen in Figure 5.42 that the progressive collapsing of the honeycomb structure is a result of the stretching the cells in the upper part of the sample. At this point, the cells in the lower rows are elasto-plastically deformed and do not participate in fractures. The auxetic structure is characterized by a similar deformation mode with regard to the orderly way of the cell collapse. However, it is combined with the folding towards the center of the entire structure under the axial loading. Accordingly, the middle cells prove the elastic-plastic bents of the both basis in the opposite direction (as it is indicated in Fig. 5.36b).

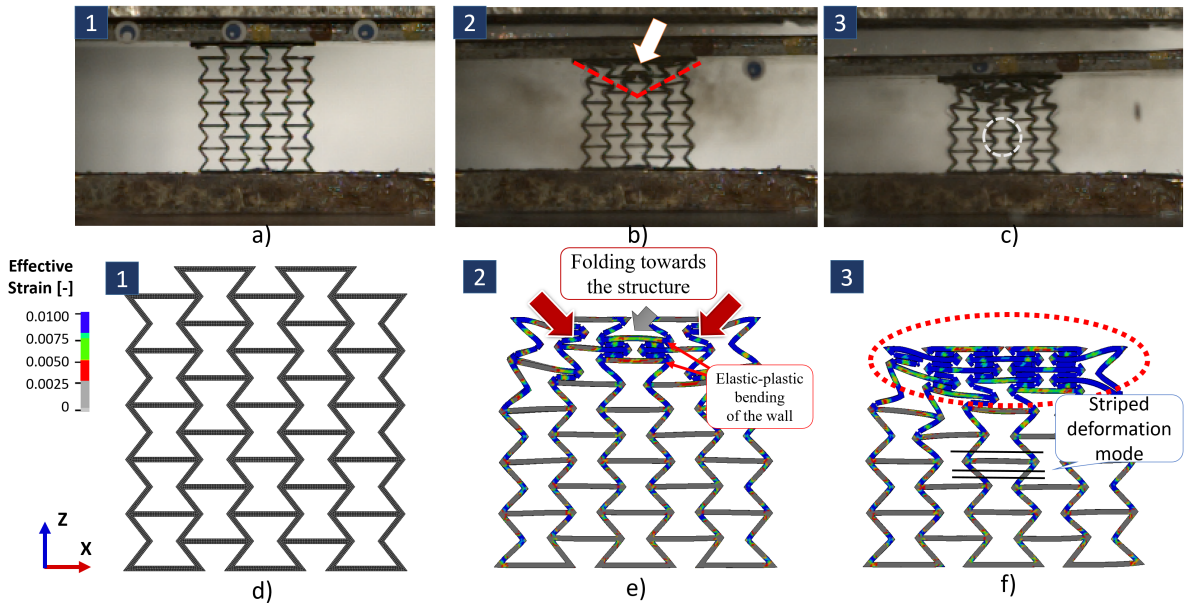

Figure 5.34: *Deformation mechanism correlation of the auxetic structure between (a-c) experimental photos with (d-f) numerical representation.*

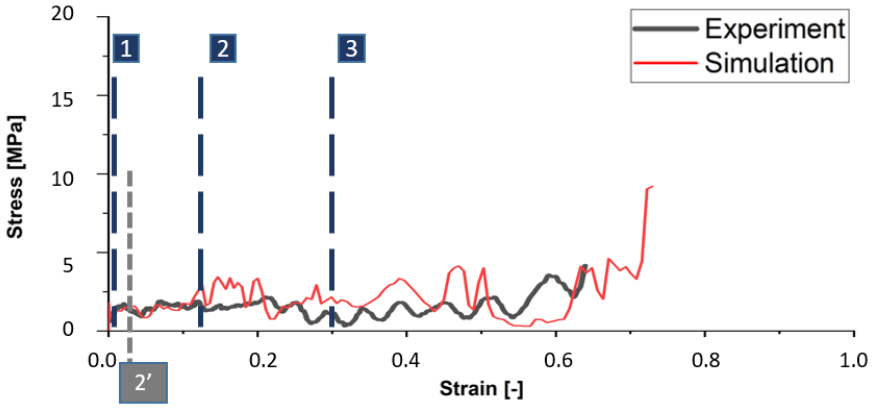

Figure 5.35: *Result comparison for the auxetic structure between the experiment and simulation with the point indication for Figures 5.34 and 5.36.*

Moreover, Figures5.33c–5.36c show that the deformations of the honeycomb and auxetic have a striped and hierarchical character. The significant strains are noticed at the corners (1 and 3 points). Therefore, the fractures take place right next to the vertexes of the hexagonal cells. While the center of the struts remains unaffected (4 point). At the same time, the upper and lower bases of the each elementary cell (2 point) are moving down and they do not take part in the fracture processes. Since the bases are 30 % of the mass of the unit cell, the partial removal would improve the efficiency of these structures while mitigating the blast energy.

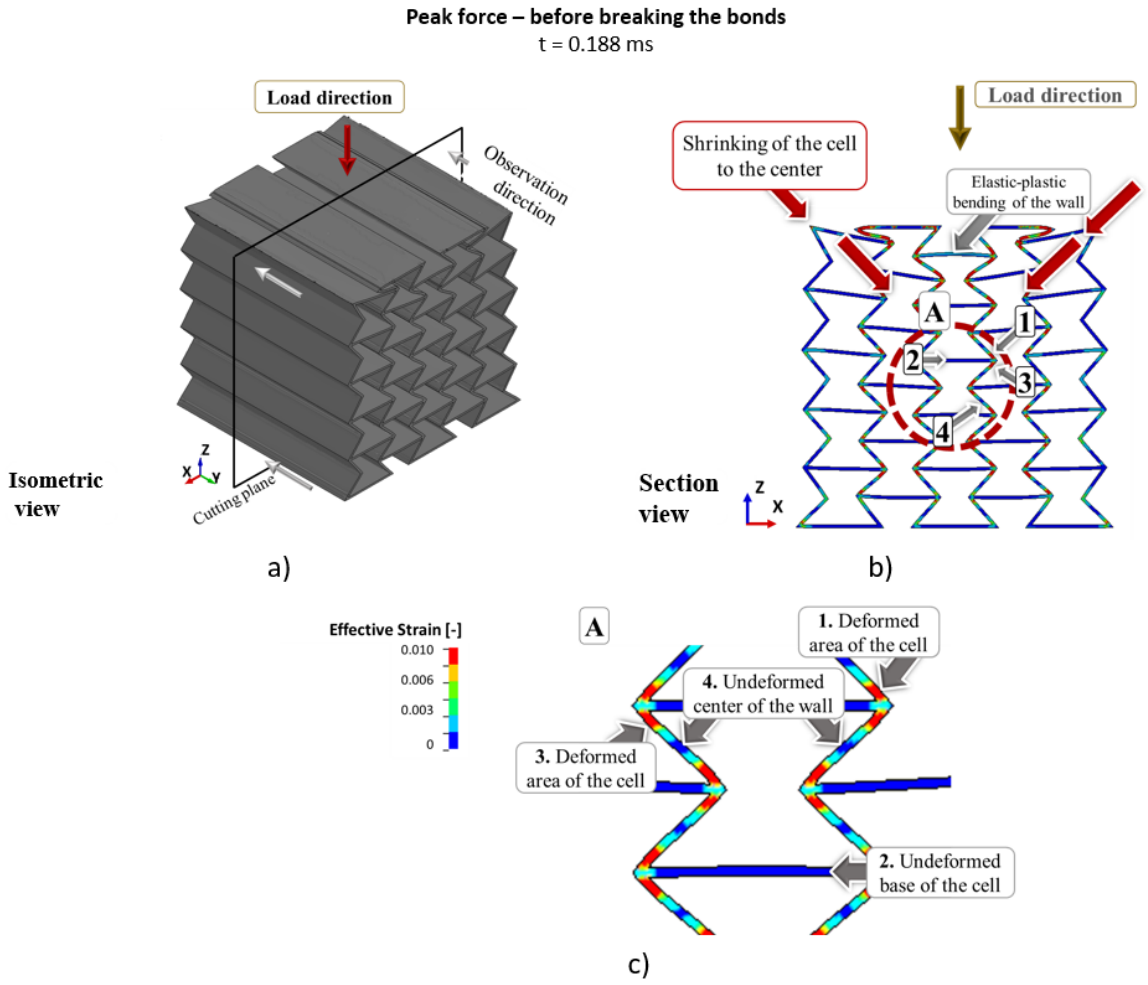

Figure 5.36: *Analysis of the effective strain results, (a) obtained by the auxetic structure during the blast loading, (b) presented in the cross-section view of the sample, and (c) focusing on the single cell.*

The foam structure is characterized by a much more complex collapse mode as shown in Figure 5.39. The shear bands of the entire structure are clearly visible on the effective strain map Fig. 5.39a. It is due to the stress concentrations occur between the vertexes at the each cell face. The unit cell geometry is characterized by the most intricate shape compared to other types of the discussed structures. It consists of 14 walls with two types of holes in the center of each face. In addition, the shear bands are shown in Figure 5.39b. They occur inside every single cell and travel from one cell vertex to the closest corner on the next face.

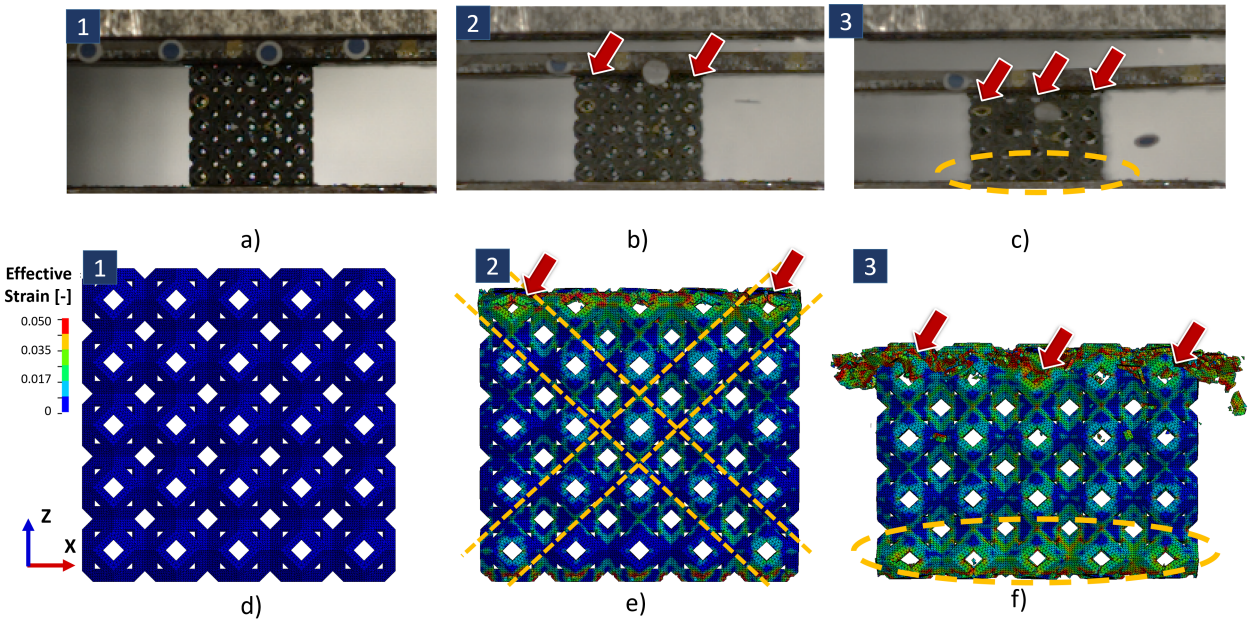

Figure 5.37: *Deformation mechanism correlation of the foam structure between (a-c) experimental photos with (d-f) numerical representation.*

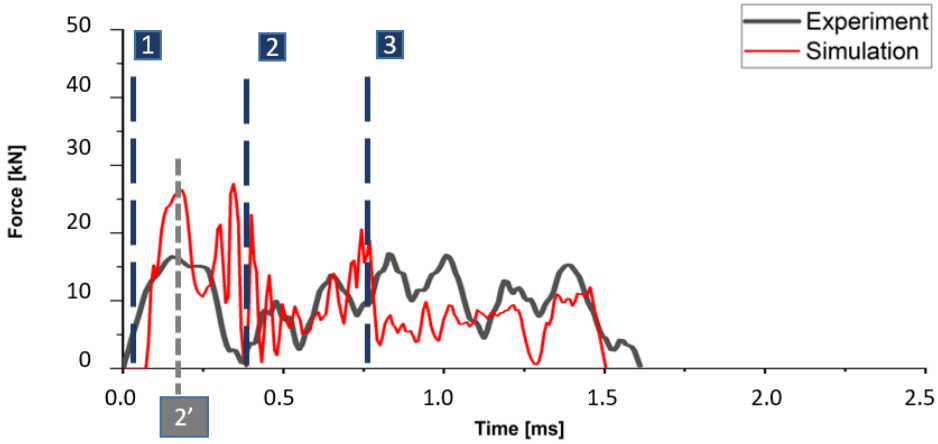

Figure 5.38: *Result comparison for the foam structure between the experiment and simulation with the point indication for Figures 5.37 and 5.39.*

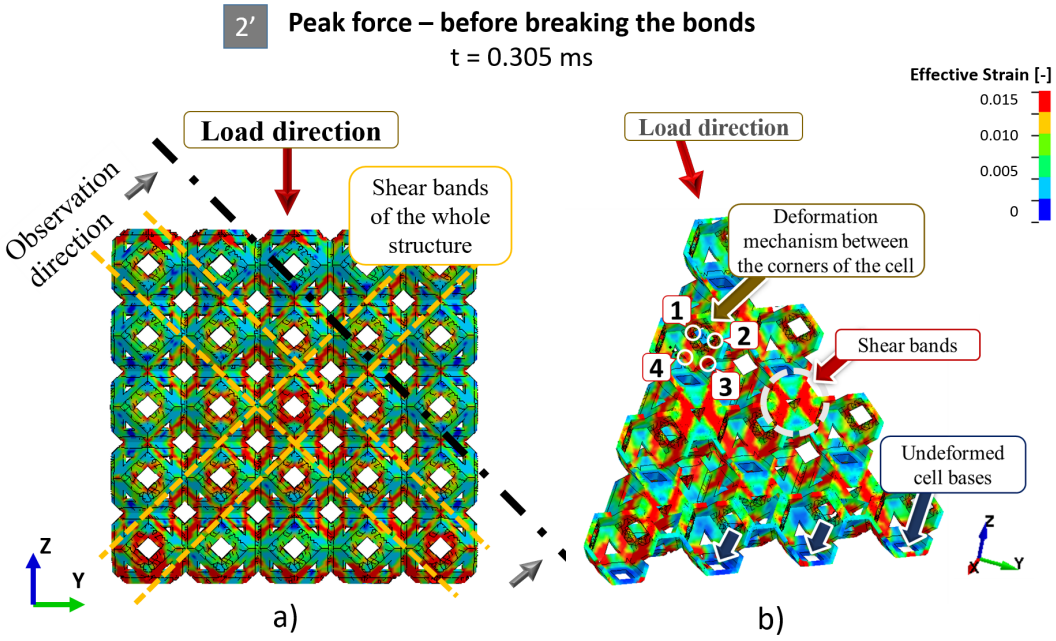

Figure 5.39: *Analysis of the effective strain results, (a) obtained by the foam structure during the blast loading, (b) presented in the cross-section view of the sample, and (c) focusing on the single cell.*

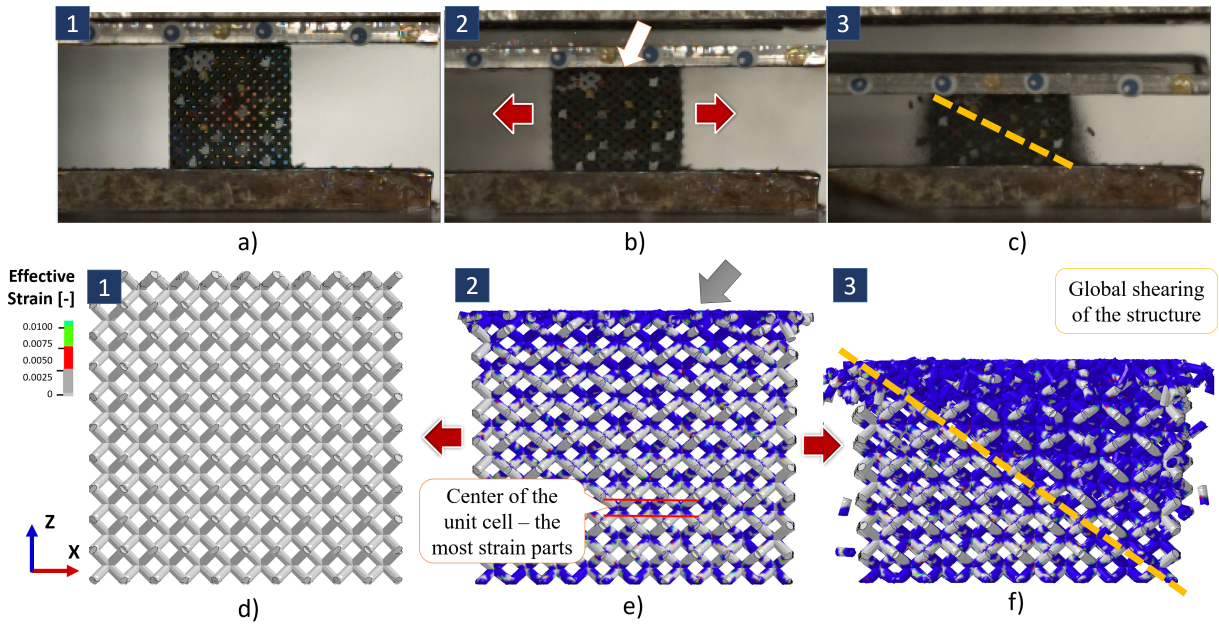

Figure 5.40: *Deformation mechanism correlation of the lattice structure between (a-c) experimental photos with (d-f) numerical representation.*

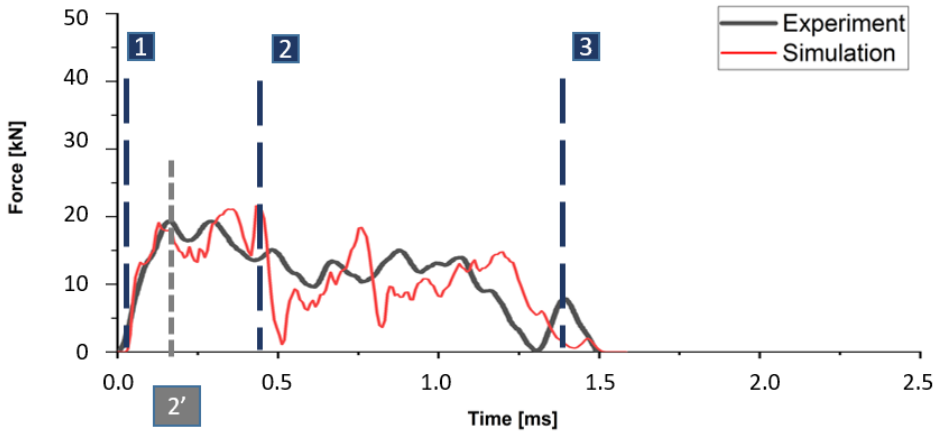

Figure 5.41: *Result comparison for the lattice structure between the experiment and simulation with the point indication for Figures 5.40 and 5.42.*

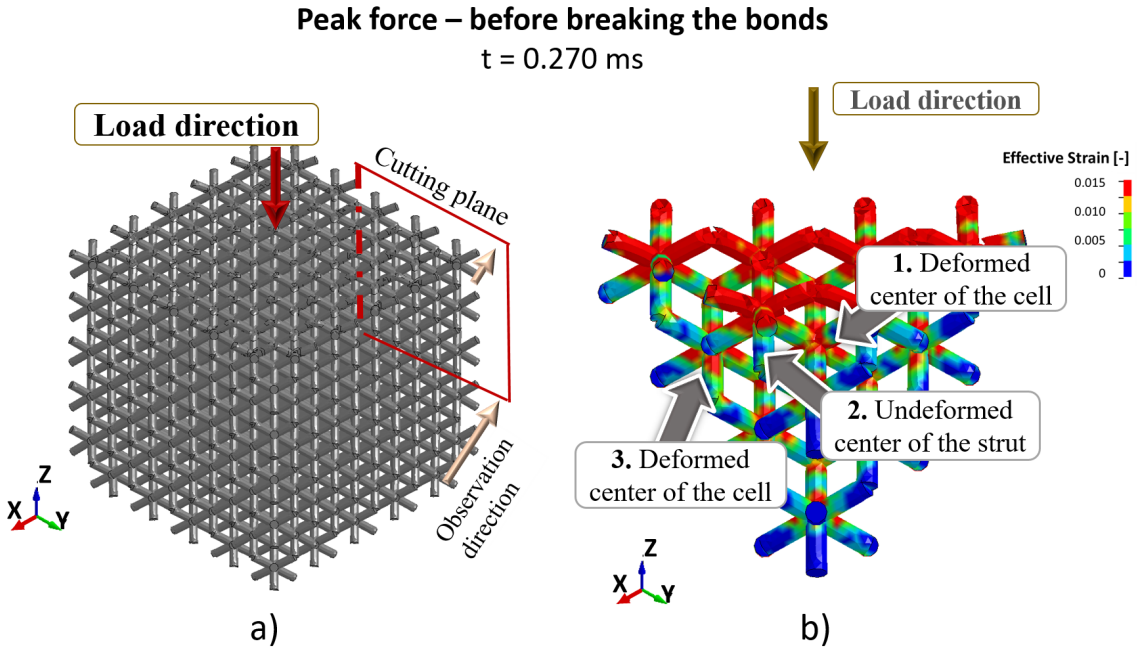

Figure 5.42: *Analysis of the effective strain results, (a) obtained by the lattice structure during the blast loading, (b) presented in the cross-section view of the sample, and (c) focusing on the single cell.*

The lattice like honeycomb and auxetic structures, is characterized by the striped deformation mode (Fig. 5.40). Except the first row which is the closest to the load, the strongest strains are visible in the center of the each cell (1 and 3 points). The center of the struts is almost undeformed (Fig. 5.42b). The simulation indicates that the damage and eventual fracture take place in the struts, close to the center of the whole cell. However, the bent struts met the struts from the cell below, which can prevent the bonds breaks. Therefore the lattice sample undergoes an extension of the entire structure – perpendicular to the load direction. Then, as the volume is

lower and mass remain almost the same, the relative density increases. Then, the global shearing is observed and the further process of the deformation is stopped. In the considered experiments, the samples have absorbed all amount of the generated energy during the explosion.

5.8 Chapter summary

The presented numerical simulations in this chapter concern an explosive test performed on the AM structures, as well as on the aluminum thin-walled honeycomb. The numerical investigation explains both the mechanism of the cell deformation and further fracture processes.

The fundamental study on the conventional structure allows estimating the influence of several parameters that affect simulations (Section 5.4). It has been proven that the selected the selected types of contact and part elements, as well as the developed boundary conditions provide consistent results. Section 5.3 exhibits that the reverse engineering method can be applied to estimate the unknown material model. The developed simulation shows the mechanism of the fold formation that cannot be analyzed during experimental dynamic loading. The shock waves travel along with the height of the structure until the stresses achieve the maximum value, forming the first fold. Since then, the deformation is localized, and subsequent folds occur to the full densification of the structure. The observed differences between the numerical and experimental results may be a consequence of the measurement method applied in the test or the imprecise parameters. The presented study on the conventional structure indicates the geometrical discrepancies between the actual and ideal structures (Section 5.4.6). The observed phenomena have been helpful in the simulation of the AM structures, in which the geometrical inaccuracies significantly influence the obtained results (Section 5.7.1). The numerical analysis have indicated the problem with the differences in dimensions of AM samples. However, after adjusting the wall thickness of the AM sample to the measured mass, all simulations are characterized by the accurate results.

In addition, the numerical simulations allow a deeper analysis of deformation modes, indicate the stress concentration, and show the largest deformations of each structure (Section 5.7.4). It has been observed that the honeycomb is characterized by the stretching of the cells outwards, and the auxetic structure by the folding of the cell towards their center. The bending of the struts is visible for the lattice structure, and the foam is characterized by the deformation mechanism that occurs between two vertexes of the cell. Moreover, the numerical results indicate non-strained areas for each structure which removal should not change the mechanism of the blast energy absorption, but may improve the SEA parameter. Therefore, the conducted research could be beneficial for further research on the geometry optimization of structures applied to attenuate explosive waves.

Bibliography

[1] C. Labra, E. Onate, J. Zarate, and J. Rojek. *Modelling and simulation of the effect of blast loading on structures using an adaptive blending of discrete and finite element methods*, pages 457–465. 2011.

[2] Ch. C. Roth, T. Fras, and D. Mohr. Dynamic perforation of lightweight armor: Temperature-dependent plasticity and fracture of aluminum 7020-t6. *Mechanics of Materials*, 149:103537, 2020.

[3] J. Donea, A. Huerta, J.-Ph. Ponthot, and A. Rodriguez-Ferran. Arbitrary lagrangian–eulerian methods. *Encyclopedia of computational mechanics*, 2004.

[4] J. D. Littell, K. Jackson, M. Annett, M. D. Seal, and E. Fasanella. The development of two composite energy absorbers for use in a transport rotorcraft airframe crash testbed (tract 2) full-scale crash test. *Annual Forum Proceedings - AHS International*, 2:984–1001, 01 2015.

[5] M. Silcock, W. Hall, B. Fox, and N. Warrior. Finite element modelling of metallic tubular crash structures with an explicit code. *International Journal of Vehicle Safety*, 1, 01 2006.

[6] A. Rabiee and H. Ghasemnejad. Finite element modelling approach for progressive crushing of composite tubular absorbers in ls-dyna: Review and findings. *Journal of Composites Science*, 6(1), 2022.

[7] Suri Bala. Contact force output to rcforc, 2019. https://www.d3view.com/ [Online; accessed 20.12.2021].

[8] A. Haufe, K. Schweizerhof, and P. Dubois. Properties and limits: Review of shell element formulations. 09 2013.

[9] Livermore Software Technology Corporation. *LS-Dyna Keyword user s manual*, 2016.

[10] quora. What is the hourglass effect in finite element analysis, 2021. https://www.quora.com [Online; accessed 18.11.2021].

[11] CEL COMPONENTS S.R.L. Honeycomb panels, 2019. https://www.honeycombpanels.eu/en/products/honeycomb/aluminium [Online; accessed 28.11.2019].

[12] Livermore Software Technology Corporation. *LS-Dyna Keyword user s manual*, 2016.

[13] G. R. Johnson and W. H. Cook. A constitutive model and data for metals subjected to large strains, high strain rates, and high temperatures. In *Proceedings of 7th International Symposium on Ballistics*, April 1983.

[14] I. Kikuo, S. Toshiro, Tomoyuki S., H. Hidemitsu, and H. Yasuaki. A study on mechanical properties of aluminum alloy. *Tokyo Institute of Technology*, 2003.

[15] metal.matdb.jp. Aluminum handbook, 2019. http://metal.matdb.jp/ [Online; accessed 01.08.2019].

[16] ASM International. *Atlas of Stress-Strain Curve*, 2002.

[17] M. Ando, Y. Suzuki, and G. Itoh. Effects of magnesium addition on threshold stress of al-mn alloys. *Journal of The Japan Institute of Light Metals*, 62:300–305, 2012.

[18] K. Higashi, T. Mukai, K. Kaizu, T. Shin, and T. Shinji. High strain-rate deformation characteristics in commercial aluminium alloys. *The Society of Materials Science.*, 39(447):1619–1624, 1990.

[19] G. Chintala and P. Gudimetla. Optimum material evaluation for gas turbine blade using reverse engineering (re) and fea. *Procedia Engineering*, 97:1332–1340, 2014. "12th Global Congress on Manufacturing and Management" GCMM - 2014.

[20] S. Nemat-Nasser, M. R. Amini, J. Y. Choi, and J. Isaacs. Experimental and computional evaluation of compressive response of single and hex-arreayed aluminum tubes. *Journal of Mechanics of Material and Structures*, 2:1910, 2007.

[21] M. Stanczak, T. Fras, L. Blanc, P. Pawlowski, and A. Rusinek. Numerical modelling of honeycomb structure subjected to blast loading. Number 115, pages 1–10. 12th European LS-DYNA Conference, Copyright by DYNAmore GmbH, May.

[22] T. Fras, A. Rusinek, R. Pecherski, R. Bernier, and T. Jankowiak. Analysis of friction influence on material deformation under biaxial compression state. *Tribology International*, 80:14–24, 12 2014.

[23] A. A. S. M. Ashab, D. Ruan, G. Lu, and A. A. Bhuiyan. Finite element analysis of aluminum honeycombs subjected to dynamic indentation and compression loads. *Materials (Basel, Switzerland)*, 9(3), March 2016.

[24] Robert-Stirling-Ring 1. Material data sheet: Eos aluminium alsi10mg, 2014. https://fathommfg.com/wp-content/uploads/2020/11/EOS 07.04.2020].

[25] S.I. Shakil, A. Hadadzadeh, B. S. Amirkhiz, H. Pirgazi, M. Mohammadi, and M. Haghshenas. Additive manufactured versus cast alsi10mg alloy: Microstructure and micromechanics. *Results in Materials*, 10:100178, 2021.

Chapter 6

Conclusions and perspectives

6.1 Conclusions

Protection against explosives and ballistic threats is a issue that should still be developed in the civil and military fields. The main objectives of this thesis are the studies of the effectiveness of the different absorbers to improve the protective system subjected to dynamic loading. As additive manufacturing ensures great freedom in design, therefore is a promising technique for increasing the energy absorption potential. Protective structures can be optimized by reducing weight through carefully designed components or by simplifying the manufacturing process. To achieve this goal, it is necessary to study the production technique possibilities and compare the absorption potential of selected structures subjected to different load conditions. In this thesis, three main themes are highlighted in order to conduct the investigation:

a) the identification of the general features of the blast treats and the characterization traditional used protective systems;

b) the determination of the main mechanical properties of the selected structure manufactured additively under quasi-static and blast loading;

c) the studies on the used manufacturing method and its impact on the microstructure of the printed AlSi10Mg components.

In **Chapter 1**, the mechanism of the blast wave formation and its influence on the absorbing structures are analyzed. The most well-known techniques of studying the wave phenomena have been described. In addition, the state of the art in energy absorbers and traditional blast protection systems are identified. The general response of metallic cellular structures to a compressive load and the ways of comparison of their mechanical properties are determined. It is found that cellular structures exhibit good characteristics to mitigate the explosive energy. They can provide a good strength to weight ratio. Therefore, the thesis is focused on the metamaterials studies of the honeycomb, auxetic, lattice and foam, manufactured by the DMLS technique. The interest in investigation of the protective features is divided on the structures composed with 2D and 3D unit cells. The selected samples are determined as the efficient and frequently used in protective systems on the market.

Secondly, the literature review of the additive manufacturing technology can be found in **Chapter 2**. The main AM methods, their general characteristics, process steps and possible material types are distinguished. The main focus is put on the DMSL method that has been used to fabricate the tested structures. The effect of the process parameters on the mechanical properties, possible defects and obtained microstructure are highlighted. In addition, a review of the literature allowed to determine the machine settings used in the EOSINT M280 system for AlSi10Mg powder, which contributed to the achievement of the density of 99 % of the final parts. In addition, it has been found that post-processing can affect material properties such as increasing the elongation to break.

Chapter 3 focuses on the material behavior of the used AlSi10Mg aluminum alloy and the influence of the print process and the external conditions on the obtained mechanical results. The dynamic and quasi-static compression tests, as well as quasi-static tensile tests have been carried out on the samples manufactured at different print direction to the build platform. The performed tests at the wide range of the strain rate and temperature changes prove that the sample orientation influences the strength results significantly. The stress-strain compression results increase, when the slop of the printed samples increase. However, the opposite trend

is observed during the tensile tests. The horizontally printed samples obtain about 80 MPa higher strength results compared to those printed vertically. However, the elongation to break is reduced by about 7 %. In addition, it is observed that the printed aluminum is only slightly sensitive to the changes in the strain rate. When the temperature increases from room condition up to 200 °C, the ultimate tensile strength can decrease twice.

Microstructure analysis of the as-fabricated and heat-treated samples allow to explain some of the observed phenomenas. A clear correlation between the microstructure anisotrophy induced by the AM process and the mechanical properties is noticed. The shape of the melt pools depends on the side of the observed sample. The performed heat treatment causes the precipitation Si grains from the Al/Si matrix. The Si particles become larger across the fine cellular structure which influences the macroscopic behavior of the manufactured samples.

The obtained material characteristics of the printed AlSi10Mg aluminum at such a wide range of external conditions complement a gap in the research on this alloy applied to the additive techniques. The obtained results prove the complexity of the material behavior. Subsequently, it was found that the Johnson-Cook model cannot sufficiently reproduce the obtained characteristics. Therefore, the modified JC phenomenological constitutive model is proposed based on the experimental results. Consequently, the average error between the experiments and analytically results for all material characteristics is minimized to 3 %.

Chapter 4 thoroughly describes the EDST test stand, emphasizing the physical aspects occurring during the explosive experiments. The knowledge gained about the behavior of the conventionally used, thin-walls, metallic honeycomb structures under the quasi-static and blast loading allows conducting an experimental campaign of the AM structures. A considerable influence of a sample topology on the deformation process is proven. The result comparison is based on the honeycomb, auxetic, lattice, and foam structures. The calculated values of the Specific Energy Abortion (SEA) parameter prove that the tested structures characterized by the 3D unit cells demonstrate a great potential to be designed as ultralight absorbers. In addition, for the 2D metamaterials, the mitigation of the explosive energy depends on the load direction. Comparing the absorptive properties between the AM and thin-wall metallic structures proves that AM structures can absorb at least twice as much energy when subjected to similar blast loading. Whereby, the sample dimensions, like height, can be significantly reduced.

A more detailed analysis of cell deformations is conducted in **Chapter 5** using the numerical simulations in LS-DYNA. The numerical task development for each structure subjected to the blast wave allows for an in-depth discussion of the deformation modes and proves the experimental results. The correlation of the experimental and numerical results shows that the honeycomb is characterized by the stretching of the cells outwards. The cell folding towards the center of the structure is observed for the auxetic. The bending of the struts is visible for the lattice structure, and the deformation mechanism characterizes the foam that occurs between two corners of the cell. The stretching of the whole 3D structures in the direction perpendicular to the explosive load and the global shear modes are also observed.

The research clearly shows that the 3D structures are more effective absorbers during an explosion than the tested 2D structures. It is proven that they can transmit higher force distributed evenly. In addition, the stress-strain results, the EA and SEA parameters have shown that the foam and lattice structures cause an increase in the energy absorption capacity to mitigate the blast effects. The numerical analysis deals in more detail with the deformation modes. The structure composed of struts due to their bending allows a sample to be globally stretched in the opposite direction to the force applied. While 2D structures loaded in the in-of-plane direction are characterized by the progressive folding of cells, reducing internal deformations.

Therefore, the strength of structures decreases. Moreover, it has been proven, based on the example of honeycomb geometry, that the structures produced additively can obtain several times more beneficial results compared to those produced by conventional methods.

6.2 Perspectives

Additive manufacturing is a promising technology that can contribute to designing superior protective structures. The conducted investigation proved that the efficiency of mitigating explosive energy could be significantly increased using AM structures compared to structures produced by traditional methods. However, the thesis also highlights several issues that still need to be improved or eliminated in order to use this technology effectively for mass production.

6.2.1 Additive manufacturing process

Material

The printed parts from used AlSi10Mg powder are characterized as brittle-ductile, and the fracture is a combination of both these modes. The enhance of the ductile and elongation of the plastic deformation before the breaking of the bones would significantly improve the toughness and minimize the peak stress. A powder used plays one of the most critical roles in the obtained mechanical properties. Therefore, changing the material to another one, characterized by better ductile properties, such as 316L Steel or Inconel 718, may improve the energy absorption capacity of the discussed structures. However, it should be taken into account that the mentioned materials are characterized by a lower volumetric energy density. Therefore, the porosity would increase, contributing to the design of parts with more internal defects. In addition, the printing process can be much more complicated, and it would require facing the additional challenges. Consequently, the whole experimental campaign should be repeated.

When considering the tested alloy, the post-processing, such as a heat treatment also can contribute to increase the ductility. The additional advantage is the stress relieving and minimization of the anisotropy. However, as it has been proven in this thesis, the annealing process causes the decreasing the hardness. It should be mentioned that only T6 type of post-process is considered in this research. Based on the literature review, only a few comprehensive works have currently been done to study the influence of heat treatment processes on the mechanical properties for the printed AlSi10Mg alloys. Therefore, it would be beneficial to investigate the influence the effects of more complex processes like a solid solution at higher temperature and then an artificial aging. In addition, it can be found in the literature that for some powders, the cooling process may resulted in a "non-equilibrium state" which can created microstructure with included a dislocation network. It can make an AM metal part much stronger, without reducing ductility.

The accuracy of the produced parts

The primary barrier for applying the AM structure in the blast protective systems may be the lack of the proper geometry accuracy of the printed components. It affects the stiffness of the structures, which can influence the amount of the transmitted force. These structures

are also characterized by the large amounts of local defects and high roughness. Therefore, the repeatability of the results can vary significantly and an additional complex post-processing may be required. The accuracy of the print depends on the material used and the process parameters that must be compatible with the powder and manufacturing method. In addition, the 5-axis printers can be a solution that allows reducing the problem of the difference in the inclination of the sample to the laser beam direction.

Transverse isotropic

Due to the layer method of manufacturing, the structures are characterized as a transversely isotropic material. This type of an anisotropy influences the macroscopic results like strength or elongation to break. Homogenization of mechanical properties would eliminate the distinction of the properties from the direction of force application. In order to eliminate the distinction of the mechanical properties from the applied force direction, extensive homogenization research must be done. As proven in the thesis, the print direction is the key factor significantly affects the obtained results. Moreover, the strength differential effect has been confirmed. The material strength depends on the load conditions.

6.2.2 Material model implementation

The proposed constitutive model developed during the course on this thesis is a promising issue to extend the scope of research on various geometries of the structures manufactured additively from the AlSi10Mg aluminum. The material model in a numerical task in this investigation is based on actual data. The advantage of this solution is the complementarity of the material behavior with the experimental results. However, such a solution has been possible for these particular structures, as their geometries are composed of the parts printed at the angle of 0°, 45°, and 90° to the build platform. The challenge now is to develop the relationship for the alloy, which would link the material behavior and print direction. Then, the implementation into a numerical program would significantly contribute to increasing the efficiency of studies and speed up the time needed to obtain correct results.

6.2.3 Topology optimization

The doctoral thesis focused on the studies four different types of samples that represent 2D and 3D cell complex structures. The advanced software allows mathematically optimizing the structure geometry to design a new shape for a given space at defined boundary conditions. The optimization program is based on the finite element method (FEM), similar to the numerical simulation. The optimization task uses gradient-based or non-gradient-based algorithms to evaluate the design performance. Nowadays, the technique is widely applied in aerospace, biochemical and civil engineering. The performed studies have indicated the limits of the absorption capabilities of each of the tested structures and clarified their deformation modes. The research constitutes the fundamental knowledge for another experimental campaign on topological optimization. The aim of further tests could be the mass reduction of the samples without affecting the force transmitted.

6.2.4 Further experimental tests

Chapter I discusses various experimental techniques. In this work, small-scale tests of the blast wave are performed. In order to implement AM structures in the protective systems, the experimental champagne should be carried out under "free-air" conditions. Both the absorption capacity of such structures under real conditions must be checked, and the safety requirements must be met.

The thesis has proven that the structures fabricated by the advanced methods of additive manufacturing can be more efficient than traditionally used absorbers when subjected to the same load condition. However, the technology itself still requires improvement and further research. The results presented in the thesis discuss in detail many issues related to the energy absorption caused by the blast wave. Therefore, the published results and analysis constitute a basis for developing a new class of absorbers to mitigate the energy causes explosion.

Below the publications related to this doctoral Thesis are listed:

- Stanczak M., Fras T., Blanc L., Pawlowski P., Rusinek A. (2021) *Numerical and experimental study on mechanical behavior of the AlSi10Mg aluminum structures manufactured additively and subjected to a blast wave*, DYMAT 2021, Madrid, Spain, https://doi.org/10.1051/epjconf/202125002017
- Stanczak M., Fras T., Blanc L., Pawlowski P., Rusinek A. *Blast-induced compression of a thin-walled aluminum honeycomb structure – experiment and modeling*, Metals 2019, 9(12), 1350; doi:10.3390/met9121350
- Stanczak M., Fras T., Blanc L., Pawlowski P., Rusinek A. (2019) *Numerical modelling of honeycomb structure subjected to blast loading*, 12th European LS-DYNA, Koblenz, Germany, 115
- Stanczak M., Rusinek A., Broniszewska P., Fras T., Pawlowski P. *Influence of strain rate and temperature on the mechanical behavior of additively manufactured AlSi10Mg alloy – experiment and the phenomenological constitutive modelling*, Bulletin of the Polish Academy of Sciences: Technical Sciences (forthcoming, accepted: 06.2022)

Seminars and conferences:

- Conference: 12th European LS-DYNA Conference: Stanczak M., Fras T., Blanc L., Pawlowski P., Rusinek A. "Numerical modelling of honeycomb structure subjected to blast loading." Koblenz, Germany, 14-16 May 2019
- Symposium: 8th Budding Science Colloquium at ISL: Stanczak M., Fras T., Blanc L. Pawlowski P., Rusinek A. Study on behavior of an aluminum honeycomb structure applied to absorb blast loadings." Saint-Louis, France, 25-26 September 2019
- Business Convention: 9th edition of APS Meetings – Advanced Prototyping Solutions, Lyon, France, 07-08 October 2020
- Symposium: 9th Budding Science Colloquium at ISL: Stanczak M., Fras T., Blanc L. Pawlowski P., Rusinek A. "Experimental and numerical studies on behavior of additively manufactured structures at different conditions." Saint-Louis, France, 25-26 November 2020
- Conference: DYMAT 2021 - 13th international conference on mechanical and physical behaviour of materials under dynamic loading: Stanczak M., Fras T., Blanc L., Pawlowski P., Rusinek A. "Numerical and experimental study on mechanical behaviour of the AlSi10Mg aluminium structures manufactured additively and subjected to a blast wave." Madrid, Spain, 20-24 September 2021
- Symposium: 10th Budding Science Colloquium at ISL: Stanczak M., Fras T., Blanc L. Pawlowski P., Rusinek A. "Behaviour of additively manufactured metallic structures under blast loading.", Saint-Louis, France, 28-29 September 2021

- Symposium: European Military Additive Manufacturing Symposium: Stanczak M., Fras T., Blanc L. Pawlowski P., Rusinek A. "Study on the Energy Absorptoion Properties of the Additively Manufactures Aluminium Structures Subjected to a Blast.", Bonn, Germany 12-13 October 2021
- Thesis symposium at the Military University of Technology, Stanczak M., Fras T., Rusinek A. "Behaviour of additively manufactured metallic structures under blast loading" Warsaw, Poland, 03 November 2021

Appendix A

LS–DYNA Keyword File For AM Structure

```
*KEYWORD

*TITLE
    AM STRUCTURE SIMULATION

*PARAMETER
    R term 0.001500
    R dtime 8.0E-8      R bintime 8.0E-8
    R tfris 0.3      R tfrid 0.2      R bfris 0.5      R bfrid 0.4

*CONTROL_ACCURACY
    OSU      INN      PIDOSU      IACC
    0          4        0             0

*CONTROL_BULK_VISCOSITY
    Q1      Q2      TYPE      btype
    1.5      0.06      -2      0

*CONTROL_CONTACT
    SLSFAC RWPNAL ISLCHK SHLTHK PENOPT THKCHG ORIEN ENMASS
    1.0       0.0          1        0          0          0          1        0

*CONTROL_ENERGY
    HGEN      RWEN      SLNTEN      RYLEN
    2            2          2            2

*CONTROL_HOURGLASS
    IHQ      QH
    5          0.04

*CONTROL_SOLID
    ESORT   FMATRX   NIPTETS   SWLOCL   PSFAIL   T10JTO
    1          0            4            1            0          0.0

*CONTROL_TERMINATION
    ENDTIM      ENDCYC      DTMIN      ENDENG      ENDMAS
    & term        0             0.0          0.0           0.0
```

```
*DATABASE_GLSTAT
    DT              BINARY      LCUR      IOOPT
    & dtime         1             0         1

*DATABASE_MATSUM
    DT              BINARY      LCUR      IOOPT
    & dtime         1             0         1

*DATABASE_NODFOR
    DT              BINARY      LCUR      IOOPT
    & dtime         1             0         1

*DATABASE_RBDOUT
    DT              BINARY      LCUR      IOOPT
    1.00000E-5      1           0         1

*DATABASE_RCFORC
    DT              BINARY      LCUR      IOOPT
    & dtime         1             0         1

*DATABASE_SLEOUT
    DT              BINARY      LCUR      IOOPT
    & dtime         1             0         1

*DATABASE_BINARY_D3PLOT
    DT              LCDT      BEAM      NPLTC      PSETID
    & bintime       0         0         0          0

*INITIAL_LOAD_NODE_SET
    NSID      DOF      LCID      SF        CID       M1        M2        M3
    1         3         1        -1.0      0         0         0         0

*CONTACT_AUTOMATIC_SURFACE_TO_SURFACE_ID
    CID       TITLE
    1           Structure RarePlate
    SSID MSID SSTYP MSTYP SBOXID MBOXID SPR MPR
    1      3      3       3       0       0       0      0
    FS        FD        DC      VC      VDC      PENCHK      BT      DT
    & bfris   & bfrid   0.0     0.0     0.0      0           0.0     1.00000E20
    SFS       SFM       SST     MST      SFST      SFMT      FSF       VSF
    1.0       1.0       0.0      0.0     1.0        1.0      1.0       1.0

*CONTACT_AUTOMATIC_SURFACE_TO_SURFACE_ID
    CID       TITLE
    2           Structure FrontPlate
    SSID MSID SSTYP MSTYP SBOXID MBOXID SPR MPR
    1      2      3       3       0       0       0      0
    FS        FD        DC      VC      VDC      PENCHK      BT      DT
```

```
    & tfris   & tfrid     0.0      0.0      0.0          0        0.0      1.00000E20
    SFS       SFM       SST       MST       SFST       SFMT       FSF       VSF
    1.0       1.0       0.0       0.0       1.0         1.0       1.0       1.0

*CONTACT_AUTOMATIC_SURFACE_TO_SURFACE_ID
    CID       TITLE
    2           FrontPlate RarePlate
    SSID MSID SSTYP MSTYP SBOXID MBOXID SPR MPR
    2      3      3      3      0      0      0      0
    FS         FD         DC       VC       VDC       PENCHK       BT       DT
    & tfris   & tfrid     0.0      0.0      0.0          0          0.0      1.00000E20
    SFS       SFM       SST       MST       SFST       SFMT       FSF       VSF
    1.0       1.0       0.0       0.0       1.0         1.0       1.0       1.0

*CONTACT_AUTOMATIC_SINGLE_SURFACE_ID      CID      TITLE
    4           Structure
    SSID MSID SSTYP MSTYP SBOXID MBOXID SPR MPR
    1      0      3      0      0      0      0      0
    FS         FD         DC       VC       VDC        PENCHK       BT       DT
    0.13       0.1       0.0       0.0      0.0          0          0.0      1.00000E20
    SFS       SFM       SST       MST       SFST       SFMT       FSF       VSF
    1.0       1.0       0.0       0.0       1.0        1.0        1.0       1.0

*SECTION_SOLID
    SECID      ELFORM      AET
    1            1           0

*MAT_PIECEWISE_LINEAR_PLASTICITY
    AlSi10Mg
    MID       RO          E          PR       SIGY      ETAN      FAIL          TDEL
    4        2.67E-9      75000.0   0.33      270.0     0.0       1.00000E21    0.0
    C          P          LCSS      LCSR      VP        LCF
    5.0E05     6.0        8         0         0.0       0

*PART
    FrontPlate
    PID    SECID    MID    EOSID    HGID    GRAV    ADPOPT    TMID
    4      1        2      0        0       0       0         0

*MAT_SIMPLIFIED_JOHNSON_COOK
    Steel 4340
    MID       RO             E           PR          VP
    2          7.86000E-9    209000.0    0.28        0.0
    A          B          N          C         PSFAIL     SIGMAX    SIGSAT        EPSO
    792.0      510.0      0.26       0.014     1.0        1.00000E28  1.00000E28    1.0

*MAT_ADD_EROSION
    MID    EXCL    MXPRES    MNEPS    EFFEPS    VOLEPS    NUMFIP    NCS
```

```
  4      999.0      999.0      999.0        0.1        999.0        1.0          1.0
  MNPRES   SIGP1   SIGVM   MXEPS   EPSSH   SIGTH   IMPULSE   FAILTM
  999.0      999.0      999.0      999.0      1.0        999.0      999.0        999.0

*MAT_RIGID_TITLE
    Rigid steel
    MID      RO              E            PR      N      COUPLE      M
    2          7.86000E-9      209000.0      0.28      0.0      0.0          0.0

*DEFINE_STOCHASTIC_VARIATION
    ID_SV   PID   PID_TYP   ICOR   VAR_S   VAR_F
    1          1      0            0        0            0
    R1      R2      R3
    0.0      0.0      0.0
    R1      R2      R3
    0.0      0.0      0.0

*DEFINE_TABLE_TITLE
    AlSi10Mg
    TBID      SFA      OFFA
    8
    VALUE      LCID
    0.001        2
    0.01         3
    0.1          4
    1300.0       5
    2900.0       6

*DEFINE_CURVE_TITLE
    0.001/s
    LCID      SIDR      SFA      SFO      OFFA      OFFO      DATTYP      LCINT
    2          0          1.0       1.0      0.0          0.0          0          0
    a1            o1
    0.0          272.4271
    0.00134      288.6023
    0.00288      303.3938
    ...

*DEFINE_CURVE_TITLE
    0.01/s
    LCID      SIDR      SFA      SFO      OFFA      OFFO      DATTYP      LCINT
    3          0          1.0       1.0      0.0          0.0          0          0
    a1            o1
    0.0          274.536
    0.00148      290.8723
    0.00311      305.9124
    ...
```

```
*DEFINE_CURVE_TITLE
    0.1/s
    LCID      SIDR      SFA       SFO       OFFA      OFFO      DATTYP    LCINT
    4         0         1.0       1.0       0.0       0.0       0         0
    a1          o1
    0.0         281.8149
    0.00169     297.2863
    0.00365     311.4886
    ...

*DEFINE_CURVE_TITLE
    1300/s
    LCID      SIDR      SFA       SFO       OFFA      OFFO      DATTYP    LCINT
    5         0         1.0       1.0       0.0       0.0       0         0
    a1          o1
    0.0         292.6335
    0.00129     331.1607
    0.00211     346.8311
    ...

*DEFINE_CURVE_TITLE
    2900/s
    LCID      SIDR      SFA       SFO       OFFA      OFFO      DATTYP    LCINT
    6         0         1.0       1.0       0.0       0.0       0         0
    a1          o1
    0.0         301.8986
    0.00168     333.2064
    0.00369     360.8824
    ...

*DEFINE_CURVE_TITLE
    Initial_load
    LCID      SIDR      SFA       SFO       OFFA      OFFO      DATTYP    LCINT
    1         0         1.0       1.0       0.0       0.0       0         0
    a1          o1
    0.0         5.6
    ...
    0.00100     0.309102
    0.00105     0.282673
    0.00110     0.259122
    ...
    0.00440     8.2782399841e-004
    0.0045      9.2355301604e-005

*INCLUDE
    PART_GEOMETRY.k

*END
```